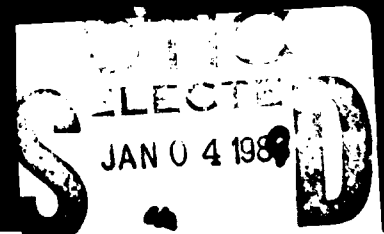
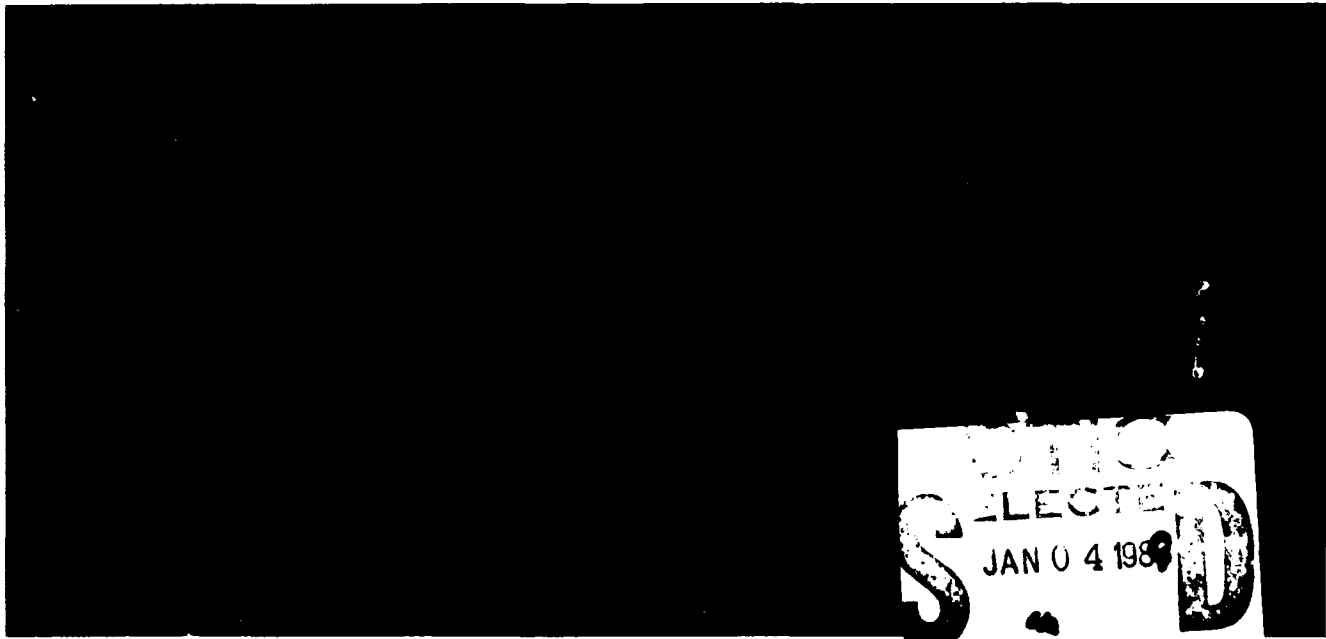


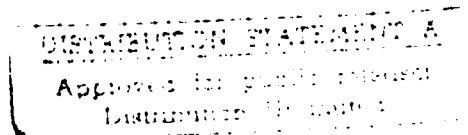
# World Materials Congress

1988

AD-A204 708



Published by



Proc. 574-50

# INCLUSIONS AND THEIR INFLUENCE ON MATERIAL BEHAVIOR

*Proceedings of a Symposium  
held in conjunction with the  
1988 World Materials Congress  
Chicago, Illinois, USA  
24-30 September 1988*

*Edited by*  
Ravi Rungta  
Battelle Columbus Division

*Sponsored by the  
International Metallographic Society  
and  
ASM INTERNATIONAL™*

*Published by*



88 12 28 024

The publication of this Conference Proceedings of the 1988 World Materials Congress has been made possible by the generous contributions of the U.S. Bureau of Mines, the U.S. Army Research Office, Cytemp Specialty Steel, ELETROMETAL S.A., and Dofasco Inc.

Copyright © 1988  
by  
ASM INTERNATIONAL™  
All Rights Reserved

No part of this book may be reproduced, stored in a retrieval system, or transmitted, in any form or by any means, electronic, mechanical photocopying, recording, or otherwise, without the prior written permission of the publisher. No warranties, express or implied, are given in connection with the accuracy or completeness of this publication and no responsibility can be taken for any claims that may arise.

Nothing contained in this book is to be construed as a grant of any right or manufacture, sale, or use in connection with any method, process, apparatus, product, or composition, whether or not covered by letters patent or registered trademark, nor as a defense against liability for the infringement of letters patent or registered trademark.

Library of Congress Catalog Card Number 88-071672  
ISBN: 0-87170-340-8  
SAN: 204-7586

Printed in the United States of America

UNCLASSIFIED

SECURITY CLASSIFICATION OF THIS PAGE (When Data Entered)

REPORT DOCUMENTATION PAGE		READ INSTRUCTIONS BEFORE COMPLETING FORM
1. REPORT NUMBER ARO 25297.8-MS-CF	2. GOVT ACCESSION NO. N/A	3. RECIPIENT'S CATALOG NUMBER N/A
4. TITLE (and Subtitle) 1988 World Materials Congress Proceedings 24-30 Sep 88, Chicago <u>Eight Volumes</u>		5. TYPE OF REPORT & PERIOD COVERED Final 1 Oct 87 - 31 Mar 89
7. AUTHOR(s) S. G. Fishman and A. K. Dhingra, editors		6. PERFORMING ORG. REPORT NUMBER N/A
9. PERFORMING ORGANIZATION NAME AND ADDRESS ASM International Detroit, MI 48202		8. CONTRACT OR GRANT NUMBER(s) DAAL03-87-G-0128
11. CONTROLLING OFFICE NAME AND ADDRESS U. S. Army Research Office P. O. Box 12211 <u>Research Triangle Park, NC 27709</u>		10. PROGRAM ELEMENT, PROJECT, TASK AREA & WORK UNIT NUMBERS N/A
14. MONITORING AGENCY NAME & ADDRESS (if different from Controlling Office)		12. REPORT DATE 1988
		13. NUMBER OF PAGES
		15. SECURITY CLASS. (of this report) Unclassified
		15a. DECLASSIFICATION/DOWNGRADING SCHEDULE
16. DISTRIBUTION STATEMENT (of this Report)  Submitted for announcement only.		
17. DISTRIBUTION STATEMENT (of the abstract entered in Block 20, if different from Report)		
18. SUPPLEMENTARY NOTES The view, opinions, and/or findings contained in this report are those of the author(s) and should not be construed as an official Department of the Army position, policy, or decision, unless so designated by other documentation.		
19. KEY WORDS (Continue on reverse side if necessary and identify by block number) Composites, Sheet Steels, Electronic Materials, Wear Resistance, Precipitation Phenomena, High Integrity Castings, Inclusions, HSLA Steels		
20. ABSTRACT (Continue on reverse side if necessary and identify by block number) The proceedings of the 1988 World Materials Congress were published by ASM and consists of the following volumes: 1. Microalloyed HSLA Steels Conference Proceedings, 2. Inclusions and Their Influence on Material Behavior, 3. High Integrity Castings 4. Precipitation Phenomena: Deformation and Aging, 5. Wear Resistance of Metals and Alloys (over)		

DD FORM 1 JAN 73 1473 EDITION OF 1 NOV 65 IS OBSOLETE

UNCLASSIFIED

SECURITY CLASSIFICATION OF THIS PAGE (When Data Entered)



ABSTRACT CONTINUED:

6. Electronic Materials and Processing .
7. Corrosion-Resistant Automotive Sheet Steels .
8. Cast Reinforced Metal Composites .

## ORGANIZING COMMITTEE

R. Rungta  
Battelle  
Columbus, Ohio  
*Program Organizer*

### Session Chairmen

W. E. White  
Ryerson Polytechnical Institute  
Ontario, Canada

E. W. Langer  
The Technical University of Denmark  
Lyngby, Denmark

### Session I Co-Chairmen

G. F. Vander Voort  
Carpenter Steel Division  
Reading, Pennsylvania

D. Dulieu  
BSC Swinden Laboratories  
South Yorkshire, England

### Session II Co-Chairmen

R. Rungta  
Battelle  
Columbus, Ohio

J. D. Boyd  
CANMET  
Ottawa, Canada

### Session III Co-Chairmen



Sold by:  
ASM International  
9639 Kinsman Road  
Metals Park, OH 44073  
Price:

DTIC	
COPY	
INSPECTED	
6	
NTIS - CHARI	J
LIB - TAG	<input type="checkbox"/>
PER - TAG	<input type="checkbox"/>
74.00 per call	
A-1 21	

## FOREWORD

Increasingly stringent requirements with regard to service performance of materials related to safety and reliability, and the threat of competitive materials has made manufacturers seek constant improvement in their product. A major aspect of such improvement has been to reduce the inclusion content of the material, in particular steels. While inclusions are mostly viewed as detrimental to the performance of the material, there are several applications where the inclusions play a very useful role. The symposium addresses processing, monitoring, controlling, and characterizing of inclusions. The emphasis, however, is on characterizing inclusions and their influence on a variety of material properties of steels.

The symposium has been jointly sponsored by the International Metallographic Society (IMS) and ASM INTERNATIONAL as a part of the '88 World Materials Congress. The encouragement and support provided by IMS officials in particular, Mr. Jim McCall, Mr. Robert J. Gray, Dr. R. D. Sisson, Jr., Dr. M. R. Louthan, Jr., Dr. W. E. White and Dr. G. F. Vander Voort is very much appreciated. I am thankful for the internal support of Dr. John Holbrook at Battelle for this meeting. Ms. Constance Laning provided excellent support as Meetings Coordinator at ASM. Finally, the authors are to be commended for meeting the stringent deadlines set by ASM.

Ravi Rungta  
Battelle Columbus Division

## TABLE OF CONTENTS

<b>Inclusions: Advantages, Disadvantages, and the Technological Trends</b> .....	1
R. Rungta, A. J. Skidmore, R. D. Buchheit	
<b>Characterization of Inclusions in Plate Steels and Their Influence on Mechanical Properties</b> .....	21
A. D. Wilson	
<b>Sulfur Content, Inclusion Chemistry, and Inclusion Size Distribution in Calcium Treated 4140 Steel</b> .....	35
D. W. Hetzner, B. A. Pint	
<b>Characterization of Inclusions in a Laboratory Heat of AISI 303 Stainless Steel</b> .....	49
G. F. Vander Voort	
<b>Beneficial Aspects of Inclusions in Alloys: Two Cases—Free Machining and Oxide Dispersion Strengthened Alloys</b> .....	65
A. Wolfenden, V. N. Cribb, C. L. Hough, B. O. Soepangkat	
<b>Inclusion Engineering for the Improved Machinability of Medium Carbon Steels</b> .....	73
S. V. Subramanian, Jiang Junpu, D.A.R. Kay	
<b>Analysis of Inclusions in Cast Co-Cr-Mo Alloy Used for Surgical Implants</b> .....	85
L. Z. Zhuang, E. W. Langer	
<b>A Review of Advances in Noninvasive Methods for Detection and Characterization of Inclusions</b> .....	93
L. J. House, R. Rungta	
<b>Sources of Errors in Particle Size Distribution Parameters</b> .....	109
D. B. Rayaprolu, D. Jaffrey	
<b>Measurement of Spatial Distribution of Inclusions</b> .....	123
M. T. Shehata, J. D. Boyd	
<b>Effect of Inclusion Distribution on the Initiation of Defects</b> .....	133
P. S. Steif, S. Iyengar	
<b>Rare Earth Inclusions and Cracking in ERW Pipe</b> .....	139
L. R. Cornwell, W. L. Bradley	

<b>The Role of Inclusions on Deformation and Fracture Under Tensile Stress in Steel . . . . .</b>	<b>143</b>
Z. R. He, L. Zheng	
<b>Roles of Inclusions in Steel for the Fatigue Properties and Machinability Problems . . . . .</b>	<b>149</b>
T. Araki	
<b>The Role of Inclusions in Corrosion Fatigue Crack Growth of Pressure Vessel Steels in High Temperature Reactor Water . . . . .</b>	<b>157</b>
H. Hänninen, M. Kemppainen, K. Törrönen	
<b>Plate-Like Rigid Inclusions and Ductile-Brittle Transition . . . . .</b>	<b>173</b>
Ing-Hour Lin	
<b>Inclusions and Their Influence on Corrosion and Corrosion-Assisted Fracture . . . . .</b>	<b>179</b>
W. E. White	
<b>Incidence of Aluminum Inclusions on the Occurrence of Seams in Hot and Cold Rolled Strip . . . . .</b>	<b>187</b>
R. Colas, E. Lee, J. Valdés, A. Valdés, H. Montemayor, A. M. Estrada, J. G. Arias, M. A. Cisneros	
<b>Nucleation of Acicular Ferrite on Oxygen-Rich Inclusions . . . . .</b>	<b>193</b>
M. Ferrante, K. Akune	

# INCLUSIONS: ADVANTAGES, DISADVANTAGES, AND THE TECHNOLOGICAL TRENDS

Ravi Rungta, Andrew J. Skidmore, Richard D. Buchheit

Battelle  
Columbus, Ohio 43201 USA

## ABSTRACT

The role of inclusions in the performance of materials is reviewed. While inclusions are advantageous for certain applications such as machining and oxide dispersion strengthened alloys, under uncontrolled conditions they can be deleterious to the performance of the material. Examples have been presented to show their influence on performance. Steel making techniques, inclusion monitoring, and inclusion identification techniques are discussed. Non-destructive inspection techniques present the best opportunities for ensuring the detection of deleterious inclusions during the processing of the material. It is the authors' view that in addition to the procedures that have been developed to improve the general cleanliness of metals with respect to certain types of inclusions, attention must be focused on defining critical size inclusions for various applications and efforts must be made to eliminate the critical size inclusions.

## INTRODUCTION

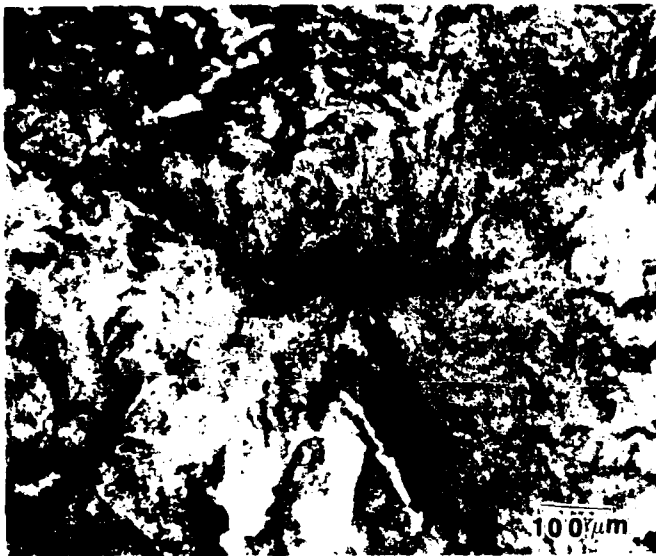
THE ASM HANDBOOK (1) defines non-metallic inclusions as particles of foreign material in a metallic matrix. The particles are usually compounds such as oxides, sulphides, or silicates, but may be any substance foreign to and essentially insoluble in the matrix. In his 1959 Howe Memorial Lecture, Sims (2) classified nonmetallic inclusions based on their origin as endogenous and exogenous. In general, the endogenous inclusions form by reactions in the molten metal and their formation is dictated either by additions to the molten metal or by changes in solubility during the solidification process. Oxides and sulphides are examples of endogenous non-metallic inclusions in steels and are controlled by the quantity of oxygen and

sulphur in solution in the melt (2-5). The exogenous inclusions in steels, on the other hand, occur as a result of trapping of slag, refractories, and oxidized metal that the liquid metal comes in contact with during the melting and casting process (2,3,5). Some of the characteristic features of exogenous inclusions in steels noted by Kiessling (3) are larger size compared to endogenous inclusions, sporadic occurrence, irregular shapes, and complex structures. Exogenous inclusions, in general, are harmful to material behavior.

The importance of inclusions is in their ability to adversely influence the behavior of materials and components in service. Examples of such influence are presented in Figures 1-4. The examples chosen here represent a range of applications where the presence of such inclusions compromise appearance, reliability, or safety. The failure of a gear tooth represents a reliability problem, the shell cracking and the associated detail cracking in rails represents a reliability as well as a safety problem (6,7), and the blemishes on a stainless steel due to the presence of copper and aluminum rich particles represents the compromising of appearance.

While more work has been done on inclusions in metals, a similar concern exists in ceramics. Pressureless sintering of SiC involves the use of sintering additives such as boron, carbon, and aluminum in various combinations. Inclusions of free carbon are found in the microstructure of sintered silicon carbide (SiC) and are believed to adversely influence the toughness of the material. Typically the inclusions are 1-2 microns in diameter but sizes as large as 10-20 microns have been observed (8).

While the examples cited relate to the negative influence of inclusions, there are several situations where inclusions serve a very useful role. Oxide dispersion strengthened alloys and free machining steels are two



(a) Fracture Surface



(b) Metallographic Section  
Through Crack Origin

Fig. 1 - Fatigue failure of 4340 steel gear tooth.  
Crack initiated at the slag inclusion

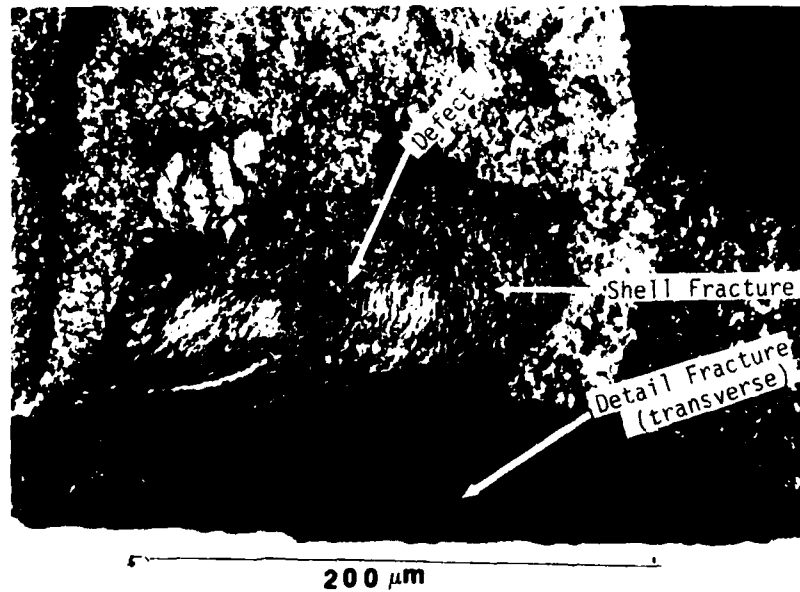


Fig. 2 - Shell fracture associated with detail fracture in a  
rail. The shell was initiated at the defect that was  
identified as a complex inclusion (6)

LT= 131 SECS

SP2 SHELL

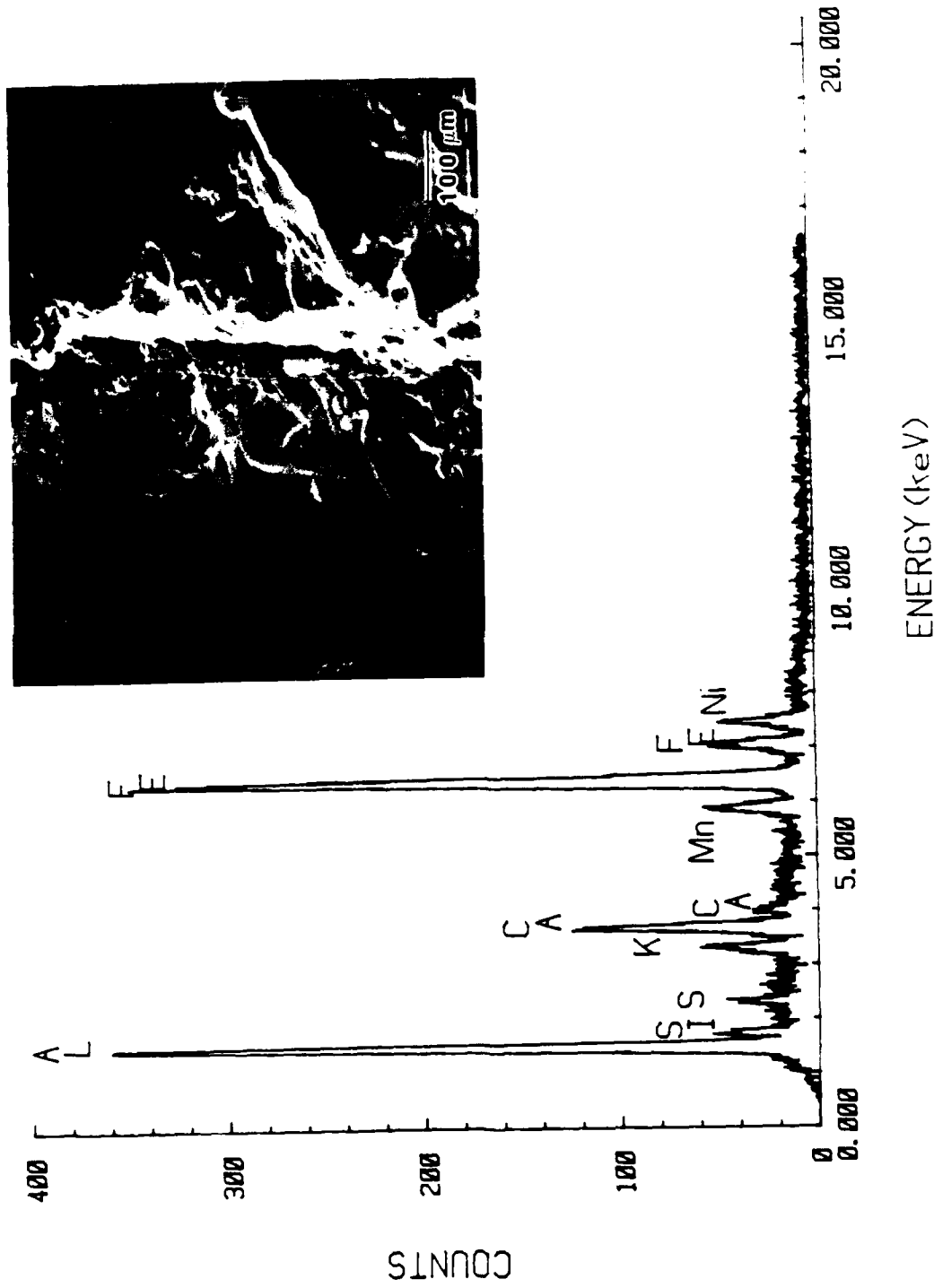
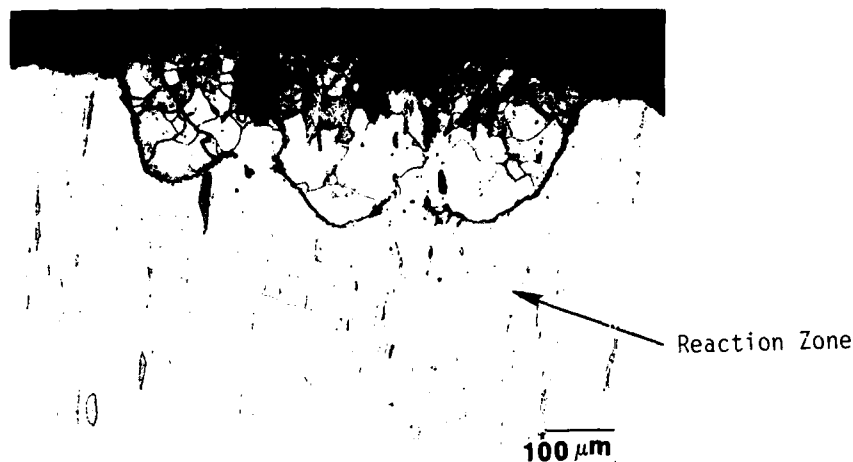


Fig. 3 - Energy-dispersive X-ray analysis of shell defect (b)





Acidified Picral Etch

Fig. 4 - Metallographic cross section through a 416 martensitic stainless steel material with a foreign particle embedded in it. Energy-dispersive X-ray analysis indicated that the particle was rich in aluminum, chromium, iron and copper. The particle produced blemishes on the surface of the stainless steel. A reaction zone around the particle suggests that the exogenous particle was trapped on the material surface prior to a heat treatment.

examples of such applications. Oxide dispersion strengthened superalloys have a uniform distribution of particles that are about 15-30 nm in diameter with an average spacing of about 100 nm. The dispersoids, commonly  $\text{ThO}_2$  and  $\text{Y}_2\text{O}_3$ , interact with dislocations in the slip plane, generating strengthening effects. An example of the comparison in yield strength data for some dispersion strengthened alloys with their non-dispersion strengthened version is presented in Figure 5 (9). It is apparent that a very significant improvement in yield strength can be obtained with the proper use of dispersoids.

Resulphurized free machining steels, on the other hand, take advantage of manganese sulphide inclusions for improving machinability (3,10). Resulphurized free-machining carbon or alloy steels have sulphur contents up to 0.3 percent. The manganese content is high enough that most of the sulphur is present as  $\text{MnS}$  inclusions promoting formation of small chips. Machinability is much improved by an increasing size and decreasing number of  $\text{MnS}$  inclusions (3). The sulphide inclusions assist in the formation of chips by acting as a stress raiser in the shear plane of the work material, where temperature is relatively low, and then providing enough plastic flow in the flow zone near the tool surface, where the temperature is much higher, to increase the shear deformation of the metal. On the contrary, oxide inclusions are detrimental to machining because of their poor flow properties over a

broad range of temperature. Calcium treated steels have improved machining characteristics because of the incorporation of calcium in both the sulphide and the oxide inclusions thereby forming inclusions with more desirable deformation characteristics (11).

It is apparent that inclusions can be detrimental or very useful to the performance of a material. Some of the factors that influence the role of inclusions in the performance of a material are their origin, type, size, shape, distribution, and quantity. Inclusions may influence almost all properties of a material, particularly those that are more widely utilized namely, formability, machinability, weldability, fatigue, fracture, creep, corrosion, and toughness. The following sections of this paper will present a case history of weld heat affected zone (HAZ) behavior as influenced by inclusions and address some of the considerations in the technological trends in inclusion engineering (HAZ) behavior as influenced by inclusions and address some of the considerations in the technological trends in inclusion engineering.

#### WELD HAZ BEHAVIOR: A CASE HISTORY

A study was undertaken to determine the cause of failure of oxyacetylene welded A-106 Grade B elbow fittings. The failures had occurred intergranularly through the HAZ and was brought about by redistribution of  $\text{MnS}$  inclusions to the grain boundaries by the

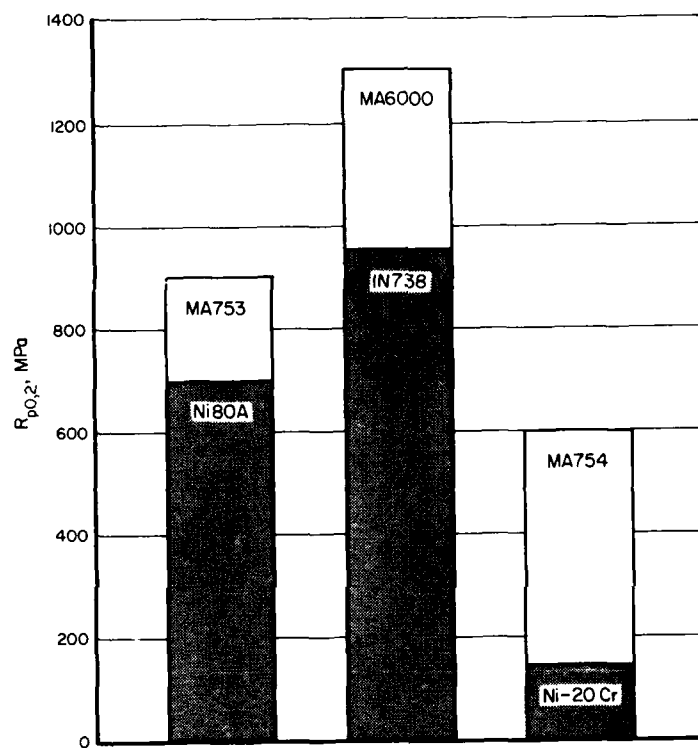


Fig. 5 - Comparison of the yield strengths of ODS alloys and similar alloys with no oxide dispersoids (9)

welding process. The case history serves as an example of how relatively harmless inclusions (such as MnS inclusions) in the material as initially produced, could become a cause of failure as the result of reactions that occurred during subsequent fabrication processes.

The fractures of the field failures were observed to follow along the boundaries of the prior austenite grains and, therefore, exhibited an intergranular fracture appearance. A region of intergranular fracture along prior austenite grain boundaries is shown by the photomicrograph in Figure 6. In all of the field failures, a phase was observed in many of the prior austenite grain boundaries. The phase occurred as a chain of disconnected, tiny globules, and occasionally, as a thin film. The phase appeared to be nonmetallic and resembled manganese sulphide inclusions. Examples of the phase which occurred in prior austenite grain boundaries in a field failure are shown by the micrographs in Figures 7 and 8. The micrograph in Figure 8 shows an agglomeration of particles as well as intergranular chains of tiny particles. The results of the electron microprobe analyses clearly indicated the intergranular phase contained sulphur and manganese in excess of the surrounding metal matrix. Similar observation was made on micrographs taken on a section of the HAZ immediately behind a laboratory induced fracture of a weld. In this case, a film at the prior austenite grain boundaries also could be seen, as is illustrated in Figure 9.

To determine if the intergranular phase in the prior austenite grain boundaries observed in the field failures could be reproduced, a series of thermal cycling tests were made on two different heats of the material. A Gleeble Testing Facility under no mechanical loading was used for simulating the thermal cycles and producing metallurgical changes that take place under conditions for welding a material. The specimens were cut into rectangular sections about 4 inches long and resistance heated to the desired temperature levels in 5 seconds, held at temperature for 5 seconds, then rapidly cooled by the copper jaws of the Gleeble. One specimen from each heat of steel was heated to temperatures in the range of 2400F to 2700F. These thermal cycles were arbitrarily chosen to be representative, if not somewhat more severe, than the heating and cooling experienced by a weld HAZ during oxyacetylene welding.

After thermal cycling, the specimens were sectioned through the heated zone and examined metallographically for the presence of the intergranular phase. The results are summarized in Table 1. Specimens heated to 2600F and above revealed the intergranular phase characteristic of that observed in the field failures.

Fractographic studies were performed to determine the mode of fracture and to further characterize and identify the intergranular phase presumed to be present on the fracture surface. For these studies a portion of the fractured face from a field failure and a laboratory induced fracture in the HAZ of the weld were used. The fractures were replicated with the conventional two-stage cellulose acetate-carbon technique, and the replicas shadowed from an angle of 45 degrees with platinum-carbon. The first replicas stripped from the specimens were examined so that particles extracted from the fracture could be analyzed by selected area diffraction. The results from the field failure are presented in Figure 10. Although the fracture surface was oxidized, the fractograph shows that the fracture was predominantly one of ductile rupture along the prior austenite grain boundaries. Particles similar to those indicated by arrows in Figure 10 were found in many areas of the fracture, and these particles were suspected to be the intergranular phase observed in the metallographic examinations. Very similar features could be observed on the laboratory induced fracture surface as shown in Figure 11. Selected area diffraction patterns for the particles were consistent with alpha-MnS.

Scanning electron microscopic examination of the Gleeble thermal cycled specimens fractured in the laboratory and the laboratory fractured weld specimens was also undertaken to establish that these fractures were similar to, or the same as, a fracture of the HAZ that failed in the field. The results of the scanning electron fractography are compared in Figures 12 and 13. The fractographs in Figure 12 illustrate the predominance of intergranular fracture propagation. In Figure 13, the dimpled fracture surfaces characterizing a ductile failure are evident in the laboratory-induced HAZ fracture and the thermal cycled fracture. In addition, many globular particles of the intergranular phase are situated within individual cup-shaped dimples. Thus, the general appearance of both the fracture surfaces are nearly identical.

The investigation showed that the fracture propagated through the HAZ by ductile rupture along prior austenite grain boundaries in which chains or films of alpha-MnS inclusions were present. The ductile rupture was a consequence of the network of proeutectoid ferrite along the prior austenite grain boundaries. These austenite grains existed in the weld HAZ at the time of oxyacetylene welding, but transformed to proeutectoid ferrite and pearlite upon cooling to room temperature. Most of the plastic deformation from stresses applied in the course of field fabrication or laboratory induced fractures would be concentrated along the proeutectoid ferrite network; therefore, small far-field

## Fracture Surface



Fig. 6 - Intergranular fracture along prior austenite grain boundaries in a field failure



Fig. 7 - Intergranular phase at prior austenite grain boundaries of HAZ in a field failure



Fig. 8 - Agglomeration of particles and intergranular phase in a field failure

strain: produced relatively large local strains in the ferrite network. The alpha-MnS inclusions in the prior austenite grain boundaries (and, consequently, in the ferrite network) lowered the amount of plastic strain required for fracture initiation along the grain boundaries. The fractographs showed that most of the ductile dimples were formed by the void-coalescence mechanism of ductile fracture propagation and were initiated by decohesion at the interface between alpha-MnS inclusions and the ferrite matrix. Therefore, the sulphide inclusions caused the fractures to be initiated at lower strains than if they were not present and imparted a brittle behavior to the fractures. It may be noted that some welded specimens did not fail during a 90 degree bend test in the laboratory even though they contained small amounts of intergranular sulphide inclusions. Some minimum amount of intergranular sulphide inclusions must, therefore, be tolerable. The quantitative degree tolerable for welded-joint integrity was not established in this study.

In a similar study conducted by Romhanyi et al.(12) on HY80 steel, low notch toughness was obtained in simulated HAZ because of the presence of manganese, chromium, (iron) sulphides present in the grain boundaries. Microvoids were observed on grain boundary surfaces of intergranular fractures of Charpy specimens. These authors noted that cleavage also was observed in some specimens. Hart (13) has suggested that increased grain boundary phosphorous contents promoting temper embrittlement may be the cause of the

Table 1 - Summary of the Results of Thermal Cycling Experiments on Two Heats of A-106 Steel

Heat No.	Sample No.	Temperature F	Intergranular Phase Present
1	1	2400	no
	2	2504	no
	3	2602	yes
	4	2648	yes
2	1	2400	no
	2	2504	no
	3	2602	yes
	4	2648	yes

13  $\mu$ m

(a) As Polished



(b) Picral Etched  
as field as (a)

Fig. 9 - Intergranular phase and film at prior austenite grain boundaries in the laboratory induced fracture of a weld



Fig. 10 - Fractograph showing ductile rupture along prior austenite grain boundaries of a field failure. (Arrows indicate particles in fracture surface)

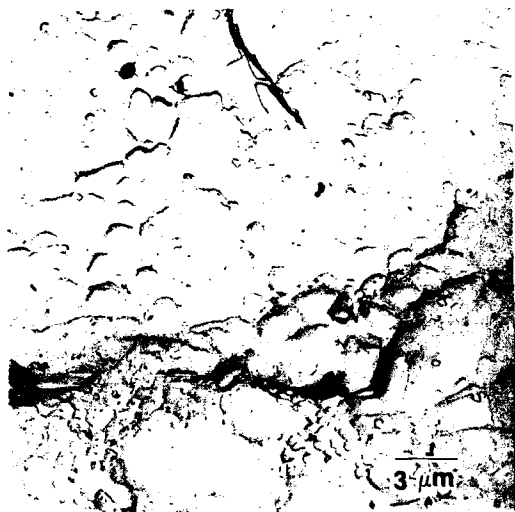


Fig. 11 - Fractograph showing ductile rupture along prior austenite grain boundaries of a laboratory induced fracture through a HAZ (Note particles on fracture surface)

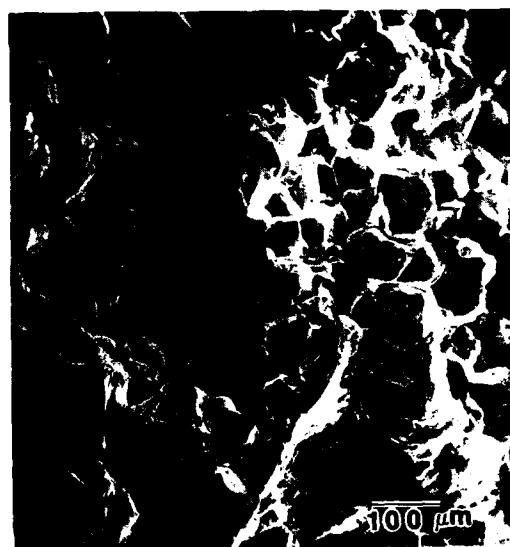
intergranular cracking of Cr-Mn and micro-alloyed steels. Although in our study, phosphorous enrichment at the grain boundary was not investigated, Romhanyi et al (12) in their work noted that the enrichment ratio for sulphur was much higher (about 60) as compared to that for phosphorous (about 8). Those levels of elemental enrichment are less than the levels of enrichment observed during temper embrittlement (12).

#### TECHNOLOGICAL TRENDS IN INCLUSION ENGINEERING

There are several examples of generic applications where the presence of inclusions have been attributed to degradation in certain properties. Lamellar tearing in carbon-manganese steel welds is one example where the presence of planar (Type II) MnS inclusions causes micro-fissures to form at these inclusions. Shear linking of these micro-fissures under load leads to the formation of a crack (14). Hydrogen-induced cracking of linepipe for sour gas service is another example where the presence of elongated MnS and clusters of  $Al_2O_3$  cause precipitation of atomic hydrogen at the interface of the matrix and inclusion. Hydrogen atoms generated at the surface through the reaction between the steel and the wet sour gas penetrate the steel and are trapped at the interface between the inclusion and the matrix. Molecular hydrogen is formed at this interface and when the internal pressure due to molecular hydrogen exceeds a certain critical value, cracks are initiated (15). One of the solutions to problems like these and many others has been to reduce the sulphur and oxygen content of the steel so as to reduce the amount of oxide and sulphide inclusions in steel. Most of

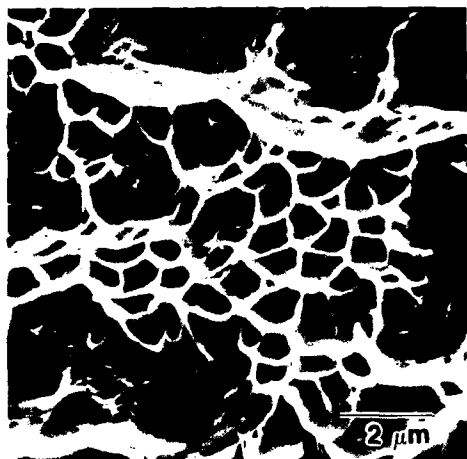


(a) Laboratory induced fracture in HAZ of a weld

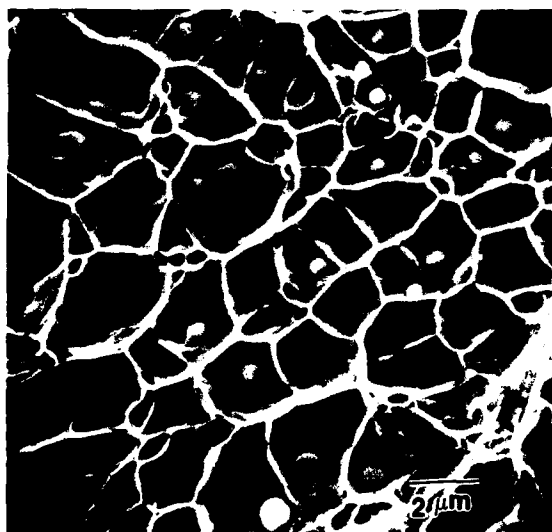


(b) Gleeble thermal cycled specimen fracture surface

Fig. 12 - Scanning electron fractographs showing intergranular fracture mode in the laboratory fractured weld and the thermal cycled specimen fracture



(a) Laboratory induced fracture in HAZ of a weld.



(b) Gleeble thermal cycled specimen fracture surface

Fig. 13 - Globular particles situated within the dimples of laboratory induced fracture surface in HAZ of a weld and the Gleeble thermal cycled specimens

these controls are exercised in the ladle refining step rather than in the melting furnace, and the following paragraphs review the secondary steelmaking steps briefly.

**INCLUSION CONTROL IN SECONDARY STEEL MAKING** - In the most general sense the objective of secondary steelmaking is the removal from the steel of undesirable concentrations of elements such as carbon, sulphur, phosphorous, oxygen, nitrogen, and hydrogen (16-18). Cleanliness in terms of inclusion content is only a part of the whole operation.

The lowest sulphur content that can be produced with the basic oxygen furnace (BOF) or the electric arc furnace (EAF) is about .001 percent (17). A sulphur content lower than this requires a subsequent desulphurization treatment in the ladle. Injection of calcium silicide or calcium carbide, or a synthetic slag on the base of  $\text{CaO-Al}_2\text{O}_3\text{-CaF}_2$  has been widely used for this purpose. Calcium serves as a strong desulphurizer as well as a deoxidizer. The treatment requires a low potential of oxygen in the steel which implies that the steel must be tapped virtually slag free. A basic lining (dolomite) and intensive stirring (by argon bubbling) contribute to rapid desulphurization. Sulphur levels as low as 30 ppm may be achieved by this procedure. Figure 14 (17) shows the sulphur content in steel after a  $\text{CaO-Al}_2\text{O}_3\text{-CaF}_2$  treatment.

An additional advantage of the calcium treatment is shape control of remaining sulphide inclusions in the steel. Spherical calcium aluminates enriched with sulphur are formed. These inclusions maintain their spherical shape during rolling operations, thereby, reducing anisotropy in ductility and in toughness behavior (16-18). Treatment with rare earth elements such as cerium can produce similar inclusion shape control.

Oxygen and oxide inclusion control also requires that the steel be tapped from the BOF or EAF slag free. The primary slag, rich in silica and iron, acts as a strong oxidizer of alloying elements such as aluminum, thereby influencing the quantity and composition of the ladle slag which forms. Low oxygen contents in steel are achieved with either the synthetic desulphurization slags with simultaneous intensive flushing as noted above or vacuum carbon deoxidation. In vacuum carbon deoxidation, the carbon-oxygen reaction is promoted when the steel is subjected to reduced pressure in the undeoxidized condition. The treatment reduces the oxygen content of the steel to a much lower level before aluminum is added. Oxygen contents as low as 10 ppm are being achieved by these treatments (17). An example of the influence of aluminum treatment and stirring on the oxygen content of liquid steel is presented in Figure 15 (19).

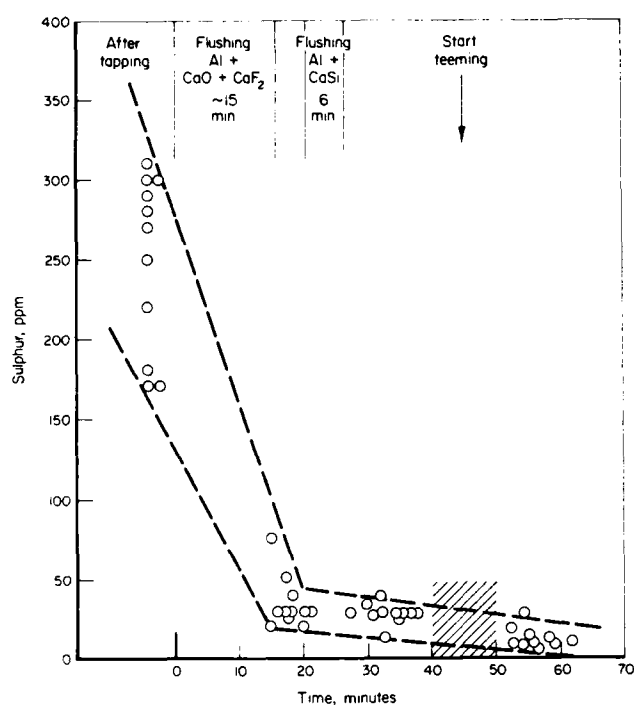


Fig. 14 - Sulphur content in steel after treatment of  $\text{CaO-Al}_2\text{O}_3\text{-CaF}_2$ -type slag in 190-ton basic lined ladle (17)

**INCLUSION FILTRATION** - Another method for reducing the inclusion contents of metals that gained some acceptance in the last few years is the filtration of molten metal to trap inclusions (20-23). Ceramic foam filters have been employed to filter a range of alloys including aluminum, steel, and superalloys. Ceramic materials including mullite, alumina, and zirconia have been employed for this purpose (20-23). The filters are generally placed either in the tundish or the runner. The choice of a filter size for a given application depends on such factors as the desired mold filling time, the pouring temperature, the pore size of the filter, and the concentration of filterable inclusions in the molten metal (23). In addition to removing the inclusions efficiently, the filter must be sufficiently rugged and chemically stable so as not to disintegrate in the flowing hot metal. The filter also must be cost effective and should not reduce the casting rate to the point that the metal fails to fill the mold (21). As a matter of fact, this last requirement seems to be a major constraint in the practical application of these filters. After a relatively short period of use the filter gets clogged by the inclusions and the flow rate drops significantly, eventually stopping completely.

The filtration efficiency of a filter depends not only on the filter material but also on the metal being filtered, with the

efficiency for a given filter material dictated by the pore size of the filter (the pore size of a filter is defined by the number of pores per linear inch, ppi). An example of filter efficiency is shown in Figure 16 (21) for several superalloys. It is apparent that alloy IN-718 is very efficiently filtered by a variety of filter types and pore sizes but that the filtering of the other superalloys is sensitive to filter material and pore size.

In the example noted above, the filter efficiency was measured as:

$$E = ((A_u - A_f)/A_u \times 100)$$

where  $A_u$  = specific oxide area of an unfiltered sample,  $\text{cm}^2/\text{kg}$  (1)

$A_f$  = specific oxide area of a filtered sample,  $\text{cm}^2/\text{kg}$

It is implicit in this definition that a highly efficient filter will produce a material with a low inclusion content on average. But a definition like this does not take into account the inclusion distribution (stringers or clusters) that can be very detrimental to the performance of the material. Another important variable that is not defined in this example is the size of the pores. The size of the pores will determine the size of the largest inclusions present in the filtered metal. It is well documented and accepted that inclusions will always be a part of the steel (24). The large inclusions will be the most detrimental in terms of performance and need to be eliminated. What is necessary is to define the critical size and shape of the deleterious inclusion for a given application and then to attempt to eliminate inclusions and inclusion stringers larger than the specified critical size (24,25). Such an approach will not only be cost effective but also more reliable in terms of material performance.

**DETECTION OF INCLUSIONS** - In terms of cleanliness evaluation for process control there are few methods available for detecting inclusions in metals. Any procedure that is adopted has to be applied to samples taken as close as possible to the process line. This entails either the sampling of liquid metal in the tundish or mold, or the cutting of slab samples. While methods based on chemical analysis serve to measure relative cleanliness of a melt and monitor events that disrupt the controlled casting process (26,27), such measurement of the bulk concentration of an element reveals nothing about its distribution in the sample. For aluminum alloys, Doutré et al (26) have noted that there is no correlation between oxygen concentration and the inclusion level ( $d > 20$  micron) in the melt. The traditional metallographic techniques, on the other hand, are very time consuming and absolutely destructive if one wishes to



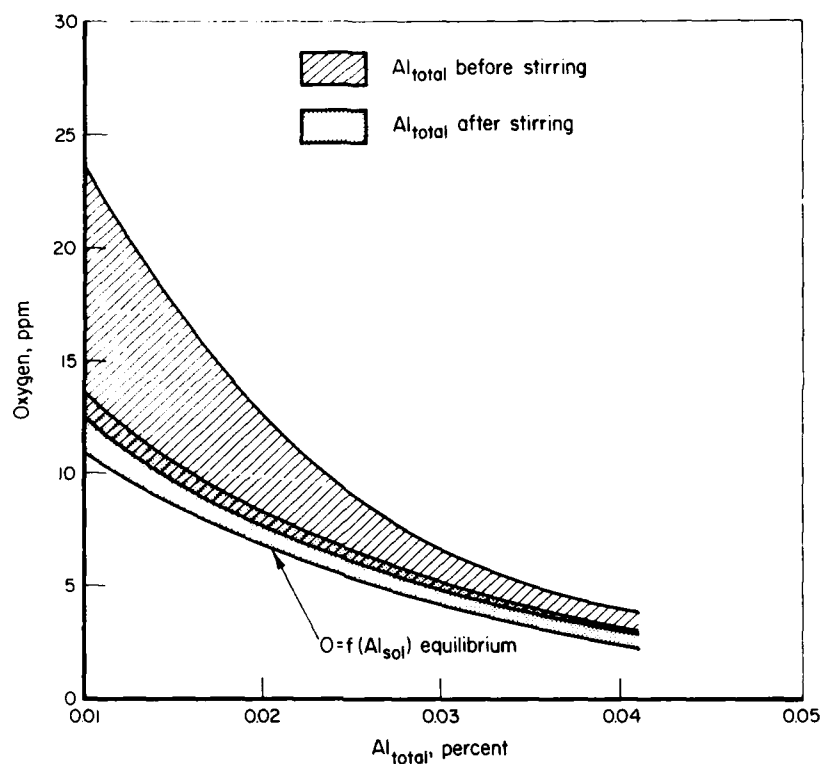


Fig. 15 - Oxygen content in liquid steel as a function of total aluminum. The influence of stirring is also apparent here (19)

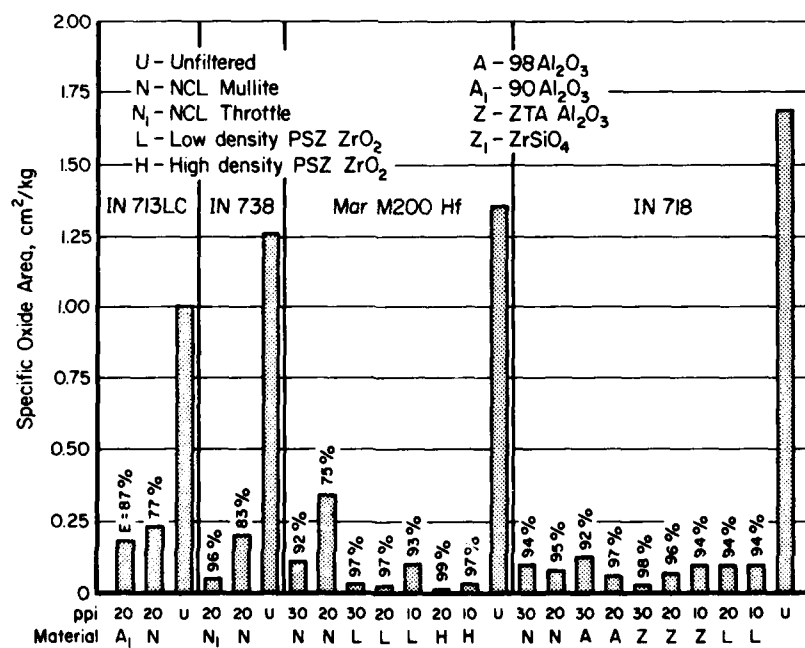


Fig. 16 - Effect of filter material and pore size (ppi) on filtration efficiency (E) of various superalloys (21)

determine the distribution of the large non-uniformly distributed inclusions. In addition, metallographic techniques examine such a small volume of material that to extrapolate the results to a large billet, for example, may not be representative.

In terms of detecting inclusions, non-destructive measures provide the best possibilities. Ultrasonic techniques have been employed most widely in the metal industry (28-35). Two of the basic arrangements that have been used for this purpose are (a) the pulse-echo system in which the pulses are sent into the material and reflected back either into the same probe or another probe, and (b) transmission through a material requiring a transmitter and a receiver whereby the presence of inclusions is indicated by the loss of transmitted energy.

Theoretically the ultrasonic techniques can detect non-uniformly dispersed individual inclusions as well as the general distribution of inclusions. In practice, however, the techniques cannot accurately differentiate between the different sizes of the detectable inclusions because of factors such as inclusion type and shape, the ultrasonic beam-intensity profile, and base-metal structure interference (33). Quantitative understanding of such interactions will have to be developed before the techniques can be used with confidence to measure inclusion size distribution in metals. The techniques have so far been used to measure the general cleanliness of steels as shown by the example in Figure 17 (35). The histograms show the contrast in the cleanliness data between a clean and dirty billet as measured by the back-echo technique. Here the number of echo returns at a given amplitude is plotted against the amplitude level and the two histograms are distinguished by the large number of high amplitude echoes detected in the dirty billet and the dramatic change in the shape of the amplitude distribution function. With ultrasonic mapping it is also possible to locate areas in a billet that have a higher degree of inclusion content (34,35). Finally, Kwun et al. (32) have noted in a recent study that the type of an inclusion material may be determined by measuring the phase of an inclusion signal. The phase of the signal will determine whether the inclusion has a higher or lower acoustic impedance than that of the base material. The study was conducted on a titanium powder compact using a focussed 10 MHz ultrasonic transducer (32).

The approaches discussed in the preceding paragraphs have been applied to solidified metals. The ultrasonic techniques have also been applied to molten metal to evaluate its cleanliness (30). The pulse-echo system described in this particular study was used to evaluate the cleanliness of molten aluminum. The relative cleanliness was measured by the attenuation of the ultrasonic signal: the cleaner melt had lower attenuation.

Recently a technique has been developed that attempts to evaluate the concentration and size distribution of inclusions in a melt (26,36). The Electric Sensing Zone (ESZ) technique measures the electrical properties of a thin liquid metal stream. Transients in the electrical field occur when an inclusion passes through the orifice. Counting the number of transients per unit volume of the material sampled provides the inclusion concentration while the amplitude of each transient provides the particle size distribution. The technique is obviously sensitive to the size of the orifice chosen (36). Since the technique is used on-line, it has the advantage of providing information for process control as well as serving as a quality control tool for the product. Figure 18 shows the agreement between results for ESZ technique and the pressure filtration technique for an aluminum alloy (26). The particle size distribution as measured by the ESZ technique is presented in Figure 19 (26).

**IDENTIFICATION OF INCLUSIONS** - Inclusions are generally multiphased and form complexes with various elements present in the melt. Since the phase of the inclusion is one of the variables that determines its influence on the performance of the material, and the control of the steelmaking process requires an understanding of the types of inclusions that may form with various treatments, it is of utmost importance that the composition of the inclusion be determined. While the inclusion phase can be identified in many cases by the experience of the observer, color and shape of the inclusion, and metallographic techniques using polarized light, the most significant advancement for inclusion identification has been the electron-probe microanalyzer. The microprobe can be used in both secondary electron and back scattered imaging modes and has a secondary electron image resolution of 70 Å. A state-of-the-art microprobe is equipped with wavelength-dispersive spectrometers for quantitative analysis of elements by wavelength dispersion, as well as an energy-dispersive system for qualitative analysis. Wavelength-dispersive analysis allows the detection of elements with atomic weights equal to or greater than that of boron, and therefore permits the quantitative study of elements such as carbon, oxygen, nitrogen, and fluorine.

An example of the application of the microprobe is presented in Figure 20. The figure shows the secondary electron image of two inclusions in a standard carbon steel rail. It is apparent by examining the various shades in the large inclusion that it is a duplex inclusion. An energy-dispersive examination (similar to the one presented in Figure 3, earlier) of the dark center of the large inclusion indicated the presence of aluminum while the lighter area indicated the presence of sulphur and manganese. X-ray

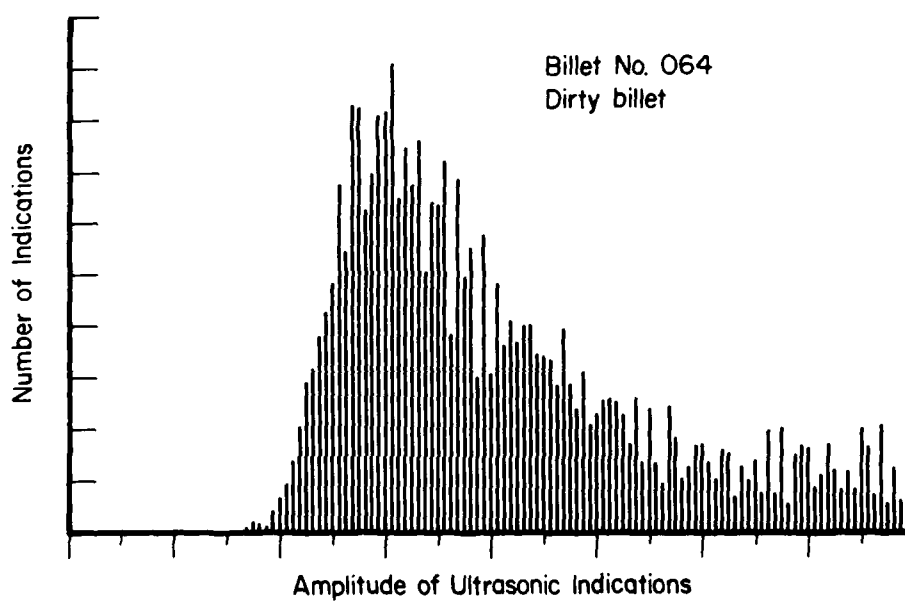
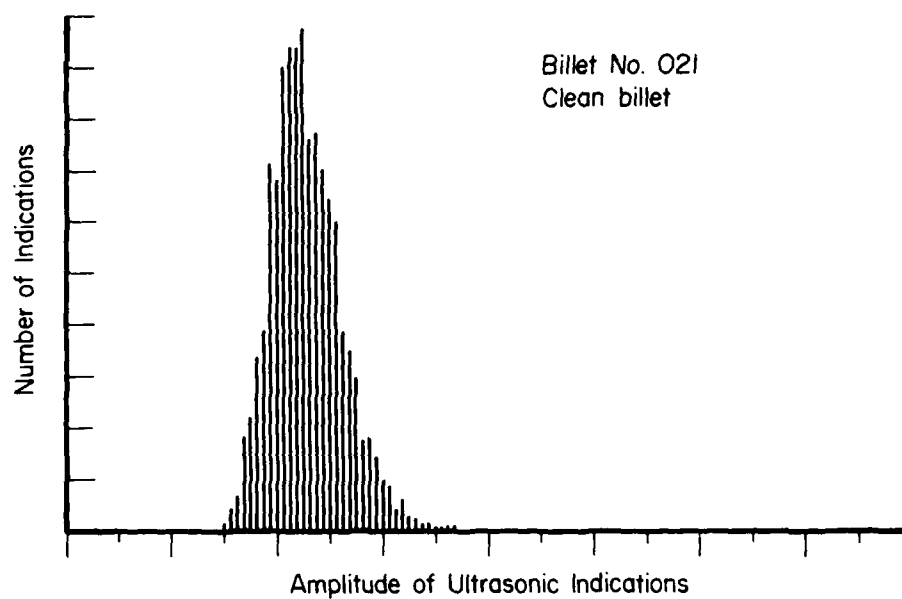


Fig. 17 - Histogram showing frequency of occurrence for the ultrasonic indications plotted against their amplitude (35)

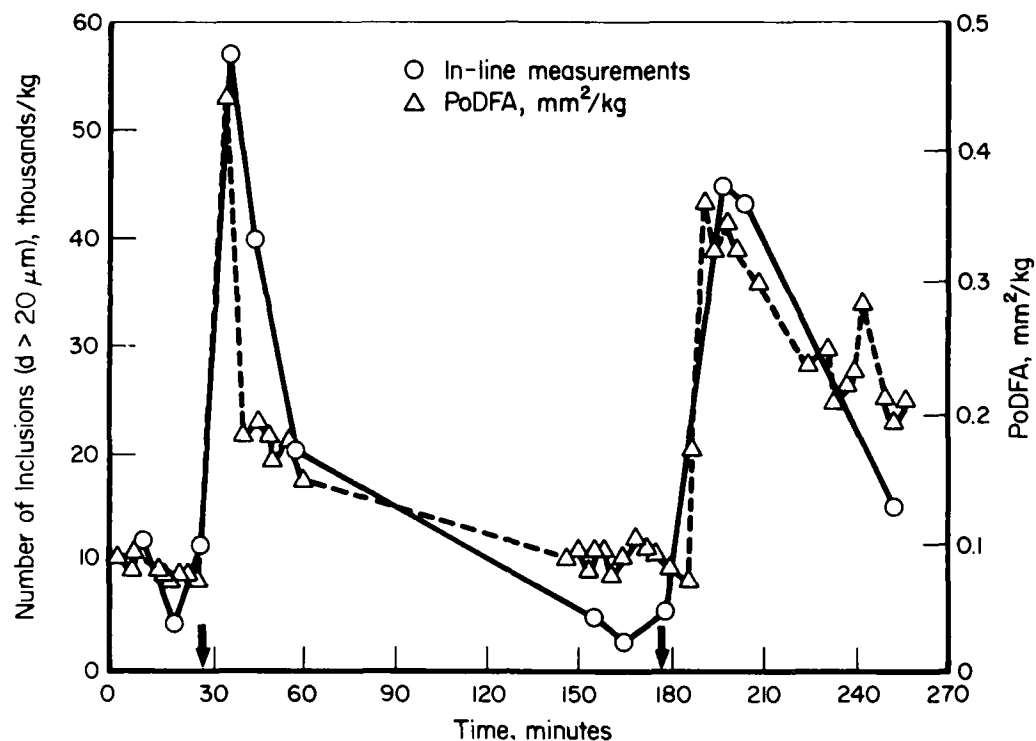


Fig. 18 - In-line electrical measurements and pressure filtration (PoDFA) results versus time. Arrows indicate times at which the furnace feeding the caster was changed (26)

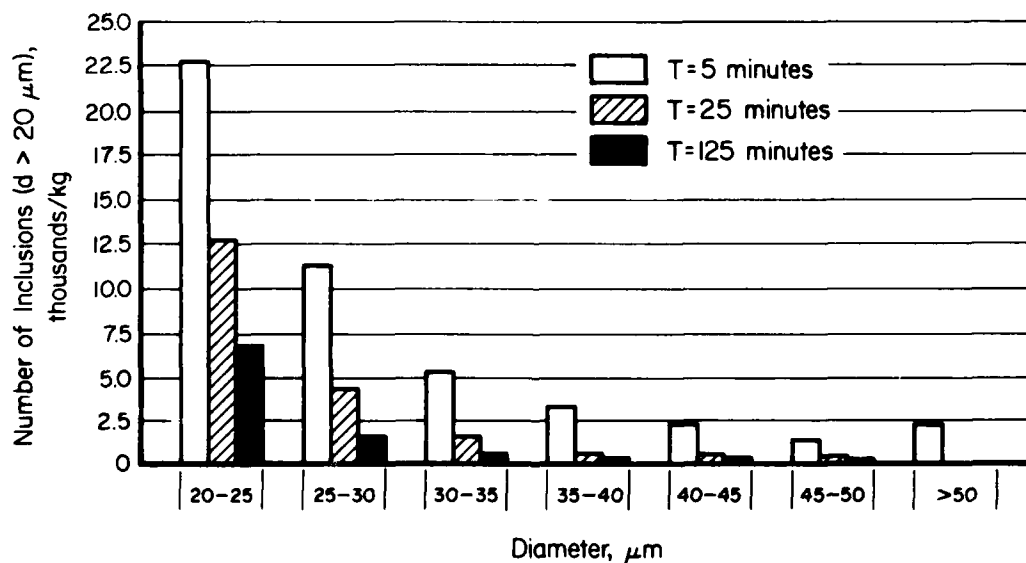


Fig. 19 - Particle size distributions provided by the in-line electrical measurements 5, 25 and 125 minutes after the first furnace change indicated in Fig. 18 (26)



2  $\mu\text{m}$

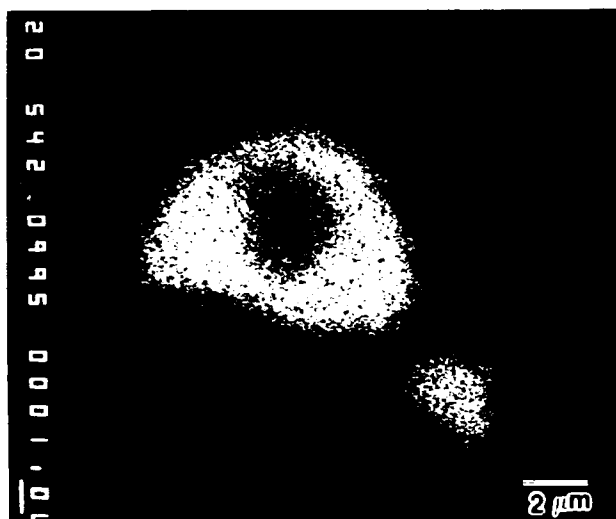
Fig. 20 - Secondary electron image of an inclusion in a standard carbon steel rail

mapping was done to determine the distribution of these various elements in the inclusion. X-ray mapping for sulphur, manganese, aluminum, iron and oxygen is presented in Figure 21. It is clear that the center dark region of the large inclusion contained aluminum and oxygen while the light region contained manganese and sulphur. The small inclusion contained manganese and sulphur only. It may be noted that oxygen mapping could only be done with wavelength dispersion. Quantitative analyses of aluminum, oxygen, manganese, and sulphur using wavelength-dispersion analytical techniques indicated that these inclusions were most likely  $\text{Al}_2\text{O}_3$  and  $\text{MnS}$ .

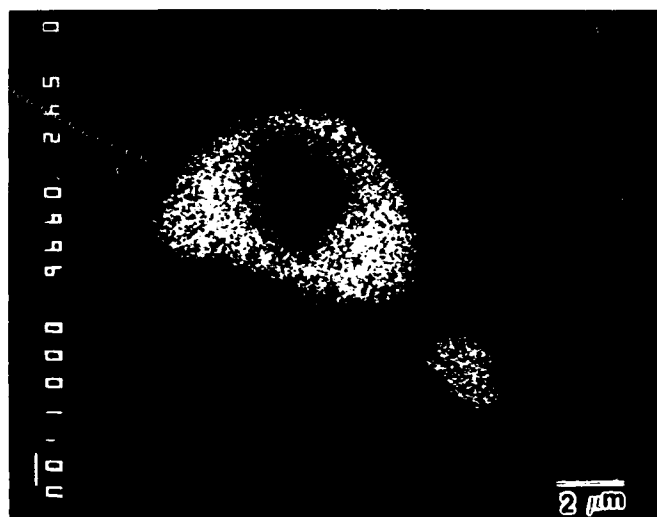
It may be noted that energy-dispersive analysis is rapid and is sufficient in most cases for the identification of heavy elements. In energy dispersion, the detector views the specimen directly and measures all of the characteristic x-rays simultaneously. This feature makes the procedure much more rapid and one can move to different points of an unknown specimen and examine for the presence of various elements. Wavelength dispersion on the other hand requires that the spectrometer be chosen for each element that needs identified. The procedure therefore becomes very time consuming. But, when quantitative analysis is needed and light elements need to be identified, the wavelength dispersive technique is the best in-situ identification technique available.

#### SUMMARY

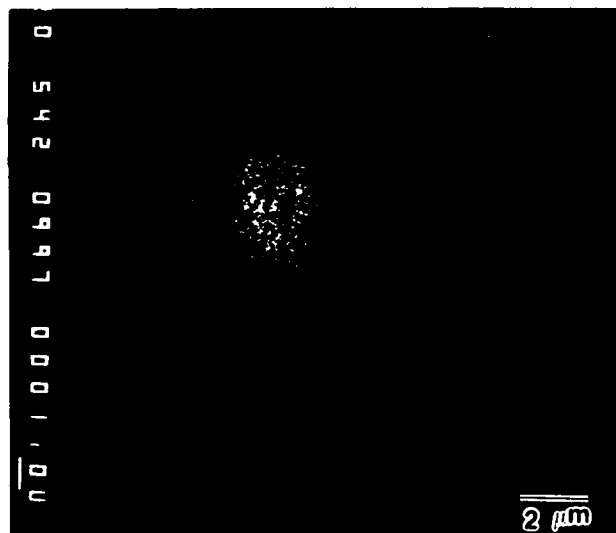
Except for the few intentionally engineered situations, it is well established that inclusions play a detrimental role in the performance of a material depending on their type, size, shape and distribution. While it is useful to develop cleaner material from the standpoint of its inclusion content, the current approach taken by the materials industry may not necessarily solve the problem of inclusion-induced poor performance of materials. While reducing sulphur and oxygen contents in steels does reduce the sulphide and oxide inclusion content of the steel, it does not prevent the possibility of a few large inclusions being present at critical locations. Filtration techniques and monitoring techniques have to be developed further to insure the elimination of such deleterious inclusions. Also, the critical size of a deleterious inclusion needs to be defined for various applications. The generalized cleanliness concept not only increases the cost of producing the material but also does not necessarily minimize the possibility of structural failure due to inclusions.



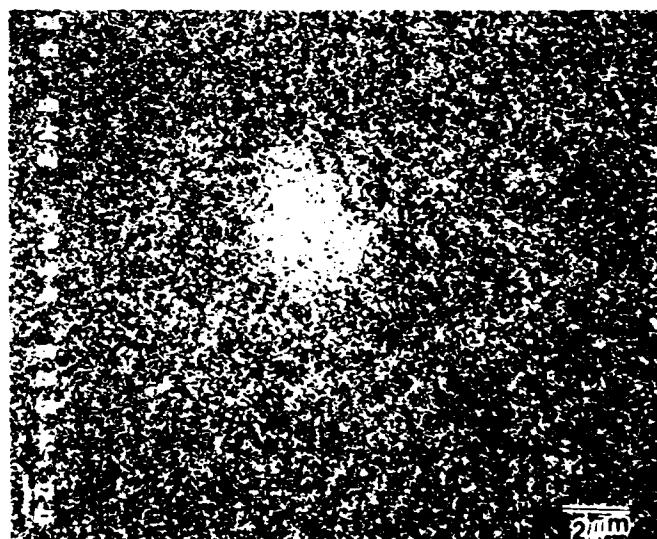
(a) X-ray map of sulphur



(b) X-ray map of manganese

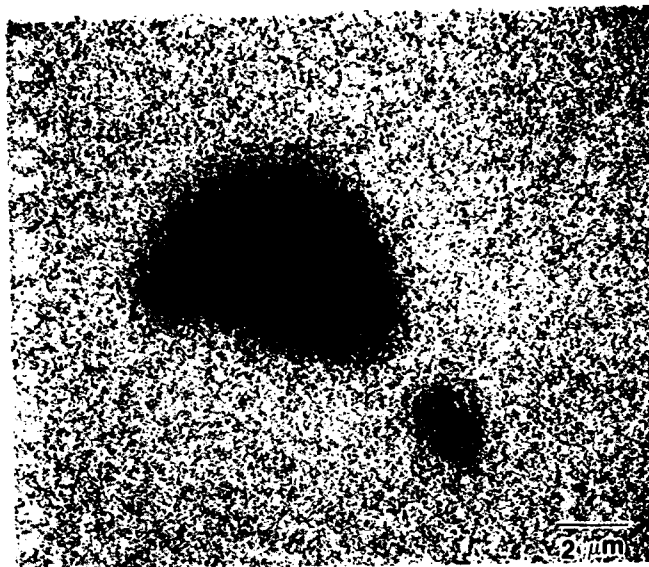


(c) X-ray map of aluminum



(d) X-ray map of oxygen

Fig. 21 - X-ray map of various elements in the inclusion shown in Fig. 20



(e) X-ray map of iron

Fig. 21 - (Continued)

#### REFERENCES

1. "Metallography and Microstructure", Metals Handbook, Vol. 9, Ninth Edition, p. 9, American Society for Metals (1985).
2. C. E. Sims, Transactions of the Metallurgical Society of AIME, 215, 367-393 (June 1959).
3. R. Kiessling and N. Lange, "Non-Metallic Inclusions in Steel", Second Edition, Book No. 194, The Metals Society, London (1978).
4. W. C. Leslie, Transactions of the Iron and Steel Society of AIME, 2, 1-24 (May 1983).
5. L. H. Van Vlack (Coordinating Editor), Review 220, International Metals Reviews, 187-228 (September 1977).
6. R. Rungta and R. C. Rice, "Shelling Behavior in Rails," Final Battelle Columbus Division Report to Transportation Systems Center, Department of Transportation, Contract No. DTRS-57-83-C-00076, February, 1987.
7. R. Rungta, R. C. Rice, R. D. Buchheit, and D. Broek, "Corrosion, Microstructure, & Metallography", Microstructural Science Vol. 12, D. O. Northwood, W. E. White, and G. F. Vander Voort (Eds), 383-406, American Society for Metals & International Metallographic Society, Metals Park, Ohio (1985).
8. R. Hamminger, G. Grathwohl, and F. Thummler, Int. J. High Technology Ceramics, 3, No. 2, 129-141 (1987).
9. G. H. Gessinger, "Powder Metallurgy of Superalloys", p. 213, Butterworths, London (1984).
10. R. Lagneborg, "Swedish Symposium on Non-Metallic Inclusions in Steels", H. Nordberg and R. Sandstrom (Eds), 285-352, Uddeholms AB, Sweden (1981).
11. V. Ollilainen, *ibid*, 429-449.
12. K. Romhanyi, M. R. Krishnadev, R. D. McDonald, J. T. Bowker, and J. T. McGrath, "Welding, Failure Analysis, and Metallography", Microstructural Science, Vol. 14, M. R. Louthan, Jr., Iain LeMay, and G. F. Vander Voort (Eds.), 115-126, American Society for Metals and International Metallographic Society, Metals Park, Ohio (1987).
13. P. H. M. Hart, "Inclusions and Residuals in Steels", J. D. Boyd and C. S. Champion (Eds.), 435-454, CANMET, Canada (1985).
14. F. Fitzgerald, "Clean Steel 3", Proceedings of the 3rd International Conference on Clean Steel, Book 394, 1-11, The Institute of Metals, London (1987).

# REFERENCES (Continued)

15. T. Taira and Y. Kobayashi, "Steels for Line Pipe and Pipeline Fittings", Book 285, 170-180, The Metals Society, London (1983).
16. A. Nicholson and T. Gladman, "Ironmaking and Steelmaking", 13, No. 2, 53-69 (1986).
17. R. Scheel, W. Pluschkell, R. Heinke, and R. Steffen, "Secondary Steelmaking for Product Improvement", Book 324, 61-72, The Institute of Metals, London (1985).
18. B. Tivelius and Xu Kuang-Di, Same as 13, 33-69.
19. J. de la Hamette, F. Meyer, C. A. Wurth, and F. Knaff, Same as 17, 101-106.
20. D. Apelian and W. H. Sutton, "Superalloys 1984", M. Gell (Ed.), 421-432, AIME, Warrendale, Pennsylvania (1984).
21. W. H. Sutton, J. C. Palmer, and J. R. Morris, AFS Transactions, 93, 339-346 (1985).
22. H. Fukuoka, Materials & Design, 8, No. 5, 247-257 (1987).
23. L. A. Aubrey, J. W. Brockmeyer, P. F. Weiser, I. Dutta, and A. Ilhan, Same as 21, 177-182.
24. R. Kiessling, Metal Science, 14, 161-172 (1980).
25. R. K. Steele, R. Rungta, and R. C. Rice, Railway Gazette International, 175-179 (March 1987).
26. D. Doutre, B. Gariepy, J. P. Martin, and G. Dube, "Light Metals", 1179-1195, The Metallurgical Society/AIME, Warrendale, Pennsylvania (1985).
27. I. Simpson, R. Serje, K. Kuit, Z. Tritsiniotis, and D. Porteous, Same as 14, 85-91.
28. K. W. Andrews, Phys. Technol. (GB), 5, No. 4, 259-277 (1974).
29. J. B. Morgan, Materials Evaluation, 28, No. 6, 121-134 (1970).
30. T. L. Mansfield and C. L. Bradshaw, Same as 21, 317-322.
31. G. Canella, F. Monti, L. Pedicelli, and A. L. 'Erede, NDT International, 16, No. 3, 151-153 (1983).
32. H. Kwun, G. P. Singh, K. Fujisawa, F. H. Froes, and D. Eylon, NDT International, 17, No. 2, 73-79 (1984).
33. S. S. Daniel and R. A. Rege, Journal of Metals, 26-37 (July 1971).
34. J. Dumont-Fillon and M. Lacroix, "Ultrasonic Measurement of the Inclusion Cleanliness of Steel," EUR 6289 EN, Contract 6210-GA/3/301, Commission of the European Communities (1980).
35. J. M. Smith, "Review of Progress in Quantitative NDE", D. O. Thompson and D. E. Chimenti (Eds.), Vol. 2B, 1431-1436, Plenum Press, New York (1983).
36. S. Kuyucak and R. I. L. Guthrie, "Proceedings International Symposium on the Control and Effects of Inclusions and Residuals in Steels", I-44 to I-61, The Canadian Institute of Mining and Metallurgy, Montreal, Canada (1986).



# CHARACTERIZATION OF INCLUSIONS IN PLATE STEELS AND THEIR INFLUENCE ON MECHANICAL PROPERTIES

Alexander D. Wilson

Lukens Steel Company  
Coatesville, Pennsylvania 19320 USA

## Abstract

A review is provided of the experiences at the Lukens Steel Company in characterizing the inclusion structures in structural, carbon and alloy plate steels and their influence on mechanical properties. Particular emphasis is given to calcium treated steels, which have been produced at Lukens for close to 15 years. The metallographic techniques that have been used to establish the efficiency of steel-making procedures are reported and the various classes of inclusions found in calcium treated steels reported. The influence of inclusions on the tensile ductility, CVN and fracture toughness, fatigue crack growth rate (air and salt water), and near-threshold behavior is reviewed.

THE CONTROL OF NON-METALLIC INCLUSIONS IN STEELS has been a challenge to the steelmaker for as long as steel has been produced. Over the years, the levels of sulfur level have been particularly addressed as important to improving the cleanliness and thus the performance of steels. During each era of steelmaking, there have been limits that appeared to be unachievable, however, as new technology was developed a push to lower cleanliness levels was possible. A quote from an early edition of the bible of the industry, Making, Shaping and Heat Treating of Steel, Volume 4<sup>(1)</sup> is appropriate:

"In view of the fact that is it becoming increasingly difficult to keep the sulfur content below 0.04%, it seems ridiculous to insist on so low a limit, when the evidence points so strongly to 0.10% as a limit that may be made to serve as well, for many purposes, at least."

It would be very easy to put up-to-date (lower) levels in for those quoted from the

above 1919 text to demonstrate, that we only can meet requirements for our products, as they are possible to be produced in the steel mill.

In recent history, there has been a significant amount of effort in inclusion control over the past 20 years. Lamellar tearing problems in welded structures have been the major factors pushing this concern. However, the benefits of low sulfur and low inclusion contents in improving toughness, ductility and fatigue properties have also been important because of the improved resistance to failure in service. These improved performing steels have been utilized in a wide range of applications. Some of these are summarized in Table I.

When inclusion control in steels is considered, the primary concerns are indigenous non-metallic inclusions, which precipitate as discrete phases during the solidification of molten steel, i.e., sulfides and oxides. These inclusions are influenced by the steelmaking techniques that are used in the melt shop, as well as other processing that is subsequently used. Some of these influences will be discussed in the following text. Although oxides and sulfides are of particular interest in steel, other inclusions can also play an important role. In steels that are not aluminum killed, silicates are an important concern. Also when nitride forming elements are used in alloying, there can be a significant influence of nitrides, for example, titanium nitrides, columbium carbonitrides, aluminum nitrides and zirconium nitrides. For purposes of this presentation, only aluminum killed steels will be considered and the importance of controlling aluminum oxide and manganese sulfide inclusions will be emphasized.

Characterizing these inclusions is an important part of identifying the influences of different steelmaking practices. A great deal of effort has taken place in this

characterization using various metallographic methods. Quantifying the inclusion content differences between steels is also of concern. Identifying the influence of these inclusions upon mechanical properties, has also been a particularly active effort. Depending on the application, a particular property may be of interest. The metallographic and mechanical property characterizations that have been undertaken at Lukens will be reviewed.

## STEEL PROCESSING

The non-metallic inclusions in plate steel are significantly influenced by the steelmaking processes that are used. This is particularly the case with sulfide inclusions. Lukens' experience has been related to electric arc furnace (EAF) produced steels and, therefore, the discussion will be directed toward this particular operation. In EAF steelmaking, the sulfur levels can be reduced through double slag practices and until approximately 15 years ago this was the primary method used to achieve the lowest sulfur levels for structural steels. With the development ladle metallurgy practices, sulfur levels could be reduced outside the EAF through various methods. One of the most popular methods that has been used is calcium treatment (CaT). One method of CaT is called calcium argon blowing or the Thyssen-Niederrhein process.<sup>(2)</sup> In this practice, calcium compound powders ( $\text{CaSi}$ ,  $\text{CaC}_2$ ) are injected into the molten steel using a submerged lance and an argon carrier gas. Further discussions of this practice will be given later in the text. A schematic of this process is shown in Figure 1. Also, calcium treatment can be performed using various calcium cored wire injection processes.<sup>(3)</sup> A schematic of this process is shown in Figure 2. It is possible to achieve very low sulfur steels (less than 0.005% S) with both processes in conjunction with other desulfurization techniques within or outside the EAF.

After molten steel has been refined through a ladle metallurgy station, it is teemed into ingots or cast using continuous casting processes. Both casting processes influence the inclusion content in the final product. In ingot casting, due to the long solidification period, there can be segregation of sulfur at the top of ingot and near the centerline. With lower sulfur steels, there is less of a concern for this problem, however. In continuous cast slabs, there can be problems with reoxidation inclusions collecting near the top quarterline of the slab. Through use of various shrouding techniques, these inclusions are minimized. In the rolling mill, there still can be an influence upon the inclusion structure remaining in a plate. When the slabs are heated to the soak temperature and remain at high temperatures (2300° F) for a significant

length of time, sulfide inclusions can be homogenized.<sup>(4)</sup> An example of this is shown in Figure 3. Upon the rolling the steel to plate, any sulfide inclusions that remain and are not modified by a calcium practice are elongated. Prior to the advent of low sulfur technology, it was common to give high quality steels extensive cross rolling to minimize the amount of elongation of inclusions in the major rolling direction and therefore give an improvement to the transverse mechanical properties.

Other methods besides calcium treatment have been used to produce low sulfur steels.<sup>(5)</sup> For example, a ladle flux practice has been used, which involves placing lime and flux making ingredients in the bottom of the ladle and tapping the molten steel from the EAF upon them. Also, new desulfurizing slags can be formed in the EAF, which are tapped together with the molten steel. Both practices result in lower sulfur levels, but not inclusion shape control. Rare earth metal (REM) additions have been found to provide a level of inclusion shape control for steels. However, great care must be taken when using these additions because of the concern for reoxidation of the REM materials upon casting. Very high quality steel can be achieved through electroslag remelting. This process involves remelting of an electrode of the steel through a molten slag and solidification in a water cooled mold. This can lead to significantly lower sulfur levels, as well as solidification benefits. Therefore the inclusions tend to very limited in number and very small in size. However, this process is very expensive.

## CALCIUM TREATMENT

The primary emphasis of this paper will be on calcium treatment of plates steels. Lukens has a great deal of experience with producing these steels over the past 15 years. Because calcium has a boiling point below steelmaking temperatures, it has been found important to use an injection method to add calcium compounds to the molten steel. Calcium has a very strong affinity for both sulfur and oxygen and therefore the benefits of both lower sulfur and oxygen content are achievable. The recognition that calcium has some limited solubility in molten steel was the key discovery, which led to the use of calcium treatment of production steels.<sup>(6)</sup> With some calcium in liquid solution, it can more efficiently combine with sulfur and oxygen, remove them from the molten steel and have the phases absorbed by the slag cover.

The effectiveness of a calcium treatment may be influenced by a number of parameters. For example, in the calcium argon blowing practice, these may include the amount and chemistry of the calcium compounds, various injection parameters (flow, pressure), use and amount of stirring after injection, molten

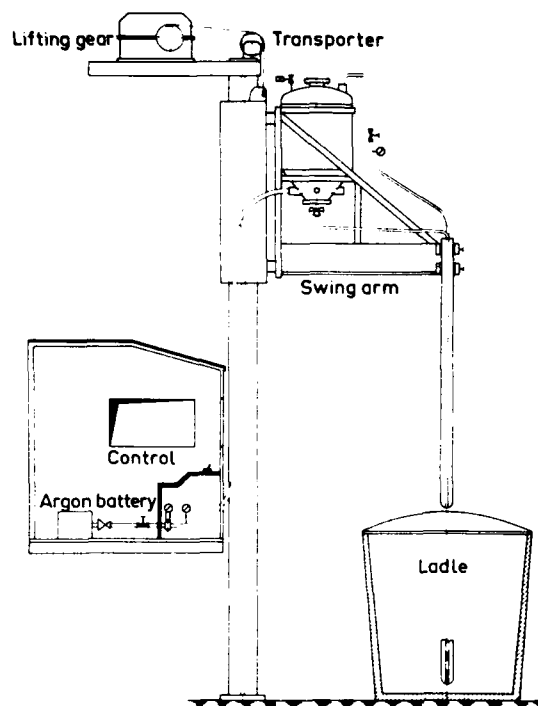


Figure 1 - T-N process for calcium argon blowing to inject calcium compounds into molten steel (2).

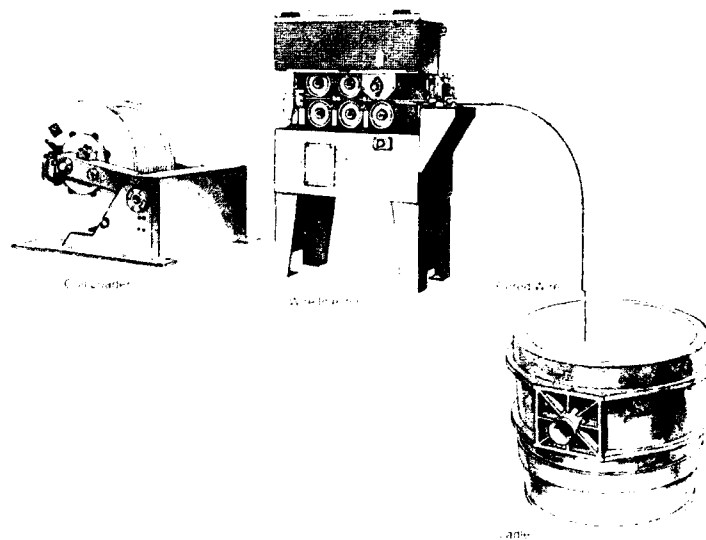


Figure 2 - Calcium cored wire feeding method of Affval (3).

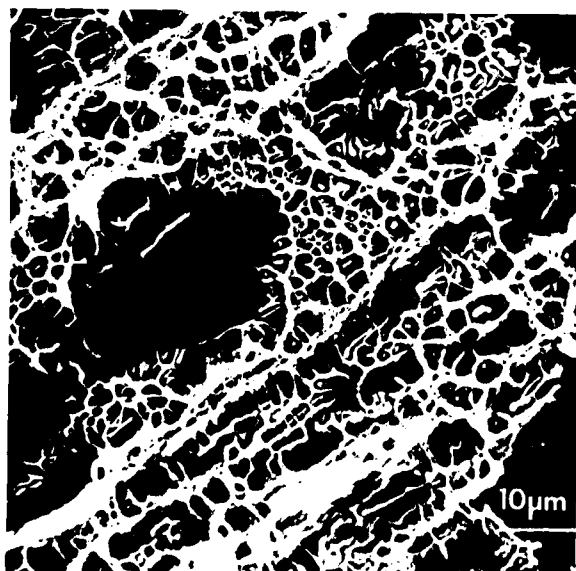


Figure 3 - Homogenization effect on extensively flattened Type II manganese sulfide inclusions from 3/4 inch (19 mm) thick, conventional sulfur level plate.

steel temperature and chemistry, tapping practices, ladle refractory composition (dolomitic versus fireclay), teeming (shrouding) and casting practices and a wide variety of other more specific parameters depending upon the melt shop of interest. Any of these may have an influence on the efficiency of calcium treatment and thus on the inclusion structure of the calcium treated steel.

The benefits of calcium treatment are best described through reviewing how manganese sulfides and alumina inclusion clusters form in a steel. In conventional steels, MnS inclusions have a low melting point and are among the last to precipitate in the solidifying steel and thus tend to accumulate in the interdendritic areas of the cast structure. By the addition of calcium, CaS phases form and rise out of the steel and are absorbed by the slag. The remaining calcium sulfide phases have melting points closer to those of steel and thus are more evenly distributed throughout the steel.

Alumina inclusion clusters form in conventional steels almost immediately after the addition of aluminum for deoxidation. These are very high melting point inclusions and they begin to rise in the molten steel, growing, contacting each other, and forming extensive three dimensional rays. Upon calcium treatment, calcium combines with alumina inclusions in a fluxing reaction, which forms much lower melting point individual, liquid, complex inclusions, which rise more easily out of the molten steel. The chemistry of these inclusions follows the phase diagram shown in Figure 4.<sup>(7)</sup> The more calcium present, the lower the melting point of the  $\text{CaO} \cdot n\text{Al}_2\text{O}_3$  inclusions (Ca-aluminates) that will form. The composition of these calcium aluminates becomes a "telltale" signature of the efficiency of the calcium treatment practice.

### CaO- $\text{Al}_2\text{O}_3$ System (Lea and Desch)

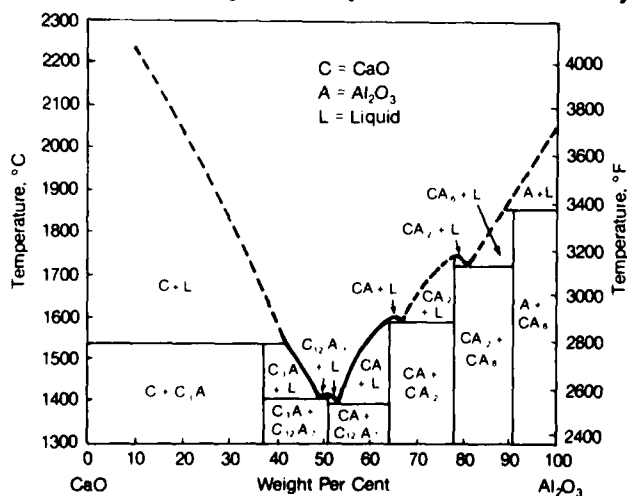


Figure 4 - Phase diagram showing effect of calcium modification on melting point of aluminate phases, from (7) via (6).

The remaining inclusions in calcium treated steels tend to be duplex calcium modified inclusions which resist deformation on hot rolling. The calcium modification of the sulfide phase makes them harder at hot rolling temperatures in comparison to the steel matrix. This is the basic building block for inclusion shape control. However, even more subtle differences can be detected in the inclusion structure of these steels, which are a direct result of the efficiency of calcium treatment.

### INCLUSION CHARACTERISTICS

It is very important to have a number of techniques available to characterize the inclusion content and distribution in a steel. Each method can have a separate contribution and therefore improve the overall understanding of the inclusion structure. Light optical microscopy is still a very valuable tool for this evaluation. In fact, at times it is the most important. Figure 5 exhibits the typical inclusions in a conventional higher sulfur steel. The benefits of calcium treatment in lowering the sulfur content and providing inclusion shape control and the removal of alumina inclusions are demonstrated in Figure 6. These enhancements are also shown through use of fractographic evaluation of various mechanical test specimens from the sample steels. Figure 5 and 6 show the same comparison for conventional steels and the calcium treated steels taken from through-thickness oriented test specimens. The group nature of the Type II manganese sulfide inclusions and the aluminum oxide clusters is evident. Calcium treatment tends to give a better distribution of the remaining inclusions and therefore has a definite effect on properties. Quantitative analysis of inclusions that are in a steel can be attempted through evaluation of mounted metallographic samples through use of manual techniques or using quantitative image analysis. The availability of microprobe analysis is also vital to understanding inclusions in steel. This is very important in identifying inclusions and provides important support in determining the efficiency of the steelmaking practice.

In studies of calcium treated steels, six classes of inclusions have been identified, which are extremely useful in defining the efficiency of a particular practice.<sup>(8)</sup> These are summarized in Figure 7. Although more than one class of inclusion is normally present in any particular steel, generally a trend is noted in an evaluation and it is very useful in representing a certain level of effectiveness of calcium treatment. A brief discussion of the origin and implications of each of these classes of inclusions is given below.

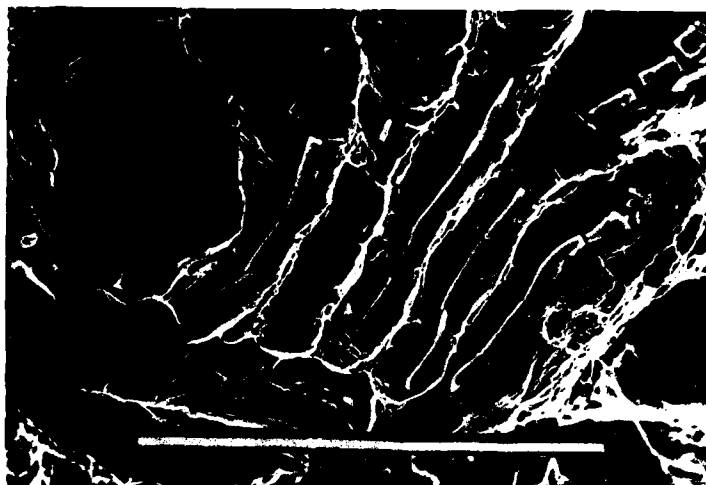
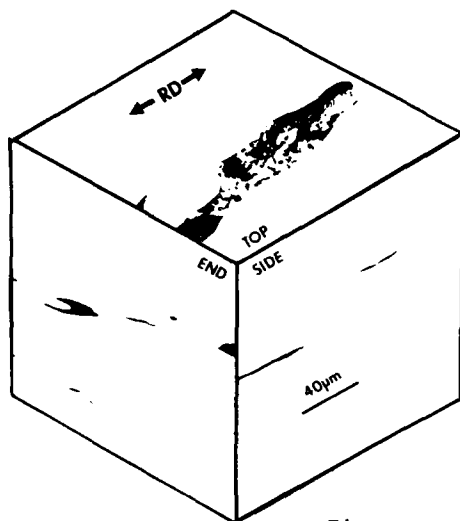


Figure 5a - Composite of light photomicrographs showing the three dimensional nature of Type II MnS inclusions in conventionally produced (CON) A633C steel. At right, these inclusions are explicitly shown in an SEM fractograph of through-thickness CVN fracture.

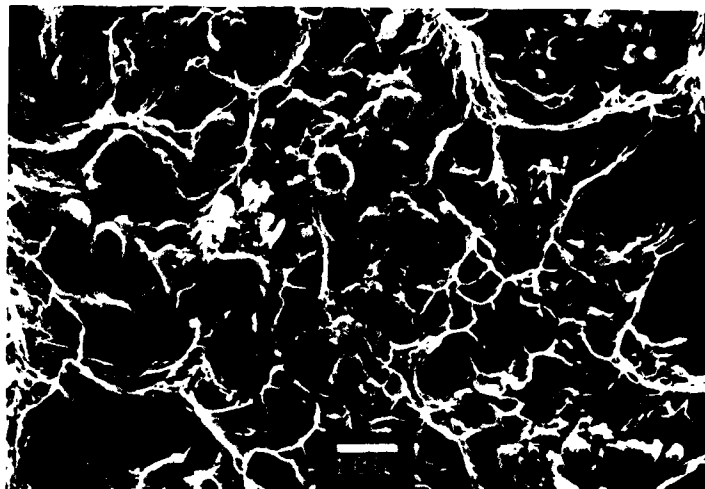
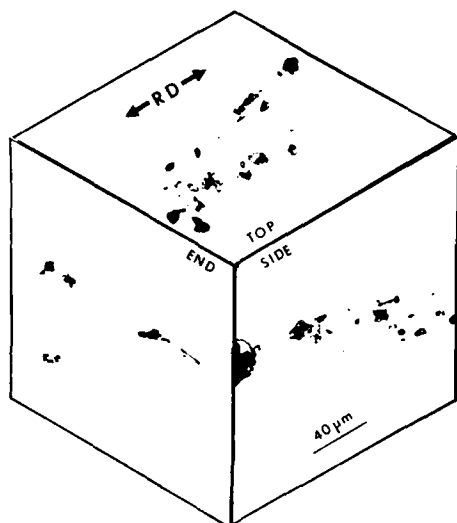


Figure 5b - This optical cube and SEM fractograph of through-thickness CVN fracture reveal  $Al_2O_3$  inclusion galaxies in CON A633C steel.

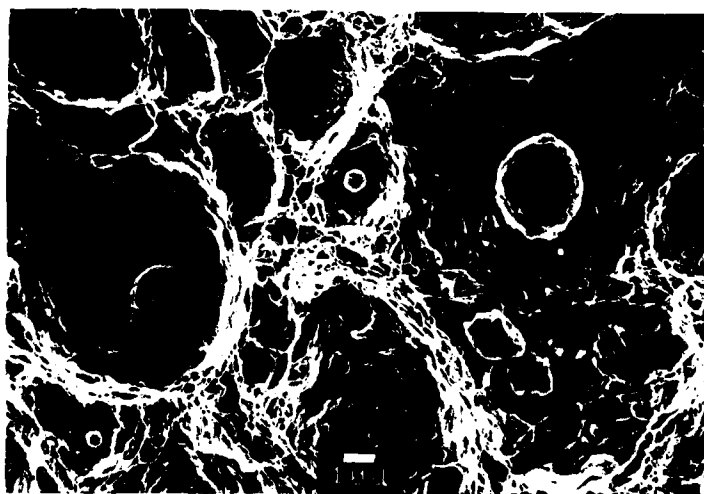
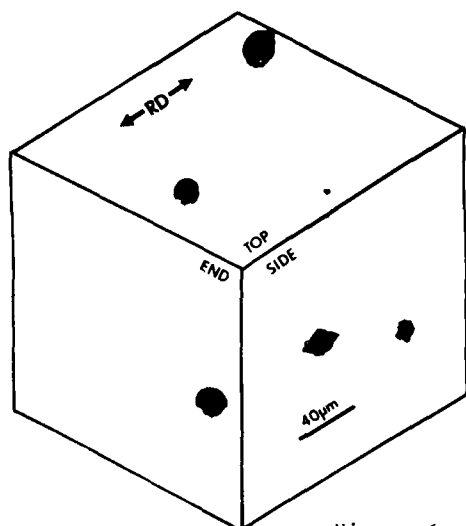


Figure 6 - Typical calcium modified inclusions are shown in a calcium treated (CaT) A633C steel. Such inclusions are usually duplex in nature, and tend to resist deformation on hot rolling.

### Inclusion Classes in Calcium Treated Steels

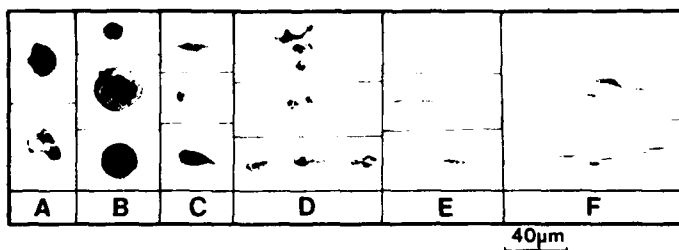


Figure 7 - Six inclusion classes identified in calcium treated steels (8).

Generally, Class A and B inclusions are most desirable and Class D and F are to be avoided. Class A inclusions are made up of intermingled aluminate and sulfide phases. These are indicative of the practice that results in highest levels of calcium being present in the aluminate phase ( $CA$  or  $Ca_{12}Al_7$ ), as can be identified by the microprobe. Class B inclusions are a "bull's-eye" type. These have a central aluminate phase ( $CA_2$  or  $CA$ ) surrounded by a sulfide phase ( $CaS$  or  $(Ca,Mn)S$ ). Class C inclusions are present when less efficient calcium treatment is present because the outer sulfide phase is not modified with calcium and thus elongates during hot rolling. Microprobe studies of examples of Class A, B and C inclusions are shown in Figure 8. Class D inclusions are alumina-like clusters present in the steel. They indicate that there is insufficient calcium present to completely flux all the alumina present and also may be indicative of a reoxidation problem during teeming of the molten steel. Class E inclusions are Type III manganese sulfides. Small Type III manganese sulfides are present in most CaT steels. It is only when extremely low sulfur levels are achieved with a very efficient calcium treatment, that these are eliminated. However, if Class F, Type II manganese sulfide inclusions are present in a steel, it is indicative of an inefficient calcium treatment practice. Not only are the individual inclusions deformed, but they are present as clusters, which can have a significant effect on the level and isotropy of properties.

Through metallographic studies of the calcium treated steel, it has been established that the presence of elongated inclusions (Classes C, E or F) can be a useful indicator of a poorer level of calcium treatment and the level of inclusion shape control. If there are clusters of inclusions present (Class D and F), this is also very important. In general, the presence of elongated inclusions or clusters of inclusions are all indications of less efficient calcium treatment. However, in steels produced on a commercial scale, there normally are a number of these inclusion classes in any particular heat of steel. This may be a result of differences top to bottom of an ingot, surface to mid-thickness, edge to

mid-width, ingot to ingot or within a continuous cast slab. To make more direct comparisons or evaluations, more quantitative techniques are required.

Efforts to quantify inclusion structures have lead to the use of a number of methods both manual and automated. However, because of the variability of the inclusion structure, manual methods have been found to be most appropriate. In particular, one method involves establishing the number of elongated inclusions and measuring the size of the largest inclusions and inclusion clusters in a particular test area. These measurements have been very successful in correlating with actual mechanical property behavior.<sup>(8)</sup>

In early studies of calcium treated steels, the measurement of calcium content could be used as an important tool in indicating quality of the steel. However, calcium measurement is only detected if it is present in inclusions, since there is no calcium in solid solution in steel. Therefore if there is a very high level of inclusions in the steels that are calcium treated, then the calcium level is measured to be very high. If methods are used whereby inclusion content in general is reduced, they will also show a lower calcium content. Figure 9 shows this concern very well. In this figure, the upper shelf energy and the through thickness tensile reduction of area are plotted versus calcium analysis. There was no correlation to speak of between calcium measurement and the proper-ties. On the other hand, there is a very good correlation with sulfur level as shown in Figure 10. Measurements of the inclusion content that were discussed previously, number of elongated inclusions and length of inclusion clusters, gave an excellent correlation. This is displayed in Figure 11. The following regression equations were established and used to generate this comparison for A633C steels.<sup>(8)</sup>

$$USET \text{ (Joules)} = 776 - 15.3p_e - 0.899 UTS -$$

$$32.7L_g$$

$$R^2 = 0.832 \quad SEE = 22.9$$

$$RAS \text{ (percent)} = 155 - 5.33p_e - 23.1L_g - 48.9$$

$$(C+Mn)$$

$$R^2 = 0.761 \quad SEE = 8.17$$

$$p_e = \text{density of elongated inclusions,} \\ \#/\text{mm}^2$$

$$L_g = \text{largest inclusion cluster length} \\ \text{(sulfide or oxide) in test area, mm}$$

$$UTS = \text{ultimate tensile strength, trans.} \\ \text{orient, MPa}$$

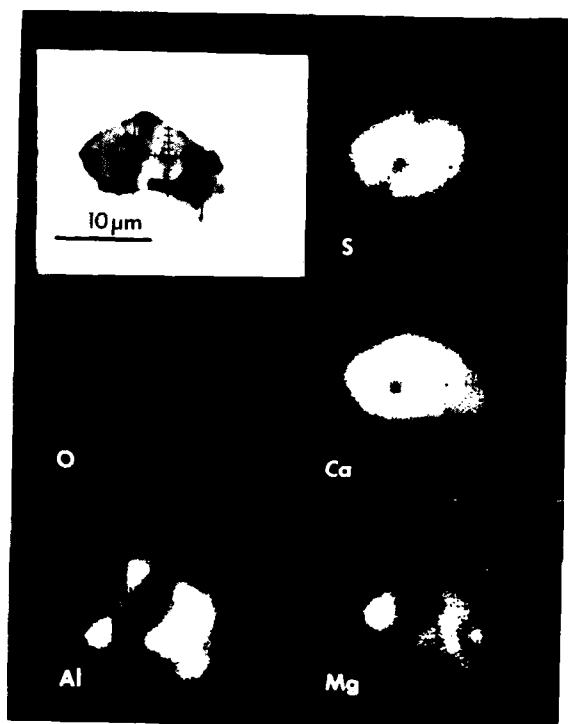


Figure 8a - Microprobe study of Class A inclusion showing intermingled sulfide and aluminate phases.

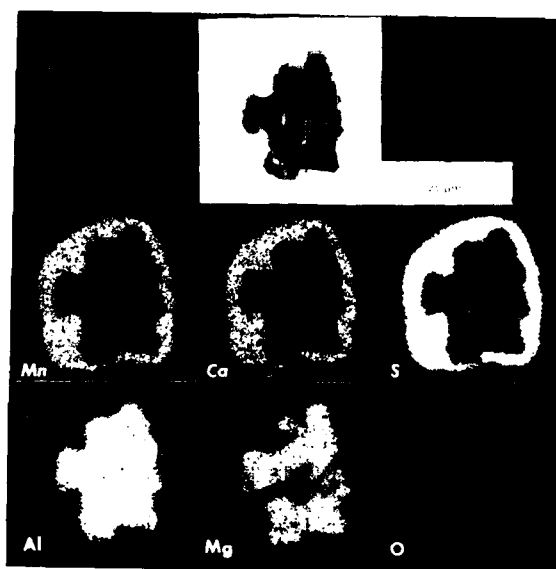


Figure 8b - Microprobe study of Class B inclusion with typical "bull's-eye" appearance.

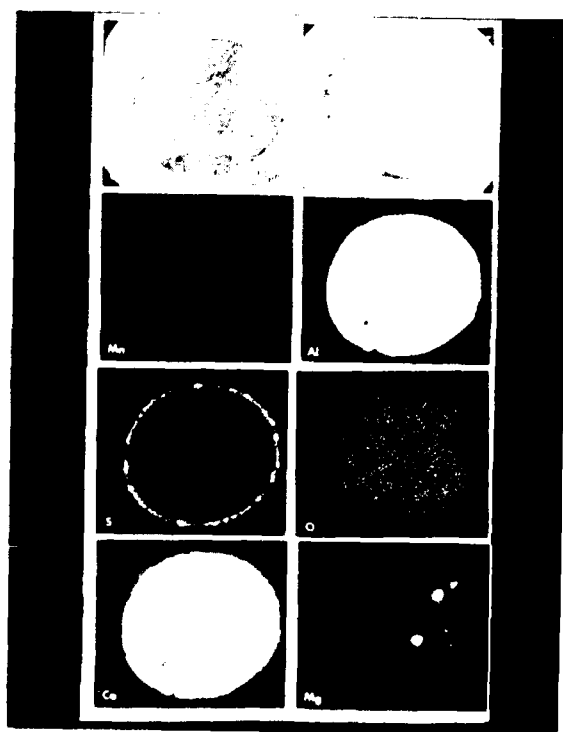


Figure 8c - Microprobe study of Class B inclusion which is primarily a Ca-aluminate.

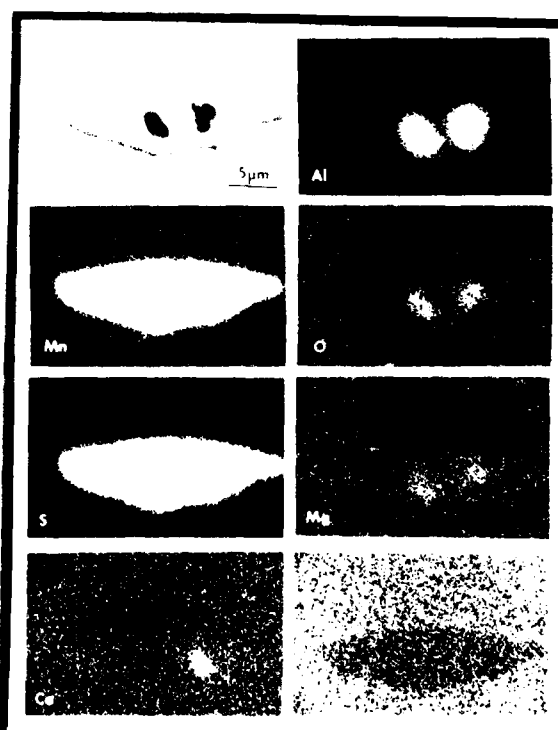


Figure 8d - Microprobe study of Class C inclusion which has deformed because sulfide phase is not modified by calcium.

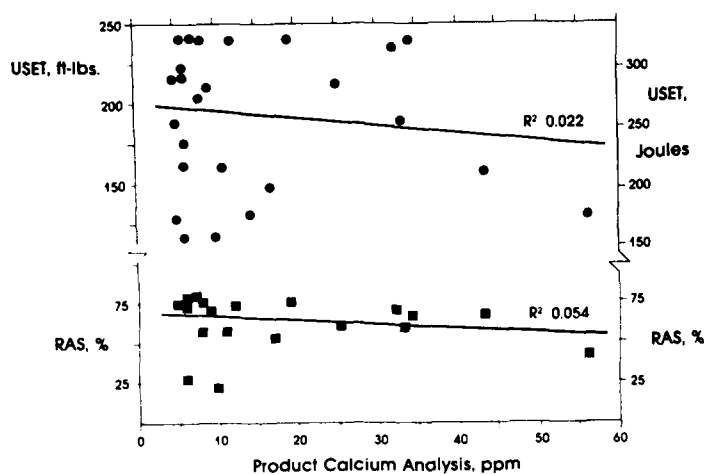


Figure 9 - Transverse CVN upper shelf energy and through-thickness reduction of area versus calcium analysis C-Mn-Cb steels.

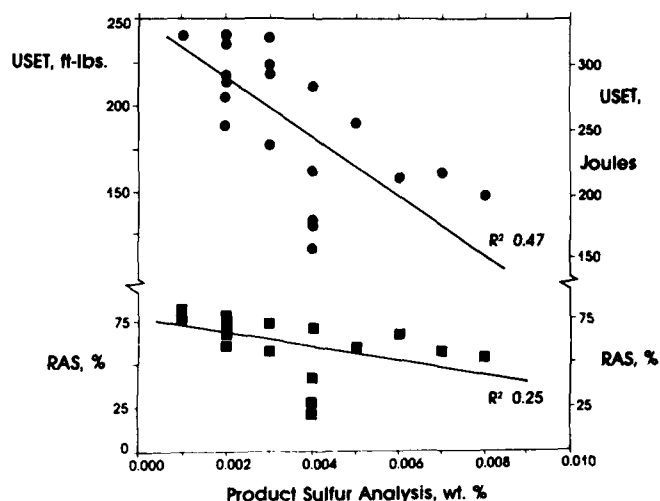


Figure 10 - Transverse CVN upper shelf energy and through-thickness reduction of area versus sulfur analysis C-Mn-Cb steels.

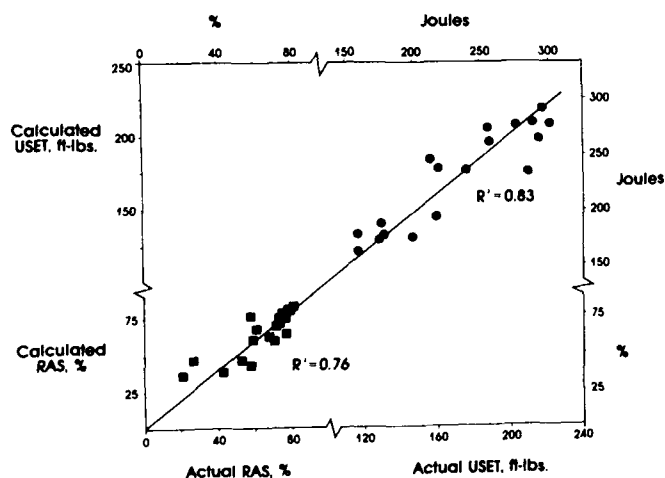


Figure 11 - Calculated versus actual values for transverse CVN upper shelf energy and through-thickness reduction of area C-Mn-Cb steels.

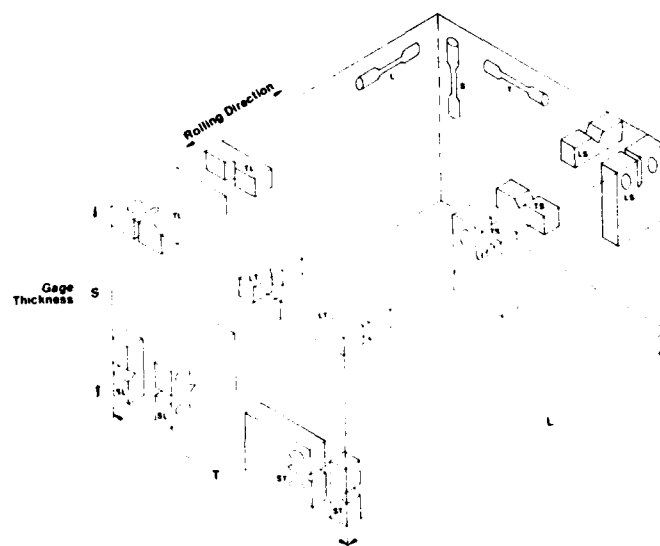


Figure 12 - Schematic drawing showing the specimen orientations and designations per ASTM E399. Actual test location varies with test program.



C,Mn - chemical analysis in weight %  
R<sup>2</sup> - multiple correlation coefficient  
SEE - standard error of estimate

#### MECHANICAL PROPERTIES

In a study of mechanical properties of steels with varying inclusion contents, it is very important to look at a number of testing orientations. Figure 12 exhibits the orientations that can be used. These orientations range from three testing orientations for tensile testing to up to six orientations for CVN and fracture toughness, and fatigue crack growth rate testing. The use of tensile reduction of area as a monitor of inclusion control, came about through the problems with lamellar tearing of steels. The test has continued to be an important quality control measure of the effectiveness of low sulfur practices. Figure 13a shows the effect of calcium treatment on the ductility in a comparison of A588 plates.<sup>(9)</sup> The primary benefit is in the through-thickness orientation(s). If greater efforts are made to lower sulfur and improve inclusion shape control, even better levels of through-thickness ductility are achieved. Figure 14 presents this comparison of the distribution of through-thickness reduction of area data for several hundred plates of A633, Grade C steel produced to 0.010% and 0.005% maximum sulfur levels.

Toughness of the steel is also significantly affected by inclusion content and the effectiveness of calcium treatment. The primary benefits are shown on the upper shelf. Once more, these benefits are more pronounced if the effectiveness of the calcium treatment and the sulfur are even lower. This is displayed in Figure 15. Figure 13b indicates that the benefits of calcium treatment are obtained not only in the through-thickness directions (ST,SL), but also in the transverse (TL) direction. The Charpy V-notch test upper shelf energy has been found to be most sensitive to changes in inclusion structure than the tensile reduction of area. This is shown by developing ratios of property anisotropy (through-thickness/longitudinal for a particular steel) and of quality (conventional/calcium treated for a particular orientation). Figure 16 demonstrates this comparison.<sup>(10)</sup>

The fracture toughness of a steel is also significantly affected by inclusion content.<sup>(9)</sup> Once more, this is primarily shown where there is completely ductile fracture behavior taking place (on the upper shelf). J-integral and crack tip opening displacement tests have particularly shown the benefits of inclusion control. Figure 17 presents the J- $\Delta a$  curves comparing conventional and a calcium treated A588 steel. The

benefits are shown through-out the range from initiation through ductile tearing. This is further shown in the presentation in Figures 13d-f where the initiation toughness and the tearing modulus are compared for the two steels.

Comparisons of fatigue crack propagation behavior exhibit less sensitivity to inclusion structures. Figure 18 displays a calcium treated steel with almost completely isotropic behavior, while a conventional steel shows significant anisotropy.<sup>(9)</sup> This is further highlighted in Figure 19 where the through-thickness orientations (SL) display the greatest difference in properties.<sup>(11)</sup> This is a result of the inclusion groups in the CON steel forming a plane of weakness to ease fatigue crack propagation. Fatigue crack propagation is one test that shows another interesting phenomena. It is only in FCP testing that there is difference between the ST and SL orientations.<sup>(10)</sup> This is displayed in Figure 20. This is a result of the smaller crack tip plastic zone in the FCP test. The effect of inclusion control in FCP testing is still most emphasized in the through-thickness direction with some effects in the TL and LS orientations. These results are summarized in Figure 13g. Figure 13h also displays the effect of inclusion control on the threshold for FCP. It was found that the inclusions in the conventional steel (CON) tended to induce a significant amount of crack closure in the threshold tests. This resulted in a wedge opening of the crack and, in fact, gave the appearance of improved threshold behavior for the conventional steel compared to the calcium treated steel. When corrections are made for this closure component, it is noted that there is a significant decrease in the threshold properties for the conventional steel.<sup>(9)</sup> When fatigue growth rate testing is performed in a corrosive environment, the benefits of inclusion control continue. Figure 21 indicates that calcium treated steels continue to show consistently slower growth rates in all testing conditions in a 3.5% NaCl environment, even at testing frequencies of 0.1 Hertz.<sup>(12)</sup>

The mechanical behavior of friction welds can also benefit from inclusion control.<sup>(13)</sup> Friction welds are a very special case where through spinning of a product and pressure being applied in an axial direction a solid state welding of material is obtained. A resulting weld is shown in Figure 22. When Charpy tests are taken from the centerline of these weldments, a significant influence of inclusions is discovered. The inclusions that are present in the steel are rotated into a plane perpendicular to the surface of the plate as a result of this welding process. Therefore, a plane of weakness is formed in the steel in that direction. Figure 23 provides the results of CVN testing performed in this location. This reveals that calcium treatment results in a significant improvement

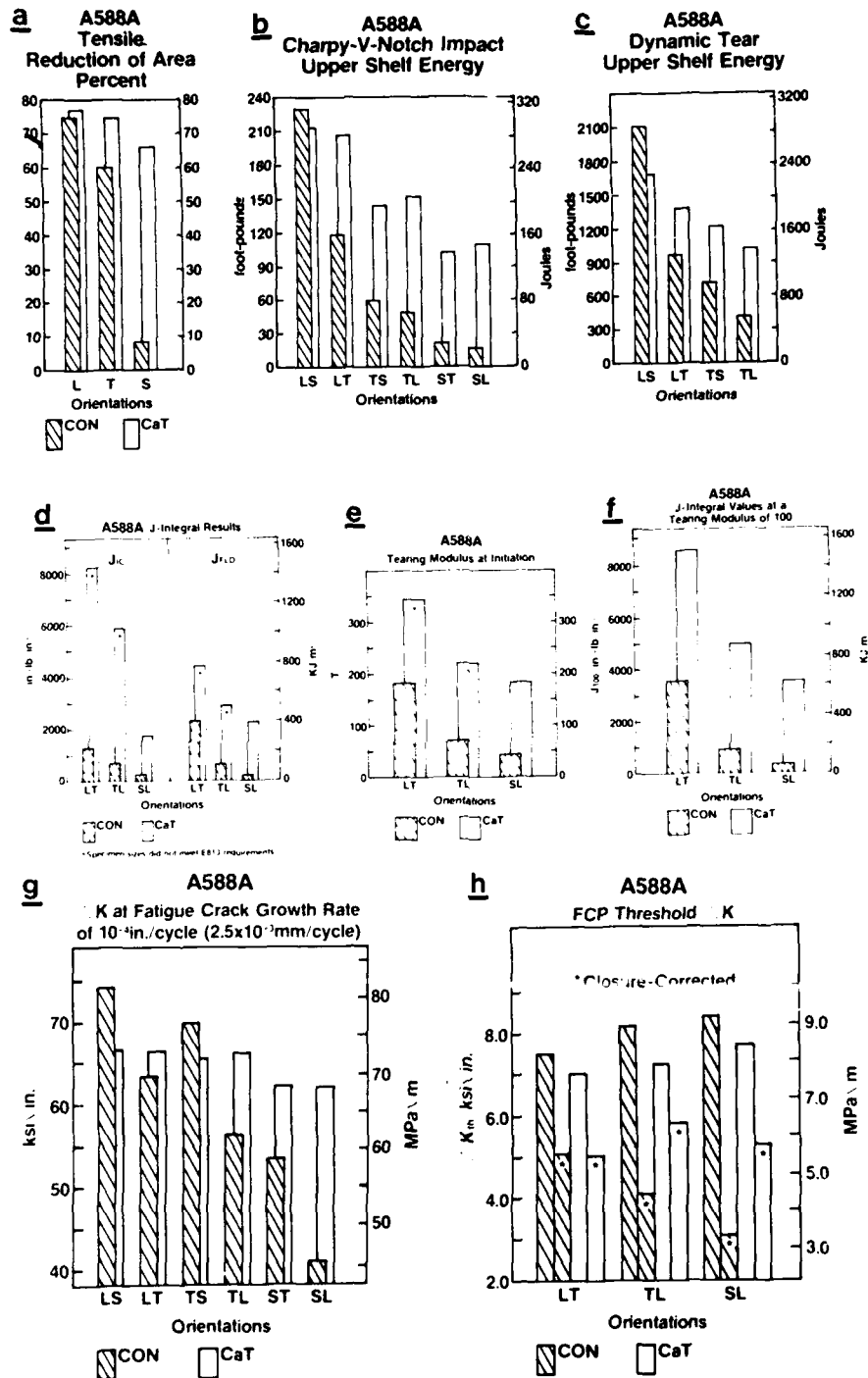


Figure 13 - Summary bar graphs of key test results of this investigation on two A588A, 3" thick plates. CON - conventional quality 0.020% S; CaT - calcium treated 0.003% S (9).

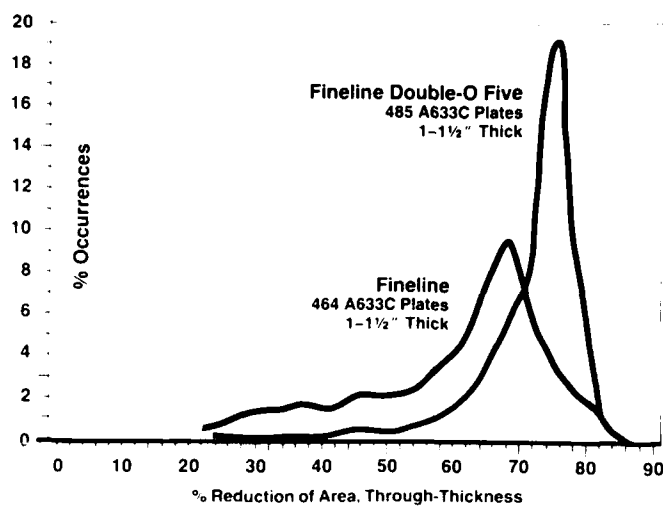


Figure 14 - Distribution of through-thickness reduction of area for 0.010% maximum sulfur level steels (Fineline) compared to 0.005% maximum.

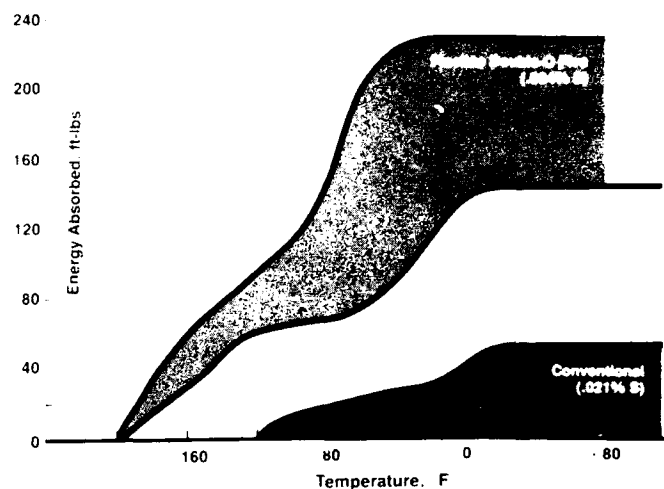


Figure 15 - Comparison of Charpy V-notch energy absorption for normalized 1-2" thick ASTM A633C plates, transverse orientation.

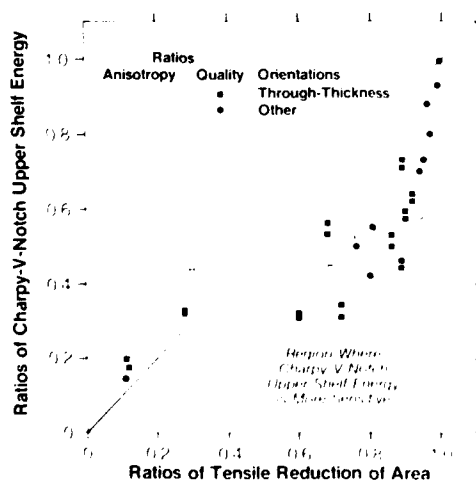


Figure 16 - Comparison of anisotropy and quality ratios for Charpy V-notch upper shelf energy and tensile reduction of area for a range of steel grades (10).

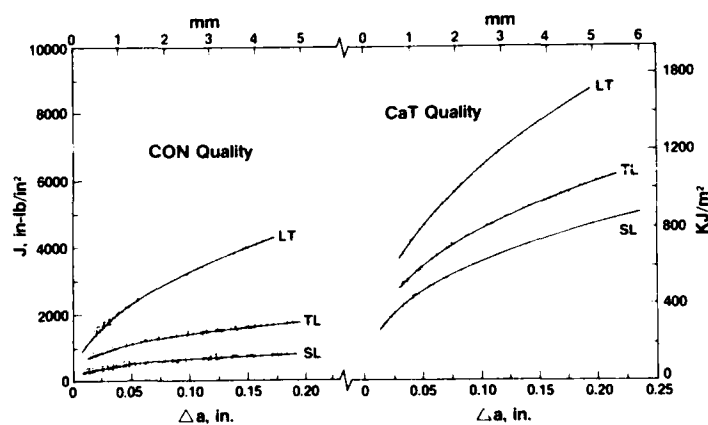


Figure 17 - J- $\Delta a$  resistance data 0.006 in. (0.15 mm) beyond the ASTM E813 "blunting-line" for each specimen (two specimens per orientation). Overall best fit power law lines are shown for these A588A steels.

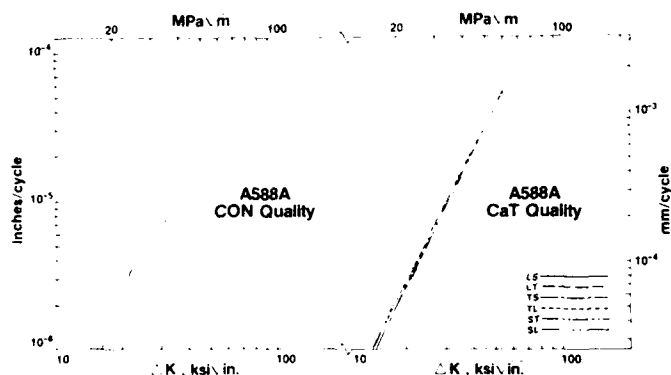


Figure 18 - FCP best fit regression lines using Paris' FCP equation for A588A steel. Six testing orientations and two quality levels are displayed. The improved isotropy of the CaT steel is evident. The CON steel exhibits the fastest growth rates in the SL orientation (9).

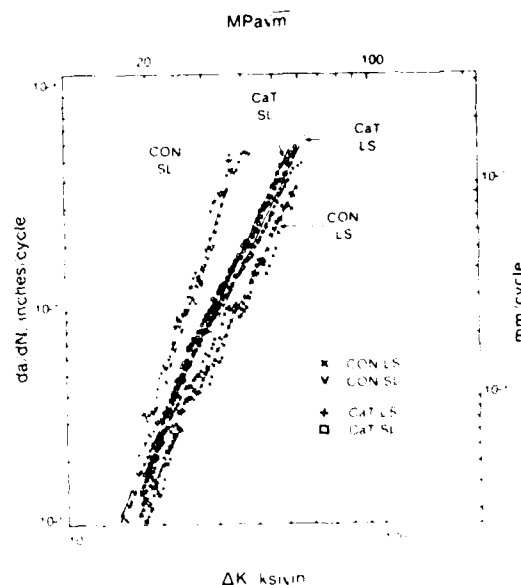


Figure 19 - FCP data and Paris' FCP regression lines for A588A steel in two quality levels in LS and SL orientations are displayed (2 test specimens per orientation and quality). The improved isotropy of the CaT steel is demonstrated. Note the higher scatter in the CON - LS tests.

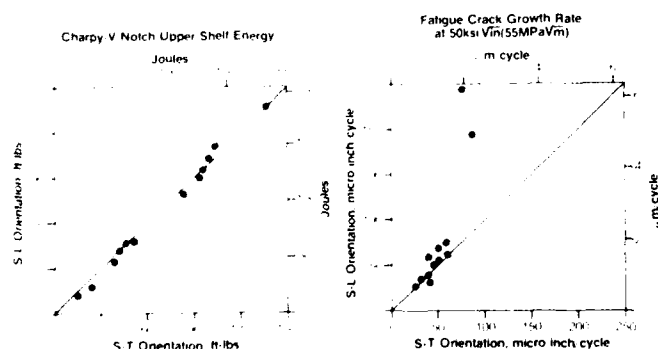


Figure 20 - Plots comparing the ST and SL orientation results for both Charpy V-notch upper shelf energy and fatigue crack growth rate at 55 MPa√m for a range of steel grades (10).

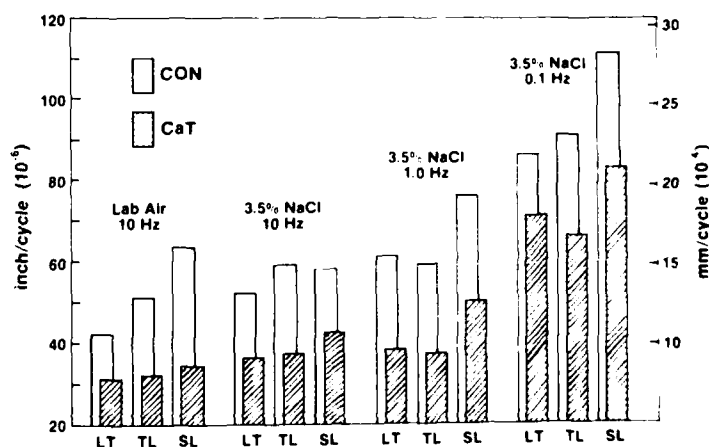


Figure 21 - The fatigue crack growth rates of CON and CaT quality A633C steels in three testing orientations and noted salt-water testing conditions are compared at a  $\Delta K$  of 55 MPa√m (50 ksi√in.). The CaT steel exhibits consistently slower rates at all testing conditions (12).

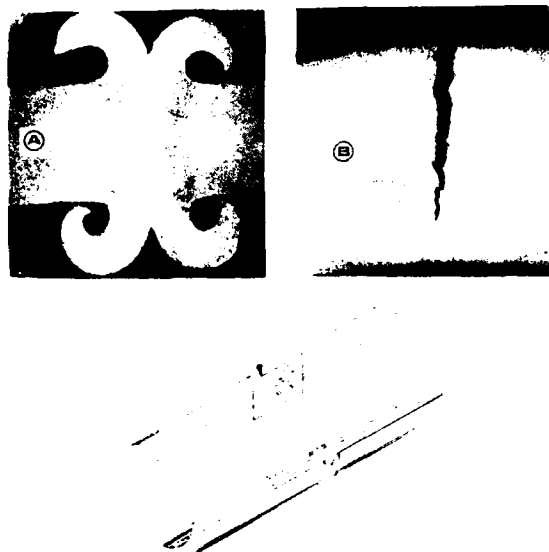


Figure 22 - Formation of a friction weld in pipe showing A - metal flow; B - tendency for cracks to propagate in the flow direction along planes of weakness such as lamellar inclusions and laps

in CVN performance over conventional higher sulfur level steels.

#### SUMMARY

In the foregoing paper, a review has been presented of Lukens' experiences with characterizing the inclusion structures in plate steels with an emphasis on calcium treated, low sulfur steels. Elongated sulfide or clusters of alumina-like inclusions are found to be most indicative of inefficient calcium treatment practices. These evaluations have been useful in evaluation of melt shop procedures, which have been enhanced over the past 15 years. These techniques will continue to be important as continual advances are made to steelmaking and refining technology. The conclusion that "inclusions are the fingerprints of the melt shop" will continue to hold true in the future.

In the investigation of the influence of inclusions on the mechanical properties of steels, different behavior has been found for each test that is used. Testing orientation is a particular discriminator of behavior. Tensile ductility, CVN and fracture toughness and fatigue properties all have unique responses to inclusion structure. Although some correlations may be possible, it is important to examine each test method separately and the influence of inclusion structure on the micromechanisms of fracture.

#### ACKNOWLEDGEMENTS

The author would like to appreciatively acknowledge the contributions of his colleagues at the Lukens Steel Company during the various research programs summarized in

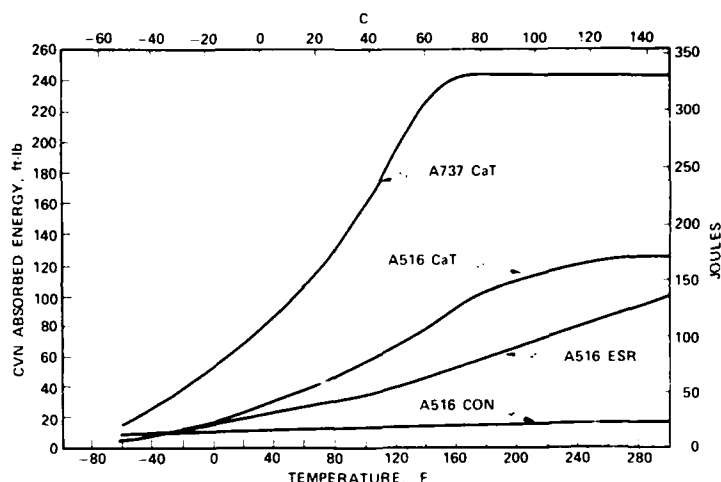


Figure 23 - CVN properties of inertia friction welds showing improvement in toughness obtained through inclusion control (13).

this paper. Particular thanks are accorded to L. P. Kerr, J. R. Lohr and J. A. Gulya. Mr. Gulya provided critical review, support and guidance throughout these efforts.

#### REFERENCES

1. J. M. Camp and C. B. Francis, "The Making, Shaping and Treating of Steel", Fourth Edition, C. 1919, Carnegie Steel Company.
2. Pircher, H. and Klapdar, W., "Proceedings Microalloying 75", Oct. 1975, Washington, D.C., pp 15-22.
3. A. L. Gueussier, E. V. Vachier, J. L. Tranchant and R. Szezesny, Iron and Steel Engineer, October 1983.
4. A. D. Wilson, Met. Trans. A, Vol. 8A, Jan. 1977, pp 201-202.
5. A. D. Wilson, "Toughness Characterization and Specifications for HSLA and Structural Steels", TMS-AIME, New York, 1978, pp 287-307.
6. Hilty, D. C. and Popp, V.T., "Proceedings Electric Furnace Conference", 1969, pp 52-66.
7. Lea, F. M. and Desch, C. H., "The Chemistry of Cement and Ceramics", London, 1956, 2nd Ed., pp 52, via Ref. 6.
8. A. D. Wilson, "HSLA Steels, Technology and Applications", ASM, 1984, pp 419-428.

9. A. D. Wilson, "Fracture Mechanics: Fifteenth Symposium, ASTM STP 833", 1984, pp 412-435.
10. A. D. Wilson, "Through-Thickness Tension Testing of Steel, ASTM STP 794", ASTM, 1983, pp 130-146.
11. A. D. Wilson, "Fracture: Interactions of Microstructure, Mechanisms and Mechanics", ed. J. M. Wells and J. D. Landes, 1984, TMS AIME, pp 235-254.
12. A. D. Wilson, Trans. ASME, J. Eng. Mat. and Tech., Vol. 106, July 1984, pp 233-241.
13. B. J. Eberhard, B. W. Schaaf, Jr. and A. D. Wilson, Welding Journal, July 1983, pp 171s-178s.

# SULFUR CONTENT, INCLUSION CHEMISTRY, AND INCLUSION SIZE DISTRIBUTION IN CALCIUM TREATED 4140 STEEL

**Dennis W. Hetzner**

The Timken Company  
Canton, Ohio, USA

**Bruce A. Pint**

Massachusetts Institute of Technology  
Cambridge, Massachusetts, USA

## ABSTRACT

Based upon specific applications, non-metallic inclusions can be beneficial or detrimental to a particular material system. For example, in critical applications where high toughness is required, non-metallic inclusions can be quite detrimental to performance. However, for gears and similar components that are not subjected to high stress levels under normal operating conditions, the presence of certain inclusions can be very beneficial to machining operations while not degrading the particular component's performance. The Timken Company manufactures two types of calcium treated steels to serve these specific requirements, Cal and Ca2. For improved machinability, Cal, having a minimum sulfur content of 0.025 percent, would be required. For improvements in mechanical properties, Ca2, having a maximum sulfur content of 0.005 percent, would be specified. Both of these alloys are unique because of their low oxygen content, generally less than 20 ppm for a 0.40 percent carbon steel.

Calcium treating steel modifies oxide and sulfide inclusion chemistry and morphology. As the sulfur content increases, the size and number of inclusions in the steel increases. The degree of inclusion shape control and the types of oxides within the steel are related to sulfur and oxygen content.

It is necessary to accurately assess inclusion chemistry and inclusion size distributions to determine how steelmaking practices affect these parameters and how these parameters eventually affect mechanical properties. The problem of chemical analysis is often complicated by the fact that the complex calcium and aluminum oxides in these alloys are generally encapsulated by (Ca, Mn) sulfides. For this analysis, steels having sulfur contents ranging from 0.002 percent through 0.036 percent and calcium contents from 14 ppm through 50 ppm were used.

The following topics are discussed:

1. An analytical EDX technique which, to a first approximation, allows for Ca X-rays originating in the sulfide phase of dual phase inclusions to be separated from Ca X-rays originating from the oxide phase.
2. The variation of inclusion chemistry and quantitative metallographic parameters such as number per unit area, average length, area, and roundness, as a function of S and Ca, is illustrated.
3. Based upon the log-normal distribution, techniques for predicting the number of inclusions per unit area greater than a given length  $l_0$  are described. The analysis considers how this parameter varies with sulfur content.

## INTRODUCTION

By calcium treating alloy steels, significant changes in properties can be realized. It is well documented that as the amount of inclusions in most material systems is reduced, ductility improves.[1]\* For alloy steels, calcium treating can be used to lower the sulfur and oxygen content as well as modify inclusion morphology, the net result being a reduction in the number of inclusions present and final shapes that are globular rather than elongated, Figure 1. This can greatly improve transverse toughness, Figure 2.

When complex parts are machined from bars or tubes, calcium treating can be used to improve a steel's machinability.[2] Calcium modifies the inclusion morphology but does not greatly reduce the number of inclusions present. When these steels are properly treated, the

oxide inclusions are primarily calcium aluminates, encapsulated by calcium-manganese sulfides, Figure 3.

As illustrated by these examples, a large change in inclusion size, morphology and chemical composition can occur over a relatively small change in sulfur and calcium content. The following discussion will focus on these effects. Two sets of 4140 calcium treated steels will be considered. The first set contains sulfur levels ranging from 0.002 percent through 0.036 percent with a nominal calcium content of 30 ppm and an oxygen content

of 20 ppm. The second set contains calcium contents ranging from 14 ppm through 47 ppm with a nominal sulfur content of 0.029 percent and 10 ppm oxygen. Quantitative metallographic analysis will illustrate how these parameters affect the inclusion distributions and how the number of large inclusions present can be predicted from the inclusion distribution. A Scanning Electron Microscope - Energy Dispersive Spectrometer (SEM-EDS) methodology which separates X-rays originating from the sulfide and oxide phases will be used to illustrate how inclusion chemistry changes with sulfur and calcium content in low oxygen alloy steels.

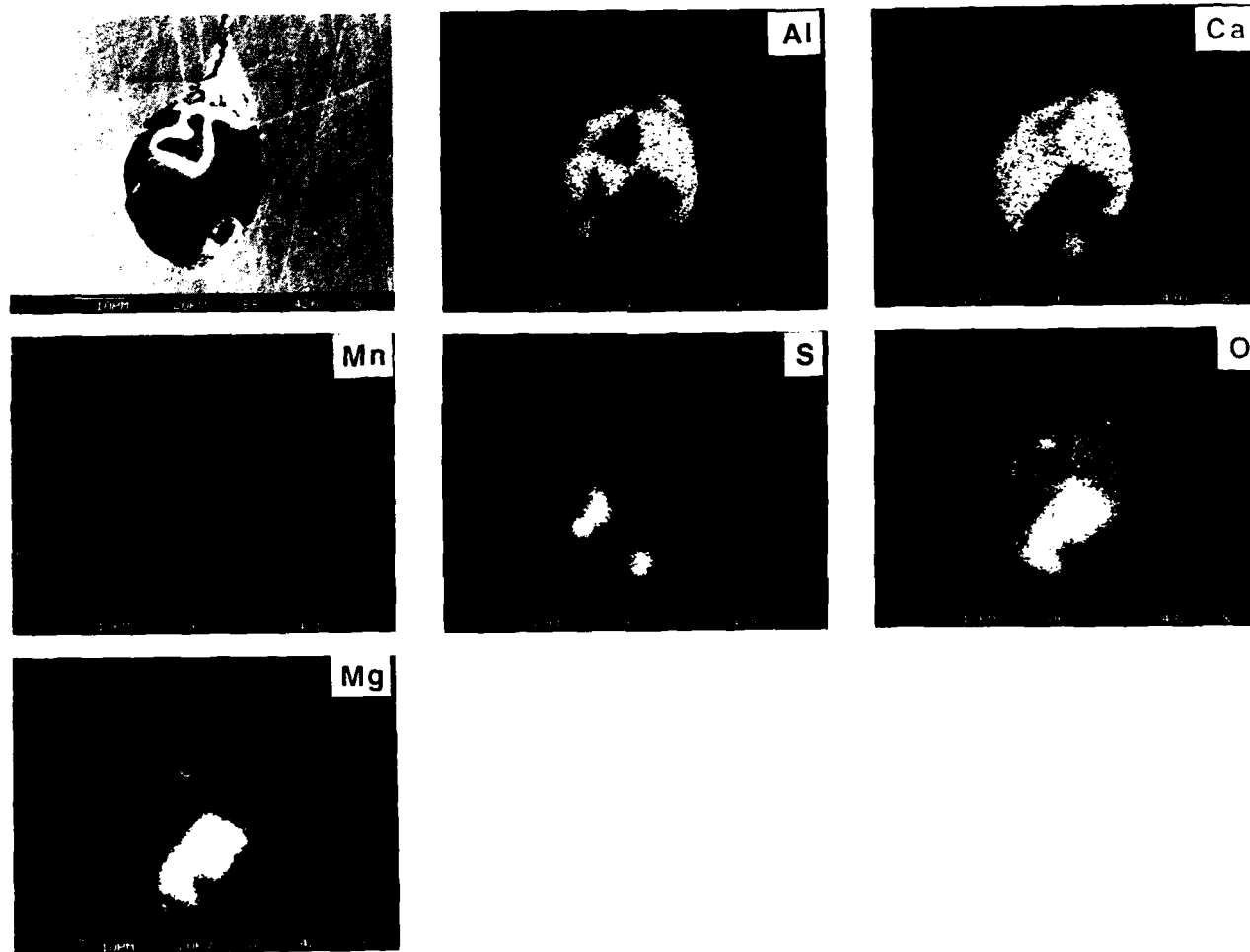


Figure 1 - X-Ray Map of an Inclusion in Heat A



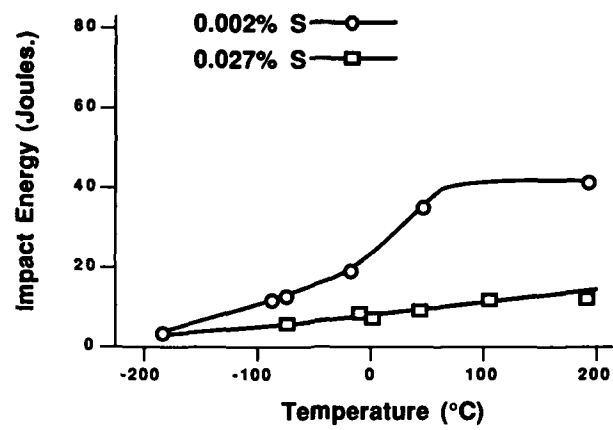


Figure 2 - Effect of Temperature on CVN Impact Toughness for a Low and High Sulfur Steel

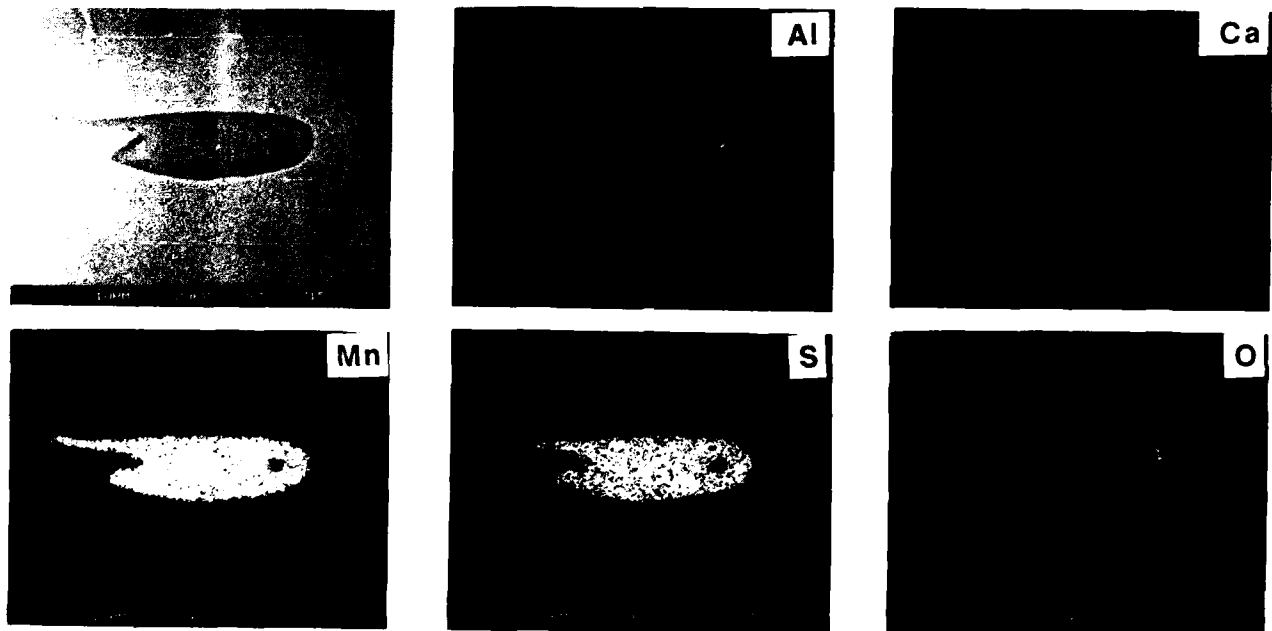


Figure 3 - X-Ray Map of an Inclusion in Heat E

## EXPERIMENTAL PROCEDURES

The steels used in this investigation were from commercial quality air melted calcium treated heats. The specific samples studied were from longitudinal mid-radius planes of polish from 150mm diameter round bars. The bars were from the mid height of an ingot and the ingots were from the middle of the heat. The sulfur, calcium, and oxygen contents of the steels are contained in Table 1.

The metallographic specimens were austenitized at 1550°F for one hour then water quenched. After mounting in bakelite, the specimens were ground on a 120 grit wheel. The samples were rough polished on a lap charged with 15 $\mu$ m diamond. After polishing with 3 $\mu$ m and 1 $\mu$ m diamond abrasive, a final hand polishing using 0.05 $\mu$ m alumina completed sample preparation for quantitative metallographic analysis (QTM). For SEM-EDS analysis, the final hand polish used 0.25 $\mu$ m diamond to prevent contamination by the alumina powder. In all instances, the specimens were cleaned with acetone to prevent the reaction of calcium with water.

Quantitative metallographic analysis was performed using a Cambridge Quantimet 900 equipped with a Plumbicon TV scanner. Using a 32x objective lens, each field of view observed was 327 $\mu$ m by 225 $\mu$ m. Each individual run consisted of 160 fields of view for a total area of approximately 13.33mm<sup>2</sup>. For the samples having sulfur contents up to 0.036 percent, 10 planes of polish were analyzed. This corresponds to a 133mm<sup>2</sup> area. For the set of specimens having a relatively constant sulfur content six planes of polish, 80mm<sup>2</sup>, were analyzed.

The steels used in this investigation have a very low oxygen content of approximately 20 ppm. This corresponds to an oxide volume fraction of approximately 0.010 percent. [3] Furthermore, due to calcium treating, the oxides are generally surrounded by a sulfide envelope. For these reasons, the entire inclusion, oxide and sulfide, was measured for QTM analysis.

## RESULTS & DISCUSSION

**QUANTITATIVE METALLOGRAPHY** - For each inclusion, the number of inclusions and the length (l), thickness (t), area (A), perimeter (P), anisotropy (length  $\div$  thickness) and

roundness ( $R = P^2/4\pi A$ ) of each inclusion was recorded. These types of measurements are referred to as feature data as compared to field data which represents the entire sum of a particular parameter for an entire field of view. For statistical evaluation, the sums and the sums of the squares of these parameters were tabulated. A typical data set is contained in Table 2.

For the specimens with the varying sulfur content, the number of inclusions per unit area ( $n_A$ ) increased as the sulfur content increased, Figure 4 and Table 1. As illustrated, there is a large scatter about the mean for each data set. In all figures, the error bands represent 95 percent confidence intervals for each data set. Similarly, the mean inclusion length and the mean inclusion area increase as the steel's sulfur content increases, Figures 5 and 6.

The mean inclusion roundness increases as sulfur content increases, up to approximately 0.018 percent S, and then appears to remain constant to levels up to 0.036 percent S, Figure 7. This indicates that increasing the sulfur level increases the number of inclusions as well as their size.

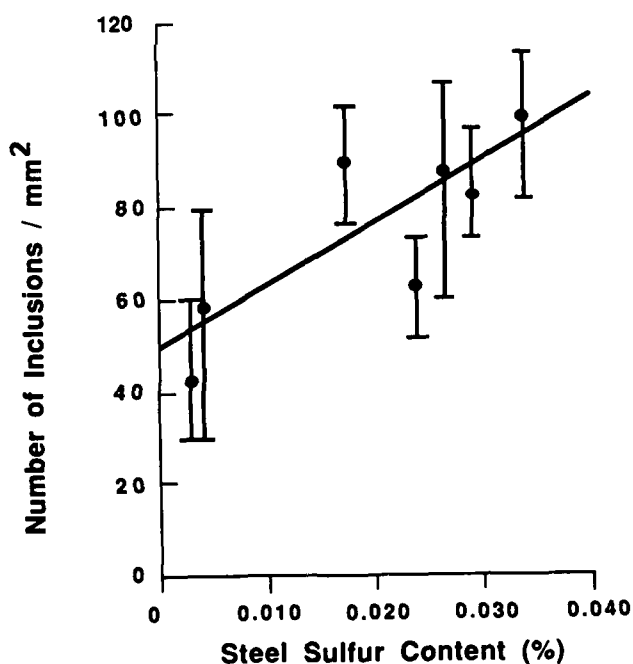


Figure 4 - Change in the number of inclusions per unit area as a function of steel sulfur content.

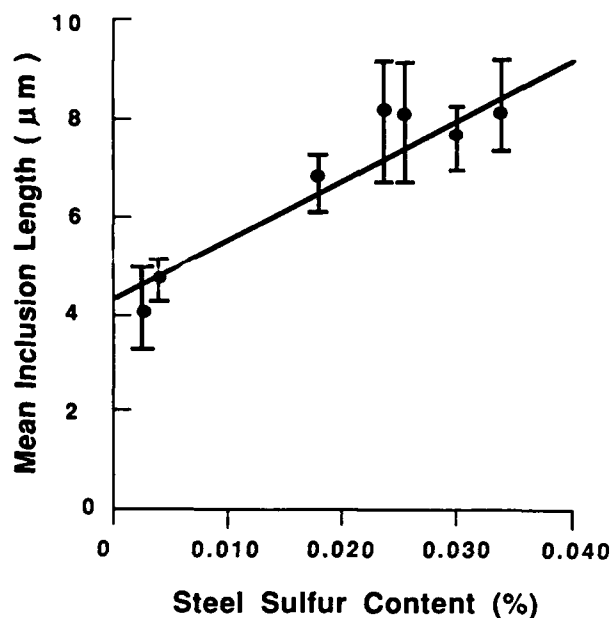


Figure 5 - Relationship between mean inclusion length and steel sulfur content.

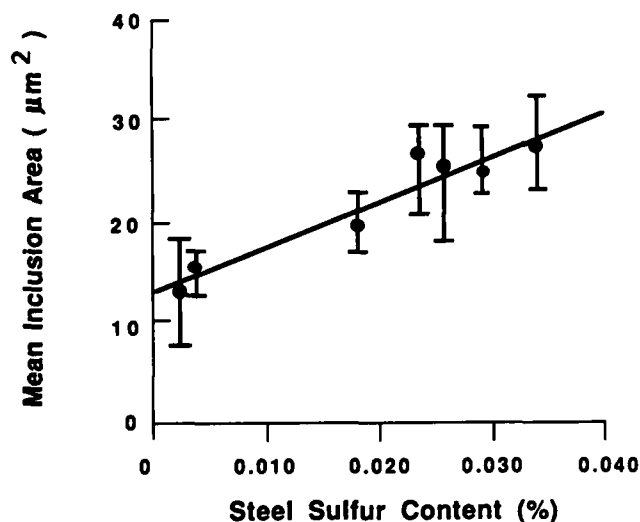


Figure 6 - Relationship between mean inclusion area and steel sulfur content.

For the steels with approximately 0.029 percent S, some different trends are observed as the calcium content varies from 14 through 47 ppm. The mean inclusion length, area, and roundness all tend to decrease as the calcium content increases, Figure 8. While the magnitude of these changes are smaller than those observed by varying the steel sulfur content, these data do indicate the tendency calcium has to produce globular rather than stringer types of sulfides in higher sulfur steels. Since the sulfur content of these steels is constant, and  $\text{CaS}$  is less dense than  $\text{MnS}$ , it would be expected that the number of inclusions per unit area would increase as the calcium content increased. However, due to the large scatter in  $n_A$ , this trend is not clearly seen, Table 1.

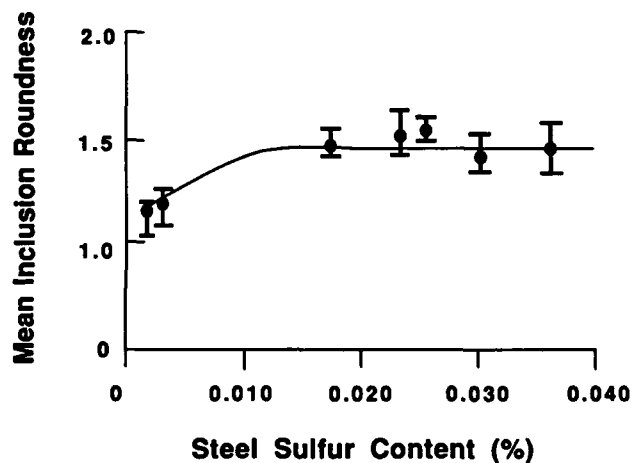


Figure 7 - Relationship between mean inclusion roundness and steel sulfur content.

The feature data and distribution of the individual inclusion lengths can be used to predict the number of particles per unit area greater than some specific size. For example, in the case of the 0.018 percent S steel, plotting the cumulative frequencies of the class boundaries on log-normal probability paper suggests that the length distribution may be approximated by a log-normal distribution, Table 3 and Figure 9; similar findings have been reported elsewhere.[4] The log-normal plots further illustrate how increasing the steel's sulfur content changes the inclusion length distributions. As sulfur increases, the median inclusion length increases and the slope

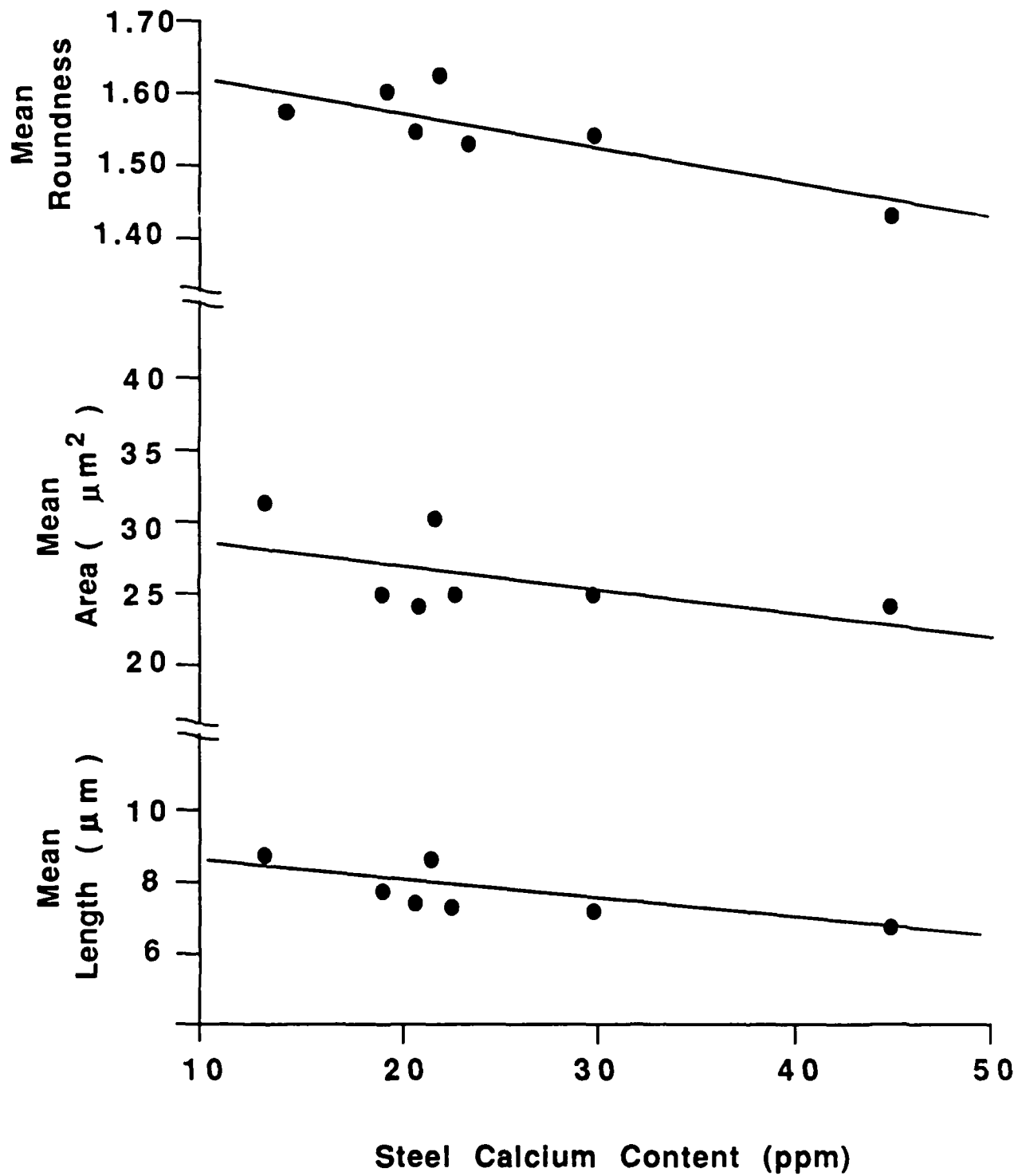


Figure 8 - Relationship Between Mean Inclusion Length, Area and Roundness with Respect to Steel Calcium Content for a Steel Containing 0.029% Sulfur

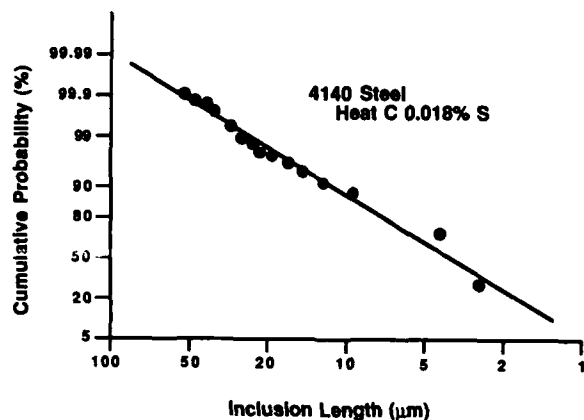


Figure 9 - Cumulative distribution of inclusion lengths in heat C.

decreases, Figure 10. For a large number of particles,  $n$ , the mean and standard deviation of the data set can be approximated by:

$$\mu = \frac{\sum \chi_i}{n} \quad (1)$$

$$\sigma^2 = \frac{n \sum \chi_i^2 - (\sum \chi_i)^2}{n(n-1)} \quad (2)$$

For the log-normal distribution in the transformed system, the mean and standard deviation,  $\alpha$  and  $\beta$  respectively, can be expressed as:

$$\alpha = \ln\{\mu/[(\sigma/\mu)^2 + 1]^{1/2}\} \quad (3)$$

$$\beta = \{[\ln\{(\sigma/\mu)^2 + 1\}]\}^{1/2} \quad (4)$$

The median (50 percent value) is

$$\chi_{50} = \exp(\alpha) \quad (5)$$

$$\text{mean}(\mu) = \exp(\alpha + \beta^2/2) \quad (6)$$

and the values of  $\chi$  corresponding to cumulative probabilities of 84 percent and 99 percent are:

$$\chi_{84\%} = \exp(\alpha + \beta) \quad (7)$$

$$\chi_{99.9\%} = \exp(\alpha + 3.09 \beta) \quad (8)$$

Based on this analysis, software was developed to obtain the number of inclusions in the length histogram, the sum of the inclusion lengths, and the sums of the squares of the inclusion lengths. These values were used to predict the number of inclusions per unit area greater than  $20 \mu\text{m}$  in length by the following procedure:

For a log-normal distribution, the density function for a standard variable is:

$$f(\chi) = \frac{e^{-(\ln \chi - d^2)/2 \beta^2}}{\sqrt{2\pi} \beta \chi} \quad (9)$$

(In this instance,  $\chi$  is the inclusion length being considered in real space;  $\ln \chi$  is the transformed length.)

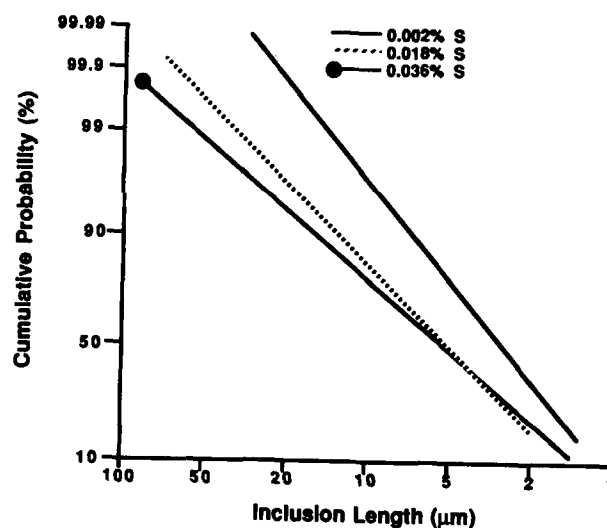


Figure 10 - Effect of steel sulfur content on inclusion length distribution.

The upper tail of the distribution is (Figure 11):

$$Q(\chi) = \frac{1}{\sqrt{2\pi}} \int_{\chi}^{\infty} e^{-t^2/2} dt \quad (10)$$

This can be approximated by (5)

$$Q(X) = f(X)(b_1t + b_2t^2 + \dots b_5t^5) + \epsilon(X) \quad (11)$$

where  $|\epsilon(X)| < 7.5 \times 10^{-8}$

$$t = \frac{1}{1 + rX} \quad (12)$$

and

$$\begin{aligned} r &= 0.2316419 \\ b_1 &= 0.31938153 \\ b_2 &= -0.356563782 \\ b_3 &= 1.781477937 \\ b_4 &= -1.821255978 \\ b_5 &= 1.330274429 \end{aligned}$$

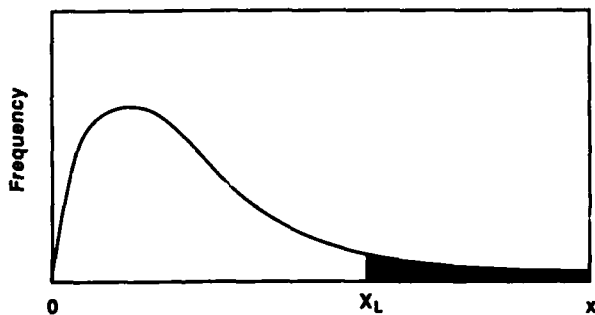


Figure 11 - Distribution of inclusion lengths. The cross-hatched region represents the fraction of inclusions having lengths equal to or greater than  $x_L$ .

For the specimens having varying sulfur contents, the number of measured inclusions greater than  $20\mu\text{m}$  was plotted for each run as a function of the steel sulfur content. A linear relationship between the number of large inclusions and sulfur content was observed, Figure 12. Using the cumulative values for  $n$ ,  $\Sigma 1$  and  $\Sigma 1^2$ , the predicted number of inclusions per unit area was found to be in agreement with the measured values, Figure 12 and Table 4. In this example, inclusions greater than  $20\mu\text{m}$  in length were selected so that a comparison between the actual measured values and the predicted values could be made. Although very large inclusions (i.e., greater than  $100\mu\text{m}$  long) were not observed, this technique could be employed to predict the probability of the presence of these inclusions in a particular system. This analysis could be useful in fracture mechanics calculations where critical flaw sizes are considered, or in assessing the effect of thermomechanical operations on inclusion distributions.

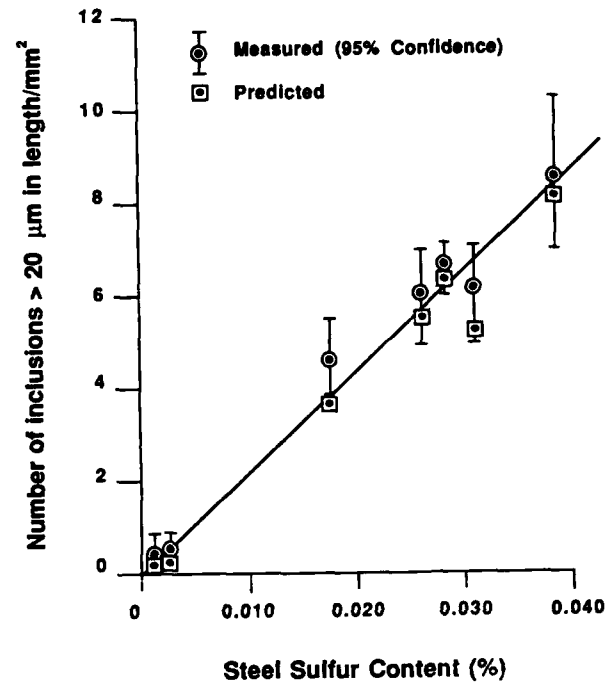


Figure 12 - Relationship between the number of inclusions per unit area greater than  $20\mu\text{m}$  in length and steel sulfur content.

**SEM-EDS ANALYSIS** - For homogeneous materials, numerous methods have been devised to accurately determine the chemical composition of various species by X-ray analysis.[6] When similar compositions are often encountered, a group of specimens having known compositions can be used to form a calibration curve. In this way, the X-ray peak of the unknown substance is compared to that of the calibration curve to measure the amount of a particular element present. For situations in which known standards are not available, reasonable analysis can be performed using atomic weight, absorption and fluorescence (ZAF) factors which have been developed for most species. All of these approaches use classical theories to determine from where X-rays originate within a material and how strong particular X-rays emitted from a specimen are with respect to similar X-rays emitted from other species within the same specimen. When an electron beam strikes a homogeneous material, a volume similar to that illustrated in Figure 13a emits X-rays.

The next level of complication arises when the composition of a simple two or three phase inclusion has to be determined. For the case of calcium treated steels having a relatively high manganese level and a low sulfur content, most of the sulfides in these steels will chemically

have the composition given by  $(\text{Ca}_x \text{Mn}_{1-x}) \text{S}$ . To properly excite X-rays from all phases present, the operating potential of the SEM in KV needs to be approximately two times the excitation level of the peak to be identified. Hence, for a Mn  $K\alpha$  peak whose characteristic energy is 5.9 KeV, a minimum potential of approximately 11KV is required. This gives rise to another problem: the higher the operating voltage of the electron microscope, the greater the volume of the material excited. In the case of small particle analysis, a certain number of X-rays from the matrix below the inclusion are in the spectrum, Figure 13b. Thus, the acquired spectrum is composed of X-rays from the inclusion as well as the matrix. The excess X-rays can be a large percentage of the total spectrum and if these X-rays are improperly evaluated, large errors in analysis can result. Similarly, when the electron beam is focused on the oxide particle in a complex inclusion, X-rays from the matrix as well as the sulfide appear in the acquired spectrum, Figure 13c.

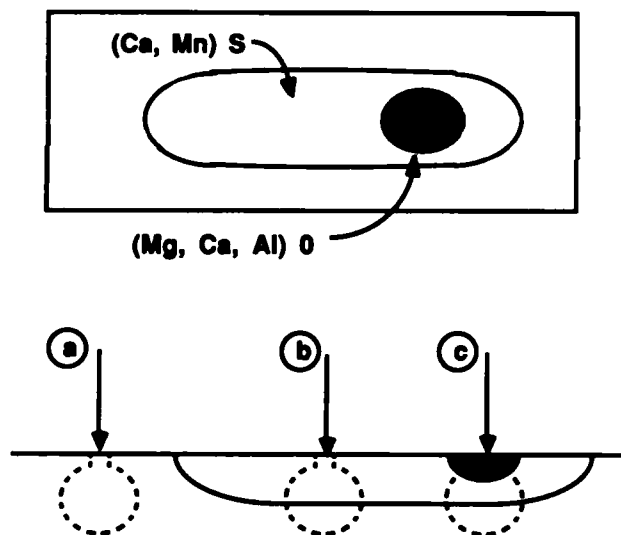


Figure 13 - Schematic illustration of an electron beam interacting with a material. The volume of material from which x-rays are emitted is indicated.

In these particular low oxygen, aluminum killed steels, the primary oxides are  $\text{Al}_2\text{O}_3$ ,  $\text{CaO}$  and  $\text{MgO}$ . The designations A, C and M, respectively, are used to represent these phases. The M present is either M·A or M. The remaining oxides are some form of calcium aluminates. Occasionally, elements such as Ti,

Zr, Si, Na and K appear in the oxides. These elements are present as the respective oxides and are not considered to be affected by the calcium treatment. In order to properly determine the chemical composition of the oxide phases, the following methodology has been devised.

The electron beam is focused in the sulfide portion of the inclusion, Figure 13b, and an X-ray spectrum is acquired. The percentages of calcium and sulfur in the sulfide are quantitatively determined.

The ratio  $r$  is defined to be the atomic percent of calcium in the sulfide divided by the atomic percent of sulfur in the sulfide:

$$r = \frac{\text{Ca}_{(s)}}{\text{S}_{(s)}} \quad (13)$$

The electron beam is then focused on the oxide particle within the sulfide. The amount of calcium, magnesium, aluminum, sulfur and manganese are quantitatively determined. In aluminum killed steels such as these, the oxide phases generally do not contain Mn or S. Hence, the Mn and S in the spectrum are from penetration of the electron beam into the sulfide below the oxide particle. Furthermore, some of the calcium in the spectrum is from the sulfide. Let  $\text{S}_{(o)}$ ,  $\text{Ca}_{(o)}$ ,  $\text{Al}_{(o)}$ , and  $\text{Mg}_{(o)}$  represent the amounts of these species measured in the oxide X-ray spectrum. Since some of the calcium and all of the sulfur are from the sulfide, to a first order approximation, the true calcium content of the oxide is:

$$\text{Ca}'_{(o)} = \text{Ca}_{(o)} - r * \text{S}_{(o)} \quad (14)$$

Thus, the calcium, magnesium, and aluminum contents of the oxide are  $\text{Ca}'_{(o)}$ ,  $\text{Mg}_{(o)}$ , and  $\text{Al}_{(o)}$ . In the case when  $\text{Ca}'_{(o)}$  is negative, there is no calcium in the oxide phase and the oxide is composed of  $\text{Al}_2\text{O}_3$  and  $\text{MgO}$ .

The magnesium in the inclusion is present as  $\text{MgO} \cdot \text{Al}_2\text{O}_3$  or MA. The calcium and aluminum can be present as several compounds. The exact species present and the corresponding atomic percentages are calculated using the following formulas.

The oxides present have the form  $\text{MgO}$ ,  $\text{Al}_2\text{O}_3$ , and  $\text{CaO}$  (M, A, and C). Since the oxygen atoms are not contained in a standard EDS analysis, the sum of the atomic weight percents (ATW) can be represented as:

$$\Sigma \text{ATW} = \% \text{Mg} + \% \text{Al} + \% \text{Ca}' \quad (15)$$

If  $2 * \% \text{Mg} > \% \text{Al}$ , then all the aluminum is combined as M·A and the excess Mg is present as M. Otherwise,

$$\% \text{Al}' = \% \text{Al} - 2 * \% \text{Mg} \quad (16)$$

is the amount of aluminum remaining to form calcium-aluminates, and Ca' is the amount of calcium available to form calcium-aluminates.

$$\text{Letting } \varnothing = \text{Ca}' / (\text{Ca}' + \text{Al}'), \quad (17)$$

The particular species present can be found by using Table 5 and the lever rule. Several examples of these calculations are contained in Appendix A.

The primary strength of this technique is that each inclusion serves as its own internal standard. The correction for the amount of calcium in the oxide phase is based on the (Ca/S) ratio of the specific inclusion being considered. The correction is not based on a global variable such as the (Ca/S) ratio of the steel or some assumption related to the distribution of all elements in the oxide X-ray spectrum.

To quantify the chemical composition of the inclusions in a steel sample, it is first necessary to decide what inclusions are representative or typical of that particular specimen. Based on the QTM analysis, a typical inclusion for each heat was defined to be any inclusion whose area was within 10 percent of the average inclusion area for that particular heat. In this manner, bias in selecting inclusions for X-ray analysis is minimized. To quantify the effect calcium and sulfur levels have on inclusion chemistry, ten typical inclusions from each heat were selected for EDS analysis. While this is a very small number of inclusions relative to the number in a heat of steel, the approach does illustrate the trends that occur as bulk chemistry varies. For the steels with varying sulfur content, as the sulfur level increases, the inclusion (Ca/Mn) and (Ca/S) weight percent ratios both exponentially decrease, Figures 14 and 15 respectively. Conversely, for a fixed sulfur level, as the bulk calcium content increases, the (Ca/Mn) and (Ca/S) ratios appear to exponentially increase, Figures 16 and 17 respectively.

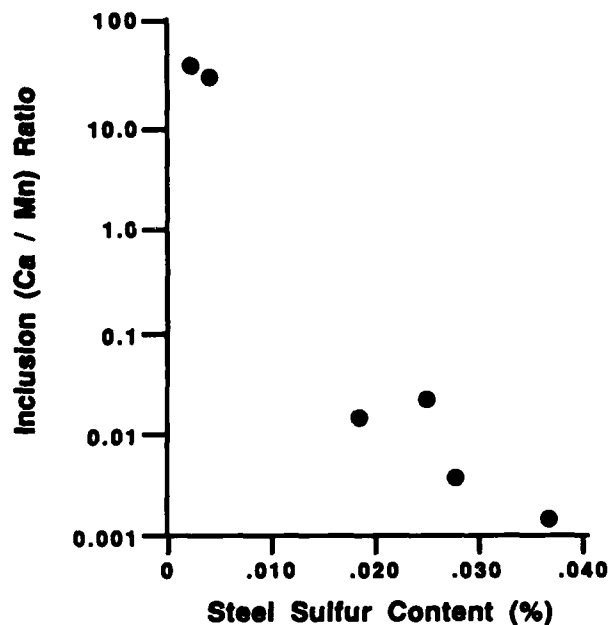


Figure 14 - Relationship between average inclusion (Ca/Mn) ratio and steel sulfur content.

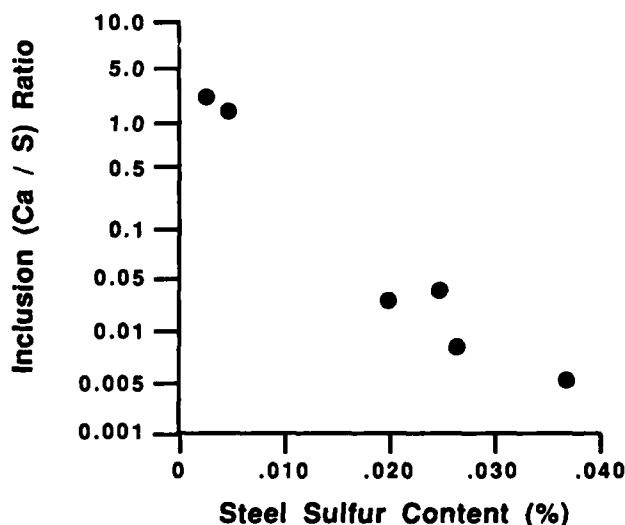


Figure 15 - Relationship between average inclusion (Ca/S) ratio and steel sulfur content.



These findings quantify effects that are well known for calcium treated steels. For low sulfur materials, calcium treating yields calcium-aluminates which are surrounded by a (Ca, Mn) S envelope. The lower the sulfur, the higher the Ca content of the envelope and the smaller the average inclusion area. For the higher sulfur alloys, as calcium levels increase, the amount of calcium in the sulfide phase increases. The increase in calcium in the sulfide phase tends to yield more globular type inclusions rather than stringers as seen in non-calcium treated steels. For both systems, the log-normal analysis can be used to predict the probability of the presence of large inclusions which can be very difficult to find metallographically.

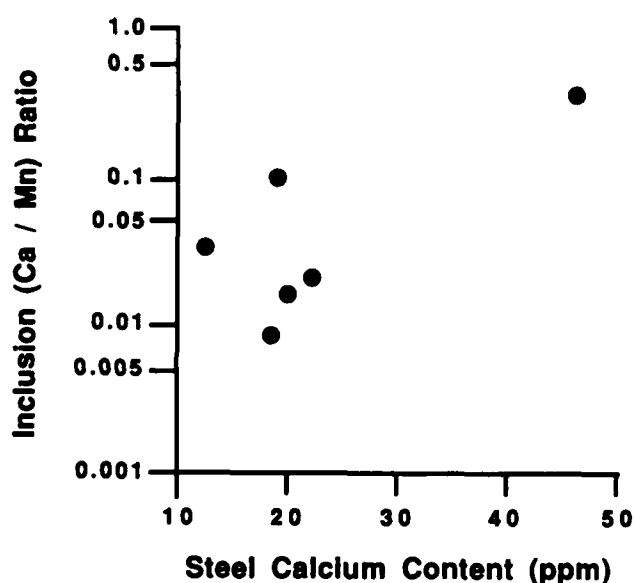


Figure 16 - Relationship between average inclusion (Ca/Mn) ratio and steel calcium content.

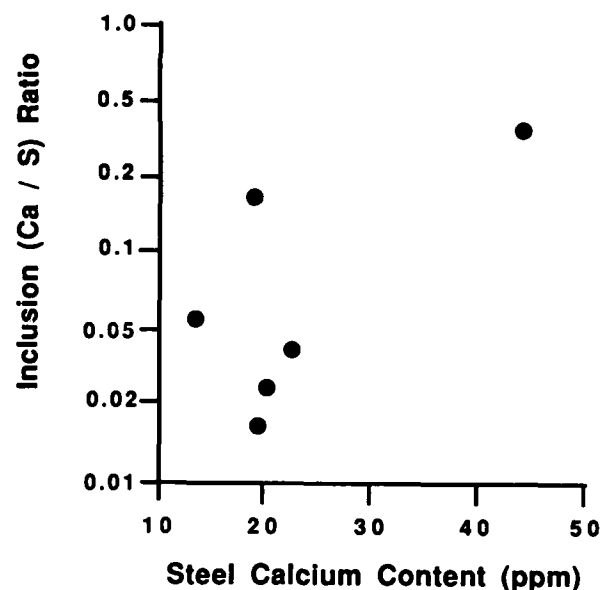


Figure 17 - Relationship between average inclusion (Ca/S) ratio and steel calcium content.

#### CONCLUSIONS

1. The relationships between the number of inclusions per unit area, mean length, area, and roundness for varying sulfur and calcium contents in 4140 steel were characterized. As sulfur content increased,  $n_A$ ,  $\bar{l}$ , and  $\bar{A}$  increased. An initial increase in  $\bar{l}$  occurred up to approximately 0.018 percent S after which  $\bar{l}$  was constant. For fixed sulfur content, as the amount of calcium increased,  $\bar{l}$ ,  $\bar{A}$ , and  $\bar{r}$  decreased.
2. Based on the log-normal distribution, a methodology to predict the number of large inclusions per unit area was presented. For inclusions greater than 20  $\mu\text{m}$  in length, excellent agreement between the number of inclusions measured and the predicted number of inclusions was obtained.
3. A SEM-EDS technique which permits calcium X-rays originating from the sulfide phase to be subtracted from those originating from encapsulated oxides was presented. This technique was used to study how the (Ca/S) and (Ca/Mn) ratios were related to bulk S and Ca content.

## Acknowledgement

The authors would like to thank The Timken Company for permission to publish this paper. Particular thanks are extended to Remy Schoone and Diane Pierce for metallographic assistance, Chuck Mozden for SEM analysis, Julie Fritsche and Beth Mills for preparing the manuscript, and Mike Leap for proofreading.

## References

1. B. Edelson and W. Baldwin, "The Effect of Second Phases on the Mechanical Properties of Alloys," *Trans. ASM*, 55, 1962, p. 238.
2. V. A. Tipnis, "Calcium Treatment For Improved Machinability," *Sulfide Inclusions in Steel*, ASM, 1975, p. 480.
3. A. G. Franklin, "Comparison Between a Quantitative Microscope and Chemical Methods for Assessment of Non-Metallic Inclusions," *JISI*, 1969, p. 181.
4. W. A. Spitzig, J. F. Kelly, and O. Richmond, "Quantitative Characterization of Second-Phase Populations," *Metallography*, 18, 3, 1985, p. 235.
5. Abramowitz and Stegun, *Handbook of Mathematical Functions*, NBS, 1968.
6. K. F. J. Heinrich, *Electron Beam X-Ray Microanalysis*, Van Nostrand Reinhold Co., NYC, 1981.

Table 1

### Steel Chemical Analysis and Quantitative Inclusion Measurements

Heat	Chemical Analysis			Inclusion Analysis			
	%S	Ca (ppm)	O (ppm)	$n_A$	$\bar{I}$ ( $\mu m$ )	$\bar{A}$ ( $\mu m^2$ )	$\bar{r}$
A	0.002	38	14	44.7	4.15	13.47	1.20
B	0.003	29	12	56.2	4.62	14.79	1.21
C	0.018	35	14	89.0	6.78	19.79	1.47
D	0.025	28	8	62.7	8.12	26.82	1.52
*E	0.027	30	9	84.7	7.99	25.91	1.54
*F	0.030	47	19	82.4	7.60	25.53	1.44
G	0.036	29	24	98.0	8.18	29.02	1.47
H	0.029	14	7	68.0	8.89	31.80	1.57
I	0.029	20	9	92.0	8.41	25.11	1.59
J	0.029	21	8	85.5	8.01	23.59	1.56
K	0.029	22	12	69.5	9.19	30.79	1.61
L	0.030	23	7	93.3	7.93	25.13	1.55

\* These heats were included in the second group with varying calcium content.

Table 2

### Typical Feature Data Acquired by QTM Analysis, Heat C, 0.018% S

Parameter	Number	Sigma X	Sigma X <sup>2</sup>
Length	1101	7226.1	110664.3
Area	1101	23525.2	2051283.0
Roundness	1101	1503.3	2543.3

Table 3

Inclusion Length Distribution Data,  
Heat C, 0.018% S

Length ( $\mu\text{m}$ )	Frequency	Cumulative Sum	Cumulative Percent
0-4	5,215	5,215	43.59
8	4,048	9,263	77.43
12	1,190	10,453	87.38
16	584	11,037	92.26
20	297	11,334	94.74
24	223	11,557	96.61
28	154	11,711	97.89
32	69	11,780	98.47
36	62	11,842	98.99
40	32	11,874	99.26
44	34	11,908	99.54
48	24	11,932	99.74
52	8	11,940	99.81
56	2	11,942	99.82
60	8	11,950	99.89
>60	13	11,963	--

$n = 11,963$        $\Sigma l = 80,256$        $\Sigma l^2 = 1,123,760$   
 $\text{mean} = 6.71$        $v = 7.00$        $\alpha = 1.5355$        $\beta = 0.8578$   
 $\chi_{50\%} = 4.64$        $\chi_{99.9\%} = 65.77$

Table 4

Number of Inclusions/ $\text{mm}^2 > 20\mu\text{m}$  in Length

% Sulfur	Measured		Predicted	
	Mean	95% CL	Mean	95% CL
0.002	0.503	0.530	0.331	0.371
0.003	0.567	0.400	0.440	0.473
0.018	4.733	0.661	3.927	0.616
0.025	6.040	0.910	5.642	1.479
0.027	6.563	0.505	6.281	0.535
0.030	5.918	0.997	5.057	1.032
0.036	8.318	1.704	7.803	1.700

Table 5

Phases in the  $\text{CaO-Al}_2\text{O}_3$  System

	A	C·6A	C·2A	C·A	12C·7A	3C·A	C
Ca							
Ca + Al	0.0	0.077	0.200	0.333	0.462	0.600	1.00

where Ca and Al represent atomic percents and A and C are  $\text{Al}_2\text{O}_3$  and  $\text{CaO}$ , respectively.

## Appendix A

### Sample X-Ray Analysis and Calculations

#### I. Inclusion 1

Element	Sulfide (at.%)	Oxide (at.%)
Mg		0.30%
Al		26.42%
S	48.04%	36.44%
Ca	1.24%	1.14%
Mn	50.72%	35.70%

Using the sulfide chemical analysis,

$$r = \frac{Ca(s)}{S(s)} = \frac{1.24}{48.04} = 0.026$$

In the oxide phase

$$\begin{aligned} Ca'_{(o)} &= Ca_{(o)} - r * S_{(o)} \\ &= 1.14 - 0.026 (36.44) \\ &= 0.20 \end{aligned}$$

Since  $2 * \%Mg < \%Al$ , all the Mg is present as M·A.

$$\begin{aligned} Al'_{(o)} &= Al_{(o)} - 2 * Mg_{(o)} \\ &= 26.42 - 2 * (0.30) \\ Al' &= 25.82 \end{aligned}$$

$$\phi = \frac{Ca'}{Ca' + Al'} = \frac{0.20}{0.20 + 25.82} = 0.008$$

Referring to Table 5 indicates that this ratio is between that for A and C·6A. Hence, the amount of C·6A in the inclusion is

$$\% C \cdot 6A = \frac{0.008 - 0}{0.077 - 0} * 100 = 10.4\%$$

and

$$\% A = \frac{0.077 - 0.008}{0.077 - 0} * 100 = 89.6\%$$

#### II. Inclusion 2

Element	Sulfide (at.%)	Oxide (at.%)
Mg		1.93%
Al		67.63%
S	48.11%	16.85%
Ca	6.14%	1.70%
Mn	45.75%	11.90%

#### Sulfide

$$r = Ca/S = 6.14/48.11 = 0.13$$

#### Oxide

$$Ca' = Ca_{(o)} - r * S_{(o)} = -0.45$$

Hence, there is no calcium in the oxide phase. Since  $2 Mg < Al$ , the oxide is composed of A and M·A.

#### III. Inclusion 3

Element	Sulfide (at.%)	Oxide (at.%)
Mg		7.39%
Al		33.41%
S	48.24%	21.33%
Ca	6.38%	15.50%
Mn	45.38%	22.37%

#### Sulfide

$$r = Ca/S = 0.13$$

#### Oxide

$$Ca' = Ca_{(o)} - r * S_{(o)} = 12.68$$

Since  $2 * Mg < Al$ , all the Mg is present as M·A.

$$Al' = Al_{(o)} - 2 * Mg = 18.64$$

$$\phi = \frac{Ca'}{Ca' + Al'} = 0.40$$

This ratio is between that for C·A and 12C·7A; hence

$$\% C \cdot A = \frac{0.40 - 0.333}{0.462 - 0.333} * 100 = 51.9$$

$$\% 12C \cdot 7A = 48.1\%$$

# CHARACTERIZATION OF INCLUSIONS IN A LABORATORY HEAT OF AISI 303 STAINLESS STEEL

**George F. Vander Voort**  
Carpenter Technology Corporation  
Reading, Pennsylvania 19612-4662 USA

## ABSTRACT

A laboratory size ingot of AISI 303 free-machining stainless steel was sampled in the as-cast condition and after forging to 54 sq. mm, 47.5 sq. mm, and 35 x 25mm section sizes (72, 78 and 91% hot reduction, respectively). As-cast and as-forged (54 sq. mm and 47.5sq. mm sections) specimens were subjected to homogenization treatments to spheroidize the sulfides.

Automatic image analysis, using the ASTM E1245 procedure, was employed to characterize the oxides and sulfides in the as-cast, as-forged, and in the homogenized specimens. Longitudinally oriented specimens were measured to obtain the area fraction, number per unit area, number of intercepts per unit length, average height or length, average area, and mean free path (mean edge-to-edge spacing) for both oxides and sulfides. Feature-specific measurements of the sulfides were performed to determine their shape factor as a function of deformation and homogenization treatment.

THIS PAPER DEMONSTRATES the use of stereological measurement procedures to characterize inclusions in a resulfurized laboratory ingot of AISI 303 stainless steel in the as-cast condition and after hot forging to three smaller sizes. Longitudinally oriented specimens were measured by image analysis to determine how hot reduction affects the measurement parameters for deformable (sulfides) and nondeformable (oxide) inclusions. As-cast and as-forged specimens were also homogenized and measured to determine sulfide spheroidization tendencies as a function of the initial shape of the sulfides. Field measurements were performed according to the new ASTM E1245(1,2) method while feature-specific measurements were

performed to assess sulfide shape.

**INCLUSION MEASUREMENT** - Measurement of inclusions is a difficult analytical task due to two basic sources of error: the inherent difficulties associated with sampling; and, the inherent errors of the measurement method. The polished cross section areas examined are very small relative to the bulk material. While this problem is typical of all qualitative or quantitative measurements, inclusions are relatively small, their volume fractions are low, they are not randomly distributed, and they deform at different rates than the matrix during working. These factors make assessment of inclusions one of the most difficult tasks for the metallographer.

The oldest procedures for rating inclusions are based on standard charts, e.g., ASTM E45. While these methods are generally adequate for quality control purposes, they do suffer from a number of deficiencies(3-9). Chart ratings depend heavily on the quality of the chart as to the relevance of the pictures compared to the inclusions in the steel and on the grading of the chart picture series. Reproducibility of chart ratings is often less than adequate. Chart ratings are difficult to quantify and use in data bases or in structure-property correlations. Because charts contain a limited number of pictures depicting severity differences, discrimination between different levels of inclusion contents is not as precise as desired. Chart ratings are generally qualitative based on worst-field conditions which can be misleading when comparing different material lots. True quantitative chart ratings are very time consuming and the data obtained is difficult to handle.

Because of these problems, other microscopical methods for assessing inclusions have been proposed. For example, indexes to summarize quantitative chart

ratings, such as the SAM index(10,11), have been developed. Another approach has been to develop chart ratings using automatic image analyzers. This has been done for the JK-charts of ASTM E45(12,13) and for the German SEP 1570-71 inclusion chart(14-17). This approach improves the reproducibility and eliminates much of the subjective nature of inclusion chart ratings. A different approach has been taken by Johansson(18,19) with a new chart classification scheme and a small computer to tally field ratings and compute test results.

Since the introduction of the first commercially available TV-based image analyzer in 1963, many researchers have utilized these devices to assess inclusions(20-31). As these systems have progressed from analog to digital devices, from hardware-driven to software-controlled devices, with improved camera resolution, they have become more reliable and more capable. Inclusions are ideal subjects for image analysis because of the good contrast difference between the inclusions and the as-polished matrix. Also, because of stage automation and the speed of analysis, a great many fields can be analyzed in a reasonable time. Because of the small quantity of inclusions present in steels, it is necessary to measure the inclusions in many fields per sample, and many samples per lot. This is a clear advantage of image analyzers compared to manual quantitative methods or manual qualitative chart methods.

While image analysis has many advantages compared to manual methods, it is still subject to many of the same problems associated with manual techniques and does have some unique problems as well. Proper sampling of the test lot is just as important for image analysis as for manual methods. Because image analysis is less tedious than manual methods, adequate sampling is easier to achieve. Also, due to the inclusion distribution variability it is better to assess a greater number of specimens than to put a great deal of effort in examining a small number of specimens. Allmand and Coleman(32), for example, showed that about 300 to 400 field measurements were required to obtain a moderate degree of accuracy but concluded that it was better to measure 100 fields on each of four specimens than to measure all 400 on one specimen. This writer's experience definitely bears out this conclusion.

Traditionally, inclusion measurements, whether manual or automated, are made on a longitudinal plane-of-polish so that the deformation characteristics can be assessed. For the majority of work, the sample is taken from a mid-thickness position, particularly for billet specimens. However, it is well known(32,38) that the inclusions vary in amount, size, shape and spacing

across steel products. Thus, for billet specimens, it may be advisable to sample the material at surface, mid-thickness, and center locations at the top, middle, and bottom.

Thanks to the improvements in automatic polishing devices, it is relatively easy to prepare the needed number of specimens with the desired quality level. Also, most of these devices can handle unmounted bulk specimens which further speeds up the process. The quality of the polish does have a pronounced influence on measurement results(23) and is more critical for image analysis work than for manual measurements. Polishing procedures for image analysis inclusion measurements have been thoroughly documented(34,35).

All systems that use the light microscope are affected by the limited resolution of the light microscope and there is a noticeable magnification influence on test results(23,36,37). As the magnification increases, and smaller particles can be resolved and detected, the volume fraction increases. At low magnifications, closely spaced particles will appear to be touching and will be counted as one while small, undetected particles will not be counted. Hence, as the magnification increases, the count will increase. If inclusion areas or lengths are measured, the closely spaced particles will be sized as one much larger particle while the small particles will not be detected and sized. Hence, average areas and lengths will decrease with increasing magnification. For field measurements, those particles that extend outside the measurement field will be undersized. This problem becomes more acute at very high magnifications and further contributes to smaller average dimensions.

As the magnification is increased, the field size decreases and the field-to-field measurement variability increases. Thus, the statistical quality of the data is adversely influenced by increasing the magnification, which can be overcome only by measuring a proportionally greater number of fields. Thus, there is an optimum magnification for inclusion measurements which is a compromise between resolution and measurement variability. For any given magnification, the relative accuracy of the measurements improves as more fields, and greater total area, are measured (9,32,37,39), either manually or automatically.

Adjusting the densitometer's threshold settings(23,39,40) to detect sulfides and oxides, either separately or collectively, is an important factor influence measurement results and reproducibility. Generally, the operator alternates between the live image and the detected image (the "flicker" method) while adjusting the threshold

settings. It is not usually possible, particularly at lower magnifications, to detect all of the small inclusions without overdetecting the largest ones. It is better to miss a few of the very smallest inclusions than to mis-size the larger ones.

Focusing(32,40) of the microscope prior to each measurement can also influence the accuracy of test results. Automatic focusing devices are becoming more reliable, even for as-polished specimens with a very low inclusion content. Spacing of the fields across the specimen surface should be based on the number of fields to be measured and the polished surface area. Fields should not be overlapped. If the polished surface is relatively large compared to the product of the number of fields to be measured and the individual field area, space the fields in a systematic pattern across the surface.

**INCLUSION DEFORMATION** - The deformation of sulfide inclusions in steels during hot- and cold-working has been studied extensively in ferritic alloys. The plasticity of the sulfides relative to the steel increases with decreasing hot working temperature(41) until the austenite-to-ferrite transformation temperature is reached(42). Below this temperature, the relative plasticity of MnS increases and then gradually decreases as the working temperature decreases to ambient(43). Globular type I MnS, as encountered in free-machining steels, are less deformable than the angular type III MnS present in aluminum-killed steels(42). It is also known that small sulfides deform less than larger ones(44) and may remain relatively undeformed until very high levels of reduction.

In these studies, and others not cited, there is no mention of fracturing of sulfides during working although Van Vlack *et al.* demonstrated sulfide fracturing using single crystal MnS embedded in powder compacts(45-47). Although some authors do not address the issue of sulfide fracturing, others have examined this possibility and found none(48). However, Radtke and Schreiber(49) measured sulfides after the rolling of a non-homogenized billet of a free-machining steel and observed that the proportion of long sulfides decreased, apparently due to fragmentation.

Deformability of oxides varies with the composition and relative hardness of the oxide. Silicates deform readily at high temperatures, but below some temperature the deformability decreases rapidly towards zero. Aluminates do not deform at any temperature. At low temperatures, these brittle oxides can fragment.

**SULFIDE SPHEROIDIZATION** - Numerous studies(48-54) have shown that sulfide size, shape, number, and spacing can be altered by

high temperature homogenization treatments, although some authors(41) reported no observed influence. Gnanamuthu *et al.*(50) reported that the volume fraction remained approximately constant, the number per unit volume decreased, the overall size increased and the shape changed with homogenization time. Wilson *et al.*(51), however, showed that the number of sulfides per unit volume first increased, reached a maximum, and then decreased with homogenization time. They also stated that the overall size decreased initially, reached a minimum, and then increased with homogenization time. The peak of the number per unit volume vs. time (at 1315C, 2400F)(51,53) occurred at a 20h soak time. The specimens used had previously been hot worked to reductions of 70 and 85%.

**INFLUENCE OF DEFORMATION** - Variation of stereological parameters, such as  $A_A$ ,  $N_A$ ,  $D$ ,  $A$ ,  $\lambda$ , and  $N_L$ , for deformable or non-deformable particles as a function of the degree of hot- or cold-working has not been carefully documented in the literature. Fisher and Gurland(55) have examined the variation of  $A_A$ ,  $N_A$  and  $\lambda$  for the case of nondeforming equiaxed particles and for the influence of rotation and preferred orientation of non-equiaxed particles deformed uniaxially. They concluded that the area fraction,  $A_A$ , the number density,  $N_A$ , and the mean free path,  $\lambda$ , do not change for the case of nondeformable equiaxed particles subjected to plastic deformation. However, for non-equiaxed particles,  $N_A$  and  $\lambda$  may be influenced by rotation of the particles into a preferred orientation during deformation. In the case of inclusions, where deformation rotates the particles so that the long axis of the inclusions are parallel to the hot-working axis, the area fractions will not be equal when evaluating  $A_A$  on longitudinal vs. transverse planes(56). Moreover, if inclusion fracturing occurs, the number density and average size will change. Furthermore, closely spaced inclusions that may be detected as one particle when deformation is limited, may be spaced apart with further deformation, thus changing the count and size information.

#### PROCEDURE

For this study, a 45.5 kg (100 lb.) air-induction heat of AISI 303 was melted. Table 1 gives the composition of the laboratory ingot. The ingot measured about 114mm sq. (4-1/2 inch sq.) at the top, 89mm sq. (3-1/2 inch sq.) at the bottom, with a 559mm (22 inch) body length. A sample was cut from the bottom end of the ingot prior to heating for forging. The balance of the ingot was heated to 1260°C (2300°F), held for one hour and press forged to size. The

Table 1 - Composition of Laboratory AISI 303 Ingot  
(Weight Percent)

<u>C</u>	<u>Mn</u>	<u>P</u>	<u>S</u>	<u>Si</u>	<u>Cr</u>	<u>Ni</u>	<u>Al</u>	<u>N</u>	<u>O*</u>
0.074	1.68	0.019	0.33	0.65	17.44	9.42	<0.005	0.053	84

\*\* ppm

ingot was forged to produce sections with three different square cross section dimensions: 54mm sq. (2-1/8 inch), 47.5mm sq. (1-7/8 inch sq.), and 35 x 25mm (1-3/8 x 1 inch). The latter section was supposed to be 25mm sq. (1 inch sq.) but the bar temperature 788°C (1450°F), was too low and cracking occurred. Reheating was not desired in this experiment because of its potential influence on the size and shape of the sulfides. These sizes correspond to 72, 78 and 91% hot reduction (3.5:1, 4.6:1, and 11.6:1), respectively.

El245 ANALYSIS - The new ASTM El245(1) method utilizes field measurements on a longitudinally oriented specimen (scan lines perpendicular to the deformation axis) to characterize the oxides and sulfides (separated by gray-level differences) by:

$A_A$  - area fraction in % (1)

$N_A$  - number per sq. mm test area (2)

$N_L$  - number of interceptions per mm of scan line length (3)

$\bar{L}$  - Average length (sum of projected height/number of inclusions per field) (4)

$\bar{A}$  - Average area ( $A_A/N_A$ ) (5)

$\bar{\lambda}$  - Mean free path (spacing) perpendicular to the deformation axis ( $(1-A_A)/N_L$  where  $A_A$  is a fraction, not a %) (6)

While stereological measurement methods are utilized, only the longitudinal plane is assessed; hence, the three-dimensional inclusion characteristics are not assessed. These measurements are made on at least 100 fields per specimen and the average and standard deviation of each measurement, based on the number of fields measured, are calculated for each specimen. Although the distribution of these measurements for an individual specimen measured with  $n$  fields is not Gaussian, the usual formulae for the arithmetic average and standard deviation are used. After a number of specimens from the lot are measured, the average measurements for all of the specimens are averaged and the standard deviation of the

sample averages for each parameter (1 to 6 above) are calculated. The distribution of the average values for a large number of specimens from a lot will generally exhibit a Gaussian distribution.

TEST PROCEDURE - Each of the sections (as-cast, 54 sq. mm, 47.5 sq. mm) were cut longitudinally at each mid-thickness location and through the center from two orthogonal directions producing sixteen specimens per size. The mid-thickness longitudinal planes, from surface-to-surface, were polished using automatic polishing procedures (Struers Abramatic system). For the 35 x 25 mm section, four adjacent specimens were cut through the center of the 35 mm face, as whole specimens (surface-to-surface). After polishing, each specimen was measured, according to El245, using a 50X objective and 100 or 200 fields. The specimens were repolished, at least once, and remeasured in the same way, to provide additional information from a parallel plane.

Sections of the as-cast ingot, and from the 54 and 47.5 sq. mm forged sections, were cut and heated to various temperatures: 1260°C (2300°F) and 1302°C (2375°F) for 8 and 24h. Because the length of the 47.5 sq. mm section was longer than the other sections, additional pieces were cut and these were heated to additional temperatures: 1149°C (2100°F) and 1204°C (2200°F) for 8 and 24h. Because the 35 x 25 mm section cracked during forging, no spheroidization treatments could be performed on this section size. The homogenized specimens were sectioned in the same manner as the as-cast and as-forged specimens and measured in the same way.

## RESULTS AND DISCUSSION

SULFIDES - Table 2 lists the measurement results for the as-cast and as-forged sections. Note that the area fraction and the mean free path decrease and  $N_L$  increases going from the as-cast condition to the 35 x 25 mm section size, i.e., with increasing hot reduction. However, the differences between the area fraction values for the 54 sq. mm and the 47.5 sq. mm sections and for the 47.5 sq. mm and 35 x 25 mm sections are not



Table 2 - Sulfide Measurements - As-Cast and As-Forged Specimens  
(Mean Values  $\pm$  95% Confidence Intervals)

	Red.	$\bar{A}_A$	$\bar{N}_A$	$\bar{L}$	$\bar{A}$	$\bar{N}_L$	$\bar{\lambda}$
Condition	(%)	(%)	(mm <sup>-2</sup> )	( $\mu$ m)	( $\mu$ m <sup>2</sup> )	(mm <sup>-2</sup> )	( $\mu$ m)
As-Cast	-	1.721 $\pm$ 0.048	1643 $\pm$ 140	2.44 $\pm$ 0.20	11.10 $\pm$ 1.08	5.90 $\pm$ 0.20	168 $\pm$ 6
54 sq. mm	72	1.637 $\pm$ 0.053	1407 $\pm$ 106	3.47 $\pm$ 0.22	11.91 $\pm$ 0.72	6.80 $\pm$ 0.22	146 $\pm$ 5
47.5 sq. mm	78	1.594 $\pm$ 0.048	1416 $\pm$ 149	4.88 $\pm$ 0.32	11.93 $\pm$ 1.19	8.54 $\pm$ 0.60	118 $\pm$ 8
35 x 25 mm	91	1.494 $\pm$ 0.134	2448 $\pm$ 567	3.70 $\pm$ 0.60	6.55 $\pm$ 1.70	11.12 $\pm$ 0.63	89 $\pm$ 5

Significance of Differences Between Means\* (Confidence Level)

Comparisons	$\bar{A}_A$	$\bar{N}_A$	$\bar{L}$	$\bar{A}$	$\bar{N}_L$	$\bar{\lambda}$
As Cast vs. 54 sq. mm	98%	99%	99.9%	NS	99.9%	99.9%
As Cast vs. 47.5 sq. mm	99.9%	99%	99.9%	NS	99.9%	99.9%
As Cast vs. 35 x 25 mm	99.9%	99%	99.9%	99.9%	99.9%	99.9%
54 sq. mm vs. 47.5 sq. mm	NS	NS	99.9%	NS	99.9%	99.9%
54 sq. mm vs. 35 x 25 mm	95%	99.9%	NS	99.9%	99.9%	99.9%
47.5 sq. mm vs. 35 x 25 mm	NS	99.9%	99.9%	99.9%	99.9%	99.9%

\* Student's t distribution, two-tailed test

NS - differences not significant (<95%)

Table 3 - Sulfide Measurements After Homogenization Treatments - As Cast Specimens

	$\bar{A}_A$	$\bar{N}_A$	$\bar{L}$	$\bar{A}$	$\bar{N}_L$	$\bar{\lambda}$
Heat Treatment	(%)	(mm <sup>-2</sup> )	( $\mu$ m)	( $\mu$ m <sup>2</sup> )	(mm <sup>-1</sup> )	( $\mu$ m)
None	1.721 $\pm$ 0.048	1643.0 $\pm$ 140.4	2.44 $\pm$ 0.20	11.10 $\pm$ 1.08	5.90 $\pm$ 0.20	167.9 $\pm$ 5.8
1260°C-8h	1.734 $\pm$ 0.047	1699.4 $\pm$ 151.2	2.12 $\pm$ 0.23	10.74 $\pm$ 1.18	5.88 $\pm$ 0.18	168.0 $\pm$ 4.9
1260°C-24h	1.733 $\pm$ 0.051	1669.9 $\pm$ 109.9	1.96 $\pm$ 0.12	10.54 $\pm$ 0.79	5.53 $\pm$ 0.16	178.1 $\pm$ 5.2
1302°C-8h	1.680 $\pm$ 0.032	1681.3 $\pm$ 94.5	2.00 $\pm$ 0.09	10.22 $\pm$ 0.56	5.46 $\pm$ 0.18	181.6 $\pm$ 6.1
1302°C-24h	1.782 $\pm$ 0.040	1629.4 $\pm$ 104.1	1.97 $\pm$ 0.05	11.06 $\pm$ 0.63	5.47 $\pm$ 0.24	180.7 $\pm$ 8.2

Significance of Differences Between Means\*  
(Confidence Level)

Comparisons	$\bar{A}_A$	$\bar{N}_A$	$\bar{L}$	$\bar{A}$	$\bar{N}_L$	$\bar{\lambda}$
As Cast vs. 1260°C-8h	NS	NS	95%	NS	NS	NS
As Cast vs. 1260°C-24h	NS	NS	99.9%	NS	99%	99%
As Cast vs. 1302°C-8h	NS	NS	99.9%	NS	99%	99%
As Cast vs. 1302°C-24h	95%	NS	99.9%	NS	98%	99%
1260°C-8h vs. 1260°C-24h	NS	NS	NS	NS	99%	99%
1302°C-8h vs. 1302°C-24h	99.9%	NS	NS	95%	NS	NS

\* Student's t distribution, two-tailed test

NS = differences not significant (<95%)

statistically significant. Note that the  $\bar{N}_A$  value for the as-cast section is statistically greater than the 54 sq. mm and 47.5 sq. mm section, but there is no difference between the  $\bar{N}_A$  values for the latter two section sizes. Note, however, that  $\bar{N}_A$  for the 35 x 25 mm section is much higher than any of the other sections. The  $\bar{A}$  values are nearly identical for the as-cast, the 54 sq. mm and 47.5 sq. mm sections but is much smaller for the 35 x 25 mm section. The  $\bar{L}$  values increase going from the as-cast state to the 47.5 sq. mm section; but, then  $\bar{L}$  decreases substantially. For the as-cast section, the sulfides are not perfectly spherical and are not oriented in the ingot axis direction; hence,  $\bar{L}$  underestimates the maximum dimension for the sulfides. Nevertheless, it is clear that a major change has occurred in the sulfides when the smallest section was forged, that is, the increase in  $\bar{N}_A$  and decrease in  $\bar{L}$  and  $\bar{A}$  suggest that a substantial portion of the sulfides fractured.

Tables 3-5 list the sulfide measurements after homogenization of the as-cast, 54 sq. mm and 47.5 sq. mm sections. All of the treatments produced a reduction of the average sulfide length, compared to the starting condition. Except for the 1260°C-8h treatment of the as-cast section, all treatments produced a reduction of the number of sulfides intercepted by the scan

lines and a consequent increase in the mean free path (mean edge-to-edge spacing between sulfides perpendicular to the hot working axis or ingot axis). As might be expected, the magnitude of these changes increased with the amount of hot reduction being smallest for the as-cast specimens and greatest for the 47.5 sq. mm specimens (78% hot reduction).

For the as-cast and the 54 sq. mm specimens, there appears to be an effect of temperature and time on the area fraction and average area. For the as-cast specimens, the 1302°C-24h treatment resulted in a significantly higher area fraction. For the 54 sq. mm section, the two 24h treatments (1260°C and 1302°C) produced a significantly greater area fraction and larger average area. Results for the  $\bar{A}_A$  and  $\bar{A}$  values of the 47.5 sq. mm specimens are more erratic and difficult to interpret. For the  $\bar{A}$  values, one treatment (1149°C-24h) resulted in a significantly lower average area; all other values are statistically similar. For the  $\bar{A}_A$  values, five of the treatments produced significantly higher values while one produced a significantly lower value. The 1302°C-24h treatment (highest temperature, longest time) produced a lower  $\bar{A}_A$  value, compared to the sequence shown, and the  $\bar{L}$  value also increased. The erratic behavior of this series of specimens may be due to the greater initial elongation of the sulfides in the 47.5 sq. mm section, and the types of changes in measurements

Table 4 - Sulfide Measurements After Homogenization Treatments - 54 mm<sup>2</sup> Specimens

Heat Treatment	$\bar{A}_A$ (%)	$\bar{N}_A$ (mm <sup>-2</sup> )	$\bar{L}$ (μm)	$\bar{A}$ (μm <sup>2</sup> )	$\bar{N}_L$ (mm <sup>-1</sup> )	$\bar{\lambda}$ (μm)
none	1.637±0.053	1407.3±105.5	3.47±0.22	11.91±0.72	6.80±0.22	145.5±4.5
1260°C-8h	1.687±0.034	1496.1±167.8	2.76±0.36	11.72±1.22	6.14±0.23	160.9±5.9
1260°C-24h	1.716±0.039	1335.9± 87.8	2.74±0.14	13.04±0.88	5.58±0.16	176.8±5.3
1302°C-8h	1.635±0.032	1362.9± 85.9	2.64±0.11	12.15±0.76	5.46±0.16	180.7±5.2
1302°C-24h	1.731±0.046	1217.3± 81.3	2.86±0.15	14.95±1.06	5.21±0.25	190.2±9.3

Significance of Differences Between Means\*  
(Confidence Level)

Comparisons	$\bar{A}_A$	$\bar{N}_A$	$\bar{L}$	$\bar{A}$	$\bar{N}_L$	$\bar{\lambda}$
As Forged vs. 1260°C-8h	NS	NS	99.9%	NS	99.9%	99.9%
As Forged vs. 1260°C-24h	99%	NS	99.9%	95%	99.9%	99.9%
As Forged vs. 1302°C-8h	NS	NS	99.9%	NS	99.9%	99.9%
As Forged vs. 1302°C-24h	99%	99%	99.9%	99.9%	99.9%	99.9%
1260°C-8h vs. 1260°C-24h	NS	NS	NS	NS	99.9%	99.9%
1302°C-8h vs. 1302°C-24h	99%	98%	98%	99.9%	NS	NS

\* Student's t distribution, two-tailed test  
NS = differences not significant (<95%)

Table 5 - Sulfide Measurements After Homogenization Treatments - 47.5 mm<sup>2</sup> Specimens

Heat Treatment	$\bar{A}_A$ (%)	$\bar{N}_A$ (mm <sup>-2</sup> )	$\bar{L}$ ( $\mu$ m)	$\bar{A}$ ( $\mu$ m <sup>2</sup> )	$\bar{N}_L$ (mm <sup>-1</sup> )	$\bar{\lambda}$ ( $\mu$ m)
none	1.594±0.048	1415.6±148.8	4.88±0.32	11.93±1.19	8.54±0.60	118.3±7.5
1149°C-8h	1.583±0.041	1440.4± 77.4	3.84±0.28	11.20±0.61	7.29±0.25	136.4±4.7
1149°C-24h	1.629±0.025	1564.4± 79.0	3.49±0.23	10.63±0.53	7.15±0.16	138.2±3.2
1204°C-8h	1.655±0.033	1517.1± 97.6	3.65±0.27	11.24±0.78	7.30±0.20	135.5±3.8
1204°C-24h	1.525±0.045	1342.4± 62.9	3.14±0.20	11.48±0.47	6.09±0.17	162.7±4.8
1260°C-8h	1.668±0.028	1480.3±109.8	3.05±0.25	11.35±0.78	6.73±0.33	146.6±7.3
1260°C-24h	1.703±0.053	1547.7± 85.8	2.86±0.21	11.15±0.74	6.34±0.15	155.4±3.7
1302°C-8h	1.706±0.035	1501.6± 74.5	2.89±0.20	11.41±0.75	6.45±0.18	152.6±4.2
1302°C-24h	1.613±0.052	1345.3± 87.6	3.19±0.23	12.20±0.87	5.80±0.18	170.5±5.5

Significance of Differences Between Means\*  
(Confidence Level)

Comparisons	$\bar{A}_A$	$\bar{N}_A$	$\bar{L}$	$\bar{A}$	$\bar{N}_L$	$\bar{\lambda}$
As Forged vs. 1149°C-8h	NS	NS	99.9%	NS	99.9%	99.9%
As Forged vs. 1149°C-24h	NS	NS	99.9%	95%	99.9%	99.9%
As Forged vs. 1204°C-8h	95%	NS	99.9%	NS	99.9%	99.9%
As Forged vs. 1204°C-24h	95%	NS	99.9%	NS	99.9%	99.9%
As Forged vs. 1260°C-8h	99%	NS	99.9%	NS	99.9%	99.9%
As Forged vs. 1260°C-24h	99%	NS	99.9%	NS	99.9%	99.9%
As Forged vs. 1302°C-8h	99.9%	NS	99.9%	NS	99.9%	99.9%
As Forged vs. 1302°C-24h	NS	NS	99.9%	NS	99.9%	99.9%

\* Student's t distribution, two-tailed test  
NS = differences not significant (<95%)

reported by Gnanamuthu *et al.*(50) and Wilson *et al.*(51). These authors(50,51) used either a single treatment temperature(51) or a range of temperatures(50) and a much wider range of times which may be required to understand the trends. Times longer than 24h were not considered in the work reported here as they are not practical commercially.

Sulfide shape factors were measured using feature specific measurements of the area, A, and perimeter, P, of individual sulfides and calculation of the classic shape factor:

$$SF = \frac{4\pi A}{P^2} \quad (7)$$

The shape factor for a circle is 1, less circular shapes, on the two-dimensional plane-of-polish, produce values less than 1, but no less than 0. About 1000 sulfides on each of four specimens (surface-to-surface) from each as-cast, as-forged, and homogenized condition, were measured to determine an average shape factor for each specimen per condition. The results for each specimen for each condition were averaged and these values are listed in Table 6. Due to the rather limited sampling, confidence

limits were not calculated and the significances of the differences between these mean values were not determined. However, the results in Table 6 do show clear trends but much more work would be needed to define the precision of these measurements. The results are in agreement with the previous data, Tables 3-5, on the homogenized specimens.

OXIDES - Measurements of the oxides in each of the specimens used to evaluate the sulfides (Tables 2-5) revealed that the homogenization treatments had no influence on the oxides, as expected. Hence, to obtain better statistical definition of the oxides, all of the data for the as-cast and as-cast and homogenized, and for the as-forged and as-forged and homogenized specimens, for each section size, were combined. Table 7 lists the average results for the as-cast, 54 sq. mm, 47.5 sq. mm and 35 x 24 mm sections, the latter had only eight measurements due to the cracking that occurred in this section during forging. Note that the oxide measurements for the as-cast specimens are significantly different than the forged sections with a much greater area fraction, number per unit

Table 6 - Shape Factors\* of Sulfides

Material		Homogenization Treatment							
		none	1149°C	8h				24h	
				1204°C	1260°C	1302°C	1149°C	1204°C	1260°C
As Cast	0.933	-	-	0.944	0.949	-	-	0.955	0.955
54 sq. mm	0.809	-	-	0.918	0.927	-	-	0.925	0.934
47.5 sq. mm	0.699	0.761	0.847	0.874	0.907	0.866	0.876	0.914	0.910
35 x 25 mm	0.668	-	-	-	-	-	-	-	-

$$* 4\pi A/P^2$$

area, size, and intercept count and a smaller spacing. This is mainly due to detection of cavities within some of the larger globular sulfides. Both have the same gray level and separation of the oxides from the cavities is not possible(2).

For the forged sections, we can see clear trends showing a decrease in the area fraction, number per unit area, size and intercept count and an increase in the spacing ( $\lambda$ ) as the degree of hot reduction increased. Most of these differences are significant, as shown in Table 7. These changes in the stereological measurements are due to examination on the longitudinal plane only and the rotation, alignment, and

spreading out of the oxides with increased hot reduction. Because  $N_A$  continually decreases, substantial fragmentation of the oxides has not occurred.

Skew and kurtosis (9) values for each measurement parameter were calculated using the oxide specimen averages for the as-cast, 54 sq. mm, and 47.5 sq. mm sections. For an ideal Gaussian (normal) distribution, the skew is zero and the kurtosis is three. Table 8 lists the skew and kurtosis values for each parameter and section size. Note that the skew values are all positive showing that the data all exhibit right-skewed distributions, that is, the mode is

Table 7 - Oxide Inclusion Measurements

Material	$\bar{A}_A$ (%)	$\bar{N}_A$ (mm <sup>-2</sup> )	$\bar{L}$ ( $\mu$ m)	$\bar{A}$ ( $\mu$ m <sup>2</sup> )	$\bar{N}_L$ (mm <sup>-1</sup> )	$\bar{\lambda}$ ( $\mu$ m)
As Cast	0.0350±0.004	111.9±10.1	0.69±0.04	3.14±0.26	0.188±0.018	7827±1285
54 sq. mm	0.0082±0.0008	66.4±5.4	0.34±0.02	1.31±0.13	0.0655±0.0042	16903±1152
47.5 sq. mm	0.0067±0.0006	60.3±6.0	0.29±0.01	1.27±0.13	0.0563±0.0043	22853±2364
35 x 25 mm	0.0040±0.0013	48.1±10.7	0.25±0.02	0.85±0.30	0.0409±0.007	25320±4089

Significance of Differences Between Means  
(Confidence Interval)

Comparisons	$\bar{A}_A$	$\bar{N}_A$	$\bar{L}$	$\bar{A}$	$\bar{N}_L$	$\bar{\lambda}$
As Cast vs. 54 sq. mm	99.9%	99.9%	99.9%	99.9%	99.9%	99.9%
54 sq. mm vs. 47.5 sq. mm	99%	NS	99.9%	NS	99.9%	99%
47.5 sq. mm vs. 35 x 25 mm	99.9%	95%	99.9%	99%	NS	99.9%
54 sq. mm vs. 35 x 25 mm	99.9%	99.9%	99.9%	99%	99.9%	99.9%

\* Student's t distribution, two-tailed test  
NS = differences not significant (<95%).

Note: The number of specimen averages were 113, 100, and 168 for the as-cast, 54 sq. mm and 47.5 sq. mm sections, respectively.

Table 8 - Skew and Kurtosis Values  
for Specimen Means - Oxide Data

	$\bar{A}_A$	$\bar{N}_A$	$\bar{L}$	$\bar{A}$	$\bar{N}_L$	$\bar{\lambda}$
Skew ( $\beta_1$ )						
As-Cast	0.748	1.635	0.0008	0.186	0.250	9.731
54 sq. mm	1.856	6.815	0.917	1.955	0.467	1.238
47.5 sq. mm	3.709	11.355	0.147	10.326	3.153	19.229
Kurtosis ( $\beta_2$ )						
As-Cast	4.081	6.963	2.285	2.559	3.093	15.324
54 sq. mm	5.295	13.577	3.888	5.008	3.690	4.188
47.5 sq. mm	9.111	20.823	3.692	18.324	8.647	34.326

Note: The number of specimen averages were: 113, 100 and 168 for the as-cast, 54 sq. mm, and 47.5 sq. mm sections, respectively.

less than the mean. If the data distribution exhibits a pronounced "tail" on the right side (higher values), the positive skew value is high, as in the case of the  $\bar{N}_A$  and mean free path data. As the kurtosis value increases above 3, it indicates that the distribution curve is more "peaked" than that of the ideal normal curve. Values above 5 indicate non-Gaussian data distributions.

Table 8 shows that, in general, the skew and kurtosis values increase with increasing hot reduction. Overall, the most normal distributions are exhibited by the average length data. The  $\bar{N}_A$  and mean free

path data are not normal, except for one case, and are generally highly skewed. The as-cast data are the most normal while the 54 sq. mm section size data are nearly as normal but the 47.5 sq. mm section size data is only normal for the  $\bar{L}$  data.

Skew and kurtosis values were also calculated for sulfides in the as-cast and as-forged (54 and 47.5 sq. mm) sections that were not homogenized (Table 9). Except for one value, the skew values are low and the kurtosis values are close to the ideal value of three for a normal distribution. The one odd set of results, for the average length of the as-cast specimens, was influenced by

Table 9 - Skew and Kurtosis Values for Specimen  
(As Cast and As Forged) Means - Sulfide Data

	$\bar{A}_A$	$\bar{N}_A$	$\bar{L}$	$\bar{A}$	$\bar{N}_L$	$\bar{\lambda}$
Skew ( $\beta_1$ )						
As Cast	0.067	0.085	5.838	0.069	0.088	0.030
54 sq. mm	0.883	0.113	0.046	0.00006	0.542	-0.117
47.5 sq. mm	0.176	0.346	-0.008	0.105	1.076	-0.104
Kurtosis ( $\beta_2$ )						
As Cast	2.356	1.777	9.951	1.897	2.750	2.844
54 sq. mm	4.388	2.313	2.662	2.450	3.450	2.782
47.5 sq. mm	2.114	2.319	2.130	2.251	3.699	2.443

Note: The number of specimen averages were: 31, 34, and 26 for the as cast, 54 sq. mm, and 47.5 sq. mm sections, respectively.

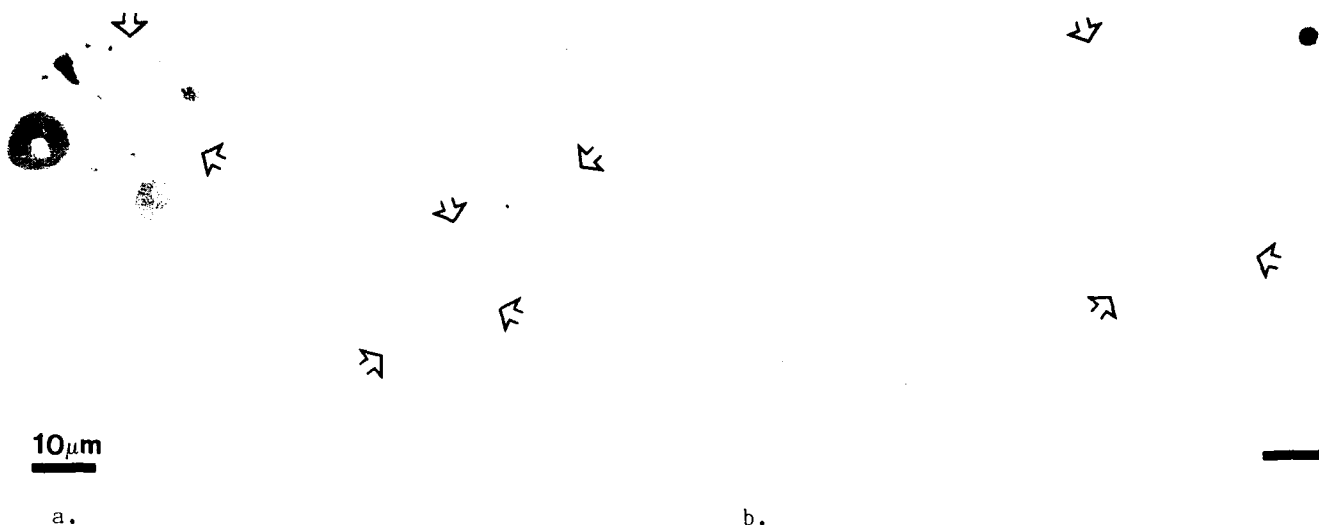


Figure 1. Examples of type I and type II (arrows) (Mn,Cr)S in the as-cast ingot (unetched).

one rather high value, which may be an outlier. Tables 8 and 9 demonstrate the influence of the amount, number and size of the second phase on measurement statistics.

**MICROSTRUCTURES** - Examination of the microstructure of the as-cast specimens revealed a mixture of type I and type II sulfides with type I much more common. Figure 1 illustrates regions containing globular type I sulfides and interdendritic type II sulfides. The latter appear as clusters of small spheres on the plane-of-polish but in three-dimensions they are rod shaped and approximately parallel. For an average oxygen content of 84 ppm, such a mixture is expected. Hollow-appearing globular sulfides were also observed as well as some with irregular shapes, as illustrated in Figure 2.

Figure 3 depicts the typical appearance of sulfides in the as-cast, 54 sq. mm, 47.5 sq. mm, and 35 x 25 mm sections. A wide range of sizes are observed and their distribution is typical of a resulfurized stainless steel. The wrought specimens show increased elongation with hot reduction but the sulfides have largely retained much of their globular appearance.

Figure 4 illustrates the appearance of oxides in the heat. The large complex oxide (Figure 4a) was the only one of this type observed. The other oxides shown are more typical. Nearly all of the oxides were associated with sulfides, either embedded inside the sulfide or at the end, or ends.

Figure 5 shows typical views of the sulfides in the as-cast and as-forged specimens after homogenization at 1260°C for

8h and 1302°C for 24h. Comparison of Figure 5 with Figure 3 demonstrates qualitatively the shape changes measured by image analysis. Homogenization of the as-cast specimens and the 54 sq. mm specimens (72% hot reduction) resulted in simple globularization of the sulfides. This is also apparent in the homogenized 47.5 sq. mm (78% hot reduction) specimens but a second effect is also observed, that is, many of the more highly elongated sulfides are necking down at one or more locations and "pinching off" to form two or more smaller, globular sulfides (see Figure 6). This effect was observed in all of the 47.5 sq. mm specimens but only a small percentage of the sulfides were so effected and very few have fully separated. It appears that the "cylinderization" and "ovulation" of sulfides(50-54) is accelerated by increased hot reduction, that is, elongated sulfides with their proportionally greater surface area undergo these processes more rapidly. This occurs because surface diffusion is the rate controlling process(52). The homogenization times used were not long enough, however, to complete this process for the hot reductions used. It is expected that the process of cylinderization - ovulation - spheroidization would have been more fully developed if the 35 x 25 mm (91% hot reduction) specimens had been available for homogenization treatments. For the experiment, a higher finishing temperature would be required to prevent cracking. This would probably have prevented sulfide fragmentation as well.

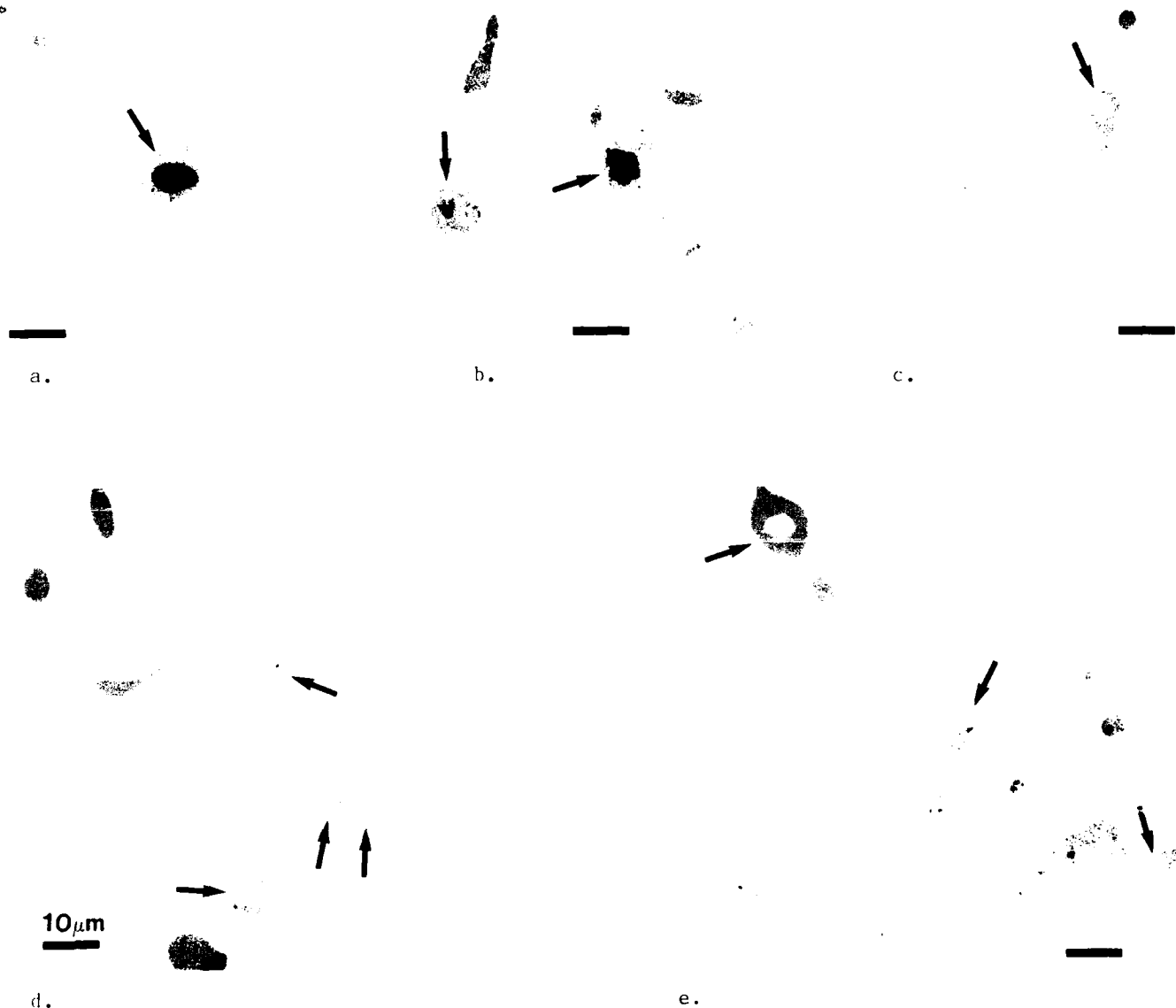


Figure 2. Examples of hollow (open-a and b, metal filled- c to e) sulfides and oddly shaped sulfides (b to e) in the as-cast ingot (unetched).

### CONCLUSIONS

Measurements of the sulfides and oxides in a laboratory size ingot of AISI 303 for as-cast and as-forged specimens with different degrees of reduction using the new ASTM E1245 image analysis procedure has permitted definition of the changes in inclusion characteristics viewed on a plane parallel to the ingot/deformation axis. The sulfide area fraction and mean free path (perpendicular to the deformation axis) decreased while the intercept count increased with deformation. The number of sulfides per unit area decreased slightly, remained constant, and then increased dramatically when the sulfides fragmented at the largest amount of hot reduction (91%) used. As the ingot was deformed, the

average sulfide area remained constant while they increased in length; however, during further reduction the sulfides fragmented producing shorter, smaller sulfides along with the large increase in number density. The decrease in volume fraction with deformation is due to the rotation and elongation of the sulfides parallel to the hot working axis, which was also the plane of examination.

Homogenization treatments on the as-cast and two of the as-forged sections (72 and 78% hot reduction) primarily affected the average length (decreased), the intercept count (decreased) and the mean free path (increased). The number density was largely unaffected. For the as-cast and least deformed (72% reduction) as-forged

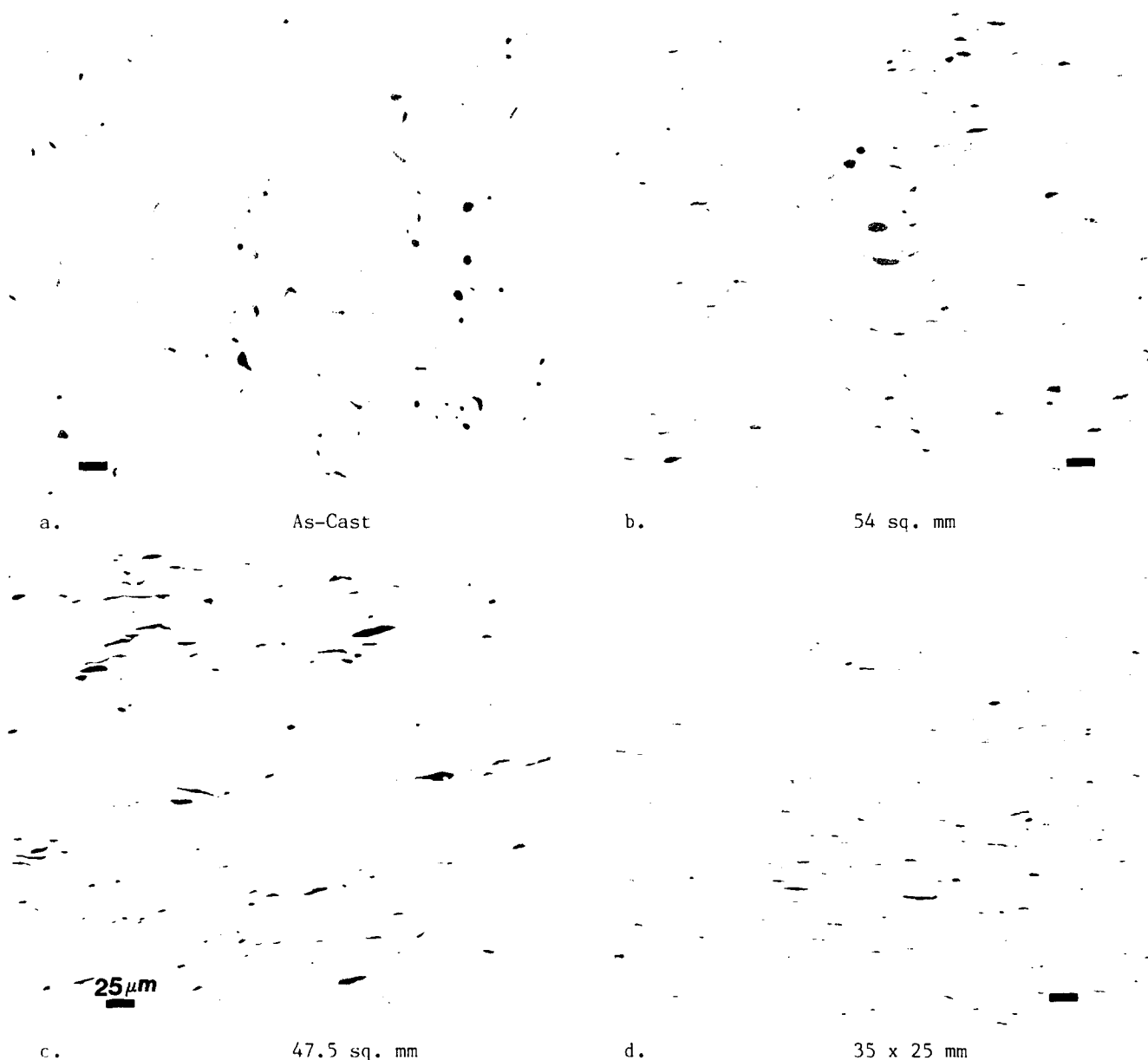


Figure 3. Examples of sulfides in the as-cast and as-forged specimens, longitudinal axis horizontal (unetched).

specimens, the longest treatments, particularly at the highest temperature, produced an increase in the average sulfide area and area fraction of sulfides. Cylinderization and ovulation of the sulfides were not observed for these specimens.

Results for the more highly deformed (78%) 47.5 sq. mm section produced little or no influence on the average sulfide areas; except for one specimen (slightly smaller), they were identical. The area fractions,

except for one sample that was similar, and one that was lower, increased slightly with homogenization. All of the homogenized specimens of this section size exhibited some evidence of cylinderization and ovulation but the latter was rarely carried to completion. Longer holding times, beyond those that are commercially practical, would be required for ovulation to be completed and for subsequent spheroidization. To maximize machinability, such a process is probably not desired as it is generally believed that large, globular sulfides are



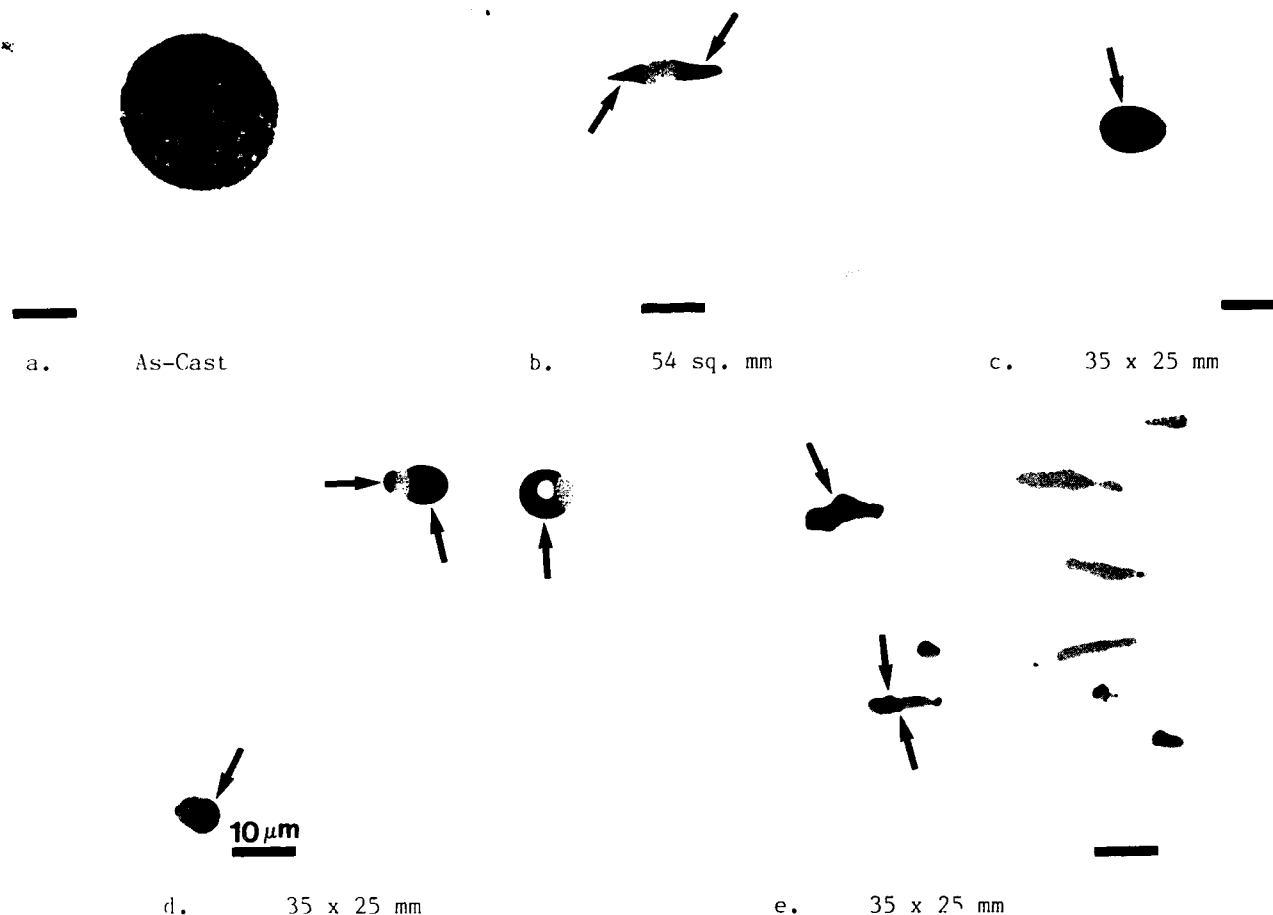


Figure 4. Examples of oxides (Mn-silicates containing Al and Ti) observed in specimens: a) large complex inclusion; c) isolated globular oxide; b), d) and e) sulfides adhering to oxides or surrounding oxides (e); sulfides gray, oxides black (unetched).

more desirable. Hence, such treatments should only be applied to less deformed starting structures so that globularization is achieved rather than cylinderization, ovulation and subsequent spheroidization.

Shape factor analysis for the as-cast and as-forged specimens revealed a decreasing shape factor with increased deformation, as expected. Homogenization treatments increased these shape factors with the degree of improvement increasing as the initial shape factor decreased, that is, homogenization produced the greatest degree of shape factor change in the most highly deformed sulfides. The shape factors increased with homogenization temperature and time.

Measurement of oxides in the as-cast specimens produced a higher area fraction, number density, average length, average area, and intercept count and a lower

spacing compared to the as-forged specimens. This was due to detection of voids within globular sulfides as well as oxides. Both features have the same gray level and cannot be separated. For the wrought specimens, the area fraction decreased, the average length decreased, and the mean free path increased with increasing deformation. The reduction of the area fraction with increased deformation was due to the rotation of the oxides during deformation and the use of a preferably oriented plane of examination, that is, a non-random section plane. Except for the comparison of the 54 sq. mm section to the 47.5 sq. mm section (72 vs. 78% hot reduction), the number density and average area also decreased with hot reduction. Also, except for the comparison of the 47.5 sq. mm section to the 35 x 25 mm section, the

1260C-8h

1302C-24h

As Cast

54 sq. mm

25  $\mu$ m

47.5 sq. mm

Figure 5. Examples of sulfides in the homogenized specimens: top-as cast; middle-54 sq. mm; bottom - 47.5 sq. mm (unetched).



Figure 6. Examples of the cylinderization and ovulation process (a to f) in sulfides from the 47.5 sq. mm homogenized sections (a - 1149C for 8h, b to f - 1302C for 24h). Only the more highly elongated sulfides were affected (unetched).

intercept count also decreased with increasing hot reduction.

#### ACKNOWLEDGEMENTS

The writer was assisted in this study by T. A. Christman, J. A. Leshner, and D. G. Kauffman, the latter performed the image analysis measurements. The writer acknowledges The Carpenter Technology Corporation for approving publication of this study.

#### REFERENCES

1. ASTM E1245-88: Standard Practice for Determining Inclusion Content of Steel and Other Metals by Automatic Image Analysis
2. Vander Voort, G. F., "Effect of Steel Manufacturing Processes on the Quality of Bearing Steels, ASTM STP 987," to be published
3. Anon, "I.S.I. SR25," 305-322 (1939)
4. Hatfield, W. H. and G. W. Giles, "I.S.I., 142, No. 2, 237P-276P (1940)
5. Eckstein, H. J. and K. Schneider, Neue Hutte, 5, 607-617 (October 1960)
6. Spies, H. J., Neue Hutte, 11, 420-427 (July 1966)
7. Blank, J. R. and T. R. Allmand, "I.S.I. 112," 1-11 (1968)
8. Hoo, J. J. C., "ASTM STP 575," 38-48, ASTM, Philadelphia (1975)
9. Vander Voort, G. F., "Metallography As a Quality Control Tool," p. 1-88, Plenum Press, New York (1980)
10. ASTM A295-84: Standard Specification for High-Carbon Ball and Roller Bearing Steel
11. ASTM E45-87: Standard Practice for Determining the Inclusion Content of Steel
12. Vander Voort, G. F., and J. F. Golden, "Microstructural Science," 10, 277-290, Elsevier, New York (1982)
13. ASTM E1122-86: Standard Practice for Obtaining JK Inclusion Ratings Using Automatic Image Analysis
14. Polzin, T., T. Kelly and W. U. Kopp, "Microstructural Science," 9, 355-362,

- Elsevier North Holland, New York (1981)
15. Lane, S., "Microstructural Science," 11, Elsevier Sci. Publ. Co., New York, 101-112 (1983)
16. Mehlo, H., Arch. Eisenhüttenwes., 54, 411-414 (October 1983)
17. Reti, T., Sz. Somogyi and P. Tardy, Metals Technology, 11, 138-144 (1984)
18. Johansson, S., "Clean Steel 3," 60-67, The Institute of Metals, London (1987)
19. Johansson, S., Scandinavian J. Metallurgy, 14, 44-48 (1985)
20. Roche, R., Microscope, 16, 151-161 (April 1968)
21. Allmand, T. R. and J. R. Blank, "I.S.I. 112," 47-62 (1968)
22. Franklin, A. G., J.I.S.I., 207, 181-186 (February 1969)
23. Rege, R. A., W. D. Forgeng, D. H. Stone, and J. V. Alger, "ASTM STP 480," 249-272, ASTM, Philadelphia (1970)
24. Johansson, S., Jernkont. Ann., 154, 423-426 (1970)
25. Johansson, S., Scandinavian J. Metallurgy, 2, 24-28 (1973)
26. Engstrom, C. H. and K. O. Karlstrand, Scandinavian J. Metallurgy, 2, 105-108 (1973)
27. Ruddlestone, R., J. R. Thornton and M. D. Bowers, Metals Technology, 3, 422-432 (September 1976)
28. Jeulin, D. and J. Serra, CDS Circ., 1165-1177 (1976)
29. Hersant, T., "Quantitative Analysis of Microstructures in Materials Science, Biology and Medicine," 144-152, Dr. Riederer-Verlag GmbH, Stuttgart (1978)
30. Steele, Jr., J. H., Practical Metallography, 17, 447-464 (September 1980)
31. Shehata, M. T. and J. D. Boyd, "Intl. Symp. on the Control and Effects of Inclusions and Residuals in Steels," III-19 to III-33, Canadian Inst. Mining and Met., Montreal (1986)
32. Allmand, T. R. and D. S. Coleman, Microscope, 20, 57-81 (1972)
33. DiGianfrancesco, E. and P. Filippi, La Metallurgia Italiana, 434-438 (1976)
34. Forgeng, Jr., W. D. and A. G. Lee, Sr., "Metallography as a Quality Control Tool," 89-100, Plenum Press, New York (1980)
35. Vander Voort, G. F., "Metallography: Principles and Practice," McGraw-Hill Book Co., New York (1984)
36. El-Soudani, S. M. and R. M. Pelloux, Metallography, 6, 37-64 (1973)
37. Chone, J. and G. Pierson, "Clean Steel 3," 107-110, The Inst. of Metals, London (1987)
38. Blank, J. R., Microscope, 16, 189-197 (1968)
39. Vander Voort, G. F., "Materials Characterization," 9th ed., 10, "Metals Handbook," 309-322, ASM Intl., Metals Park, Ohio (1986)
40. Brandis, H., K. Wiebking, and F. Berentzen, Practical Metallography, 6, 728-741 (December 1969)
41. Maunder, P. J. H. and J. A. Charles, J.I.S.I., 206, 705-715 (July 1968)
42. Baker, T. J. and J. A. Charles, J.I.S.I., 210, 680-690 (September 1972)
43. Gove, K. B. and J. A. Charles, Metals Technology, 1, 425-431 (September 1974)
44. Segal, A. and J. A. Charles, Metals Technology, 4, 177-182 (April 1977)
45. Wood, L. E. and L. H. Van Vlack, ASM Trans. Quart., 56, 770-772 (1963)
46. Chao, H. C., L. Thomassen and L. H. Van Vlack, ASM Trans. Quart., 57, 386-398 (1964)
47. Chao, H. C. and L. H. Van Vlack, ASM Trans. Quart., 58, 335-340 (1965)
48. Scheil, E. and R. Schnell, Stahl und Eisen, 72, 683-687 (June 5, 1952)
49. Radtke, D. and D. Schreiber, Steel Times, 193, 246-259 (August 19, 1966)
50. Gnanamuthu, D., T. Z. Kattamis, M. C. Flemings and R. Mehrabian, Met. Trans., 5, 2557-2567 (1974)
51. Wilson, P. C., Y. V. Murty, T. Z. Kattamis and R. Mehrabian, Metals Technology, 2, 241-244 (June 1975)
52. Y. V. Murty, J. E. Morral, T. Z. Kattamis and R. Mehrabian, Met. Trans., 6A, 2031-2035 (1975)
53. Y. V. Murty, T. Z. Kattamis, R. Mehrabian and M. C. Flemings, Met. Trans., 8A, 1275-1282 (1977)
54. McFarland, W. H. and J. T. Cronn, Met. Trans., 12A, 915-917 (1981)
55. Fisher, J. R. and J. Gurland, Met. Trans., 12A, 167-171 (1981)
56. Private communication with E. E. Underwood, National Science Foundation, Washington, D.C.

# **BENEFICIAL ASPECTS OF INCLUSIONS IN ALLOYS: TWO CASES — FREE-MACHINING BRASS AND OXIDE DISPERSION STRENGTHENED ALLOYS**

**A. Wolfenden, V. N. Cribb**

Amorphous Materials Research Group and  
Mechanical Engineering Department  
Texas A&M University  
College Station, Texas 77843 USA

**C. L. Hough**

Mechanical Engineering Department  
Texas A&M University  
College Station, Texas 77843 USA

**B. O. Soepangkat**

Industrial Engineering Department  
Texas A&M University  
College Station, Texas 77843 USA

## **ABSTRACT**

In certain materials, inclusions are introduced to promote specific beneficial properties. We give two examples. In free-machining brass up to 3.5 wt. % Pb is present in the form of inclusions distributed mostly on the grain boundaries. The beneficial function is the promotion of excellent free machining properties, namely, discontinuous chip formation. Our experiments have explored the influence of Pb inclusions on machining parameters such as speed, feed and depth of cut. Additionally, an ultrasonic technique known as the piezoelectric ultrasonic composite oscillator technique (PUCOT) has been used at 40 kHz to monitor the behavior of the Pb inclusions as a function of temperature up to and beyond the melting point of Pb. The physical form of the inclusions has a pronounced effect on the mechanical damping of the brass. In oxide dispersion strengthened (ODS) alloys small percentages of inclusions are necessary to promote the desired high temperature mechanical properties such as strength and creep resistance. For several standard ODS alloys we have calculated the influence of chemical composition on the elastic modulus, including the effects of the inclusions and preferred orientation of the grain structure. Some details of the experimental techniques and results are discussed.

A MERE GLANCE at the list of contents of this Symposium is enough to convince us that the presence of inclusions in materials has wide-ranging

consequences. The detrimental characteristics of inclusions are well publicized in steels because of their profound effects on fatigue cracking, cleavage fracture, stress corrosion cracking and corrosion fatigue cracking. Conversely, the beneficial effects of inclusions in some materials are well known, such as the enhancement of machining properties in stainless steels, medium carbon steels and brass. Research over a number of years has revealed that the chemical composition, and the size, shape and distribution of the inclusions in materials are variables that affect the properties. Techniques are being developed to control these variables, thus enlarging the scope for continued research on inclusions.

In this paper we deal with some of the beneficial aspects of inclusions in materials. These aspects are illustrated by consideration of a material well-known for its free-machining characteristics, brass, and then of some materials known as oxide dispersion strengthened (ODS) alloys. For brass, the experiments explored the role of lead inclusions on chip temperature, cutting force, feed force and thickness of the deformed chip. The cutting force and feed force were found

to be described best by a power law model as a function of feed rate and depth of cut. In terms of the thickness of the deformed chip, a linear model as a function of cutting speed and feed rate characterized the cutting relationships best. Additionally on brass, experiments with an ultrasonic technique were used to monitor the behavior of lead inclusions up to and

beyond the melting point of lead (327°C). The technique showed that the physical form of the lead has a pronounced effect on the mechanical damping (internal friction) or vibration damping of the free-machining brass. For seven ODS alloys we performed calculations of the influence of chemical composition on the elastic modulus (Young's modulus), with the elastic compliances ( $S_{ij}$ ) of the elements, the moduli of the inclusions, and some measure of the preferred orientation of the grain structure of the alloys as input parameters. The calculated values of elastic modulus were found to be within 6.3% (on average) of the measured values taken from the literature.

#### EXPERIMENTAL PROCEDURES AND CALCULATIONS

1. MACHINING EXPERIMENTS ON FREE-MACHINING BRASS - The experiments were carried out on an engine lathe (a 406 mm Monarch Series 62 retrofitted with an infinitely variable spindle speed drive) with the free-machining brass (Copper Association Alloy C36000) of chemical composition listed in Table 1. Carbide tool inserts (style TNMG 332, uncoated type K68) from Kennametal with a DTANRS-123 toolholder gave a side rake angle of  $-5^\circ$ , side clearance of  $5^\circ$ , back rake of  $-5^\circ$ , side cutting edge angle of  $0^\circ$  and a tool overhang of 80 mm. The contact length at the chip/tool interface was approximately 1 mm. The tubular workpiece, prepared from a cold drawn bar, was cantilevered in a three jaw chuck for orthogonal turning. The outer surface of the 44 mm cold drawn bar was turned to 42 mm to eliminate the effects of the cold drawn surface and variation due to hardness on measured forces. The bar was drilled and bored to the appropriate inside diameter to give the desired wall thickness representing depth of cut or unformed chip width. Four equally spaced levels of depth of cut (in the range 3.378 to 6.960 mm), three levels of feed representing the undeformed chip thickness (in the range 0.216 to 0.383 mm/rev) and three different speeds (in the range 100 to 200 m/min) were used during machining. Double replicates of each of the resulting 36 experimental conditions were taken to give a better estimate of the variation. The data were taken in completely random order to avoid concentrating extraneous errors on any one group of observations. Two

components of feed force, cutting force ( $F_c$ ) and feed force ( $F_f$ ), were measured by a Kistler three component piezoelectric dynamometer (model 9257A) and recorded. Sample chips were collected for each of the 72 observations and the deformed chip thickness was measured. Of course, in the case of free-machining brass the chips were discontinuous. From the samples, certain chips were chosen and examined in the Scanning Electron Microscope (SEM). Also for each observation, the average shear plane angle was calculated using the chip thickness measurements, and the temperature rises in the primary and secondary deformation zones of the chip were estimated from the force data and shear plane angle using the equations given earlier (1). The properties of free-machining brass used in the calculations are: density 8497 kg/m<sup>3</sup>, specific heat 376 J kg<sup>-1</sup> K<sup>-1</sup> and thermal conductivity 9.66 W m<sup>-1</sup> K<sup>-1</sup>. Further details of the machining experiments are available elsewhere (2,3).

2. MECHANICAL DAMPING MEASUREMENTS ON LEADED AND ON LEAD-FREE BRASS - The method used was the piezoelectric ultrasonic composite oscillator technique (PUCOT) (4-6). The mechanical damping or internal friction ( $Q^{-1}$ ) was measured continuously for specimens undergoing longitudinal, sinusoidal vibration at 40 kHz with maximum strain amplitude of  $3 \times 10^{-7}$  in the temperature range 25 to 400°C. Heating or cooling rates of 16 or 50°C/h were employed. The specimens of leaded (nominally C36000 brass) and lead-free brass (see Table 1 for compositions) were annealed at 400°C for 30 min before the ultrasonic experiments were started. Full details of the technique are given elsewhere (6).

3. CALCULATION OF YOUNG'S MODULUS FOR ODS ALLOYS - A simple empirical approach was used to attempt to relate the effects of texture and anisotropy of ODS alloys, containing typically 1 to 2% inclusions, to the measured values of Young's modulus. Seven alloys were chosen for this study. Their chemical compositions are given in Table 2. The modulus was calculated as follows. First, the values for  $S_{ij}$  for the principal elements in the alloys were incorporated in the equation to calculate the maximum anisotropy in Young's modulus  $E$ . The equation for the anisotropy factor (AF) is:

$$AF = E_{111}/E_{100} = S_{11}/(S_{11}-2((S_{11}-S_{12})-S_{44}/2)/3). \quad (1)$$

Next, the average value of Young's modulus for polycrystalline specimens of a particular element was modified (reduced or increased) by the use of a modulus biased toward that for the [100] direction, since this is the common texture in the ODS alloys. The arbitrary factor  $(1+AF)/2$  was used. For example, for aluminum the value of AF is 1.2 and the modified modulus then became  $70 \text{ GPa}/1.1 = 63.6 \text{ GPa}$ . Finally, the rule of mixtures was used to calculate the modulus for the alloy as the sum of the products (fraction by weight)  $\times$  (modified modulus) for the principal elements in the alloy. The value of the modulus for the inclusion (dispersed oxide) was taken to be 500 GPa and was not modified by some portion of the anisotropy factor since this factor is unknown for such an inclusion. In total, the formula is:

$$\text{orientation modified modulus} = \text{Summation (wt frac)}_i \times (2/(1+AF_i)) \times (\text{modulus})_i + (\text{wt frac})_{\text{inclusion}} \times 500 \text{ GPa}, \quad (2)$$

where the summation is taken over  $i$  elements or components in the alloy. Table 3 shows the anisotropy factors for six elements that are usually contained in ODS alloys.

## RESULTS AND DISCUSSION

1. MATHEMATICAL MODELING OF THE TOOL FORCES AND THICKNESS OF THE DEFORMED CHIP (FREE-MACHINING BRASS) - In conjunction with an examination of the results from the machining experiments on free-machining brass, a rigorous postulation of mathematical models was performed (2,3) to represent the relationships between the dependent variables (tool forces and thickness of the deformed chip) and the independent variables (cutting conditions). Only the most important features of the research will be summarized here. The rigorous statistical analysis led to the following equations:

$$F_c = A f^{0.753} d^{0.999} \quad (3)$$

$$F_t = B f^{0.499} d^{0.963} \quad (4)$$

$$t_1 = C + aV_w + bf, \quad (5)$$

where  $A$ ,  $B$ ,  $C$ ,  $a$  and  $b$  (with  $b \gg a$ ) are constants dependent on the units employed,  $f$  is the feed rate,  $d$  is the depth of cut,  $t_1$  is the thickness of the deformed chip, and  $V_w$  is the workpiece velocity. Clearly, the depth of cut had the most effect on the tool forces, while the feed rate had the

most effect on the thickness of the deformed chip. The tool forces measured in the experiments on free-machining brass were independent of cutting speed. Of course, there is to be expected a big reduction in tool forces resulting from the presence of lead inclusions (7), but lead-free brass was not investigated in this study. In the next three sections we have included the measured values of the tool forces and thickness of the deformed chip in calculations of the temperatures generated in the chip with the aim of assessing whether the lead inclusions melted during the machining process.

2. TEMPERATURE RISE IN THE PRIMARY DEFORMATION ZONE OF CHIPS (FREE-MACHINING BRASS) - In considering the plastic deformation of the chip, there are two aspects - the deformation in the primary zone and the reworking of the chip in the secondary zone. Each aspect is considered separately here. The rate of working for the primary zone is given as the product of the shear force and the shear velocity. An allowance is made for the heat conducted back into the workpiece. Thus, the equation for the temperature rise  $\Delta T_p$  in the primary deformation zone of the chip was presented (1) as:

$$\Delta T_p = (1-\beta_{\phi}) (F_c \cos \phi - F_t \sin \phi) \cos \alpha / (\rho c w_o t_o \cos(\phi - \alpha)), \quad (6)$$

where  $\beta_{\phi}$  is the proportion of the shear plane heat that is conducted back into the workpiece,  $\phi$  is the average shear plane angle,  $\alpha$  is the tool rake angle,  $\rho$  is the mass density of the material,  $c$  is the specific heat,  $w_o$  is the width of the undeformed chip, and  $t_o$  is the thickness of the undeformed chip. With this equation and the known or measured parameters, the temperature rises were found to be in the range 87 to 117°C, much less than the melting point of the lead inclusions (327°C).

3. TEMPERATURE RISE IN THE SECONDARY DEFORMATION ZONE OF CHIPS (FREE-MACHINING BRASS) - The regions of the chip next to the rake face are now reworked in the secondary deformation zone. For this calculation the equation is (1):

$$\Delta T_s (\text{max}) = D ((F_c \sin \alpha + F_t \cos \alpha) / L w_o) (r V_w)^{1/2}, \quad (7)$$

where  $\Delta T_s (\text{max})$  is the maximum temperature rise along the secondary zone,  $D$  is a constant dependent on the units employed,  $L$  is the contact

length, and  $r$  is the chip thickness ratio ( $t_c/t_1$ ). With the experimentally determined parameters inserted into this equation, the temperature rises were found to be in the range 91 to 269°C. Again, these temperatures are much less than the melting point of lead.

4. THE MAXIMUM TEMPERATURE AT THE END OF THE CONTACT LENGTH OF THE CHIP (FREE-MACHINING BRASS) - Since the machining process is a rapid deformation process, we have assumed that the maximum temperature  $T(\max)$  at the end of the contact length of the chip is the sum of the temperatures gained in the primary and secondary zones. Thus:

$$T(\max) = \Delta T_p + \Delta T_s + T(\text{ambient}), \quad (8)$$

where  $T(\text{ambient})$  is room temperature. The use of this formula yielded values of  $T(\max)$  in the range 247 to 432°C. Therefore, for some combinations of feed, speed and depth of cut it appears that the lead inclusions had the opportunity to melt. The various equations showed that speed and feed affected  $T(\max)$ , while the depth of cut did not affect  $\Delta T_p$  and  $\Delta T_s$ .

5. SEM EXAMINATION OF DISCONTINUOUS CHIPS (FREE-MACHINING BRASS) - Direct evidence of the role of lead inclusions in the formation of discontinuous chips during the machining of free-machining brass was obtained in the SEM study of the deformed surfaces of selected chips. Figures 1 and 2 show SEM micrographs of the smooth (the underside surface of the chip that was adjacent to the rake face) and of the rough (the free surface) sides of chips formed at workpiece speeds of 100 and 200 m/min, respectively. For both cases the feed rate was 0.384 mm/rev and the depth of cut was 6.96 mm. For the rough side of the chip there was no significant change in the morphology of the fracture surface when the speed was increased (Figures 1a and 2a). For the smooth side of the chip it was noticed that as the speed was increased, the surface became progressively smoother (Figures 1b and 2b). In particular, it was seen that at the highest speed investigated, the lead was smeared on the smooth surface of the chip. It was difficult to see a difference between the rough and smooth surfaces of the chips for lower speeds. In all the micrographs there was evidence of cuplets or elongated dimples which arise via the void-sheet mechanism of crack propagation discussed by Rogers

(8) for the fracture of ductile metals. In the case of the smooth side of the chip for the speed of 200 m/min, these cuplets are smoothed out. It has been considered (1) that shear fracture is initiated in the primary zone by void formation at the lead inclusions. In the secondary zone, the main function of the lead inclusions is to provide regions of low strength and to provide internal lubrication as the chip passes over the rake face. The present SEM observations tend to confirm these considerations.

6. THE INFLUENCE OF LEAD INCLUSIONS ON THE MECHANICAL DAMPING IN BRASS - Mechanical damping or internal friction is a measure of the ability of a material to dissipate vibrational energy. The level of damping is extremely sensitive to the microstructure of the material. For studies of defects in materials one of the most sensitive properties to be measured is damping. Internal friction techniques are able to detect the effects of defects at the atomic level (dislocations, impurities, etc.) and to monitor the gross changes in damping due to macroscopic defects such as porosity and cracks. In this study we demonstrate that a damping technique was able to distinguish easily the effects on the internal friction of the presence of lead inclusions in free-machining brass. Two brasses were used in the damping studies - leaded brass, containing 3.5 wt % Pb, and lead-free brass, containing 0.03 wt % Pb (Table 1). Thus there was over two orders of magnitude difference in the lead contents. Most of the lead in the leaded brass was present in the form of inclusions on the grain boundaries. Figure 3 shows the temperature dependence of the mechanical damping during heating or cooling over the range 240 to 400°C for the two brasses. The curves for the lead-free brass showed no evidence of damping peaks over the complete range of temperature investigated (25 to 400°C). Significantly, the curves for the leaded brass showed several interesting features. On heating the specimen the damping increased slowly and then started to decrease at 319±1°C before it rose to a peak at 327±0.5°C, while on cooling the specimen the damping decreased smoothly until 305±1°C when it increased to about the original level for heating at 280±1°C. This behavior was a consequence of the lead in the brass. For the leaded brass the



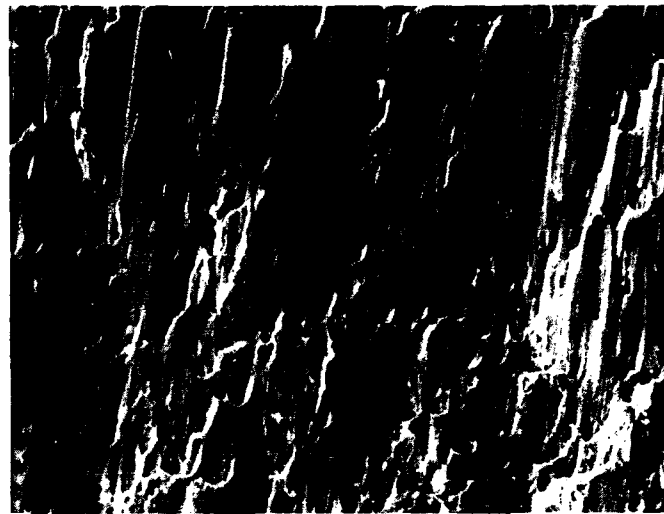
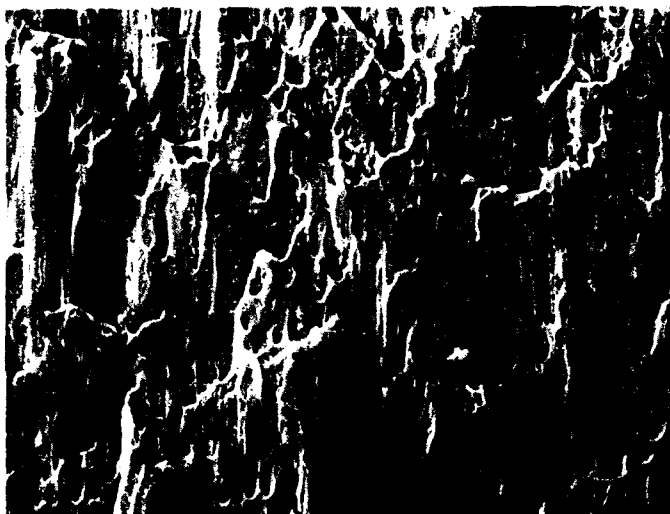


Figure 1: SEM Micrographs of Chips of Free-machining Brass  
(Workpiece Speed 100 m/min)  
left: Rough side of chip  
right: Smooth side of chip

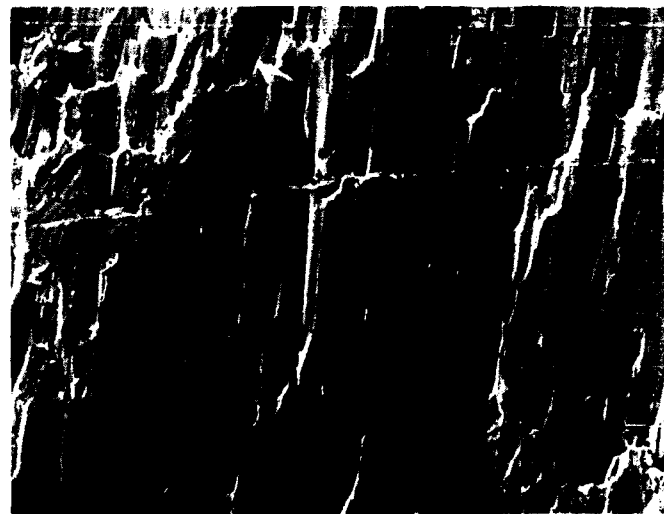
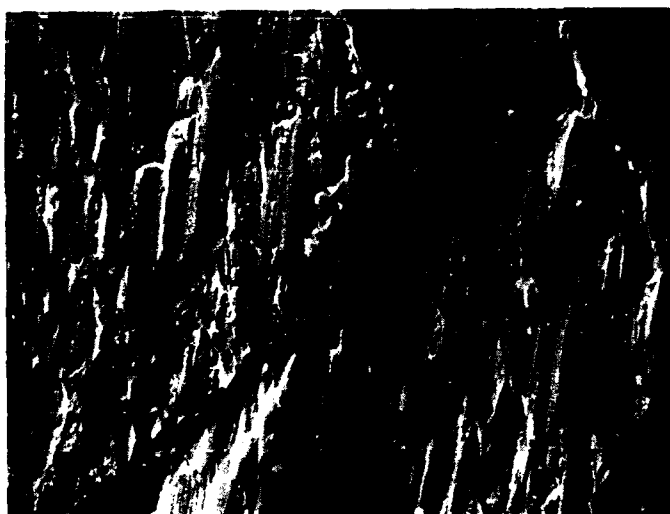


Figure 2: SEM Micrographs of Chips of Free-machining Brass  
(Workpiece Speed 200 m/min)  
left: Rough side of chip  
right: Smooth side of chip

TABLE 3

Calculation of Anisotropy Factor for Various  
Elements from the Values of  $S_{ij}$

Element	Anisotropy Factor
Al	1.195
Fe	2.182
Mo	0.816
Ni	2.212
W	1.000
Cr	0.766

temperature dependence of the damping described a hysteresis loop, whose shape was dependent on the exact details of the temperature time history of the specimen in the temperature range 260 to 360°C. For example, Figure 4 shows the influence of particular temperature swings (or oscillations) on the appearance of the damping peaks near 327°C. Clearly, the mechanism controlling the damping peaks involved kinetic processes (i.e. both temperature and time influence the picture). These and related investigations of damping (6) led to the following explanation of the damping peaks in leaded brass. The decrease in damping at 319±1°C on heating was associated with the onset of melting of the Pb-Zn eutectic (0.5 wt % Zn), while the sharp peak at 327±0.5°C was due to the complete melting of the lead inclusions in the brass. On cooling the specimen the damping rise starting at 305°C and finishing at 280°C was caused by the redistribution of lead in or near the grain boundaries. These experiments showed that the presence of lead at the 3.5 wt % level had significant effects on the mechanical damping in the system. It would be an interesting exercise to do further research to see if this phenomenon is present in other alloy systems where one component is melted as the alloy is heated.

7. YOUNG'S MODULUS FOR ODS ALLOYS - The results of the calculations of orientation modified modulus for seven ODS alloys containing up to 2 wt % oxide inclusions (usually yttria or thoria) are listed in Table 4. For good agreement the ratio  $E(\text{calculated})/E(\text{handbook})$  should be near unity. An examination of the ratio shows that its value for the seven alloys falls in the range -15 to +32% of unity, with an average value of +6.3%. The agreement between calculated value and experimental value is within 13% of unity for three of the materials - MA 754, YD NiCrAl and MA 953. Although this approach to calculating the modulus for the ODS alloys shows modest success, its attraction lies in a potential savings in alloy development schemes. These alloys are expensive to produce and the measurements of modulus at temperatures up to 1500°C present considerable experimental difficulties. Thus this simple approach, although empirical, shows some potential for estimating the modulus of these alloys of complex compositions. The

augmentation of the modulus due to the oxide inclusion is about 10 GPa. While this is only a percentage increase of around 5%, the further advantage of the presence of the oxide inclusions is the enhancement of properties other than modulus, such as strength, oxidation resistance and creep resistance - all at high temperatures. It is obvious that what is needed is a better measure of anisotropy or texture for these alloys and a more exact way of modifying the moduli of the individual elements and the oxide inclusions. Also, it is not known if the orientation of the oxide inclusions contributes significantly to the effects of texture of the ODS alloys. The use of other weighting factors besides weight fraction for the moduli of the components (volume fraction and atomic fraction) are being explored.

#### CONCLUDING REMARKS

Some of the beneficial aspects of inclusions in materials have been discussed in this paper. These include the well-known enhancement of machining properties of leaded brass by lead inclusions and the enhancement of the elastic modulus of ODS alloys by oxide inclusions. In brass the lead inclusions play an important role in the relationships of cutting force, feed force and thickness of the deformed chip to machining conditions. Also in leaded brass, lead inclusions have a critical role in providing mechanisms for vibration damping peaks at temperatures near the melting point of lead. The calculations of modulus for several ODS alloys from the individual moduli of the components included the contributions of the oxide inclusions. These conclusions contribute to the general findings that the chemical composition of inclusions in materials are important variables that affect the physical and mechanical properties.

#### REFERENCES

1. Wolfenden, A. and P. K. Wright, *Metals Technology*, 6, 297-302 (1979).
2. Soepangkat, B. O., Ph.D. Dissertation, Texas A&M University, May 1988.
3. Soepangkat, B. O. and C. L. Hough, Jr., to be submitted to *Metals Technology*.
4. Marx, J., *Rev. Sci. Instrum.*, 22, 503 (1951).

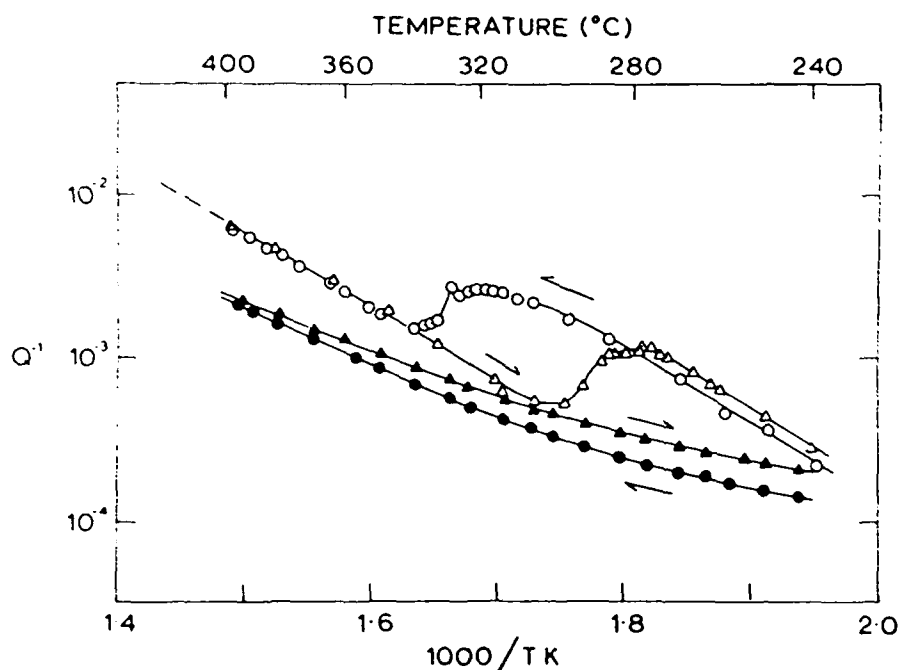


Figure 3: Temperature Dependence of the Mechanical Damping for Specimens of Leaded (Open Data Points) and Lead-free (Filled Data Points) Brass

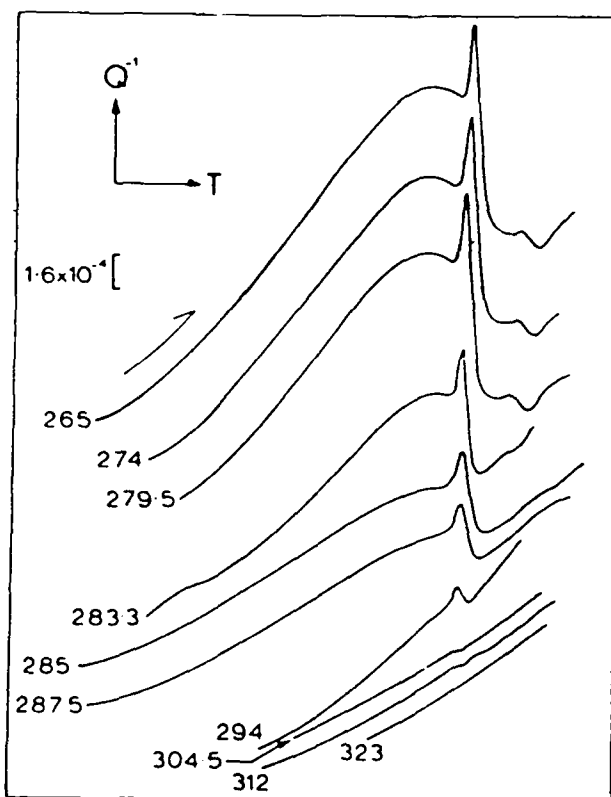


Figure 4: Schematic Tracings of Damping  $Q^{-1}$  as a Function of Temperature for Sequential Experiments in which the Temperature was Oscillated Between about 340°C and the Temperature Specified on each Curve to Monitor the Re-appearance of the Peak at 327°C in Leaded Brass.

## ACKNOWLEDGMENTS

5. Robinson W. H., and A. Edgar, IEEE Trans. Sonics and Ultrasonics, SU 21, 98 (1974).  
 6. Wolfenden, A. and W. H. Robinson, Acta Met., 25, 823-826 (1977).  
 7. Williams, J. E., E. F. Smart and D. R. Milner, Metallurgia, 81, Part II, 51 (1970).  
 8. Rogers, H. C., Trans. AIME, 218, 498 (1960).

The authors are grateful to Dr. Terry Bower of Chase Brass and Copper Company for the provision of specimen materials and for continued encouragement in this research field, and to Dr. J. D. Whittenberger of NASA Lewis Research Laboratory for many discussions on high temperature materials.

TABLE 1

Chemical Composition of Lead and of Lead-free Brass  
(wt. %)

Element	Ref. 2,3	Ref. 6	
	Lead	Lead	Lead-free
Cu	61.15	61.32	70.4
Pb	2.46	3.5	0.03
Fe	0.061	0.05	<0.01
Zn	36.1	35.0	29.5
Ni	0.093	<0.01	<0.01
Sn	0.016	0.12	<0.01

TABLE 2

Chemical Composition of Some Oxide Dispersion  
Strengthened Alloys  
(wt. %)

Alloy	Ni	Cr	Al	Mo	V	Fe	Ti	Oxide*
MA 754	78	20	0.3	0	0	0	0.5	0.6
TD Ni	98	0	0	0	0	0	0	2.0
TD NiCr	78	20	0	0	0	0	0	2.0
TD NiCrAl	76.7	16.2	4.8	0	0	0	0	1.88
YD NiCrAl	78.1	15.7	4.5	0	0	0.2	0	0.98
8077	77.3	15.3	4	0	0	1	0.1	1.66
MA 953	40.2	18	4.8	0	0	35.6	0	0.21

\* Usually yttria (YD) or thoria (TD)

TABLE 4

Calculation of Young's Modulus for Some ODS  
Alloys Using the Composition of Each Alloy, the Modulus  
Value for Each Element in the Alloy, Modification due to  
Anisotropy, and the Rule of Mixtures

Alloy	E(Handbk)	E(Calc)	Ratio
	(GPa)	(GPa)	E(Calc)/E(Handbk)
MA 754	145	159.3	1.099
TD Ni	152	128.6	0.846
TD NiCr	130	159.3	1.226
TD NiCrAl	191.8	149.9	0.781
YD NiCrAl	133.6	150.3	1.125
8077	113	149.0	1.319
MA 953	147.3	154.1	1.046

# INCLUSION ENGINEERING FOR THE IMPROVED MACHINABILITY OF MEDIUM CARBON STEELS

**S. V. Subramanian, D.A.R. Kay**

Department of Materials Science and Engineering,  
McMaster University  
Hamilton, Ontario

**Jiang Junpu**

University of Iron and Steel Technology  
Beijing, China

## Abstract

Tool wear and chip formation are two distinct phenomena which have to be considered in the design of steels of improved machinability by inclusion engineering.

Abrasion of the tool by inclusions or second phase particles in the workpiece which are 'harder' than the tool contribute significantly to tool flank wear. Alumina inclusions which result from conventional aluminum deoxidation practice are particularly harmful and their elimination, or modification to inclusions which are 'softer' than the tool, is one of the features in the production of modern free machining steels. In order to reduce tool flank wear, standard deoxidation practices are modified in secondary ladle steelmaking processes by calcium injection and wire feeding processes to give 'soft' anorthitic ( $\text{CaO} \cdot 2\text{SiO}_2 \cdot \text{Al}_2\text{O}_3$ ) or gehlenitic ( $2\text{CaO} \cdot \text{SiO}_2 \cdot \text{Al}_2\text{O}_3$ ) inclusions in the case of silicon/manganese deoxidized steels and duplex calcium aluminate/calcium sulfide inclusions in the case of aluminum deoxidized steels.

Thermodynamic models are used to relate liquid steel and inclusion compositions as a function of the temperature and soluble oxygen content. The predictions of these models are compared with the industrial results obtained from the calcium treatment of continuously cast medium carbon steels.

Chips formed during the machining of low and medium carbon steels over a wide range of cutting speeds exhibit microstructural features characteristic of ductile fracture. The concept of critical accumulated damage is used to rationalize the fracture behaviour of these steels in chip formation during metal cutting.

At moderate cutting speeds ( $v < 100\text{m/min.}$ ), the traditional approach to promote chip formation is to introduce free-cutting additives, such as sulfur, which generate 'soft' inclusions. Voids nucleate at these inclusions to initiate ductile fracture. The role of these free cutting additives is to lower the critical accumulated damage in a given steel without contributing to abrasive tool wear. The resulfurization of calcium treated 'clean' steels is based on this approach.

At high cutting speeds ( $v > 100\text{m/min.}$ ) both phenomenological observations and theoretical analysis suggest that chip

formation is facilitated by increased damage rates and strain localization. It is concluded that at high strain rates ( $\dot{\epsilon} > 10^3/\text{s}$ ), characteristic of high productivity machining, it may be possible to machine 'clean' steel with an attendant gain in fatigue life and through thickness ductility.

**TOOL WEAR AND CHIP FORMATION** are two distinct phenomena which have to be considered in the design of steels of improved machinability by inclusion engineering.

Abrasion by inclusions or second phase particles in the workpiece which are 'harder' than the tool, contribute significantly to tool flank wear. 'Hard', abrasive alumina inclusions, which result from conventional aluminum deoxidation practice, are particularly harmful and their elimination or modification to inclusions which are 'softer' than the tool, is an essential feature in the production of modern free machining steels with a given matrix. The presence of 'soft' silicate inclusions can also reduce crater wear, through the formation of an oxide film between the chip and the rake face of the tool which acts as a barrier against the high temperature interdiffusion of elements between the tool and the workpiece.

Tool wear can also be decreased by increasing the hardness of the tool surface relative to that of second phase particles in the workpiece. This can be achieved through the use of 'hard' coatings such as titanium carbide or titanium nitride. Significant progress has also been made in the development of sintered carbide and fibre reinforced ceramic tool inserts. This new development in tool materials has resulted in the attainment of industrial cutting speeds of up to 600m/min.

Tool wear is also influenced by matrix properties. As the flow stress of the matrix increases, the normal force acting on the tool tip increases. Limiting strains for tool failure can be brought about by a matrix, that is inherently 'hard'. On the other hand, a 'soft', ductile matrix without any second phase particles is equally difficult to machine in terms of chip disposal. Thus, "inclusion engineering" is an integral part of workpiece design for optimising microstructure with respect to tool wear and chip formation.

Chips formed during the machining of low and medium carbon steels over a wide range of cutting speeds, exhibit microstructural features characteristic of ductile fracture [1,2]. The primary role of free machining additives in

steel is the production of controlled dispersions of second phase particles which facilitate chip formation during machining through the ductile fracture process of void formation, growth and coalescence. Traditionally, free machining additives, such as sulfur and lead, are used to promote the chip fracture process at moderate cutting speeds ( $v < 100\text{m/min}$ ) through the formation of 'soft' manganese sulfide and lead inclusions which do not contribute significantly to tool flank wear. These steels have inferior mechanical properties, however, particularly strength, through thickness ductility and toughness. However, enhanced ductility and toughness can be achieved through the production of clean steel by calcium treatment. In this case chip segmentation can be promoted by high strain rate machining.

The first section of this paper discusses the control of steelmaking deoxidation and calcium treatment practices for the production of inclusions of controlled composition, volume fraction and morphology, in order to facilitate chip formation without promoting tool wear. In the second section, the concept of critical accumulated damage is used to rationalize chip formation in low and medium carbon steels at low and high cutting speeds.

## DEOXIDATION AND LADLE STEELMAKING CONTROL

The composition domains of 'soft' silicate inclusions, as defined by Bernard et al. [3], in both the  $\text{MnO-Al}_2\text{O}_3\text{-SiO}_2$  and  $\text{CaO-Al}_2\text{O}_3\text{-SiO}_2$  systems are shown in Figures 1a) and b), respectively. The shaded areas at high silica contents give the compositions of 'hard' supercooled silicate liquid(s) while the shaded areas at lower silica contents represent the composition of 'hard' inclusions which have either partially or wholly recrystallized when subjected to the specific thermal history of the study.

The production of 'soft' inclusion dispersions is the key to the development of steels of improved machinability in terms of tool wear. Deoxidation practices can be controlled to produce 'soft' spessartite ( $3\text{MnO-Al}_2\text{O}_3\text{-SiO}_2$ ) inclusions in the  $\text{MnO-Al}_2\text{O}_3\text{-SiO}_2$  system for example. For inclusions in the  $\text{CaO-Al}_2\text{O}_3\text{-SiO}_2$  system, standard deoxidation practices are modified by calcium ladle treatments to give either anorthitic/gehlenitic ( $\text{CaO-Al}_2\text{O}_3\text{-2SiO}_2$ )/( $2\text{CaO-Al}_2\text{O}_3\text{-SiO}_2$ ) inclusions in the case of silicon/manganese deoxidized grades, or duplex calcium aluminate/calcium sulfide inclusions in aluminum deoxidized grades. In the latter case, abrasive alumina inclusions are modified to calcium aluminates on which 'soft' calcium sulfide can precipitate. Where the soluble aluminum content is too low ( $< 0.01\%$ ) for conventional grain refinement, use is made of established microalloying technology.

The prerequisite for inclusion engineering is a deoxidation control system in which liquid steel compositions are related to corresponding equilibrium inclusion compositions using measured temperature and soluble oxygen activity data obtained from commercially available oxygen probes. Comparison of the thermodynamic predictions with the results of industrial practice can then be used to determine the significance of any kinetic effects during liquid steel treatment and the extent of reoxidation during transfer processes.

A thermodynamic model, which can be used to predict the composition of silicate inclusions during liquid steelmaking, and hence provide some measure of deoxidation control, is described below.

**THE THERMODYNAMIC DATA BASE** – For most oxide systems relevant to steelmaking deoxidation practice,

the experimental thermodynamic data base relating inclusion compositions to the corresponding oxide activities, is incomplete, and use has to be made of slag (inclusion) models to give a complete data base over the range of temperatures and inclusion compositions encountered in industrial steelmaking. In addition, the first order free energy interaction parameters, which are used to calculate the activities of elements in solution in steel from their corresponding weight percent concentrations, have usually been determined experimentally at  $1600^\circ\text{C}$ . In this application, their use is considered to be valid over the temperature range of steelmaking deoxidation.

In developing deoxidation control for inclusion engineering, a statistical thermodynamic slag model developed by Gaye (11) is used to calculate component oxide activities at a given temperature from the corresponding weight percent oxide inclusion composition. The equilibrium Henrian activities of elements in solution in the liquid steel are then calculated for a given Henrian oxygen activity using the thermodynamic data given in Table 1. The weight percent contents of the elements in solution are obtained from the corresponding Henrian activities using the free energy interaction parameter data given in Table 2.

**INCLUSIONS IN THE  $\text{MnO-Al}_2\text{O}_3\text{-SiO}_2$  SYSTEM** – The importance of soluble oxygen content and temperature in deoxidation control can be illustrated by calculation of weight percent steel compositions in equilibrium with 'soft' inclusions in the  $\text{MnO-Al}_2\text{O}_3\text{-SiO}_2$  system using an AISI 1045 plain carbon steel base. Iso-weight percent curves for silicon and manganese are plotted as a function of inclusion composition at  $1600^\circ\text{C}$  on the ternary phase diagram in Figures 2a) and 2b). The curves are computed for Henrian oxygen activities of 0.0070 in Figure 2a) and 0.0080 in Figure 2b). From the data given in Figure 2a), a steel containing 0.60% soluble manganese and 0.17% soluble silicon with a Henrian oxygen activity of 0.0070 at  $1600^\circ\text{C}$  would be in equilibrium with an inclusion containing 36%MnO, 31% $\text{SiO}_2$  and 33% $\text{Al}_2\text{O}_3$  by weight, i.e., the inclusion composition is given by the intersection of the two iso-weight percent curves. The corresponding equilibrium inclusion composition of 45%MnO, 37% $\text{SiO}_2$  and 18% $\text{Al}_2\text{O}_3$  by weight for a similar steel with a Henrian oxygen activity of 0.0080 at  $1600^\circ\text{C}$  is obtained from the data in Figure 2b). Aluminum iso-weight percent curves may be calculated for these figures, but the soluble aluminum contents are too small in this case ( $< 10\text{ ppm}$  by weight) for their use as a control variable in steelmaking. These results clearly indicate the importance of oxygen activity measurements in the production of steels of controlled inclusion composition.

The pronounced effect of temperature on the composition of an AISI 1016 steel in equilibrium with an inclusion containing 30% MnO, 50%  $\text{SiO}_2$  and 20%  $\text{Al}_2\text{O}_3$  is shown in Figures 3a) and 3b), where the silicon and manganese contents, respectively, are shown as a function of the Henrian activity of oxygen. Contents of 0.28% Mn and 0.10% Si by weight at  $1550^\circ\text{C}$  are to be compared with contents of 0.42% Mn and 0.30% Si at  $1600^\circ\text{C}$  for a given Henrian oxygen activity of 0.0070.

The prediction of the composition of exogeneous inclusions in this system is important since it often provides the base for downstream inclusion modification by aluminum and/or calcium additions.

## INCLUSIONS IN THE CaO-Al<sub>2</sub>O<sub>3</sub>-SiO<sub>2</sub> SYSTEM -

For the inclusion engineering of anorthitic and gehlenitic inclusions in the CaO-Al<sub>2</sub>O<sub>3</sub>-SiO<sub>2</sub> system, the analysed total aluminum and calcium concentrations in the liquid steel are very low and are not known with sufficient accuracy during liquid steel processing to be used as estimates of their respective soluble concentrations. Although the soluble silicon content can usually be approximated to the analysed total silicon content, inclusion compositions cannot be calculated for measured temperatures and soluble oxygen contents using the silicon content alone. In addition, the generally accepted standard free energy of formation of calcium oxide is too negative (7) and results in unreasonably low calculated calcium solubilities for given soluble oxygen contents.

For inclusions in the CaO-Al<sub>2</sub>O<sub>3</sub> system, however, the total analysed aluminum contents of the liquid steel are higher (typically 0.015-0.060%) and are reasonable estimates of the soluble aluminum contents. They can therefore be used as control variables in the calculation of inclusion compositions for measured temperatures and soluble oxygen contents, using thermodynamic data in the literature (7).

Predicted aluminate inclusion compositions in two liquid steel heats after industrial calcium treatment, are compared in Table 3 with the compositions of inclusions found in the corresponding continuously cast billets. Reoxidation between the ladle station and the caster is a possible cause of the 'fade' in calcium modification.

The formation of liquid aluminates in the calcium modification of aluminum killed steels, minimizes the possibility of nozzle clogging through the precipitation of alumina and solid aluminates during continuous billet casting.

## DAMAGE ACCUMULATION AND CHIP FORMATION

A basic understanding of fracture processes associated with chip formation in metal cutting is essential in order to improve the machinability of a given grade of steel for a given rate of metal removal. The deformation process associated with chip formation is a heterogeneous one, involving high strain rates (10<sup>4</sup>-10<sup>6</sup>/sec) and large strains (>1) in a highly localized zone, a few microns thick in the workpiece, extending from the tool/workpiece interface. Figure 4 shows an SEM montage of a quick-stop section of a low carbon, resulfurized steel, at a cutting speed of 70 m/min. Void nucleation is associated with the fragmentation of cementite plates and there is also evidence of decohesion around MnS inclusions. Even at higher cutting speeds, ductile rupture regions are clearly seen. Figures 5a) and 5b) are SEM pictures of a chip obtained from a medium carbon (0.45 wt.%C) low alloy steel, at a cutting speed of 2000 m/min. The coalescence of voids into cracks has culminated in fracture processes leading to chip segmentation.

The various stages leading to total failure due to ductile fracture may be summarized as follows:

- (i) As the material is progressively worked, second phase particles and interphase interfaces start acting as centres for the formation of voids. Void initiation occurs because of the inherent deformation incompatibilities which exist between the second phase particles and the surrounding matrix. In the case of oxides which are harder than the matrix, void nucleation starts by particle cracking, and in the case of sulfides which have a lower interfacial energy between the inclusion and the matrix, decohesion occurs at the inclusion/matrix interface, even at low strains

- (ii) Increasing plastic strain promotes void growth.
- (iii) With continuing deformation, damage accumulates to a critical value at which microstructural instability occurs, resulting in void coalescence and microcrack formation.

Thus the fracture process in chip formation is analysed in terms of damage accumulation to ductile fracture. The damage, in turn, can be assessed from the areal fraction of voids measured on SEM micrographs. The metal cutting conditions define the macroscopic strain distribution in the primary and secondary shear zones. The geometry of the metal cutting operation and the cutting velocity are the key variables of the metal cutting process. The microstructure, and in particular, the second phase particle dispersion, determines the strain localization and consequently the microscopic flow of the material. Thus, both microscopic and macroscopic flow influence the damage process.

## MICROSCOPIC DAMAGE OBSERVATION ON

CHIPS - The microscopic criteria for chip fracture involving second phase particles have been studied using the phenomenological approach. Detailed SEM studies of chips and quickstop samples, generated at various cutting speeds, were undertaken for different steels with the objective of mapping the damage associated with the type, size, amount and local dispersion of second phase particles. One of the salient observations resulting from these SEM studies of chip fracture surfaces relates to the influence of cutting velocity on accumulated damage. For example, an AISI 1045 steel, subjected to a spheroidizing treatment, exhibits void nucleation associated with carbides rather than extended void growth, at low cutting velocities (<100 m/min), see Figure 6.

Conversely, at higher cutting velocities (>200 m/min), a medium carbon steel (0.45 wt.%C), with a microstructure consisting of carbides and MnS inclusions, exhibited pronounced growth of the voids associated with MnS inclusions and carbide particles, indicating that void growth dominates at higher cutting velocities.

At very high cutting speeds, the tendency for segmentation increases with cutting speed but the degree of segmentation is incomplete until a critical speed is exceeded. Figure 7 shows a typical fully segmented chip, obtained at 2000 m/min, from a medium carbon steel in the quenched and tempered condition with the following typical analysis:

Material	C	Si	Mn	P	S	Cr	Mo
42CrMoS4V	0.42	0.33	0.74	0.0012	0.029	1.04	0.18

A detailed examination of the SEM pictures of the fracture surface shown in Figure 8 shows two distinct regions. The ductile rupture region shows characteristic dimples. Inclusions and carbides in this region are associated with extensive void growth and linkage. The segmented fracture surface is smooth and undeformed. Thus, following the region of ductile rupture there appears to be a region of catastrophic crack propagation. Extensive void growth is the characteristic feature of chip fracture surfaces obtained at high cutting velocities (>200 m/min). Figures 9a) and 9b) show extensive damage or void growth associated with MnS inclusions in a chip from the same steel referred to in Figure 7, but generated at a lower cutting velocity of 200 m/min. The segmentation of the chip is incomplete in this case.

**MACROSCOPIC DAMAGE ANALYSIS** – In order to predict the cumulative damage occurring in the plastic zone enveloped between the entry and exit slip lines, it is essential to develop a model which allows the determination of the stress and strain, and strain rate history at any point within the plastic zone of the chip. Hence, an elemental volume of material can be followed along a streamline, and the damage accumulation can be integrated over the path. Phenomenological observations of damage occurring in quick-stop samples do indicate that the hydrostatic pressure does not vary linearly from the surface of the chip to the tool tip. The hydrostatic pressure is compressive in the vicinity of the tool tip and becomes less compressive in the interior region of the chip. The hydrostatic pressure is equal to the flow stress of the material at the free surface of the chip. In principle, positive damage is possible within the deformation zone providing one of the in-plane principal stresses is positive (tensile).

Sowerby and Chandrasekaran [12] have considered this problem using a modified Slip Line Field theory [13]. The theory was modified to take into account strain hardening. The influence of temperature and strain rate was also considered. According to their analysis, the damage rate can be related to the  $p/k$  ratio, where  $p$  is the local hydrostatic pressure and  $k$  is the local flow shear stress of the material.

Figure 10a) shows the variation in the  $p/k$  ratio as a function of distance from the free surface of the chip towards the tool, along a  $\beta$ -slip line located near the middle of the primary deformation zone. Two cutting velocities were considered. These quantitative results clearly show that the effect of increasing the cutting velocity is to decrease the  $p/k$  ratio, making the local stress more tensile, thereby increasing the damage rates. The variation in damage rate along an interior streamline, containing the 'maximum damage rate' is plotted in Figure 10b) for cutting velocities 50 and 200 m/min., respectively. The slip line field is shown in the inset diagram. Clearly, the 'maximum damage rate' increases with an increase in the cutting velocity. This is a significant result which can account for the phenomenological observations.

At the free surface, where no damage occurs, the  $p/k$  ratio is unity. In the interior region of the chip, the local hydrostatic pressure decreases to less than the local flow stress of the material. Under the conditions where  $p/k < 1$ , one of the principal stresses will be tensile, which contributes to a positive damage rate. The problem is one of integrating the damage rate along a stream line from entry to exit slip line. Microcracking will occur if the damage accumulated exceeds a critical value, which is characteristic of a given material. Since void growth dominates the damage process, the interparticle spacing and the particle size are important microstructural parameters.

Damage rates can be increased by increasing  $k$ , the local shear flow stress, relative to the local hydrostatic stress,  $p$ . As the  $p/k$  ratio is decreased, the triaxiality of stress is increased. The shear flow stress is a material property that is a function of strain, strain rate and temperature. It will be increased by an increase in strain and strain rate, but will be decreased by an increase in temperature. The effect of increasing the velocity is to increase the strain rate in the primary shear zone.

**THE INFLUENCE OF CUTTING SPEED ON DAMAGE RATES** – The chips generated at high cutting velocities (2000 m/min) in low alloy steels show extensive void growth in comparison with chips generated at low cutting speeds. There is no microstructural evidence of high temperature softening of the structure. The strain measurements carried out on second phase carbide particles yielded

values comparable with those in chips generated at moderate and moderately high cutting velocities (60-100 m/min). Thus the increased damage rates can be rationalized by the increase in flow stress brought about by the higher strain rates.

**ESTIMATING CRITICAL ACCUMULATED DAMAGE** – Deformation incompatibilities which exist between the matrix and second phase particles/ inclusions normally result in local (microscopic) radial stresses at the particle/matrix interface, giving rise to void nucleation by decohesion; alternatively the second phase particles could crack, resulting in void formation. The growth of these voids in the matrix, when subjected to a triaxial stress system in the gauge length set up between the adjacent voids, determines the damage process. The dispersion of second phase particles in a given material determines the critical gauge length, through a material parameter  $\ln(\lambda/d)$  where  $\lambda$  is the initial void spacing and  $d$  the initial void dimension along the chosen orientation. The void growth under a triaxial stress system is complicated by the matrix deformation behaviour, which is a function of strain, strain rate and temperature. Sowerby and Chandrasekaran [14] have developed an upsetting test using a collar specimen to obtain a well defined strain path. The test allows the determination of critical accumulated damage by integrating damage along the strain path and at fracture, according to McClintock's model for void growth [15].

Machining tests carried out on an AISI 4340 steel, subjected to different heat treatments are summarized in Table 4, from which it can be seen that discontinuous chip formation is promoted in steels with low CADF values (12).

**DESIGN CRITERIA FOR STEELS FOR HIGH STRAIN RATE MACHINING** – The design of microstructure for improved machinability can be analysed in terms of (a) critical accumulated damage at fracture and (b) damage rate as a function of strain rate. At moderate and low cutting speeds, the machinability of steels can be improved by making free cutting additives that essentially lower the critical accumulated damage at fracture. In the past, the speed of cutting has been limited by tool life. At moderate cutting speeds ( $< 100$  m/min), the strain rate sensitivity is not significant, and therefore the machinability can be improved by increasing the volume fraction of coarse second phase particles or inclusions, thereby decreasing the critical accumulated damage at fracture. The MnS inclusion population is increased by resulfurizing the steel and with further free cutting additives, such as lead or bismuth, the critical accumulated damage (at fracture) is decreased.

With the recent advances in tool materials, high cutting speeds have become a reality. Sintered carbide tools, ceramic tools, and tools coated by PVD and CVD techniques have vastly improved tool life performance. High strain rate machining imposes high normal stress at the tool tip. Modern tools are capable of performing well under this condition, thus paving the way for high productivity machining. In view of the economic gains in high productivity machining, the technological forecast is the development of high speed machining processes taking full advantage of high performance ceramic tools. Under conditions of high strain rate machining, it is possible to increase the damage rate through the dramatic increase in flow stress brought about by high strain rates. This would imply that free cutting additives are no longer required to lower the critical accumulated damage. Microalloying additions may then be used to strengthen the steel, as long as they do not adversely affect the strain rate sensitivity of the material.



# ACKNOWLEDGEMENTS

The financial support of the Department of Energy, Mines and Resources (CANMET) is gratefully acknowledged. Special thanks are due to Mrs. Teresa Castillo for her assistance with the SEM work. The provision of steelmaking data by Algoma Steel Corporation Ltd. and the technical support of the Niobium Products Company Inc. is also gratefully acknowledged.

The high speed chips used in this investigation were provided by the research group headed by Professor Tönshoff at IFW, University of Hanover, GFR.

# REFERENCES

1. S.V. Subramanian and D.A.R. Kay: 'Development of Non-Leaded Free Machining Steel - Phase IV'. Final Report, DSS File No. 128V-23440-3-9134, 1985.
2. S.V. Subramanian and D.A.R. Kay: 'Microstructural Engineering for Improved Machinability'. CSIRA/ISIJ Japan/Canada Seminar, Tokyo, December 3-4, 1985.
3. G. Bernard, P.V. Riboud and G. Urbain: Rev. Met. CIT, vol. 78, no. 5, 1981, pp. 421-434.
4. H. Gaye, C. Gatellier, M. Nadif, P.V. Riboud, J. Soleil and M. Faral: IRSID PCM-RE.1277, May, 1986.
5. D. Ghosh and D.A.R. Kay: J. Electrochem. Soc., vol. 124, 1977, pp. 1836-1845.
6. J.F. Elliott: 'Electric Furnace Steelmaking', 1985, p. 265, AIME.
7. D.A.R. Kay, S.V. Subramanian and R.V. Kumar: 'Inclusions in Calcium Treated Steels', Proceedings of the Second International Symposium on the Effects and Control of Inclusions and Residuals in Steels, 25th Conference of Metallurgists, Toronto, 1986, CIM.
8. G.K. Sigworth and J.F. Elliott: Metal Science, vol. 8, 1974, pp. 298-310.
9. M. Kohler, H-J. Engell and D. Janke: Steel Research, vol. 56, no. 8, 1985, p. 419.
10. J.F. Elliott, M. Gleiser and V. Ramakrishna: 'Thermochemistry for Steelmaking', vol. II, Addison-Wesley Publ. Co. Inc., 1963.
11. H. Gaye and D. Coulombet: IRSID PCM-RE.1064, March, 1984.
12. D.A.R. Kay, S.V. Subramanian, R. Sowerby and N. Chandrasekaran: 'Metallurgical Aspects of Machinability in Medium Carbon Steels', D.S.S. File No. 20ST-23440-5-9055, October 1987.
13. R.N. Roth and P.L.B. Oxley: J. Mech. Engg. Sci., vol. 14, 1972, p. 85.
14. R. Sowerby and N. Chandrasekaran: Matls. Sci. and Engg., vol. 79, 1986, pp. 27-36.
15. F.A. McClintock: Trans. ASME, J. Appl. Mech., vol. 35, 1968, pp. 363-371.

Table 1 - Thermodynamic Data Base

Reaction	Log K	Reference
$[\text{Si}]_{\text{lw/o}} + 2[\text{O}]_{\text{lw/o}} = \text{SiO}_2(\text{s})$	$(31040/T) - 12.0$	4
$[\text{Mn}]_{\text{lw/o}} + [\text{O}]_{\text{lw/o}} = \text{MnO}(\text{s})$	$(15050/T) - 6.70$	4
$2[\text{Al}]_{\text{lw/o}} + 3[\text{O}]_{\text{lw/o}} = \text{Al}_2\text{O}_3(\text{s})$	$(61304/T) - 20.37$	5,6
$[\text{Ca}]_{\text{lw/o}} + [\text{O}]_{\text{lw/o}} = \text{CaO}(\text{s})$	$(25655/T) - 7.65$	7

Table 2 - Interaction Parameters  $e_i^j$

$\begin{matrix} i \\ j \end{matrix}$	Al	C	Si	O	Mn	S	Ca
Al	0.045(4)	0.043(8)	0.058(4)	-1.170(4)	-	0.035(8)	-0.072(4)
C	0.091(4)	0.140(8)	0.180(4)	-0.130(4)	-0.070(4)	0.110(8)	-0.337(4)
Si	0.056(4)	0.078(8)	-0.107(4)	-0.140(4)	0.060(4)	0.063(8)	-0.097(4)
O	-1.980(4)	-0.098(10)	-0.250(4)	0.0	-0.083(8)	-0.270(8)	-
Mn	-	-0.012(8)	0.033(4)	-0.030(4)	-0.003(4)	-0.026(8)	-0.010(9)
S	0.030(4)	0.046(8)	0.056(4)	-0.133(4)	-0.004(4)	-0.028(8)	-
Ca	-0.047(8)	-0.097(8)	-0.068(8)	-	-	-	-

Note: Figures in parentheses refer to the references in the literature.

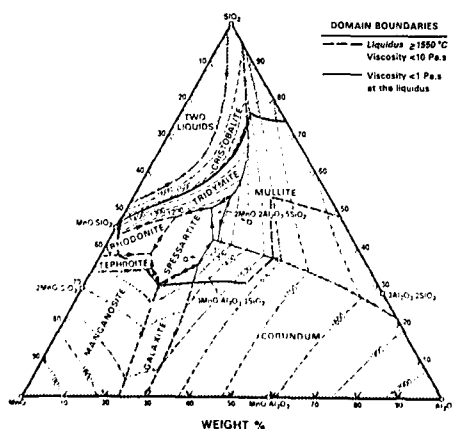
Table 3 – Comparison of Aluminate Inclusion Compositions

Oxygen probe		[O] <sub>sol</sub> ppm	[Al] <sub>sol</sub> %	Aluminate Composition*	
Temp. F	E-mv			Predicted	Billet
2929	-156	5	0.032	CA + liquid	CA + CA <sub>2</sub>
2923	-156	5	0.028	CA + liquid	CA <sub>2</sub>

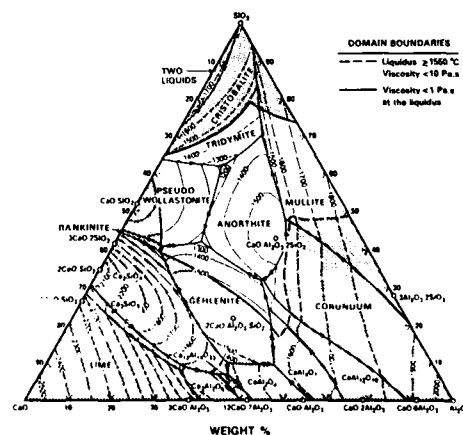
\* C = CaO, A = Al<sub>2</sub>O<sub>3</sub>

Table 4 – Results of Machining Tests and CADF Measurements for an AISI 4340 Steel.

Heat Treatment	Hardness	CADF	Discontinuous Chips
OIL QUENCH	56 ROCKWELL "C"	0.172	Yes, at 136 m/min
OIL QUENCH AND TEMPERED	47 ROCKWELL "C"	0.224	Yes, at 234 m/min
AS RECEIVED	298 BHN	0.367	No, at Max Speed 400 m/min
SPHEROIDIZED	224 BHN	0.755	No, at Max Speed 400 m/min

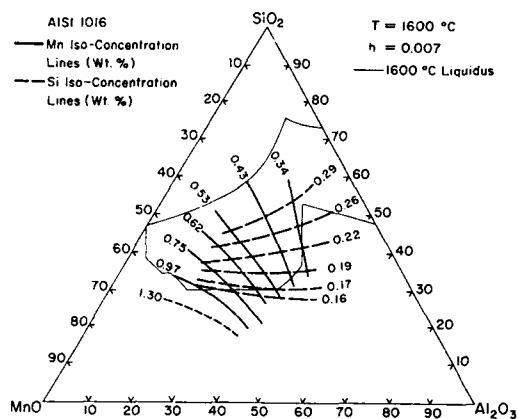


(a)

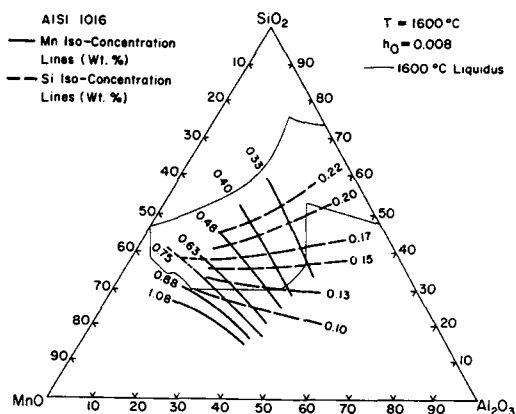


(b)

Figure 1 – a) The MnO-Al<sub>2</sub>O<sub>3</sub>-SiO<sub>2</sub> phase diagram and b) the CaO-Al<sub>2</sub>O<sub>3</sub>-SiO<sub>2</sub> phase diagram, showing the composition domains of 'deformable' silicate inclusions.

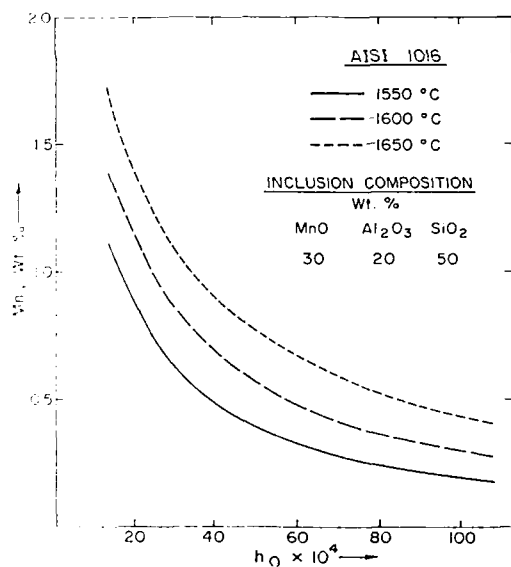


(a)

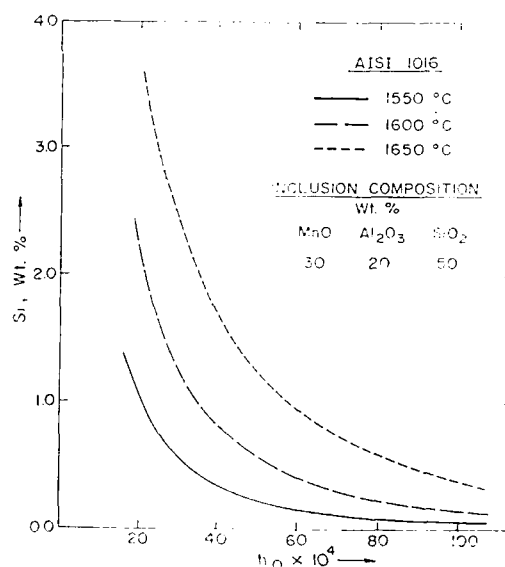


(b)

Figure 2 — Iso-weight percent curves for silicon and manganese in the  $\text{MnO-Al}_2\text{O}_3\text{-SiO}_2$  system for an AISI 1016 steel at 1600C. a)  $h_0 = 0.007$  and b)  $h_0 = 0.008$ .



(a)



(b)

Figure 3 — The effect of oxygen activity and temperature on a) the silicon content and b) the manganese content of an AISI 1016 steel in equilibrium with an inclusion containing 30% MnO, 20%  $\text{Al}_2\text{O}_3$  and 50%  $\text{SiO}_2$  by weight.

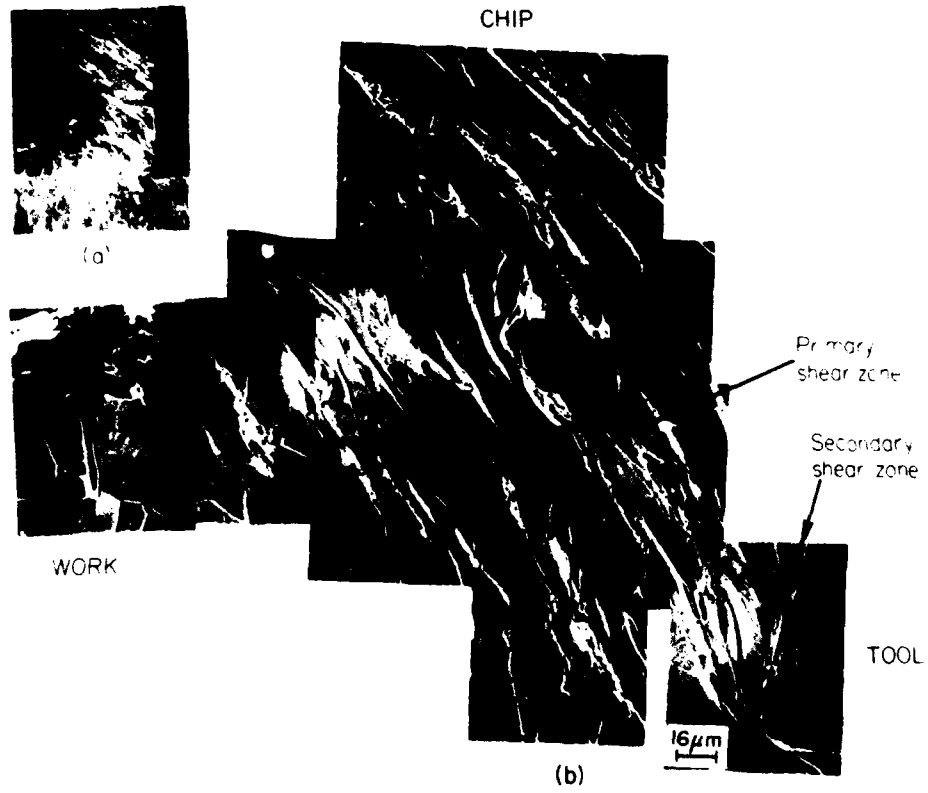


Figure 4 — a) Section of a 'quick-stop' chip from a low carbon resulfurized steel, and b) an SEM montage, corresponding to the region marked in a), showing the primary and secondary shear zones.

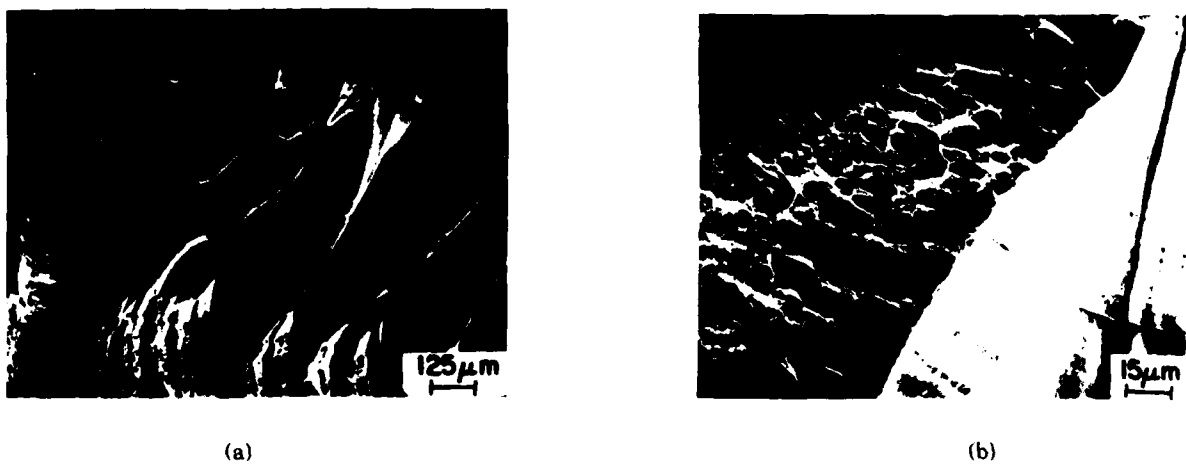


Figure 5 — a) Ductile and shear zones of fracture in a shear localized chip obtained from a medium carbon low alloy steel machined at a cutting speed of 2000 m/min., and b) Voids around inclusions in the ductile rupture zone.

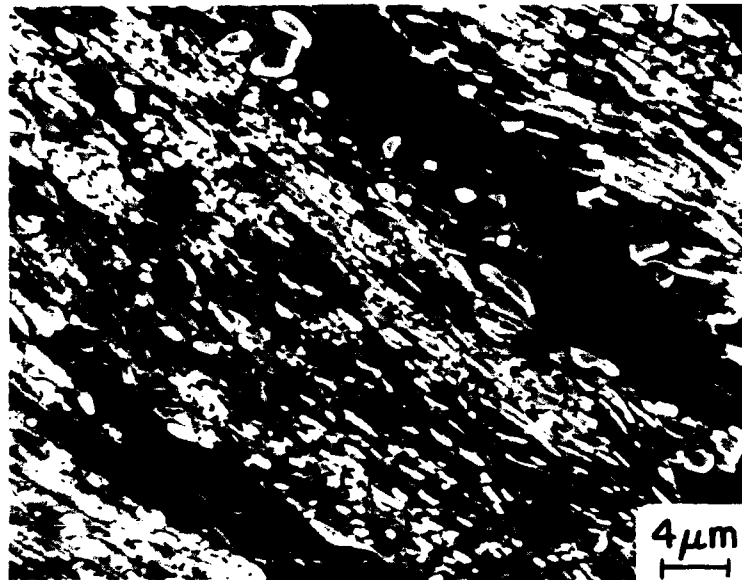


Figure 6 — SEM micrograph of the primary shear zone in a 'quick-stop' chip obtained from a partially spheroidized AISI 1045 grade steel at a cutting speed of 60 m/min.



Figure 7 — A fully segmented chip showing well-deformed crack initiation and crack propagation regions obtained from a 42 CrMoS4V steel at a cutting speed of 2000 m/min.



Figure 8 — The fracture surface of a fully segmented chip obtained from a 42 CrMoS4V steel at a cutting speed of 2000 m/min., showing that the coalescence of voids is complete on the crack initiation region.



(a)



(b)

Figure 9 — a) an SEM micrograph showing damage in the fracture surface of a partially segmented chip obtained from a 42 CrMoS4V steel at a cutting speed of 200 m/min., and b) an SEM micrograph showing extensive void growth (damage) associated with MnS inclusions in the chip in a) above.

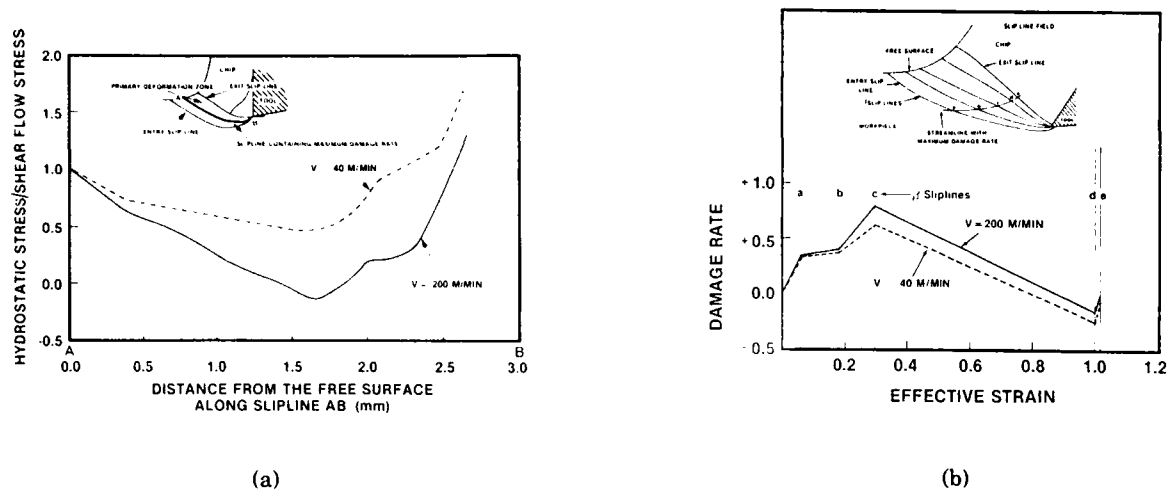


Figure 10 — a) The hydrostatic shear/flow stress ( $p/k$ ) ratio as a function of the distance from the free surface of the chip (see insert); and b) Damage rate along a streamline containing the maximum damage rate as a function of effective strain.

# ANALYSIS OF INCLUSIONS IN CAST Co-Cr-Mo ALLOY USED FOR SURGICAL IMPLANTS

L. Z. Zhuang, E. W. Langer

Department of Metallurgy  
The Technical University of Denmark  
DK-2800, Denmark

## Abstract

Cast Co-Cr-Mo alloys are widely used as surgical implant materials. The proper development of this alloy system for such applications requires a sound understanding of the microstructural characteristics and the structure-property relationships in this material. In the work described here, non-metallic inclusions in the cast Co-Cr-Mo alloys are examined considering their significant effects on the performance of this surgical implant material. Optical microscopy, scanning electron microscopy and transmission electron microscopy have been used to examine the morphologies and distributions of inclusions. EDS (energy dispersive spectroscopy) technique has been used to determine the composition and structural formula of the inclusions. Electron microprobe analysis and X-ray radiation mapping techniques also have been used to study the element distributions in the non-metallic inclusions. The influence of inclusions on mechanical properties of alloys is discussed.

A PROSTHETIC MATERIAL must function mechanically without permanent deformation or failure while leaving the biological tissues completely unaltered. Therefore, the materials used for surgical implants must be resistant to corrosion by physiological fluids; strong enough to withstand the normal physiological forces without fracture, either in the short term associated with overloading or in the longer term due to fatigue often imposed on prosthetic appliances; resistant enough to stress corrosion to withstand high stresses while in the corrosive environment and they must have a high degree of biocompatibility to ensure correct healing after insertion (1-4).

Cast Co-Cr-Mo alloys have a long history of successful use as surgical implants(5). However,

a significant number of such implants have been found to fracture during implantation, excision or while in use (6). Such failures, when they occur, are important to all concerned. Consequently, premature failures in service of surgical implants inside the human body should be avoided by all means. Investigations concerning the causes of failures of metallic orthopedic implants indicated that many implant failures have been attributed primarily to metallurgical or manufacturing faults (7-9).

There are several metallurgical defects in the cast Co-Cr-Mo alloys (10), including large non-metallic inclusions, large inclusion population, abnormally coarse crystals, undissolved master alloy particles, abnormal carbide segregation, interdendritic segregation, shrinkage, gas porosity etc, which are considered as being the main causes of failures in metallic orthopedic implant materials. Non-metallic inclusions in cast Co-Cr-Mo alloys affect both corrosion resistance properties and mechanical properties, especially the fatigue behavior of the alloys because they are regarded to be the crack nucleating sites in fatigue.

## MATERIALS AND EXPERIMENTAL PROCEDURE

Cast Co-Cr-Mo alloys, commercially known as Vitallium or H.S.21, are examined. The chemical composition of the material which is used is (in wt.%): Cr-29.15, Mo-6.50, Fe-0.06, Si-0.05, Mn-0.10, C-0.16, and Co-balance. Specimens are examined optically and by scanning electron microscopy as well as transmission electron microscopy using commercial cast material in the as-cast condition.

Metallographic specimens are prepared by mechanical polishing and using electrolytic etching with etchant: 60 pct  $\text{HNO}_3$  + 40 pct distilled water by volume, 10-25 sec at 5V. Bulk specimens which are prepared in the same way as the metallographic specimens are used for EDS analysis and electron microprobe analysis as



well as X-ray radiation mapping experiments. In order to determine the chemical composition and structural formula for inclusions without matrix interference, carbon replica specimens with extracted inclusion particles are prepared for EDS analysis. The preparation of replica specimens is carried out as follows: After the original specimens have been electrolytically etched, a thin film of carbon is vacuum deposited on the specimen surface. Scored grids of carbon film are removed from the specimen surface by electrolytic etching with etchant: 60 pct  $\text{HNO}_3$  + 40 pct distilled water by volume, about 2 min at 8-10V. Transmission electron microscopy is performed using disc-shaped specimens 3 mm in diameter. Final thinning is executed using an electrolyte of 10 pct perchloric acid + 20 pct ethanol + 70 pct butanol by volume. Electrolyte temperature has been maintained between  $-20^\circ\text{C}$  and  $-30^\circ\text{C}$  throughout thinning and operation potential is 30V. The specimens are examined in Philips EM301 transmission electron microscope operating at 100 KV.

## RESULTS AND DISCUSSION

### MORPHOLOGY AND DISTRIBUTION OF INCLUSIONS:

It is reported (8) that the inclusion content of cast Co-Cr-Mo alloys is low compared to the inclusion content of most stainless steels which are also used for implants and referring to ASTM standards (11) which gives the recommended maximum for metals and alloys. However, the results of this investigation proved that most of the non-metallic inclusions in cast Co-Cr-Mo alloys are present in unfavorable ways for the material performance. According to the chemical composition analysis results of inclusion particles which we will discuss later, we found that there are two kinds of oxides in cast Co-



**Fig. 1** Large oxide inclusion population in cast Co-Cr-Mo alloy. Escolaite oxide (E),  $100\text{Cr}_2\text{O}_3$ . Unetched.

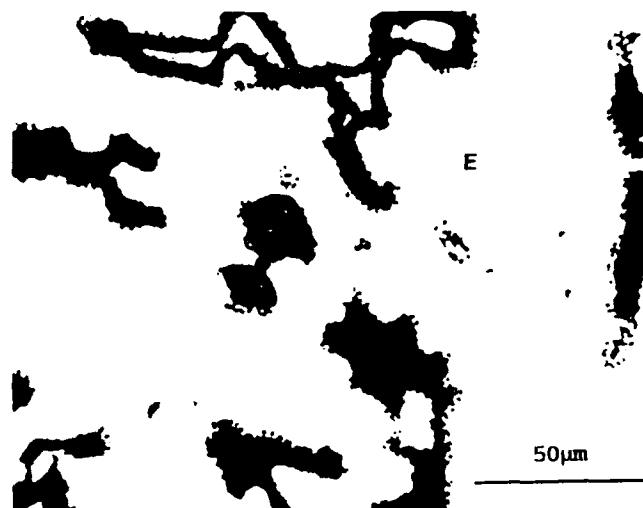


**Fig. 2** Large oxide inclusion population formed by oxide films with casting shrinkage porosities in cast Co-Cr-Mo alloy. Escolaite oxide (E),  $100\text{Cr}_2\text{O}_3$ . Unetched.

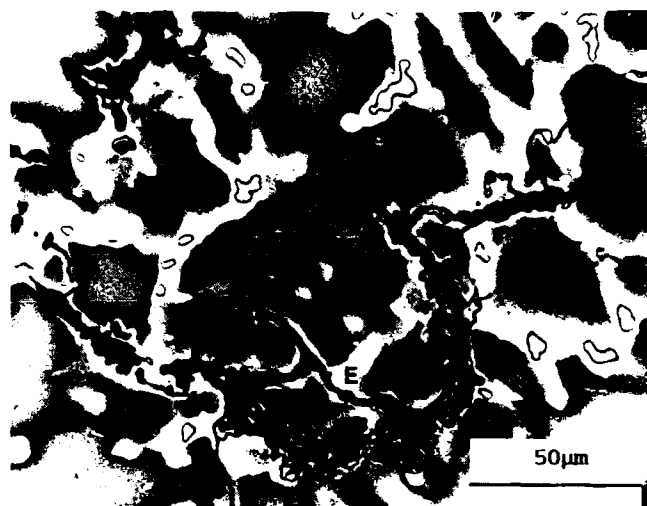


**Fig. 3** Continuous grain boundary oxide inclusion precipitation in cast Co-Cr-Mo alloy. Escolaite oxide (E),  $100\text{Cr}_2\text{O}_3$ . Electrolytically etched with 60 pct  $\text{HNO}_3$  + 40 pct  $\text{H}_2\text{O}$ .

Cr-Mo alloys. They are classified to: escolaite oxide ( $\text{Cr}_2\text{O}_3$ ) and Cr-galaxite oxide ( $\text{MnO} \cdot \text{Cr}_2\text{O}_3$ ) respectively (12). These two oxides are different, both in morphology and distribution. The majority of oxide particles in the cast alloys are escolaite oxide.

Escolaite oxide ( $\text{Cr}_2\text{O}_3$  phase), which has a hexagonal structure, is common in chromium steel inclusions. Sometimes separated oxide particles of this type oxide in our specimens show the appearance with plane surfaces, hexagonal or regular in section, similar to Cr-galaxite

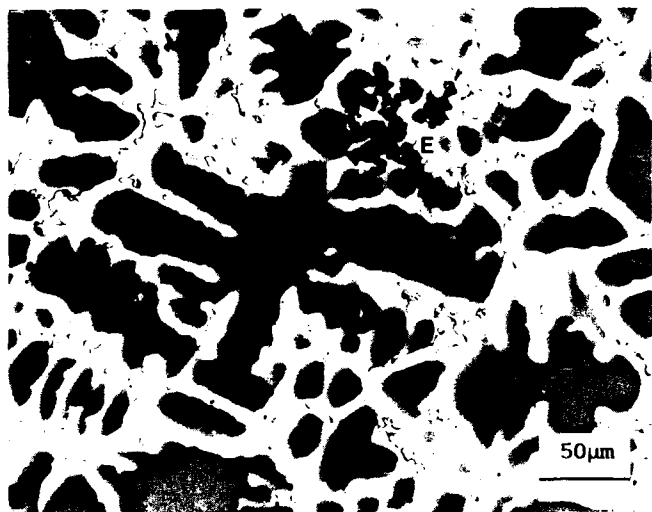


**Fig. 4** Large oxide inclusions precipitated near the grain boundary in cast Co-Cr-Mo alloy. Escolaite oxide (E),  $100\text{Cr}_2\text{O}_3$ . Electrolytically etched with 60 pct  $\text{HNO}_3$  + 40 pct  $\text{H}_2\text{O}$ .

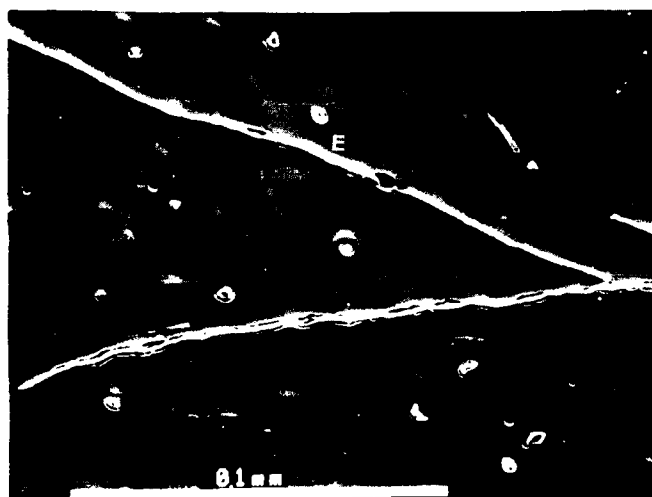


**Fig. 5** Oxide inclusions precipitated in long strings inside a crystal grain in cast Co-Cr-Mo alloy. Escolaite oxide (E),  $100\text{Cr}_2\text{O}_3$ . Electrolytically etched with 60 pct  $\text{HNO}_3$  + 40 pct  $\text{H}_2\text{O}$ .

oxide. This oxide morphology indicates that oxide particles have a higher melting point than matrix. The typical morphologies and distributions of escolait oxide in cast Co-Cr-Mo alloys are shown in Fig.1 to Fig.5. Large inclusion population, as shown in Fig.1, is caused by abnormal oxide segregation in certain severe oxide-rich areas. Fig.2 shows another kind of large inclusion population which is produced by large oxides combined with casting shrinkage porosities. In general, these oxides are oxide films with a certain thickness around the shrinkage porosities. Inhomogeneous distribution of

oxides leads to the formation of continuous grain boundary oxide inclusion precipitations and large oxide inclusions near grain boundaries, as shown in Fig.3 and Fig.4 respectively. Long oxide strings are also observed, both inside a crystal grain as in Fig.5 and along grain boundaries.

Usually, chromium galaxite oxide ( $\text{MnO} \cdot \text{Cr}_2\text{O}_3$  phase) can be easily identified in microsec-

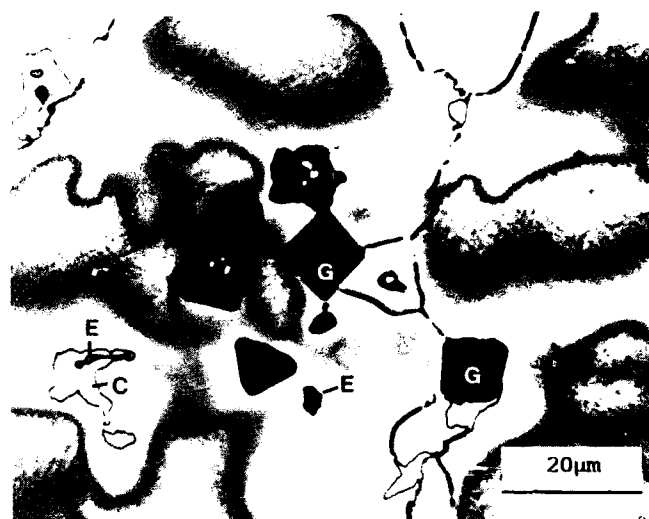


**Fig. 6** Typical Cr-galaxite oxide precipitations in cast Co-Cr-Mo alloy. Cr-galaxite oxide (G),  $\text{MnO} \cdot \text{Cr}_2\text{O}_3$  with 12-15MnO,  $\sim 85\text{Cr}_2\text{O}_3$ . Escolaite oxide (E),  $100\text{Cr}_2\text{O}_3$  and Carbide (C),  $\text{M}_{23}\text{C}_6$ . Electrolytically etched with 60 pct  $\text{HNO}_3$  + 40 pct  $\text{H}_2\text{O}$ .

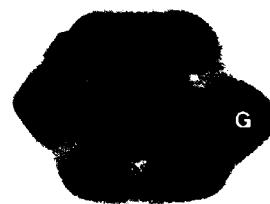


**Fig.7** Hexagon-shape sectioned Cr-galaxite oxide particle with regular distributed spots (eutectic oxide structure) in cast Co-Cr-Mo alloy. Cr-galaxite oxide (G),  $\text{MnO} \cdot \text{Cr}_2\text{O}_3$  with 12-15MnO,  $\sim 85\text{Cr}_2\text{O}_3$ . Electrolytically etched with 60 pct  $\text{HNO}_3$  + 40 pct  $\text{H}_2\text{O}$ .

tions. Crystals of Cr-galaxite oxide are often idiomorphic with regular sections. This oxide phase is also a common phase in chromium steel inclusions. Cr-galaxite oxide has a cubic structure and is of the spinel type (12). This oxide inclusion normally occurs as separated particles in cast Co-Cr-Mo alloys. Large oxide inclusion population of this kind of oxide is

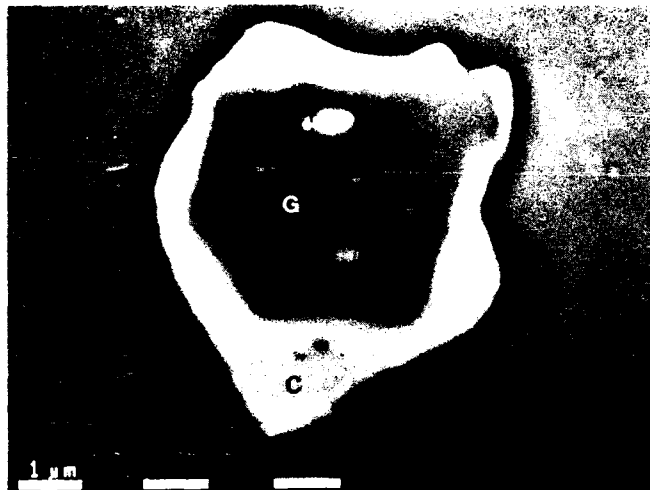


**Fig. 8** Multiphase oxide/carbide particle precipitated in cast Co-Cr-Mo alloy. Cr-galaxite oxide (G),  $\text{MnO} \cdot \text{Cr}_2\text{O}_3$  with 12-15MnO,  $\sim 85\text{Cr}_2\text{O}_3$ . Carbide (C),  $\text{M}_{23}\text{C}_6$ . Electrolytically etched with 60 pct  $\text{HNO}_3$  + 40 pct  $\text{H}_2\text{O}$ .

seldom observed. Fig.6 to Fig.9 show the typical morphologies of chromium galaxite oxides in the cast Co-Cr-Mo alloys. They show sharp regular polygon microsections and many of them have a number of white spots, which are considered as the product of eutectic oxide structure, on the section surfaces. Fig.6 gives a small group of Cr-galaxite oxide particles precipitated at or near a grain boundary. There are also a few small esclaite oxide particles and some of them act as nuclei for carbide precipitations, so that large carbide particles are favored to form at these places. In Fig.7, there is an isolated chromium galaxite oxide which has a hexagonal regular section with six white spots which are also distributed regularly. Multiphase precipitation of oxide and carbide is shown in Fig.8. Fig.9 is a transmission electron microscopy photograph showing a long plate-shaped oxide and a very small hexagonal oxide particle.

#### COMPOSITION AND CHEMICAL FORMULA ANALYSIS:

Both bulk specimens and carbon replica specimens with extracted oxide inclusion particles are used for quantitative composition analysis of two different kinds of oxide phases in the cast Co-Cr-Mo alloy by EDS and SEM. The results are listed in Table 1 and Table 2 respectively. Table 1 shows the analysis of bulk specimens corresponding to Fig.10 for esclaite oxide and Fig.11 for chromium galaxite oxide. Comparing the analysis results both from bulk specimens and carbon replica specimens with extracted oxide particles, it is obvious that the results obtained by using the replica specimens are much more accurate and reliable because they are free

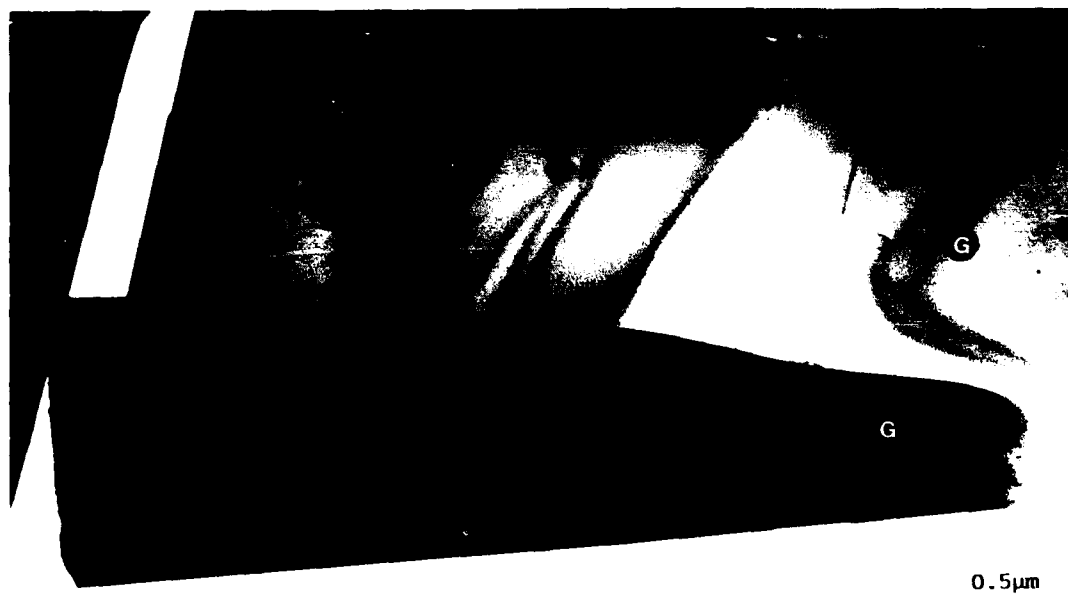


**Fig. 9** TEM micrograph showing a long plate-shaped and a quite small hexagonal shaped Cr-galaxite oxide particles in cast Co-Cr-Mo alloy. Cr-galaxite oxide (G),  $\text{MnO} \cdot \text{Cr}_2\text{O}_3$  with 12-15MnO,  $\sim 85\text{Cr}_2\text{O}_3$ .  $\bar{Z} \parallel [1\bar{1}0]_{\text{fcc}}$ .

Table 1 EDS Analysis of Oxide Inclusions in Bulk Specimens

Escolaite Oxide, Cr <sub>2</sub> O <sub>3</sub>			Cr-galaxite Oxide, MnO•Cr <sub>2</sub> O <sub>3</sub>		
	Wt%	At%		Wt%	At%
Mo	2.57	1.42	Mo	1.66	0.92
Cr	92.32	93.99	Cr	82.73	84.20
Co	5.11	4.59	Mn	13.24	12.75
			Co	2.37	2.13
Chemical Formula			Chemical Formula		
2.67MoO <sub>3</sub> •4.47CoO•92.86Cr <sub>2</sub> O <sub>3</sub>			1.72MoO <sub>3</sub> •2.10CoO•12.02MnO•84.16Cr <sub>2</sub> O <sub>3</sub>		

Table 2 EDS Analysis of Oxide Inclusions with Replica Specimens

Escolaite Oxide, Cr <sub>2</sub> O <sub>3</sub>			Cr-galaxite Oxide, MnO•Cr <sub>2</sub> O <sub>3</sub>		
	Wt%	At%		Wt%	At%
Mo	0.04	0.02	Mo	0.12	0.07
Cr	99.79	99.83	Cr	84.36	85.12
Co	0.17	0.15	Mn	15.35	14.66
			Co	0.17	0.15
Chemical Formula			Chemical Formula		
0.05MoO <sub>3</sub> •0.15CoO•99.80Cr <sub>2</sub> O <sub>3</sub>			0.13MoO <sub>3</sub> •0.15CoO•13.87MnO•85.85Cr <sub>2</sub> O <sub>3</sub>		

Table 3 Calculated Composition of MnO•Cr<sub>2</sub>O<sub>3</sub> from Table 2

	Wt%	At%	Chemical Formula
Cr	84.61	85.31	13.84MnO•86.16Cr <sub>2</sub> O <sub>3</sub>
Mn	15.39	14.69	

from the effects caused by the matrix. If we neglect the presence of trace elements: Mo and Co, in these oxide phases, the escolaite oxide should be 100Cr<sub>2</sub>O<sub>3</sub>, and the corrected result from Table 2 for Cr-galaxite oxide is shown in Table 3. In this chromium galaxite double oxide, MnO content is lower than the ideal formula for the Cr-galaxite phase, which is 32MnO•68Cr<sub>2</sub>O<sub>3</sub> (12). The range of MnO content extends, according to the present investigation, from about 12MnO•88Cr<sub>2</sub>O<sub>3</sub> to 15MnO•85Cr<sub>2</sub>O<sub>3</sub>. The presence of two different kinds of oxide phases is also confirmed by the X-ray radiation mapping from inclusions using electron microprobe system in SEM, as shown in Fig.10 and Fig.11. The results are consistent with the EDS analyses.

It is discussed in the literature (12) that the Cr<sub>2</sub>O<sub>3</sub> oxide inclusions in high chromium steels generally are transformation products from chromite. They did not dissolve or join the slag in the steel when the chromite was dissolved. They also may act as nuclei for indigenous precipitation of MnO, so Cr-galaxite oxides MnO•Cr<sub>2</sub>O<sub>3</sub> are formed during steel-making.

#### EFFECTS OF INCLUSION ON MATERIAL PROPERTIES:

A considerable number of investigations concerning the failures of implant materials has confirmed (10, 13-15) that most of the implant failures may be classified as fatigue fractures. But in many investigations, such failures have been simply reported as due to "fatigue" or other general failure mechanisms, and the underlying causes for the initiation of these mechanisms, starting with the original injury or condition, is seldom examined and discussed.

Apart from other factors, oxide inclusions play an important role in the fatigue failures of the cast Co-Cr-Mo alloys. There have been some publications concerning the effects of hard inclusions on the mechanical properties of materials (12, 16-22). A direct correlation between the occurrence of large and hard inclusions and fatigue life of alloys has been proved since the inclusions act as stress-raisers in the materials. Micromechanics of fatigue crack initiation at inclusions concerning the physical events which occur at the oxide inclusions during fatigue crack nucleation has been studied

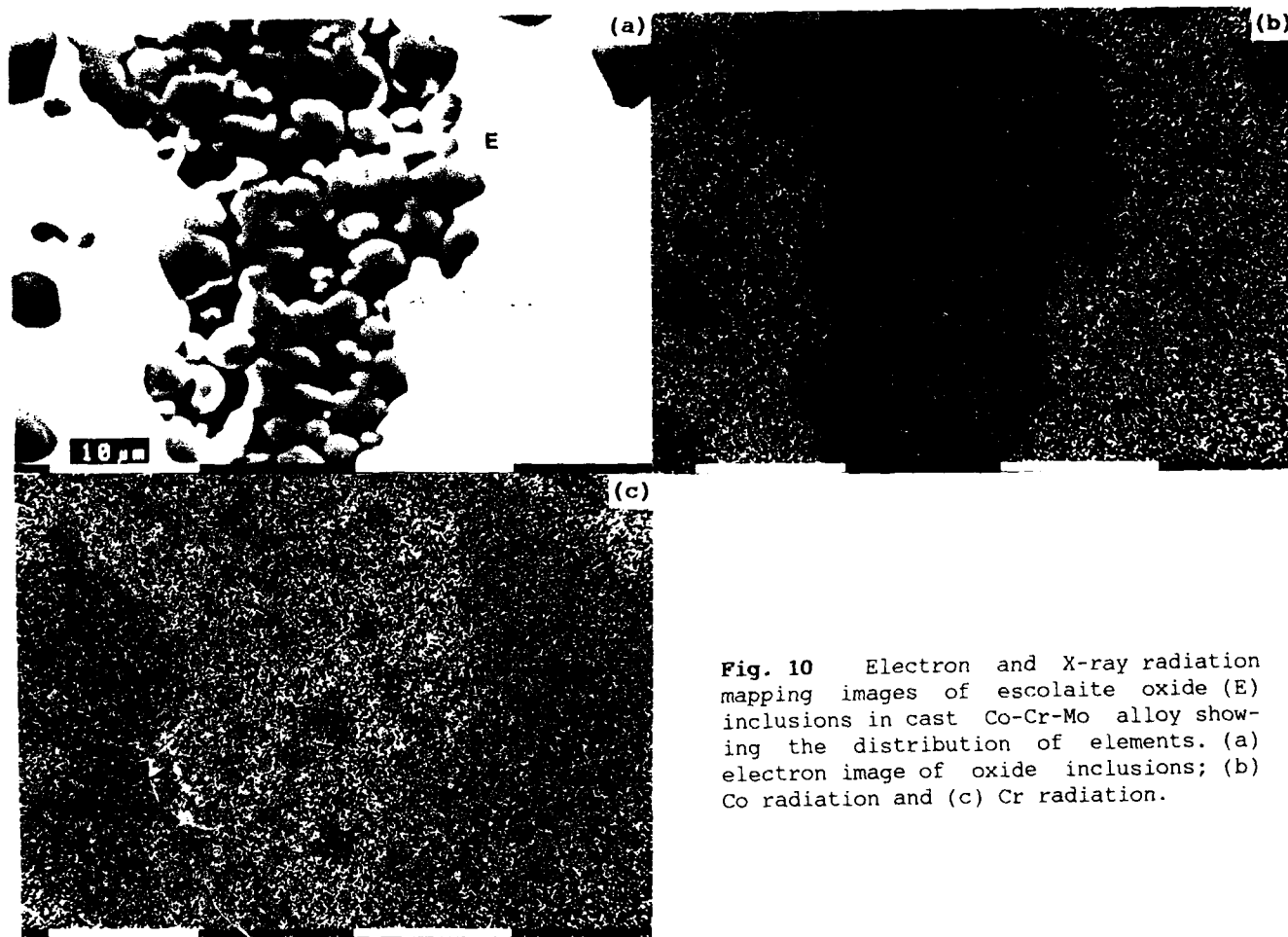


**Fig. 10** Electron and X-ray radiation mapping images of esclaite oxide (E) inclusions in cast Co-Cr-Mo alloy showing the distribution of elements. (a) electron image of oxide inclusions; (b) Co radiation and (c) Cr radiation.

by Lankford et al (23-24). The void formation between the inclusion particle and the matrix is caused by the generation of stresses at the interface of inclusion/matrix. These stresses are generated as a result of a shape misfit between a homogeneously deformed matrix element and the hard inclusion particle. Therefore, hard inclusions can be the nuclei for the formation of voids during the deformation processes of materials. These voids normally show sharp edges which have the same effects on the materials as cracks. Thus, for fatigue fractures, the nucleation stage of the fracture crack is already passed and the crack propagation is the limiting stage for the fatigue life of the materials.

According to the study of Sundström (25), the deformation ratio between inclusion and matrix (the deformation index) could be related to the flow stress ratio between two phases. As the hardness of a phase is roughly proportional to its flow stress, to a first approximation, the relationship established by Sundström should also hold between the deformation index and the hardness ratio. It seems reasonable to assume that inclusions which have a lower deformability may induce fatigue cracks in the alloys. This depends on their inability to transduce stresses existing at the interface of inclusion/matrix by

appropriate deformation processes so that critical peak stresses may be reached around these inclusion particles during the working conditions. In the cast Co-Cr-Mo alloys, the Vickers hardness of matrix is about 320, the hardness of chromium galaxite oxide is ranged 1500-1700, 4-5 times higher than that of matrix, and the hardness of esclaite oxide is usually higher than the hardness of Cr-galaxite oxide (12). Therefore, according to the theory of the deformation index, the influence of esclaite oxide in the cast Co-Cr-Mo alloys on the mechanical properties should be much more severe.

Even though most of the oxide inclusions are small particles, if their separating distances are small, they would constitute a severe defect. It has long been recognized that fatigue fracture is very strongly influenced by large inclusion population, as shown in Fig.1 and Fig.10. Essentially when many small cracks are closely spaced, the matrix ligaments between are weakened, and the cracks rather rapidly link up so that large cracks are generated. The morphologies and distributions of oxide inclusions as shown in Fig.2 to Fig.5 are also presumably harmful to the fatigue properties of the alloys. Of course, such effect is also dependent upon the magnitude of the applied stresses.

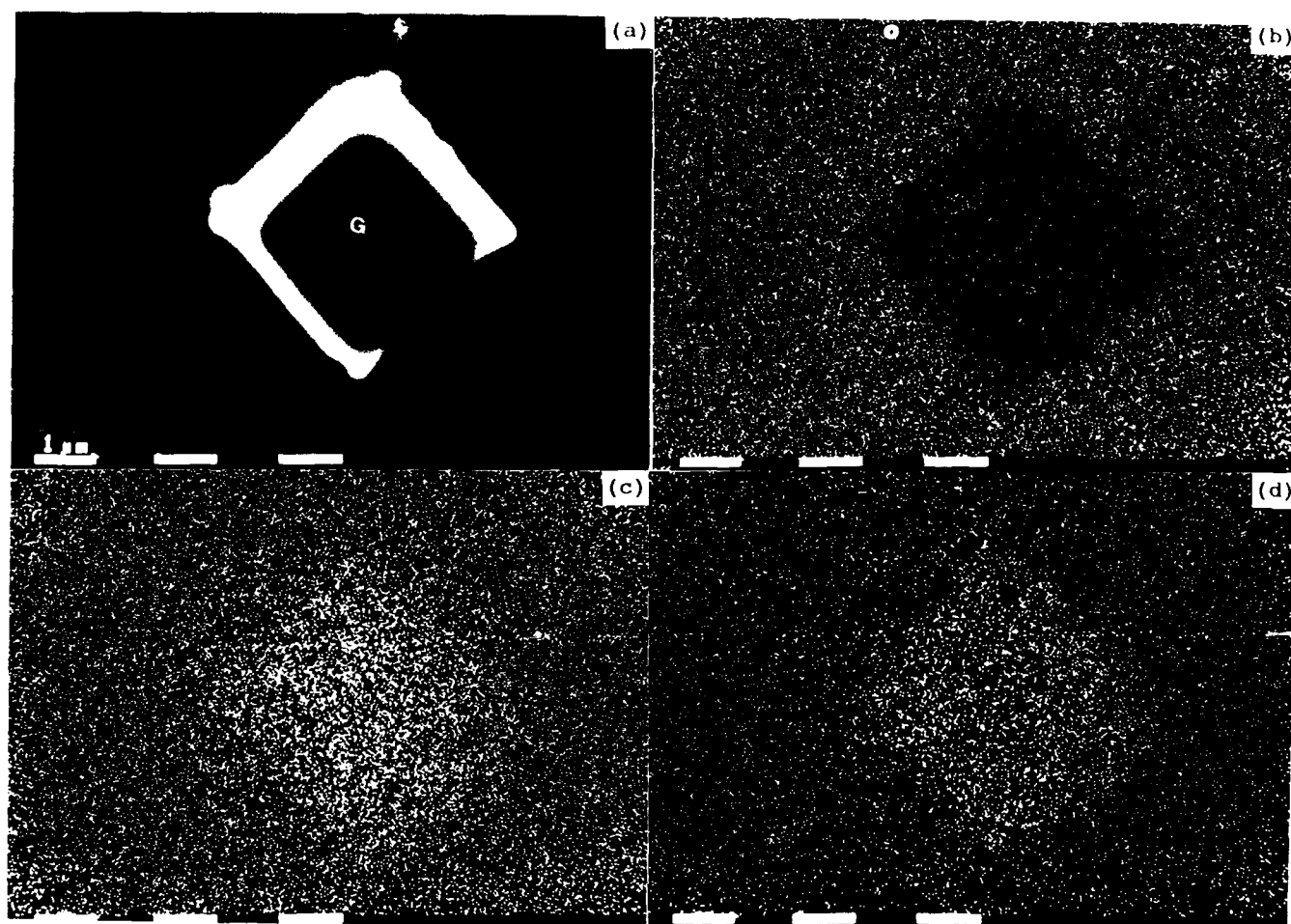


Fig. 11. Electron and X-ray radiation mapping images of chromium galaxite oxide (G) in cast Co-Cr-Mo alloy showing the distribution of elements. (a) electron image of oxide particle; (b) Cr radiation; (c) Mn radiation and (d) Cr radiation.

Additionally, it must be admitted that the presence of inclusions may well cause other effects, apart from the build-up of stresses which may lead to cracking. Oxide particles may act as nuclei for the precipitations of other phases such as carbides, as shown in Fig. 6 and Fig. 7. Many material properties which are dependent on the formation, size and distribution of these important compounds may therefore directly be related to the presence of oxide inclusions. Grain boundary growth is also influenced by the presence of non-metallic inclusions. The influence of oxides on the grain boundary, for example, can be seen in Fig. 8.

It is very important to consider the connection between casting practices and the presence of inclusions to produce better situations. This can be achieved by improving the casting technique. In this way, the various and different casting alloys are examined. Further developments are achieved by the control of the casting process to restrict the formation of inclusions and to control the amount,

morphology and distribution of the inclusion precipitations, for example, using argon or helium protective atmosphere during the casting processes of the alloys.

## CONCLUSIONS

1. It is proved that there are two different kinds of oxide inclusions present in the cast Co-Cr-Mo alloys. One is the escholaite oxide which is a single phase  $100\text{Cr}_2\text{O}_3$  oxide. Another one is the chromium galaxite oxide which is a double oxide phase. The range of MnO content in Cr-galaxite oxide extends from about  $12\text{MnO} \cdot 88\text{Cr}_2\text{O}_3$  to  $15\text{MnO} \cdot 85\text{Cr}_2\text{O}_3$ .
2. The majority of oxide inclusions in the cast Co-Cr-Mo alloys consist of escholaite oxides. Distributions of this kind of oxide inclusions which are generally accepted as being deleterious to fatigue properties, such as large oxide particles, large oxide inclusion population, continuous grain boundary oxide precipitation and long oxide strings are

observed. Chromium galaxite oxide inclusions normally occur as well separated particles in the cast Co-Cr-Mo alloys.

3. Considering the property character of the oxide phase itself, which has high hardness and low deformation index, combined with the oxide amount and their distribution, it is proposed that the influence of the esclaite oxide inclusions in the cast Co-Cr-Mo alloys on the mechanical properties, especially the fatigue behavior should be much more severe than the effects of chromium galaxite oxide inclusions.

#### REFERENCES

1. D. C. Mears, Intern. Met. Rev. Vol. 22, 1977, pp. 119.
2. D. S. Crimmins, J. Metals, Vol. 21, 1969, pp. 38.
3. J. Cohen, J. Mater. Sci. Vol. 1, 1966, pp. 354.
4. W. Bonfield, Metals and Materials, Vol. 3, No. 12, 1987, pp. 712.
5. F. R. Morral, J. Mater. Sci. Vol. 1, 1966, pp. 384.
6. J. T. Scales, J. Bone Joint Surg. Vol. 53B, 1972, pp. 344.
7. J. R. Cahoon and H. W. Paxton, J. Biomed. Mater. Res. Vol. 2, 1968, pp. 1.
8. J. R. Cahoon and H. W. Paxton, J. Biomed. Mater. Res. Vol. 4, 1970, pp. 223.
9. J. O. Galante, W. Rostoker and V. M. Doyle, J. Bone Joint Surg. Vol. 57A, 1975, pp. 230.
10. W. Rostoker, E. Y. S. Chao and J. O. Galante, J. Biomed. Mater. Res. Vol. 12, 1978, pp. 635.
11. Annual Book of ASTM Standards, Vol. 03.01, E45-85, Practice for Determining the Inclusion Content of Steel, 1987, pp. 318.
12. R. Kiessling and N. Lange, Non-metallic Inclusions in Steel, 2nd Ed. London, 1978.
13. H. L. Miller, W. Rostoker and J. O. Galante, J. Biomed. Mater. Res. Vol. 10, 1976, pp. 399.
14. C. M. Rimnac, T. M. Wright, D. L. Bartel and A. H. Burstein, ASTM STP 918, 1986, pp. 377.
15. O. E. M. Pohler, Metals Handbook, 9th Ed. Vol. 11, Failure Analysis and Prevention. 1986, pp. 670.
16. B. I. Kevebring, The Behavior of Nonmetallic Inclusions in Steel. Dissertation, 1975, The Royal Inst. of Tech., Sweden.
17. S. Rudnik, J. Iron & Steel Inst. Vol. 204, 1966, pp. 374.
18. T. J. Baker and J. A. Charles, J. Iron & Steel Inst. Vol. 210, 1972, pp. 680.
19. E. Rozovsky, W. C. Hahn and B. Avitzur, Metall. Trans. Vol. 4, 1973, pp. 927.
20. M. T. Shehata, G. J. Bieffer and J. D. Boyd, Corrosion, Failure Analysis, and Metallography (Proc. Conf.), Philadelphia, Pennsylvania, USA, 15-18 July, 1984, Eds. S. A. Shiels et al, ASM, Metals Park, Ohio, USA, 1986, pp. 263.
21. R. B. Scarlin, C. Berger, K. H. Mayer and W. Oberparleiter, Life Assessment of Dynamically Loaded Materials and Structures (Proc. Conf.), Vol. 1, Lisbon, Portugal, 17-21 Sept. 1984, Ed. L. O. Faria, Engineering Materials Advisory Services Ltd, UK, 1985, pp. 99.
22. J. Lankford, Intern. Met. Rev. Vol. 22, 1977, pp. 221.
23. J. Lankford and F. N. Kusenberger, Metall. Trans. Vol. 4, 1973, pp. 553.
24. J. Lankford, Eng. Fract. Mech. Vol. 9, 1977, pp. 617.
25. B. Sundström, J. Comp. Mater. Vol. 5, 1971, pp. 277.

# A REVIEW OF ADVANCES IN NONINVASIVE METHODS FOR DETECTION AND CHARACTERIZATION OF INCLUSIONS

L. J. House, R. Rungta

Battelle Columbus Division  
Columbus, Ohio 43201-2693 USA

## ABSTRACT

Advances in noninvasive technologies for detecting and characterizing inclusions are enabling a more quantitative nondestructive evaluation of the influence of inclusions on the behavior of materials. These advances are two-fold: (1) development of analytical models providing quantitative descriptions of wave and field interactions with inclusions and (2) development of advanced sensors and instrumentation that improve measurement sensitivity and accommodate a more diverse range of applications. The advances in these technologies provide an opportunity to apply new and innovative methods of materials characterization to a wider range of research and practical inspection problems. In this paper an overview of some of the progress associated with enhanced detection and quantitative characterization of inclusions is presented. Noninvasive technologies based on interactions of elastodynamic and electromagnetic fields with inclusions are the primary focus of this review.

INCLUSIONS FORM IN MATERIALS primarily by reactions in the liquid metal or by precipitation from the metal during cooling and solidification. They also form by mechanical entrapment of slags and refractories during processing of the liquid metal. The exogenous inclusions can serve as heterogeneous nuclei on which the primary inclusions can precipitate forming a multiphase inclusion. In steels the most common inclusions are the sulphides and oxides [1]; the elemental and phase composition of the inclusions depending upon the processing of the steel. Oxide inclusions in steel can nearly always be referred to as  $AO-SiO_2-B_2O_3$ , where A stands for one or several of the binary metals Mn, Fe<sup>2+</sup>, Mg and Ca; B for one or several of the ternary metals Al, Cr and Fe<sup>3+</sup> [1]. Other metals, such as Sr, Ti, Zr, V and Nb are sometimes also present in oxide inclusions, but they

are almost always found in solid solution in these phases [1]. A similar summary of sulphide inclusions important to steel making is shown in Table 1 [1].

Because of the generally deleterious influence of inclusions on mechanical behavior of materials there is a trend in the industry to control inclusion content. Such control entails among other considerations, elimination of inclusions larger than a critical size for a given application. Traditional metallographic methods for determining the size, shape, and distribution of inclusions in metals are destructive in nature and as such are limited to sampling small volumes of material to define the overall inclusion distribution in the material. When the component being examined is large and prone to process dependent segregation, extrapolation of data from small volumes of the material are likely to exhibit wide margins of error. There is also the possibility that critical size inclusions will be present in the material and not be detected in the sampled volume of material. Noninvasive techniques become very important in such situations because of the opportunity to nondestructively examine large volumes of material providing an excellent alternative to statistical sampling as a quality control tool.

A particularly detrimental influence manifested by the presence of inclusions is the introduction of localized stresses in the material. Localized stresses can occur in the neighborhood or proximity of inclusions. Stress localization occurs around inclusions because of differences in the thermal coefficient and the elastic coefficients between the inclusion and the matrix [2-5]. When the steel is cooled after heat treatment, the difference in the thermal coefficient between the inclusion and the matrix can generate tessellated stresses given by [2]:

$$\sigma_T = \phi(\alpha_2 - \alpha_1) T \quad (1)$$

where  $\phi$  is a function of elastic moduli of the inclusion and matrix, and of inclusion shape,



Table 1. Summary of Important Sulphide Inclusions in Steels [From (1)]

<u>Sulphide System</u>	<u>Group in per Table</u>	<u>Phases Encountered in Steelmaking (ex.)</u>
Those Most Important in Steelmaking		
Fe-S	VIII	FeS
Mn-S	VII	MnS
Mn-Me-S	VII	(Mn, Me)S, MnS Me <sub>2</sub> S <sub>3</sub>
With Transition Metals		
La-elements-S	III	LaS, CeS
Ti,Zr,Hf-S	IV	TiS
V,Nb,Ta-S	V	VS
Cr,Mo,W-S	VI	CrS,MoS <sub>2</sub>
Co,Ni-S	VIII	Ni <sub>3</sub> S <sub>2</sub>
With Non-Transition Metals		
Cu,Ag-S	I	Cu <sub>2</sub> S
Mg,Zn,Cd-S	II	MgS
Ca,Sr-S	II	CaS
Al-S	III	Al <sub>2</sub> S <sub>3</sub>
Sn,Pb-S	IV	...
With Non-Metals		
Me-S-X	X=O,C,N	Ti <sub>4</sub> C <sub>2</sub> S <sub>2</sub> , Ce <sub>2</sub> O <sub>2</sub> S
Me-Se	...	MnSe
Me-Te	...	MnTe

size, and distribution;  $\alpha_2$  and  $\alpha_1$  are the coefficients of thermal expansion of the matrix and inclusion respectively, and  $T$  is the temperature change. Brooksbank and Andrews [4] determined the mean linear coefficient of thermal expansion of some inclusions (Figure 1) and predicted that inclusions having the lowest coefficient of thermal expansion as compared to iron would be the most damaging to mechanical properties of steels. Residual tensile stresses develop around such inclusions. On this basis the worst inclusions in Figure 1 would be cordierite ( $2\text{MnO} \cdot 2\text{Al}_2\text{O}_3 \cdot 5\text{SiO}_2$ ), the various calcium aluminates and  $\text{Al}_2\text{O}_3$ . Iron oxides and CaS would be neutral because of having about the same coefficient of thermal expansion as iron. MnS would be beneficial because of its larger coefficient of thermal expansion. During cooling from an elevated temperature, compressive residual stresses will be generated in the surrounding iron matrix, until voids form [5]. The tessellated stresses that develop have an influence zone that depends on their shape and size. For spherical inclusions, for example, the stresses in the matrix varies inversely as the cube of the distance from the inclusion/matrix boundary [5].

In addition to tessellated stress, the inclusion also magnifies the far field applied stress because of the difference in the moduli between the inclusion and matrix. The tangential stress for an inclusion in a matrix with a far field applied stress  $\sigma_0$  is given by:

$$\sigma_1 = \beta \sigma_0 \quad (2)$$

where  $\beta$  is the stress concentration factor varying with  $E_i/E_m$  [5]. The magnified local stress field is not symmetrical and varies with inclusion size, shape, orientation, and location relative to the surface.

From the considerations presented above then, the properties and characteristics of inclusions that would be useful to determine noninvasively are size, shape, orientation, location, and mechanical properties such as elastic moduli and strength related properties of the inclusion. Also of benefit would be an ability to measure the changes in the macro-mechanical properties affected by the inclusions and to noninvasively map residual stresses and stress distributions in the host material generated by the inclusions.

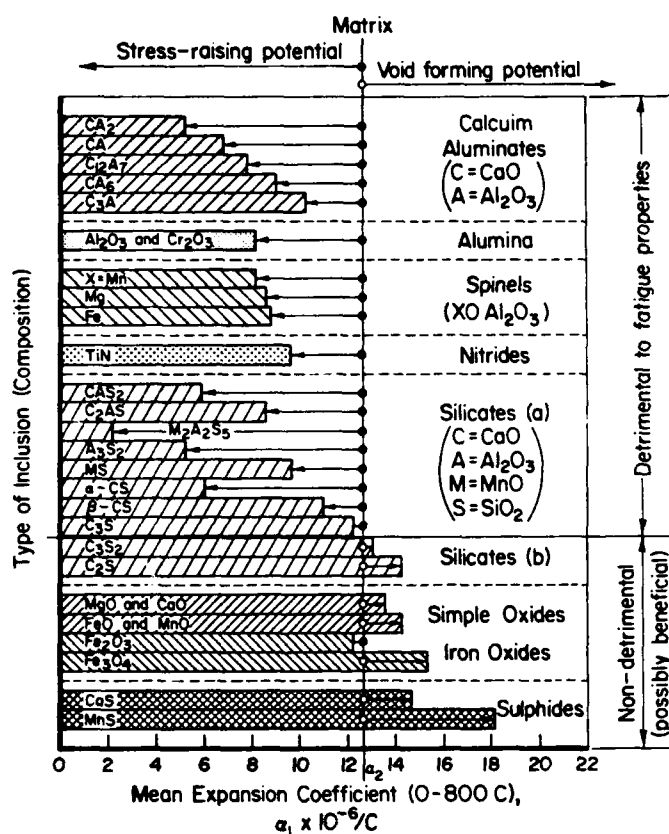


Figure 1. Stress-raising properties of inclusions in 1% C-Cr-bearing steel (from (4))

In this review inclusion characteristics are divided into four general categories. These are: (1) macroscopic, (2) proximate, (3) boundary related, and (4) intrinsic properties of the inclusion. Specific characteristics or properties associated with each of these categories are:

- Macroscopic
  - Detectability
  - Number or volume fraction
  - Size distribution
  - Spatial distribution
  - Macro-mechanical properties
- Proximate
  - Stress/strain field
- Boundary Related
  - Size and shape
  - Bonding
- Intrinsic
  - Elemental and phase composition
  - Mechanical properties
    - Strength related
    - Elastic moduli
    - Fracture toughness
    - Ductility
  - Physical properties
    - Mass density
    - Thermal expansion coefficient

Although much of the progress in noninvasive technologies has been associated with detecting and characterizing other types of defects besides inclusions, many of the advances are relevant to the problem of characterizing a number of the properties of inclusions listed above. Before discussing these advances the fundamental elements of noninvasive measurement systems are described in the next section.

## BACKGROUND

Noninvasive methods for detection and characterization of inclusions rely on waves and fields of various energy forms interacting with or propagating through a material and being absorbed, scattered or in some way, directly or indirectly, perturbed by any of a number of physical mechanisms. The types of waves and fields employed in noninvasive characterization of inclusions are usually either electromagnetic or elastodynamic.

The fundamental elements of a noninvasive measurement system for detection and characterization of inclusions consists of a sensing element, a signal conditioning element, a signal processing element and a data presentation element as shown in Figure 2. The sensing element consists of a source or transmitter to generate the wave field that interacts with the inclusion and a receiver to detect and measure the effects of the interaction between the wave field and inclusion. The signal conditioning element provides for conversion of the sensor output to a suitable form for processing. This may include amplification, analog to digital conversion, filtering, or other modifications to the sensor signal. The signal processing element may improve the inclusion signal-to-noise ratio through coherent or incoherent noise suppression, deconvolve instrumentation and host material influences on the signal from the effects of the inclusion on the measured wave field parameter, or provide image enhancement through improvement of lateral resolution using a number of focusing techniques. The data presentation element displays the results of the noninvasive measurement in a format convenient for interpretation, such as an image or map of the spatial distribution of an ensemble of inclusions, the boundaries of an individual inclusion, or the gradient in a material property resulting from the presence of an inclusion.

In the application of noninvasive methods there are two fundamental problems. The first is describing the interaction of the wave field with the inclusion and surrounding material. This is called the forward problem and involves predicting the effect on the wave field for a given set of inclusion and matrix properties (i.e., the inclusion and material properties are given and the scattered wave field is predicted). The second problem is backward propagation of the wave field or inversion of the wave field interactions to determine characteristics of the

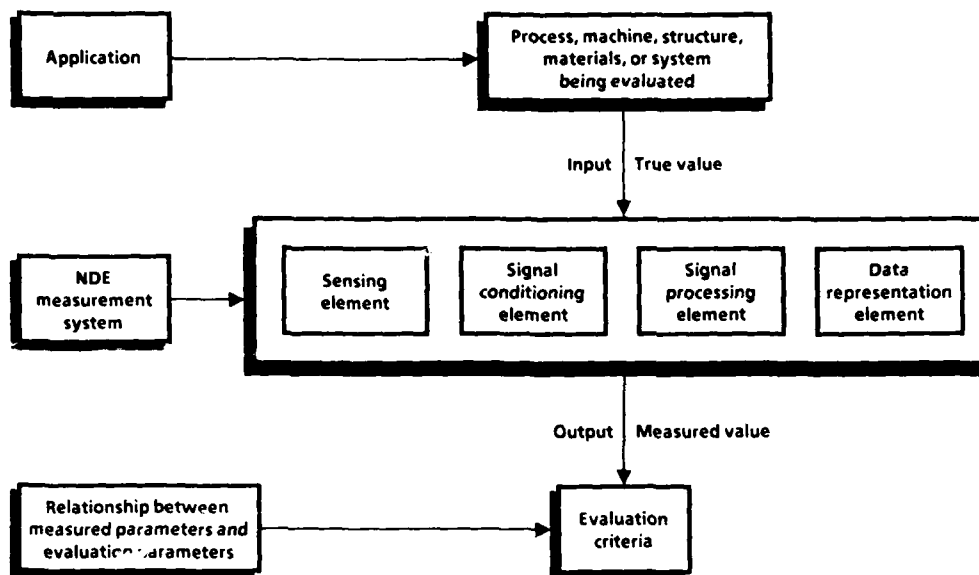


Figure 2. Generic structure of a noninvasive measurement system

inclusion from the measured wave field parameters. This is called the inverse problem and involves predicting the inclusion characteristics from the scattered wave field or other changes in wave field parameters due to interaction with the inclusion. The inverse problem is the more difficult problem of the two but for which the solution also provides a more useful capability.

The solutions of both the forward and inverse problems depend on the size classification of the inclusion. From the perspective of metallurgists, inclusions may be classified as metallic or nonmetallic, brittle or ductile, etc., whereas, from the perspective of noninvasive characterization, inclusions are classified as small or large depending on whether the inclusion's linear dimensions are less or greater than the wavelength of the interrogating field. The size of the inclusion with respect to the wavelength determines in practical terms how well the inclusion can be characterized. The larger the ratio between the inclusion size and the wavelength the less information one can extract concerning the properties and characteristics of the inclusion.

**NONINVASIVE METHODS AS A RESEARCH TOOL** - Noninvasive detection and characterization of inclusions would be useful for providing sufficient a priori information to design experiments to analyze the effect of particular inclusion characteristics on material properties. Samples of a material containing inclusions with

known characteristics would be extremely valuable for developing an empirical and phenomenological understanding of the influence of inclusion on material behavior. This would assist in the derivation of analytical models describing this behavior in terms of the inclusion and host material properties. By being able to non-destructively characterize the inclusion before, during and after thermo-mechanical testing one could considerably enhance the knowledge gained in an experiment to determine the influence of inclusions on material behavior.

**NONINVASIVE METHODS AS AN INSPECTION TOOL** - Understanding the influence of inclusions on material behavior has little utility if methods are not available to detect whether inclusions are present or the methods are incapable of measuring the characteristics of inclusions that affect the performance related properties of the structure or component in which they are found. Thus, noninvasive methods serve an essential function as an inspection tool providing in-process, end-product and in-service evaluation of materials and structures.

With this general background on noninvasive measurement systems and their advantages we proceed with a review of the advances in this technology relevant to characterization of inclusions and their influence on material behavior. Advances in noninvasive methods for characterizing inclusions and their influence on material behavior are discussed under the heading

of each of the categories of inclusion characteristics properties outlined in the Introduction.

### MACROSCOPIC CHARACTERISTICS

**DETECTABILITY** - Detectability is a measure of the ability to determine the presence of inclusions within a volume of a material. Detectability is the single most important aspect of noninvasive characterization since detection is a precursor to measuring the properties of inclusions as well as evaluating the influence of their presence on material behavior.

Detectability is addressed on two levels: (1) detection of a single isolated inclusion, and (2) detection of clusters or fields of inclusions. This distinction is important because it is often possible to detect clusters of inclusions even though the individual inclusions in the cluster population are smaller than the minimum detectable size for a single isolated inclusion. Another important distinction is between the meaning of detectability and sensitivity.

Sensitivity is usually defined as the linear dimension of the smallest defect that can be detected. It is not possible to assign a generally valid value to this dimension because of the complex influence of many metallurgical, physical and instrumentation dependent factors. It has been demonstrated, however, that there is no theoretical limit to sensitivity in ultrasonic tests and that it is possible to detect by means of ultrasonics, flaws in steel which are much smaller than the ultrasonic wavelength [6].

Detectability of a single isolated inclusion depends on its size, shape, orientation, certain physical properties such as mass density, elastic constants, morphological characteristics such as surface roughness, and the microstructural and physical characteristics of the material surrounding the inclusion. In contrast to sensitivity, detectability can decrease with increasing defect or inclusion size. This is usually the case when an elastodynamic wave field obliquely impinges on an inclusion. Detectability is determined by the sensor (transmitter and receiver) directivity, and the inclusion reflectivity and directivity. The detectability of clusters of inclusions, on the other hand usually depends on more macroscopic characteristics such as how the mass density, electrical or elastic properties of the volume of the host material populated by the inclusions are affected.

The effect of size and orientation on detectability using methods based on scattered elastodynamic waves is illustrated in Figure 3, [7].

The surface roughness of the material can also affect the detectability of inclusions. The effect of surface roughness and defect orientation on detectability is illustrated for elastodynamic waves in Figure 4 [8].

Canella, et al. [9], analyzed sensitivity obtainable with conventional immersion ultrasonic testing with 10 MHz and 15 MHz focussed transducers. The samples in this study included:

- manganese sulphide, alumina and alumina silicate inclusions in plate samples of continuous-cast HSLA steel having a ferritic-pearlitic structure with small islands of very brittle martensite, and
- manganese sulfide inclusions in forged medium alloy round bar having a bainitic structure.

The objective of Canella's work was to assess the dependence of scattered wave signals from small inclusions ( $\leq 1\text{mm}$ ) on the size and position of the inclusions relative to the focal area of the transducer. Comparison with metallographic examination of the plate samples showed that detection of alumina and aluminum silicates posed no problems while reasonably large sulphides ( $50\text{--}100\text{ }\mu\text{m}$ ) in both plate and forged samples were often not detected at 10 MHz. Using a 15 MHz, 100 mm focal length transducer the detectability of the sulphide inclusion showed significant improvement over the 10 MHz, 208 mm focal length transducer (i.e. detected the small sulphide inclusions). However because the depth of field (axial distance over which the wave field remains focused) of the 15 MHz transducer is less than that for the 10 MHz transducer the amplitude of the flaw signal falls off much more rapidly with distance from the inclusion. This illustrates the importance of transducer design for a particular application and the need to dynamically focus wave fields to improve inclusion detectability.

Using conventional ultrasonic methods (focused 10 MHz transducer) alumina ( $\text{Al}_2\text{O}_3$ ) and silica ( $\text{SiO}_2$ ) inclusions  $180\text{ }\mu\text{m}$  and larger have been detected in Ti-6Al-4V powder compacts [79]. However inclusions as small as  $50\text{ }\mu\text{m}$  effect the fatigue performance of this titanium alloy. Thus the need exists to improve the detectability of inclusions.

Progress in improving the detectability of inclusions includes:

- development of signal processing methods for target signal enhancement,
- improved axial and lateral resolution in imaging systems through signal processing and transducer lens and array designs,
- development of sensors with enhanced sensitivity and sensors that can accommodate a wider range of environments such as hot steel,
- development of automated systems providing rapid, large volume coverage.

**Signal Processing** - If the inclusion is large compared to grain size then coherent noise suppression techniques can be used to improve the target signal to noise ratio. Spatially coherent noise can be suppressed by cross-correlation,

### WÜSTENBERG DIAGRAM

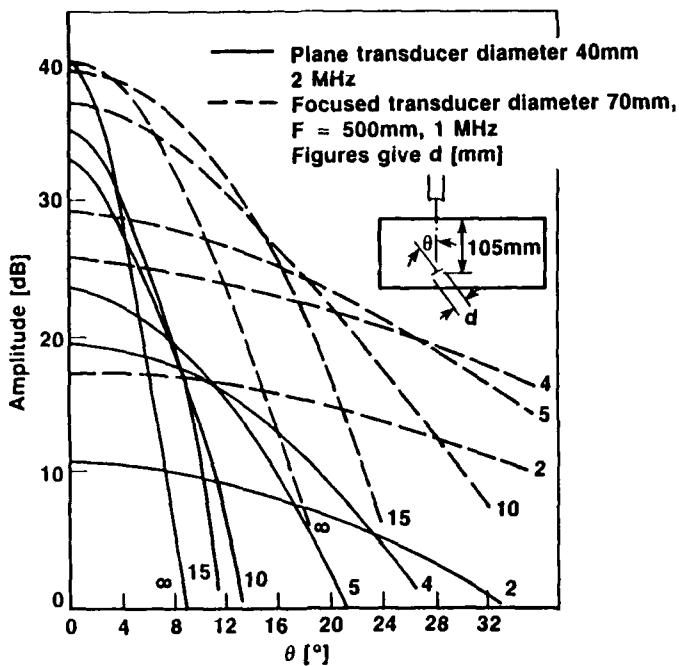


Figure 3. Wüstenberg diagram illustrating the effect of size and orientation on detectability (from (7))

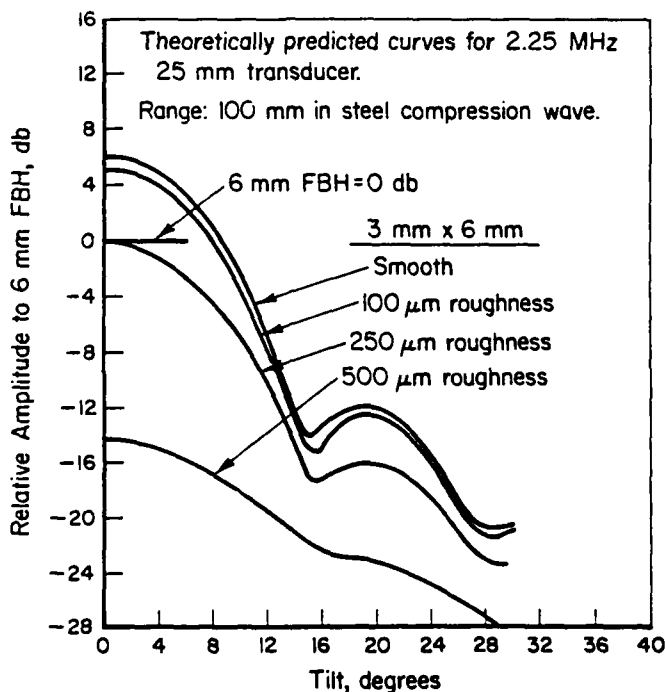


Figure 4. Effect of defect orientation and surface roughness on signal amplitude (from (8))

spatial averaging, frequency averaging and split-spectrum processing [10,11]. Split-spectrum processing has improved the target signal to noise ratio for a 1.19 mm artificial target in titanium with an average grain size of 15  $\mu\text{m}$  by a factor of eight. Split-spectrum processing algorithms have been found to give signal enhancement between 4 and 27 for stainless steel with grain sizes ranging from 75  $\mu\text{m}$  to 160  $\mu\text{m}$  [10]. The principle of split-spectrum processing is illustrated in Figure 5.

The enhancement of inclusion detectability by spatial averaging of ultrasonic data is illustrated in Figure 6 [12]. The inclusions in Figure 6 are slag inclusions in austenitic stainless steel welds where ultrasonic noise due to grain boundary scattering can mask the presence of inclusions [12,13].

**Resolution Enhancement** - To improve detectability of individual inclusions within a cluster of inclusions a number of methods to improve the axial and lateral resolution of imaging systems have been developed [14-21]. Pulse-compression and time-domain deconvolution have been used to both increase axial resolution and signal-to-noise ratio. The principle of pulse-compression is illustrated in Figure 7 and the improvement in axial resolution of a swept frequency transmitted signal after pulse compression is illustrated in Figure 8. This processing technique also enables greater penetration depths in highly attenuating materials. Synthetic focussing (SAFT), phased-arrays, and other focusing techniques have been developed to improve the lateral resolution of ultrasonic imaging systems. Phased-arrays and fixed lens focusing methods also enhance detection sensitivity by concentration of the energy emitted by a relatively large diameter transducer in the small area of the focal zone [14].

Focusing using SAFT and phased-arrays offer an advantage over fixed focus lens systems by enabling the focal plane to be swept through the thickness of the material automatically. Disadvantages of synthetic focusing techniques include computer processing time (particularly in complex structures) and decreasing signal to noise ratios with penetration depth due to the point nature of the wave source employed [14]. The improvement in lateral resolution using SAFT is illustrated in Figure 9 [15]. Phased-arrays are presently the subject of considerable development but technological problems with the production of these devices have not yet been resolved [14].

**Sensors** - The development of a superconducting quantum interference device (SQUID) has provided an extremely sensitive device for measuring changes in magnetic flux providing new opportunities to improve the sensitivity and depth of detection of inclusion based on electromagnetic interactions [22].

Other sensor developments that have improved to the point of practical implementation and are

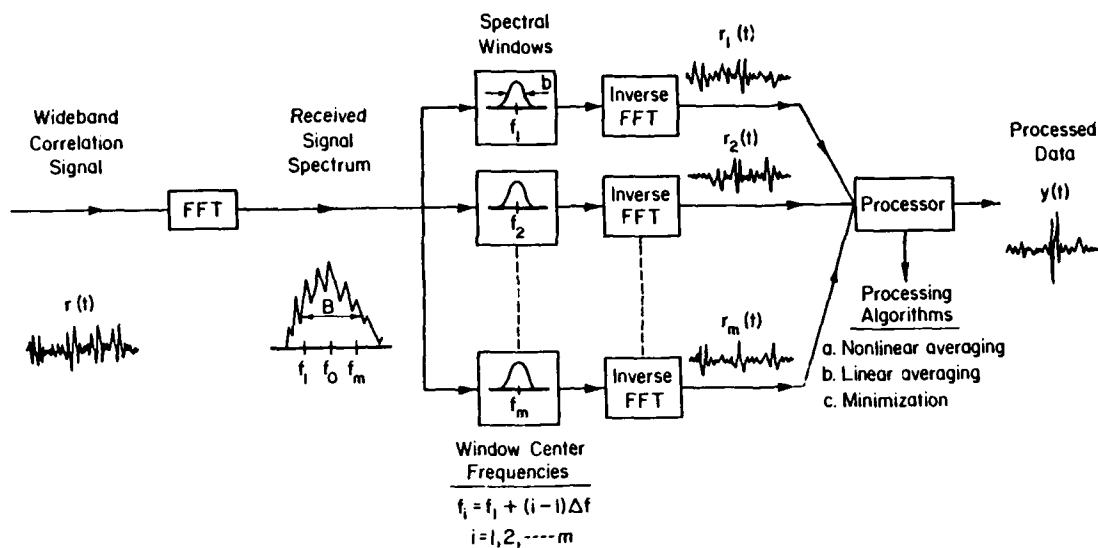


Figure 5. Split spectrum processing technique (from (10))

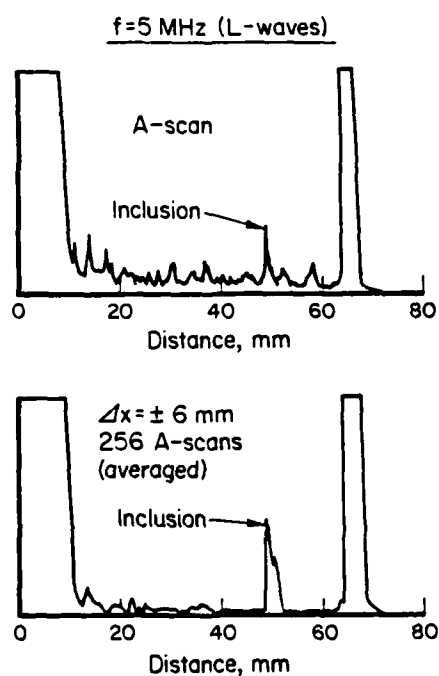


Figure 6. Spatial averaging enhancement of inclusion detectability

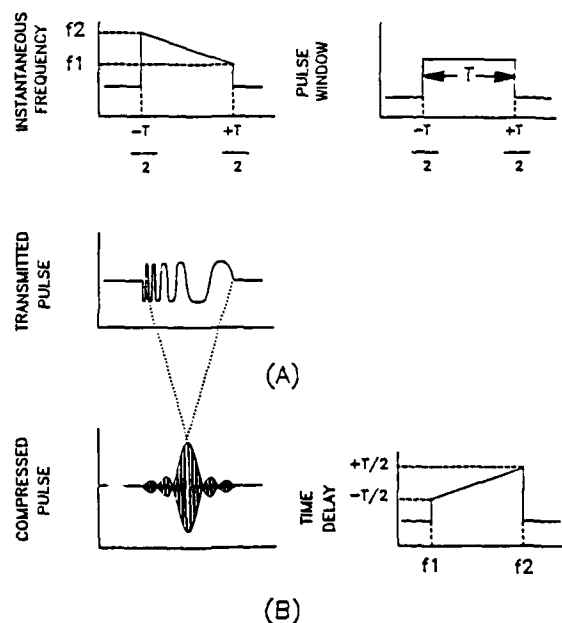


Figure 7. Pulse-compression process: (A) description of chirp waveform to drive the transmitter, and (B) illustration of the time delay filter characteristic and resulting compressed pulse

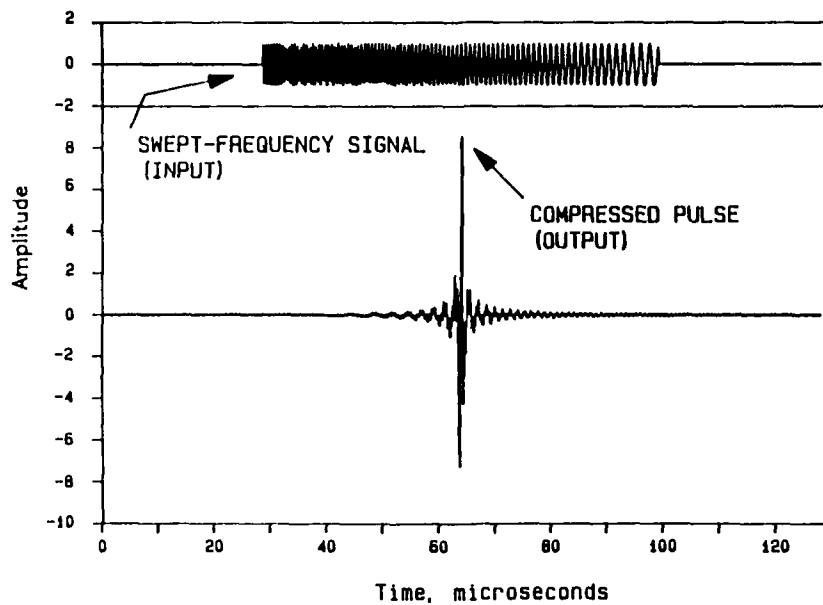
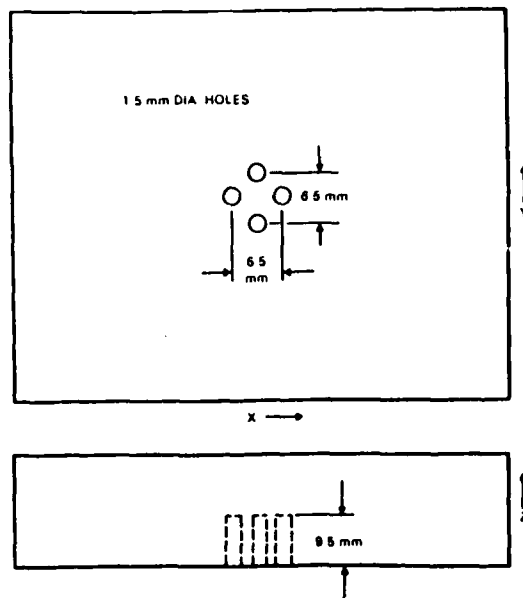
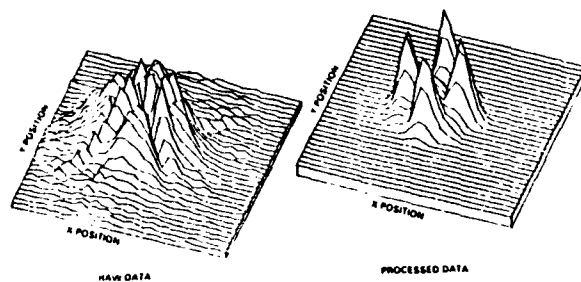


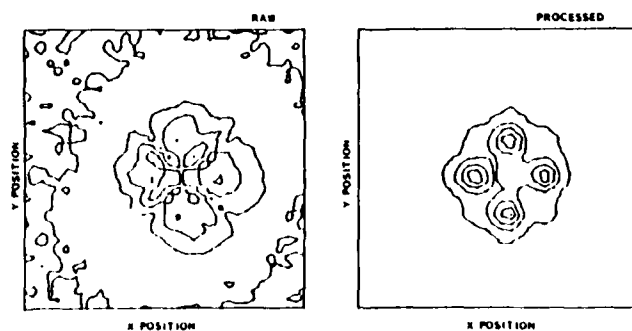
Figure 8. A signal with a downward swept frequency (upper), and the result of applying pulse compression to the signal (lower)



(a) Illustration showing the arrangement of flat-bottom holes in a 20-mm-thick aluminum test specimen



(b) Perspective plot of the raw and SAFT-processed data obtained using the test specimen illustrated in (a) (10-MHz ultrasound was used.)



(c) Contour plot of the raw and the SAFT-processed data obtained using the test specimen illustrated in (a)

Figure 9. Illustration of resolution enhancement using a synthetic focussing technique, (from (15))

experiencing more extensive utilization include laser induced ultrasound (LIUS) and electromagnetic acoustic transducers (EMATs). These technologies offer the advantage of eliminating a need for liquid coupling normally required with conventional piezoelectric ultrasonic transducers. Some work has also been performed to generate convergent ultrasonic wave fields by LIUS techniques. EMATs and LIUS are being developed to detect slag inclusions in hot steel.

Improvement of near surface detectability through development of new electromagnetic and ultrasonic surface wave techniques is being achieved. Rossmanith and Dally [23] have studied Rayleigh wave interactions with near surface cavities and inclusions and have improved the understanding of this wave interaction using dynamic photoelastic methods to visualize the wave field.

**Computer-Automated Systems** - The development of computer assisted or automated data acquisition for nondestructive evaluation systems has promoted the introduction of advanced noninvasive techniques. The enhanced performance of noninvasive measurement systems is complemented by better and more information displays of the results so that the user is provided with much improved information concerning the condition of the test piece [24].

**SPATIAL DISTRIBUTION** - The location of inclusions with respect to the boundaries of the host material has been identified to be important in determining the influence of inclusions on material behavior. Mapping the spatial distribution of inclusions has been approached in a number of different ways.

Computed x-ray tomography has been used to nondestructively probe rare samples of the Allende meteorite for calcium- and aluminum-rich inclusions [25]. This allows the object to be cut to obtain samples for analysis in the areas of interest eliminating the necessity of crushing each meteorite to expose candidate inclusions for analysis. Regions of high and low atomic number were resolved on a scale of millimeters.

Backscattering of an ultrasonic elastic wave field is another approach to mapping inclusion locations. This approach has been used to detect 40-50 mm extended regions of manganese sulphide inclusions in 22-NiMoCr-3-7 pressure vessel steel providing a quantitative indication of the extent of the region of inhomogeneities from the spatial extent of the backscattered amplitude [12].

Ultrasonic time domain reflectometry is frequently used to map the spatial distribution of inclusions in metals and ceramics. The accuracy of this method has been improved by enhanced axial resolution using pulse-compression methods.

Imaging methods are also often employed to map the spatial distribution of defects such as inclusions. If the principle interest is in

simply mapping the volume of material occupied by a cluster of inclusions, conventional ultrasonic imaging and x-ray radiographic methods can be used. However, if determining the interspacing of small inclusions is required, then enhanced lateral resolution becomes necessary. Enhancement of lateral resolution in ultrasonic imaging has been obtained using a number of fixed lens and synthetic focussing methods.

**VOLUME FRACTION** - The scattering of an elastodynamic wave field by inclusions gives rise to velocity dispersion [26-30]. This interaction has been studied for two-phase microstructures by Sayers [26-28] and Latiff and Fibre [30]. Based on Sayers an expression can be derived relating the wave velocity to the volume fraction of inclusions

$$(v/v_0) = 1 + \frac{1}{2}(\Delta V/V)(A+Bk^2a^2) \quad (3)$$

where  $v$  is the wave velocity with inclusions,  $v_0$  is the wave velocity without inclusions,  $\Delta V/V$  is the fractional volume of inclusions,  $k$  is the wave number,  $a$  is the radius of the inclusion, and  $A$  and  $B$  are constants. Since velocity dispersion is a result of scattering and absorption mechanisms in general (Kramers-Kronig relation), scattering from grain boundaries, dislocation damping, and other intrinsic loss mechanisms associated with the surrounding material will also give rise to dispersion. However, if the grain size is known from an independent measurement, and the contribution of other loss mechanisms are relatively small then velocity dispersion can be used to estimate inclusion volume fraction. Also, if an identical sample of material, without the inclusions, is available then the contribution of dispersion from the various attenuation mechanisms can be measured and used to normalize the measurements on the sample containing the inclusions. Underlying assumptions for validity of the model used in derivation of (3) are that the matrix material is homogeneous and isotropic, the inclusions are randomly distributed and of approximately the same size, the distance of separation,  $r$ , between inclusions is large compared to the linear dimensions,  $R$ , of the inclusion ( $r \gg R$ ), and inclusion dimensions are such that scattering falls in the Rayleigh region,  $R/\lambda \ll 1$ , where  $\lambda$  is the ultrasonic wavelength.

Measuring the change in elastic wave velocity and attenuation has been used to determine the volume fraction of cavities or pores (porosity) in sintered ceramics and compacted powder metals. Considerable success has been achieved in empirically correlating the changes in both velocity and attenuation with porosity volume fraction provided the matrix is otherwise homogeneous, and the pores are spheroidal or cylindrical and randomly but uniformly distributed such that multiple scattering is negligible. The advantage of



ultrasonic scattering methods over velocity measurements is that depth profiling is possible.

For example Rose [31] has shown that for aluminum, sensitivities of ultrasonic scattering measurements to pore concentrations as small as 0.1% can be expected when the pore and grain sizes are comparable. The method will be increasingly sensitive as the ratio of pore-to-grain size increases. Sensitivities on the order of 1.0% may be expected for iron and nickel based alloys provided the pores are more than five times the grain size.

Papadakis and Petersen [32] have also used ultrasonic velocity measurements to map density variations due to porosity in sintered powder steel parts.

**MACRO-MECHANICAL PROPERTIES** - Nondestructive methods are being developed to determine the change in mechanical properties (such as elastic moduli and strength related properties) due to the presence of inclusions. For example Fu and Sheu [33] have evaluated the effect of spherical aluminum inclusions in germanium on bulk and shear modulus, mass density and porosity using ultrasonic attenuation and velocity measurements. Vary has studied quantitative ultrasonic evaluation of the mechanical properties of engineering materials [34] which are summarized in Table 2.

House, Nestleroth and Rungta [35] have studied the possibility of using elastodynamic and electromagnetic wave field interactions with low alloy ferritic steels to monitor creep damage and perform insitu measurement of yield strength on low alloy pipeline steels. Although correlations between nondestructive measurements and changes in mechanical properties have been established a number of problems remain to be solved in order to make absolute nondestructive determinations of mechanical properties.

Electromagnetic and magnetic methods to characterize mechanical properties of steels have been studied extensively in the Soviet Union [36-51]. A number of useful empirical correlations have been established, however, in none of the literature has anyone successfully solved the inverse problem of predicting mechanical properties from nondestructive measurements.

**CLEANLINESS** - A common application of conventional ultrasonic methods is to rate the inclusion cleanliness of steel [52-57]. Progress in this area has been primarily in increased inspection rates through automation of ultrasonic scanning, data acquisition and data processing.

Conventional automated ultrasonic C-scanning has been used by Smith [54] to rate steel cleanliness based on histograms consisting of the number of echoes plotted versus the amplitude of the ultrasonic indications. In other work ultrasonic cleanliness rating has also been correlated with mechanical properties of certain steel alloys. For example tensile ductility,

yield strength and to some degree fracture toughness have exhibited correlations with an ultrasonic cleanliness rating index for 4340 steel containing nonmetallic inclusions [57].

### PROXIMATE CHARACTERISTICS

As discussed previously, localized stresses can occur in the neighborhood or proximity of inclusions. Stress localization occurs around inclusions because of differences in the thermal and elastic coefficients of the inclusion and the matrix.

Computer-assisted ultrasonic time-of-flight tomography has been used for mapping the internal stresses in metals [58]. Typically for steel the stress resolution is approximately 6900 kPa.

Kino [59] has mapped stress distributions around holes, Figure 10, and notches in tensile samples. This method could potentially be extended to mapping stress distribution around an inclusion if sufficiently large or given sufficient resolution in the ultrasonic time-of-flight measurements.

However, despite an extensive body of knowledge the results of ultrasonic mapping of residual stresses has been disappointing. The inability to separate velocity change associated with internal stress fields from velocity changes associated with any nonhomogeneous character of the propagating medium remains a serious problem. Measuring velocity changes as a function of magnetic field eliminates some of the problems but is generally restricted to ferromagnetic materials and the sample geometries accommodating the magnetic field measurement severely restricts the potential applications.

### BOUNDARY RELATED CHARACTERISTICS

**SHAPE, SIZE AND DISTRIBUTION** - There are two general approaches to determining the shape and size of an inclusion. One is by inversion of long wavelength scattering data where the linear dimensions of the inclusion are small compared to the wavelength. The other is by imaging short wavelength wave fields scattered from the inclusion (i.e., where the linear dimensions of the inclusion are large compared to the wavelength). Acoustic microscopy [60-68] represents the latter approach.

Advantages of acoustic microscopy outlined in [60] are:

1. Optical opacity in thick samples of metal, ceramic, etc. can be avoided with acoustic microscopy; internal structures are differentiated on the basis of intrinsic elasticity variations among the structural components.
2. Microstructure within solids can be observed nondestructively without resorting to laborious sectioning, polishing, and etching.
3. The real time feature of the technique permits investigation of dynamic behavior, for

Table 2. Capabilities of Ultrasonics for Nondestructive Evaluation of Material Properties

Material Property	Ultrasonic Measurement	Applicable Materials
Longitudinal Modulus	Longitudinal Velocity	Most Engineering Solids
Shear Modulus	Transverse Velocity	Most Engineering Solids
Grain Size, Microstructure	Attenuation, Acoustic Microscopy	Polycrystalline Metals
Porosity, Void Content	Velocity, Attenuation	Fiber Composites, Ceramics
Hardness or Hardness Gradient	Velocity, Velocity Dispersion	Polycrystalline Metals
Tensile Strength	Velocity Stress Wave Attenuation	Brittle Metals, Ceramics, Fiber Composites
Yield Strength	Frequency-Dependent Attenuation	Polycrystalline Metals
Fracture Toughness	Frequency-Dependent Attenuation	Polycrystalline Metals
Bond Shear Strength	Resonance, Spectrum Analysis	Metal-Metal Adhesive Bonds
Interlaminar Shear Strength	Attenuation, Stress Wave Attenuation	Fiber Composites
Stress/Residual Stress	Velocity	Most Engineering Solids

Adapted from [34]

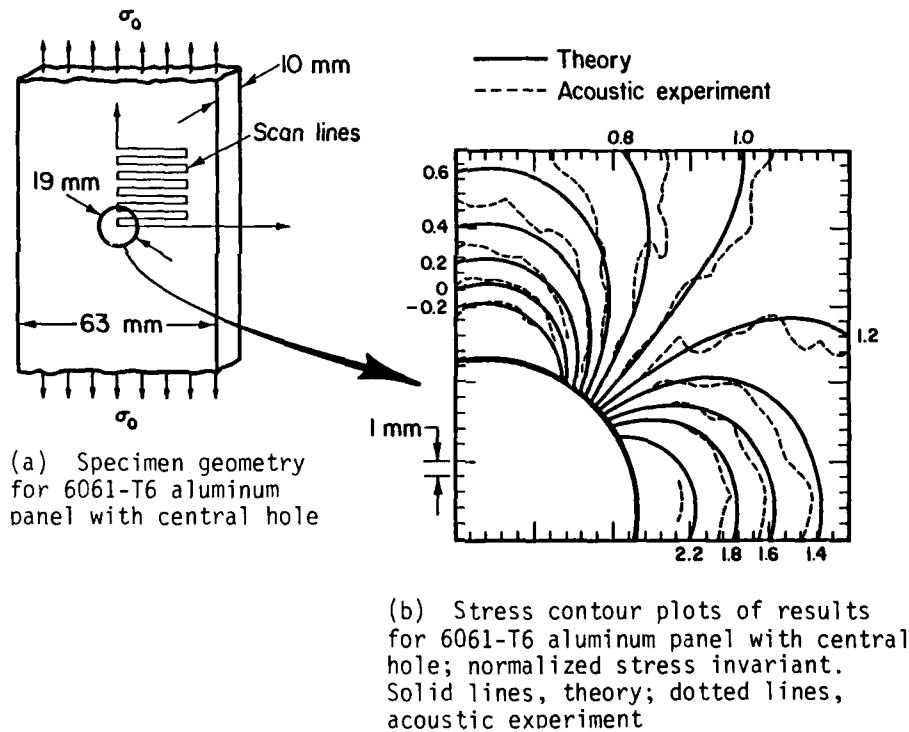


Figure 10. Ultrasonic mapping of stress distributions (from (59))

example, materials under stress can be observed during the formation of plastic zones and during fracture initiation.

4. Physical and elastic properties of structure are brought out by acoustic microscopy. Quantitative data on acoustic indices of refraction are available with acoustic interference microscopy. The acoustic interferograms are related to the compressibility and density characteristics of the sample on a micro size scale.

Inclusions of iron, silicon and carbon as small as 100  $\mu\text{m}$  were detected in silicon nitride disks using a scanning laser acoustic microscope (SLAM) [69]. SLAM size determinations of inclusions are deduced from measurement of the first diffracted circle. This method of estimating inclusion size gives results that are consistently larger than the sizes of the inclusions determined metallographically. These discrepancies were found to increase with the depth of the inclusion from the surface of the sample. This is to be expected since the diffraction pattern expands as the scattered wave field leaves the inclusion. SLAM is a high frequency device thus limiting its utility to materials with low attenuation or to near surface examinations. However, pulse compression techniques have been applied to acoustic microscopes to increase penetration depth [68]. SLAM operates at approximately 100 MHz and can resolve individual defects with linear dimensions of approximately 50  $\mu\text{m}$ . For comparison, ultrasonic holographic imaging resolution at 10 MHz is approximately 1 mm [70].

An advantage of ultrasonic imaging is being able to focus through the depth of the object enabling random ultrasonic scatter to be identified. If the inclusion is large compared to the grain diameter then the fall in scatter with a drop in ultrasonic frequency is less for the inclusion than for the grain structure. Thus grain scatter in high resolution images can be eliminated to reveal a less noisy image of the inclusion [70]. Another way of implementing dynamic focussing enabling the focussing of the image at various depths is electronic beam forming using ultrasonic phased arrays as discussed earlier. Gebhardt [71] gives a thorough review of the phased array technology.

Considerable progress in the development of signal processing algorithms to perform inversion of long wavelength ultrasonic scattering data to yield the size, shape, and orientation of flaws has been made in recent years. A particular drawback with long wavelength inversion is the practical problem of obtaining elastic wave scattering measurements from the inclusion at several viewing angles. Presently ultrasonic transducers are not available which permit this to be done efficiently and conveniently in the long and intermediate wavelength end of the spectrum [72]. Nevertheless, the use of the inverse Born approximation (IBA) to characterize inclusions in elastic media has been studied both

experimentally and theoretically. The one dimensional IBA has been used to characterize voids and, less extensively, inclusions. The 1-D IBA was used by Hsu, et al. [72], to provide information on size, shape and orientation. In the latter case the authors concentrated on ellipsoidal shapes because the results would be of general value since a wide variety of flaw shapes can be approximated by using different ellipsoidal aspect ratios. Hsu, et al., [72] experimentally determined the size, shape and orientation of nonspherical inclusions in terms of six parameters (three semiaxes and three Euler angles) of an equivalent ellipsoid using a non-linear least squares fitting procedure. With this technique successful reconstructions were achieved for an approximately prolate spheroidal inclusion in a plastic and an oblate spheroidal void in titanium. Practical limitations of this method involve construction of transducers with sufficiently large apertures and broad enough bandwidths for accurate reconstructions.

Hsu, et al. [73] also performing an inversion using the 1-D Born approximation algorithm was able to determine the radii of near surface spherical inclusions. The results of actual versus calculated radii by Born inversion of measured ultrasonic data are given in Table 3. These inclusions were stainless steel embedded in plastic disks.

The performance of an inversion procedure for a given set of scattering data improves with the amount of correct a priori information. In order for the Born approximation to be effective, it is assumed the material properties of the inclusion are close to those of the matrix material. To determine the size and shape of an inclusion with unknown boundaries by application of Born inversion algorithms it must generally be assumed that the material properties of the inclusion are known. Alternatively a probabilistic approach to the inverse problem uses a stochastic measurement model which provides an output that is the most probable flaw given the set of scattering measurements and available a priori information [74].

Sablik and Beisner [75] discuss procedures for determining inclusion shape from measurement of magnetic leakage fields from inclusions in magnetic materials. A magnetic field is applied to a steel sample and inclusions are detected by measuring perturbations in the applied field [76,77]. The change in the applied field due to this perturbation is known as the leakage field and exhibits a field distribution depending on the type of inclusion, its location, its approximate size, and its orientation. This improves on other established theories which treat spherical inclusions only. Although the discussion of Sablik and Beisner suggests several tests for inclusion shape, these tests require switching of the scanning planes from constant x to constant y. Unfortunately, the experimental scans can be made only at the surface of the sample thus prohibiting the switch

Table 3. Comparison of Actual Radii and 1-D Born Inversion Results for Spherical Inclusions at Various Depths, (from (73))

$z$	$r$ , Actual	$r$ , 1-D Born
35 $\mu\text{m}$	54 $\mu\text{m}$	50 $\mu\text{m}$
200	59	57
440	58	52
710	56	56

to a perpendicular scanning surface. The authors however, suggest that the field direction be switched by  $90^\circ$ . To test for inclusion shape, an estimate of the direction of the symmetry axis from trackings at different  $z$  are first obtained. The external field is then aligned with the defect symmetry axis and finally the field is switched to a direction perpendicular to the original one. Accordingly, this has the following effects:

- (1) Separation of the peak leakage field intensity should decrease if the inclusion is prolate; increase if oblate
- (2) Peak amplitude of the leakage field intensity should increase if prolate; decrease if oblate.

If the inclusion does not have a symmetry axis a suggested approach would be to use the major and minor dimension of the inclusion as one axial direction, with the other dimension as the perpendicular direction.

Although the model developed assumes an infinite media it has been observed empirically for spherical inclusions that the amplitude-volume and peak separation-depth relationships retain their linearity if the leakage field measurement is made at a boundary surface outside the medium. However deviation from the expected values of the slopes of these relationships are sufficiently large that development of theory to describe the effect of the material boundary would be useful. Another assumption is that the material has a constant linear permeability independent of magnetic field intensity and hence independent of spatial position in the medium. Experiments according to the authors indicate that for inclusions it may be reasonable to neglect nonlinear permeability effects.

**BONDING** - Work on the characterization of bonding has been extensive but has not been very successful, with some exceptions for a few specific adhesively bonded systems, in quantitative measurement of strength related properties. Even so, much of the fundamental work has been for semi-infinite substrates and not related specifically to inclusions.

## INTRINSIC CHARACTERISTICS

**ELEMENTAL COMPOSITION AND PHASE** - Khuri-Yakub and Kino [78] have studied the use of very high frequency (200-500 MHz) ultrasound to detect and identify inclusions ranging in size from 25-500  $\mu\text{m}$  in ceramics. The identification concept was based on different types of inclusions having different frequency responses. The different response between a void and a tungsten carbide inclusion are shown in Figure 11.

**MECHANICAL PROPERTIES** - Except for the work described previously on determining macro-mechanical properties the literature appears devoid of any successful noninvasive measurements of intrinsic mechanical properties of inclusions.

## SUMMARY AND CONCLUSIONS

The major advances in noninvasive technologies relevant to inclusion characterization are:

- Development of high resolution acoustic microscopes,
- improvement in resolution of imaging systems through signal processing and image reconstruction such as deconvolution, pulse-compression, synthetic focussing techniques, and tomographic reconstruction,
- advanced sensors such as phased arrays, superconducting quantum interference device (SQUID), electromagnetic acoustic transducer (EMAT) and laser generated ultrasound,
- computer automated systems for rapid data acquisition and interpretation of data,
- progress in theoretical understanding of wave field interactions with defects and material and progress in inversion of ultrasonic and electromagnetic field data to determine flaw shape and size.

Considerable advances have been made in extending the list of inclusion properties that can be either qualitatively or quantitatively examined in a noninvasive manner. However much progress remains to be made in making the complete transition from qualitative evaluation to quantitative measurement of inclusion characteristics and their influence on material behavior.

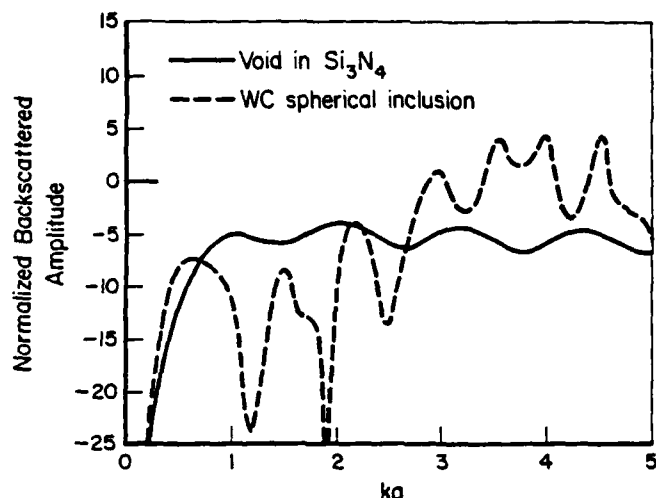


Figure 11. Theoretical backscattered spectra of a spherical void and a WC inclusion in  $\text{Si}_3\text{N}_4$  (from (78))

#### REFERENCES

1. R. Kiessling, *Non-Metallic Inclusions in Steel*, Second Edition, Book No. 194, The Metals Society, London (1978)
2. F. Laszlo, *J. Iron & Steel Inst.*, 147, 173-199 (1943) ; 152, 207-228 (1945)
3. D. Brooksbank and K. W. Andrews, *ibid*, 206, 595-599 (1968); 207, 474-483 (1969); 208, 495-499 (1970); 208, 582-586 (1970)
4. D. Brooksbank and K. W. Andrews, "Production and Application of Clean Steels", pp. 186-198, The Iron & Steel Institute, London, (1972)
5. R. Kiessling and H. Nordberg, *ibid*, pp. 179-185
6. E. Marianeschi and T. Tili, *NDT International*, Vol. 16, No. 2., 75-77 (1983)
7. R. Saglio, *NDT International*, Vol. 9, No. 4, 193-196 (1976)
8. A. Rogerson and R. A. Murgatroyd, *Research Techniques in Nondestructive Testing*, R. S. Sharpe, Editor, Vol. IV, Academic Press (1980)
9. B. Canella, et al., *NDT International*, Vol. 16, No. 3, 151-153 (1983)
10. V. L. Newhouse, et al., *Ultrasonics*, Vol. 20, No. 2, 59-68 (1982)
11. V. L. Newhouse and E. S. Furgason, "Research Techniques in Nondestructive Testing", R. S. Sharpe, Editor, Vol. III, Academic Press (1977)
12. K. Goebbels, "Research Techniques in Nondestructive Testing", R. S. Sharpe, Editor, Vol. IV 148-153, Academic Press (1980)
13. K. Goebbels and P. Höller, *Ultrasonic Backscattering Measurements*, Ultrasonic Materials Characterization, H. Berger and M. Linzer (Eds.), 67-74, National Bureau of Standards Special Publication 596, Gaithersburg, Maryland, (1978)
14. R. Saglio and A. C. Prot, "Research Techniques in Nondestructive Testing", R. S. Sharpe, Editor, Vol. VIII, Academic Press (1985)
15. Busse, L.J., Collins, H.D., and Doctor, S.R., "Review and Discussion of the Development of Synthetic Aperture Focusing Technique for Ultrasonic Testing (SAFT-UT)", Pacific Northwest Laboratory, NUREG/CR-3625, PNL-4957 (March 1984)
16. J. Seydel, "Research Techniques in Nondestructive Testing", R. S. Sharpe, Editor, Vol. VI, Academic Press (1982)
17. S. O. Harrold, "Research Techniques in Nondestructive Testing", R. S. Sharpe, Editor, Vol. VI, Academic Press (1982)
18. C. VandenBroek, et al., *Ultrasonic Materials Characterization*, H. Berger and M. Linzer (Eds.), 249-257, National Bureau of Standards Special Publication 596, Gaithersburg, Maryland, (1978)
19. W. A. Simpson, Jr., *Materials Evaluation*, Vol. 44, No. 8, 998-1003 (1986)
20. F. K. Lam and M. S. Hui, *Ultrasonics*, Vol. 21, No. 3, 107-112 (1982)
21. F. Lam and J. Szilard, *Ultrasonics*, Vol. 14, No. 3, 111-114 (1976)
22. H. Weinstock, "Review of Progress in Quantitative Nondestructive Evaluation", Vol. 5A, 699-703, D. O. Thompson and D. E. Chimenti, Editors, Plenum Press (1986)
23. H. P. Rossmanith and J. W. Dally, *Strain*, Vol. 19, No. 1, 7-14 (1983)
24. P. J. Mudge, "Research Techniques in Nondestructive Testing", R. S. Sharpe, Editor, Vol. VIII, Academic Press (1985)

25. J. R. Arnold, et al., "Science, Vol. 219, No. 4583, 383-384 (1983)
26. D. R. Allen, et al., Research Techniques in Nondestructive Testing, R. S. Sharpe, Editor, Vol. VI, 151-209, Academic Press (1982)
27. C. M. Sayers, J. Phys. D, Appl. Phys., Vol 14, 413-420 (1981)
28. C. M. Sayers, J. Phys. D, Appl. Phys., Vol 13, 179-184 (1980)
29. C. M. Sayers and R. L. Smith, Ultrasonics, Vol. 20, No. 5 (1982)
30. R. H. Latiff and N. F. Fiore, J. Acoust. Soc. Am. Vol. 57, No. 6, Part II, 1441-1447 (1975)
31. J. H. Rose, "Review of Progress in Quantitative Nondestructive Evaluation, Vol. 4B, 909-917, Plenum Press (1985)
32. E. P. Papadakis and B. W. Petersen, Materials Evaluation, Vol. 37, No. 5, 76-80 (1979)
33. L. S. Fu and Y. C. Sheu, Composite Structures, Vol. 2, No. 4, 289-303 (1984)
34. A. Vary, Ultrasonic Materials Characterization, H. Berger and M. Linzer (Eds.), 41-53, National Bureau of Standards Special Publication 596, Gaithersburg, Maryland, (1978)
35. L. J. House, J. B. Nestleroth, and R. Rungta, unpublished work, corporate funded internal research, Battelle Memorial Institute, Columbus Division. To be presented at Fall Materials Research Society meeting, Boston, Massachusetts.
36. V. A. Burganova, et.al., The Soviet Journal of Nondestructive Testing, Vol. 10, No. 4, 432-437 (1974)
37. I. A. Kuznetsov, et.al., The Soviet Journal of Nondestructive Testing, Vol. 10, No. 4, 464-468 (1974)
38. G. S. Tomilov, The Soviet Journal of Nondestructive Testing, Vol. 12, No. 3, 254-262 (1971)
39. I. A. Kuznetsov, et.al., The Soviet Journal of Nondestructive Testing, Vol. 7, No. 1, 78-84 (1971)
40. B. S. Natapov and E.S. Fal'kevich, Zavodskaya Lab. (English Translation), Vol. 24, No. 8, 1130-1131 (1958)
41. M. A. Mel'gui, et.al., The Soviet Journal of Nondestructive Testing, Vol. 7, No. 3, 248-252 (1971)
42. M. N. Mikheev and E. S. Gorkunov, The Soviet Journal of Nondestructive Testing, Vol. 17, No. 8, 579-592 (1981)
43. G. A. Pyatunin and V. I. Slavov, The Soviet Journal of Nondestructive Testing, Vol. 14, No. 11, 1027-1031 (1978)
44. G. S. Tomilov, The Soviet Journal of Nondestructive Testing, No. 2, 177-181 (1969)
45. G. S. Tomilov, The Soviet Journal of Nondestructive Testing, No. 4, 1966, 316-322 (1966)
46. T. Jakel, British Journal of NDT, 287-290 (July, 1984)
47. R. Ranjan, O. Buck and R. B. Thompson, "Review of Progress in Quantitative Nondestructive Evaluation", Plenum Press D. O. Thompson and D. E. Chimenti (Editors), Vol. 5B, 1335-1343 Plenum Press (1986)
48. V.F. Kovikov and V.V. Nasonov, Soviet Journal of Nondestr. Testing, Vol. 20, No. 3, 217-221 (1984)
49. G. Dobmann and P. Höller, Res. Techn. in Nondestr. Testing, Vol. IV, R.S. Sharpe, Editor, 39-69, Academic Press, (1980)
50. N.M. Naumov and L.Ya. Zarubinskaya, Soviet Journal of Nondestr. Testing, Vol. 16, No. 2, 75-79 (1980)
51. N. Davis and P.A. Norris, Journal of Physics E: Scientific Instruments, Vol. 5, 12-14 (1972)
52. J. B. Morgan, Materials Evaluation, Vol. 28, No. 6, 121-134, (1970)
53. S. S. Daniel and R. A. Rege, Journal of Metals, Vol. 23, No. 7, 26-37 (1971)
54. J. M. Smith, "Review of Progress in Quantitative NDE", Vol. 2B, D. O. Thompson and D. E. Chimenti (Eds.), 1431-1436, Plenum Press, (1983)
55. J. M. Joilvet, Transactions of the Iron and Steel Institute of Japan, Vol. 24, No. 7, B221, (1984)

56. J. Dumont-Fillon and M. Lacroix, "Ultrasonic Measurement of the INclusion Cleanliness of Steel", Final Report, Contract No. 6210-GA/3/301, Commission of the European Communities, Technical Steel Research, Directorate-General Scientific and Technical Information and Information Management.
57. C. J. Carter, et al., "Effect of Inclusions as Measured by Ultrasonic Methods on the Mechanical Properties of Aircraft Quality Steel", Technical Report AFML-TR-68-303, (January 1969)
58. B. P. Hildebrand and T. P. Harrington, Materials Evaluation, Vol. 39, 383-390, (1981)
59. G. S. Kino, Journal of Nondestructive Evaluation, Vol. 1, No. 1, 67-77 (1980)
60. L. W. Kessler and D. E. Yuhas, "High Resolution Real Time Acoustic Microscopy", ASNT 37th National Fall Conference, October 3-6, 1977, Detroit, Michigan.
61. L. J. Inglehart, et al., Journal of Nondestructive Evaluation, Vol. 1, No. 4, 287-293 (1980)
62. D. E. Yuhas and L. W. Kessler, Scanning Electron Microscopy, 385-391 (1980)
63. R. D. Weglein, IEEE Transactions on Sonics and Ultrasonics, Vol. SU-32, No. 2, 225-234 (1985)
64. E. R. Generazio and D. J. Roth, Materials Evaluation, Vol. 44, No. 7, 863-870 (1986)
65. D. J. Roth, et al., "Quantitative Void Characterization in Structural Ceramics Using Scanning Laser Acoustic Microscopy", NASA Technical Memoranda 88797 (1986)
66. B. Nongaillard and J. M. Rouvaen, "Acoustical Imaging", Vol. 10, Alais and Metherell, Editors, 797-802 (1980)
67. R. D. Weglein, "Development and Capabilities of the LLNL Focused-Beam Reflection-Mode Acoustic Microscope", University of California Final Report, UCRL-53522, May 1984
68. M. Nikoonahad, "Research Techniques in Nondestructive Testing", R. S. Sharpe, Editor, Vol. VIII, 217-258, Academic Press, (1984)
69. G. Birnbaum and G. S. White, "Research Techniques in Nondestructive Testing", R. S. Sharpe, Editor, Vol. VII, 259-365, Academic Press, (1984)
70. E. E. Aldridge and M. J. Clement, "Ultrasonic Testing", J. Szilard, Editor, pg. 145., John Wiley and Sons (1982)
71. W. G. Gebhardt, "Research Techniques in Nondestructive Testing", R. S. Sharpe, Editor, Vol. VII, 115-143, Academic Press (1984)
72. D. K. Hsu, et al., "Review of Progress in Quantitative NDE", Vol. 2B, D. O. Thompson and D. E. Chimenti (Eds.), 995-1018 Plenum Press (1983)
73. D.K. Hsu, et al., "Review of Progress in Quantitative NDE", Vol. 2A, D. O. Thompson and D. E. Chimenti (Eds.), 795-812, Plenum Press (1983)
74. J. M. Richardson, "Estimation of the Boundary of an Inclusion of Known Material from Scattering Data", Review of Progress in Quantitative NDE, Vol. 2B, D. O. Thompson and D. E. Chimenti (Eds.), 989-994, Plenum Press, (1983)
75. M. J. Sablik and R. E. Beissner, J. Appl. Phys., Vol. 53, No. 12, 8437-8450 (1982)
76. C. N. Owston, Br. J. Non-Destr. Testing, Vol. 16, No. 6, 162-168 (1974)
77. F. Förster, Br. J. Non-Destr. Testing, Vol. 17, No. 6, 168-171 (1974)
78. B. T. Khuri-Yakub and G. S. Kino, "High Frequency Defect Characterization", pp. 139-141, 1977 IEEE Ultrasonics Symposium Proceedings, Phoenix, Arizona, IEEE 77CH1264-1SU, October 26-28, (1978)
79. H. Kwun, et al., NDT International, Vol 17, No. 2, 73-79 (1984)

# SOURCES OF ERRORS IN PARTICLE SIZE DISTRIBUTION PARAMETERS

**D. B. Rayaprolu**

Dept. of Mechanical Engineering  
University of Bristol, Bristol, England

**D. Jaffrey**

Invetech Operations Pty Ltd  
PO Box 152, Clayton 3168, Australia

## ABSTRACT

Manganese Sulphide inclusions in steel have been chosen as a model dispersion to study the sources and the magnitudes of the errors (variations) which arise in the quantitative optical metallographic determination of size distributions of dispersed second phase particles. The errors were shown to rise from three sources viz.:

- (i) from methods used for sectioning correction;
- (ii) the characteristics of the system under study;
- (iii) the instruments employed for the measurement of the section distribution.

The upper limit of the inclusion diameters have been established for each of the above sources beyond which significant errors are not introduced into the size distributions. The one factor analysis of variance has been employed to estimate the extent of the total error in the conventionally derived parameters (such as mean particle diameter and the total number of particles per unit volume) from these distributions. A procedure has been described to determine the above parameters with a chosen accuracy.

To minimise errors in the parameters, the benefits of using a volume fraction based analysis rather than a number based analysis have been demonstrated.

FROM AN EXAMINATION of the features present on a two-dimensional section, quantitative metallography deduces certain spatial parameters such as the number of particles within a unit volume, their interfacial area, volume fraction, etc. Because one dimension is lost when sectioning the particles, statistical generalisations have had to be used in deriving the relationships between the parameters describing the particle and section distributions. Additionally, in most situations, experimentation involves observation of a small, 'sample' area on which is based the conclusions about the whole population. Therefore in quantitative metallography a measurement cannot be considered as

exact but must be associated with an error or a confidence range. The usefulness of a measured or deduced parameter depends on its accuracy. Hence a quantitative metallographic study should involve not only the measurement of a parameter but concurrent estimate of its accuracy. Only then can a model or theory be put to the test with confidence.

In the following, the sources of variations (errors) associated with the optical metallographic determination of particle size distributions are defined and either estimated or determined. The Fe-MnS system has been utilised for this study because of several inherent advantages but the results have a far wider relevance.

Broadly speaking, the various errors arise from three categories of sources:

- (i) the methods of analysis employed in converting the 2-D section distribution to a 3-D particle distribution;
- (ii) the characteristics of the particular distribution; and
- (iii) the instrument employed in the measurement of the 2-D section distribution.

These three sources are individually examined in separate sub-sections.

**METHODS OF ANALYSIS** - In utilising sectioning correction techniques to derive particle size distributions the following possible sources of error need to be considered.

(a) differences in the 3-D size distributions arising solely from the use of different sectioning correction techniques; and

(b) the choice between the upper limit of the interval (ULI) and the interval centre (IC) as the representative particle diameter for each size interval.

**THE EFFECT OF SYSTEM CHARACTERISTICS** - The determination of the section size distribution from any one surface of a specimen is associated with a statistical error due to variations from one field to another. The accuracy determined for a distribution on



T A B L E I  
Chemical Analysis of the As-Cast Ingots (wt.%)

Material	Al	C	Cr	Fe	Mn	Ni	P	S	Se	Si
S Steel	0.024	0.28	NA	Bal.	1.20	NA	0.015	0.29	<0.005	0.07

Bal = Balance

NA = Not analysed

one surface cannot be assumed to apply for the entire distribution, unless the particles are known to be distributed randomly. In most metallic systems, due to processing variables, variations occur within the specimen (micro-inhomogeneity) and from specimen to specimen (macro-inhomogeneity). The differences in derived size distributions due to these variables are of particular significance to the present system of MnS inclusions in steels since inhomogeneity is a known characteristic [1].

The sectioning correction models apply to systems of discrete spherical particles, randomly dispersed. Therefore in the determination of size distributions, it is essential to know

(a) whether the particles meet the shape requirement of the correction procedures, and if not,

(b) an estimate of the variation in the size distribution arising from this deviation alone.

**INSTRUMENT VARIATION** - Variations in size distributions may arise from several of the instrument features. A detailed study was previously made [2] of several of these variables (viz. the resolution limit, sensitivity, edge effect) and by observing the procedures recommended in that study the associated errors can be minimised. Two important variables which depend on the instrument operator are:

(i) optimum focus setting; and

(ii) threshold setting for the grey level detection [3,4].

Finally, an aspect that must be considered is the resolution limit of the optical system. This dictates the minimum measurable size and the error associated with its measurement.

#### EXPERIMENTAL DETAILS

Laboratory melts of high purity constituents were made in a vacuum induction melting/casting furnace. The full chemical analysis of the as-cast ingot is given in Table I. No sign of macro-segregation was revealed in

the ingot sulphur prints. Samples of 15 x 10 x 8 mm were cut from the ingot and annealed at 1050 °C or 1350 °C for a duration of 1, 2, 5, 10, 50 or 100 hours in an atmosphere of dried gas mixture of argon and 5% hydrogen.

A 'Quantimet 720' quantitative television analysis machine was used as a typical high quality, routine instrument. The number and area fractions of the particle sections present within a test area of each specimen in the unetched condition were determined by an experienced operator. The fields of view were chosen to be at the centres of a regular array of sites which divided the specimen surface into portions of equal area [5]. Each optically resolvable section distribution was measured via the use of two objective lenses. An oil immersion lens of 125 x magnification and a numerical aperture (NA) of 1.3 was used for section diameter in the range 0.5 µm to 5.0 µm. The larger sections were imaged through a 32 x magnification lens of NA = 0.5. The entire size distribution was determined in 14 diameter intervals whose limits were chosen to give a constant logarithmic variation in interval widths. The section sizing was based on the diameter of a circle of equivalent area. Computer programs were developed to convert (a) the section number distribution to the number of particles size distribution (NPD) using the Saltykov technique [6] or (b) the area fraction distribution to the volume fraction distribution (VFD) via the Johnson-Saltykov (J-S) method [6].

In this study definitions of the following parameters were taken from Underwood [6].

The mean particle diameter is

$$\bar{D} = \frac{\sum_{i=1}^m N_{vi} \cdot D_i}{N_v} \quad (1)$$

where  $D_i$  is the upper limit of the interval (ULI) group  $i$ ,  $N_{vi}$  is the number of particles per unit test

volume within that interval,  $N_v$  is the total number of particles per unit test volume and  $m$  is the total number of group intervals.

The mean particle diameter based on volume fraction distribution is defined as

$$\overline{D}_v = \frac{\sum_{i=1}^m V_{vi} \cdot D_i}{V_v} \quad (2)$$

where  $V_{vi}$  is the volume fraction of inclusions within a size interval  $i$  and  $V_v$  is the total volume fraction of the particles in the matrix.

## RESULTS

The sulphide inclusions were type II [7]. They lay as clusters of rods in interdendritic locations surrounded by proeutectoid ferrite, Fig 1. Occasionally sulphides occurred within pearlite colonies and appeared to be spheroidal. Annealing at temperatures greater than 950 °C resulted in spheroidisation and subsequent coarsening of the particles. With increased duration at any temperature the inclusions tended to become randomly distributed.

VARIATIONS DUE TO THE METHODS OF ANALYSIS - Prior work [8,9] showed the following.

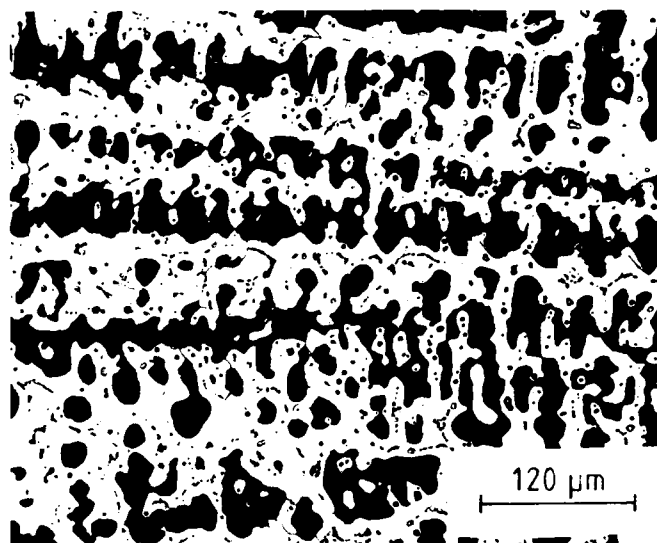
(a) The choice of either the Schwartz-Saltykov or the Saltykov technique (ie a choice between the arithmetic or logarithmic scale of intervals) does not influence the accuracy of NPD. In practice, minor differences may arise due to other variables such as the statistical accuracy of counting, the non sphericity of the particles etc., but not due to the analysis technique.

(b) The Johnson-Saltykov (J-S) method introduces errors up to 27% in the number of inclusions per unit volume determined within a chosen size interval. These errors arise from the assumption of size interval mean area in the J-S approach and may be eliminated by the use of modified coefficients of the per cent relative cross sectional area [8].

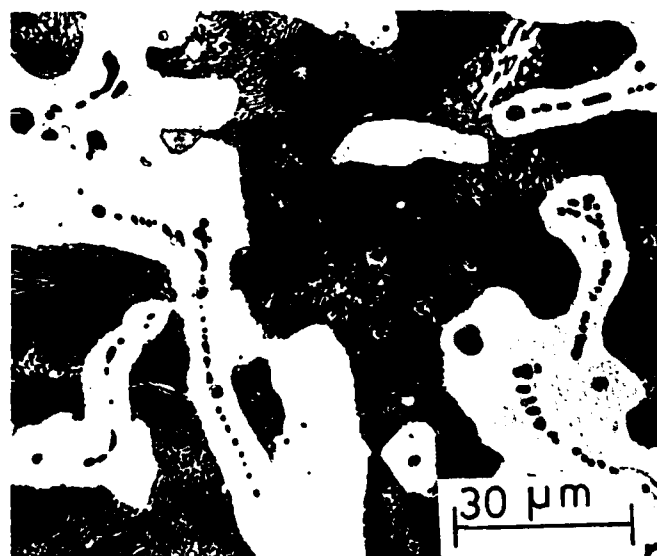
(c) The upper limit of the interval is the representative particle diameter to be used for further computations.

VARIATIONS INTRODUCED BY THE SYSTEM - To determine the errors introduced into the size distributions from the different sources belonging to this category, two specimens, A and B, were chosen for study and annealed at 1350 °C for different durations. Specimen A\* represented a relatively coarse distribution. Specimen B\* exhibited a much finer distribution.

\* Specimen A was a specimen chosen from sulphur steel ingot and annealed at 1350 °C for a duration of 100 hours. Specimen B was from the same ingot, annealed at 1350 °C for 10 hours.



(a)



(b)

Fig. 1 - Location of MnS inclusions in the interdendritic spaces in the as-cast steel; (a) MnS mostly surrounded by proeutectoid ferrite and (b) occasionally by pearlite.

To minimise the effort involved in determining the section distribution with a desired level of accuracy at an acceptable level of statistical confidence, the minimum number of fields to be examined has to be determined. For this determination, the inherent variability of the distribution from field to field, ie the standard error of the observations within each size interval, had to be deduced. The number of

TABLE 2 : DETERMINATION OF THE NUMBER OF FIELDS (nf) TO BE ANALYZED FOR A 20% ACCURACY (WITH THE 95% LEVEL OF CONFIDENCE) IN  $N_{vi}$  AND THE EXPECTED PER CENT ERROR IN  $N_{vi}$  (E) WITH 75 FIELDS UNDER A 125x OBJECTIVE LENS AND WITH 50 FIELDS UNDER A 32x OBJECTIVE LENS - THE SPECIMEN WAS A CAST S STEEL ANNEALED AT 1350 °C FOR 100 HOURS (SPECIMEN A)

Diameter limits of the section groups, $\mu\text{m}$	Average number of particles per unit volume $N_{vi} \times 10^{-9} \text{ m}^{-3}$	Standard deviation of $N_{vi}$ , $s_{N_{vi}} \times 10^{-9}, \text{m}^{-3}$	Number of fields required nf	E at the 95% level of confidence
0.5 - 0.73	$1.17 \times 10^5$	$1.02 \times 10^5$	1814	98
0.73 - 1.10	$5.41 \times 10^5$	$6.32 \times 10^4$	33	13
1.10 - 1.59	$2.55 \times 10^5$	$5.35 \times 10^4$	106	24
1.59 - 2.32	$2.88 \times 10^5$	$4.57 \times 10^4$	60	18
2.32 - 3.48	$1.95 \times 10^5$	$2.56 \times 10^4$	41	15
3.48 - 5.00	$9.54 \times 10^4$	$1.8 \times 10^4$	86	21
5.00 - 6.95	$2.66 \times 10^4$	$1.87 \times 10^3$	12	10
6.95 - 9.65	$6.54 \times 10^3$	$5.14 \times 10^2$	15	11
9.65 - 13.38	739.0	122.0	66	23
13.38 - 18.44	5.94	14.4	14100	336
18.44 - 25.74	9.51	30.0	24000	438
25.74 - 35.90	0.0	0.0	0	
Total number of particles per $\text{m}^3$ , $N_v \times 10^{-15}$	1.53	0.107	12	8
Average diameter, $\bar{D}$ , $\mu\text{m}$	2.09	0.14	11	8
After $N_{vi}$ datum for $<0.73 \mu\text{m}$ particles was excluded				
Total number of inclusions per $\text{m}^3$ , $N_v \times 10^{-15}$	1.41	$6.85 \times 10^{-2}$	6	6
Average diameter, $\bar{D}$ , $\mu\text{m}$	2.19	0.086	4	4

sections present within each size interval were counted in steps of 25 fields for both the 125x and 32x objective lenses. Ten such measurements were made making a total of 250 fields under each lens. From these observations, the mean number of inclusions per unit volume in each diameter interval  $i$  and their standard deviation  $s_{N_{vi}}$  were evaluated. If the maximum allowable per cent error in  $N_{vi}$  is specified as E, then the approximate minimum number of fields (nf) required may be estimated from the following equation [10] for each size interval.

$$nf = \frac{Z_{1-\alpha/2} \cdot s_{N_{vi}} \cdot 100}{E \cdot N_{vi}}$$

Where  $Z_{1-\alpha/2}$  is the  $(1-\alpha/2) \times 100$  per cent point of a standard normal distribution. The resultant values of  $N_{vi}$ ,  $s_{N_{vi}}$  and nf for an allowed per cent error of  $E = 20\%$  in the determination of  $N_{vi}$  at the 95% level of confidence ( $\alpha = 0.05$ ) are listed in Table 2, for Specimen A. It has been suggested [5] that an adequate number of fields is achieved when the standard error of the number of particles in any size range does not exceed 2% of the total number of

particles. The results in Table 2 indicate that on average, 75 fields under the 125 x objective lens and 50 fields under the 32 x lens satisfy the above condition.

The error range of  $\pm 98\%$  for  $0.73 \mu\text{m}$  diameter inclusions was so large that the  $N_{vi}$  results may not be considered as reliable. Therefore in subsequent analyses the  $N_{vi}$  for this size range was deleted from the computations. The large error range for inclusions of diameter greater than  $13.38 \mu\text{m}$  hardly affects the calculations of  $\bar{D}$ , since the proportion of these particles is so small.

The present study has shown that although the per cent error in the determination of  $N_{vi}$  for individual intervals within the useful size range ( $0.73 - 13.0 \mu\text{m}$ ) may be as high as 24%, the two parameters  $N_v$  and  $\bar{D}$  are less susceptible to statistical errors (Table 2). Therefore  $N_v$  and  $\bar{D}$  are more reliable parameters than  $N_{vi}$ .

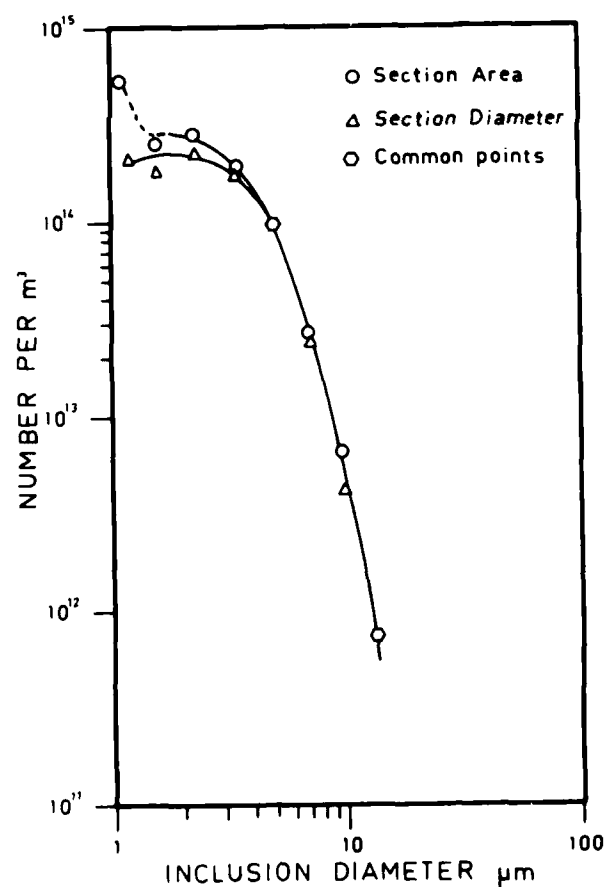
To determine the magnitude of the errors due to the non-sphericity of the inclusions the size distribution of the sulphide inclusions in Specimen A was redetermined with the grouping of the sections being based on their diameters rather than their areas. The results shown in Fig 2 and Table 3 indicate that no variation is noticeable between the two distributions for inclusion diameters greater than  $1.1 \mu\text{m}$ . Therefore beyond this size, the assumption that sulphide inclusions can be considered as spheres of equivalent volume has been justified. For inclusions of diameters less than  $1.1 \mu\text{m}$  the data are inconclusive.

TABLE 3 : COMPARISON OF THE SIZE DISTRIBUTIONS DERIVED FROM MEASUREMENTS OF (i) SECTION AREAS: AND (ii) SECTION DIAMETERS. ALSO, A COMPARISON OF THE DISTRIBUTIONS OF THE ORIGINAL AND DUPLICATE SPECIMEN (BASED ON SECTION AREAS MEASUREMENTS). SPECIMENS TESTED WERE SPECIMAN A AND ITS DUPLICATE.

Diameter limits of the section groups, $\mu\text{m}$	Number of inclusions per $\text{m}^3$ , $N_{vi} \times 10^{-9}$		
	Based on section area	Based on section diameter +	Duplicate
0.73 - 1.10	$(5.4 \pm 0.4) \times 10^5$	$(2.1 \pm 0.7) \times 10^5$	$(7.3 \pm 1.0) \times 10^5$
1.10 - 1.59	$(2.6 \pm 0.3) \times 10^5$	$(1.8 \pm 0.6) \times 10^5$	$(4.2 \pm 1.0) \times 10^5$
1.59 - 2.32	$(2.9 \pm 0.3) \times 10^5$	$(2.2 \pm 0.5) \times 10^5$	$(3.8 \pm 0.7) \times 10^5$
2.32 - 3.48	$(2.0 \pm 0.2) \times 10^5$	$(1.7 \pm 0.3) \times 10^5$	$(3.3 \pm 0.5) \times 10^5$
3.48 - 5.00	$(9.5 \pm 1.1) \times 10^4$	$(9.0 \pm 1.8) \times 10^4$	$(8.5 \pm 1.8) \times 10^4$
5.00 - 6.95	$(2.7 \pm 0.1) \times 10^4$	$(2.4 \pm 0.2) \times 10^4$	$(1.9 \pm 0.2) \times 10^4$
6.95 - 9.65	$(6.5 \pm 0.3) \times 10^3$	$(4.1 \pm 0.9) \times 10^3$	$(5.7 \pm 0.6) \times 10^3$
9.65 - 13.38	$(7.4 \pm 0.8) \times 10^2$	$(7.0 \pm 2.9) \times 10^2$	$(7.2 \pm 1.7) \times 10^2$
13.38 - 18.44	$(5.9 \pm 8.9)$	0.0	0.0
Total number of inclusions per $\text{m}^3$ , $N_v \times 10^{-15}$	$1.41 \pm 0.09$	$0.903 \pm 0.11$	$1.98 \pm 0.12$
Mean particle Diameter, $\bar{D}$ , $\mu\text{m}$	$2.19 \pm 0.09$	$2.57 \pm 0.1$	$2.09 \pm 0.08$

+ Because of machine limitations, the chosen section interval diameter limits were different for the analyses based on section area and section diameter. For most of the intervals these differences are not significant (refer Fig. 2).

Fig. 2 - Comparison of the size distributions derived by Quantimet; sizing was based either on section area or diameter to test the sphericity of the inclusions. Specimen A was used for analysis. For purposes of clarity the confidence limits of the measurements are not presented in this figure but are given in Table 3 (See Discussion for the significance of the broken line.)



In order to discover whether or not the distribution of particles within a specimen is homogeneous, Specimen B was repeatedly sectioned and analysed. The size distributions deduced from different surfaces (Fig 3, Table 4) match in all size ranges except the 0.73 - 1.1  $\mu\text{m}$  one. Hence of the reliable groups of data, only those for the 0.73 - 1.1  $\mu\text{m}$  interval displayed an influence from micro-segregation and this is probably worse than the average of the differences between the three surfaces.

To test for the variations due to macro-segregation, the size distribution determined for Specimen B was compared with that from its 'duplicate' specimen. Both specimens were selected at random from the original ingot and both the specimens were heat treated together. The results (Table 4, Fig 4), suggest that the distributions differ significantly within the intervals 0.73 - 1.1  $\mu\text{m}$  and 1.1 to 1.59  $\mu\text{m}$  but not at larger sizes. Similar conclusions were reached from a comparison of the results from Specimen A and its duplicate, Table 3. Thus macro-segregation may influence the size distributions up to an inclusion diameter of 1.59  $\mu\text{m}$  but probably not beyond. However, its effect on  $N_{vj}$  is significantly large because of the large numbers of the smaller particles.

**VARIATIONS INTRODUCED BY THE INSTRUMENTS** - The factors belonging to this category and which influence the measured parameters arise from the operational characteristics of the Quantimet machine and the limitations on the resolution of any optical system. These variables are:

Errors due to the instrument - Of course, certain errors can be minimised by observing the suggested precautions [2,11]. It may be taken as read that such procedures should be and were always adopted. However, other variables are less easy to control and it is their effects that are discussed here.

Tests carried out to determine the influence of drift in the instrument settings have shown a maximum variation of 14% in the measured area fraction when the image of the largest section was not greater than 10 picture points (pp) on the screen. However, this variation reduces to 2% when fields containing larger inclusions (up to 100 pp image size) were examined. A series of tests was performed to establish the influence of setting the optimum focus, and the intensity on the monitor screen.. These were found to have no measurable influence.

Earlier studies [2, 3] indicated that (i) the threshold setting influences considerably the number of sections 'counted', and (ii) near the optimum setting of the threshold level, the area fraction of the second phase determined increases lineally with an increase in the level of the threshold setting. During this experimental work an area basis was used to size the sections and thus it was desirable to have a reliable estimate of its influence. The group most likely to be affected by this threshold level setting is the smallest one, therefore Specimen B was chosen for this test. The test was conducted by resubmitting Specimen B unmarked, amongst different groups of specimens, without the knowledge of the operator. The results of the comparison are shown in Table 4 and Fig 5. They indicate that there was no significant difference generated by this influence alone.

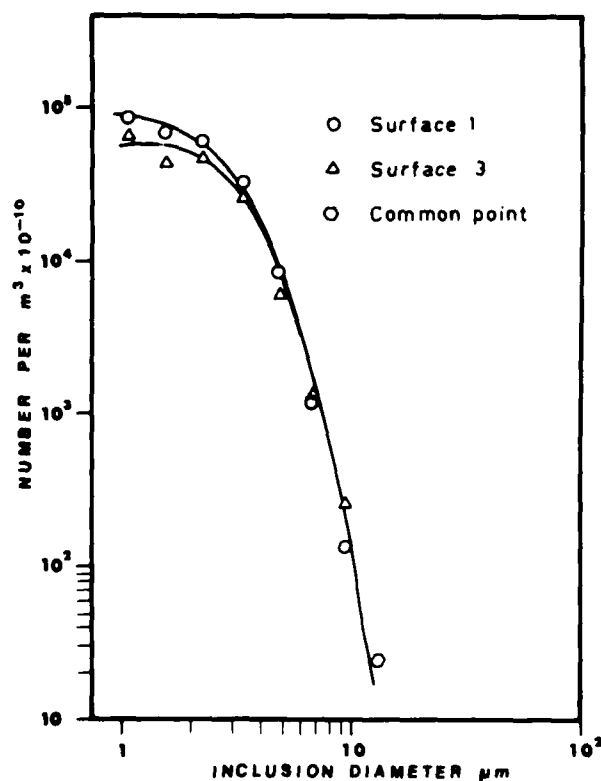


Fig. 3 - Influence of microsegregation revealed by a comparison of the distributions derived from different surfaces (Surfaces 1 and 3) of Specimen B. Analysis was based on section area. The confidence limits are omitted from this figure for clarity but are given in Table 4.

#### Variations due to the optical resolution limit -

The purposes of the study were to find (a) at what level are the measurements influenced by the limited optical resolution and (b) the reliability of 'Quantimet' measurements to isolate the second factor. The machine measurements on a particular specimen were checked by manual counting. Two possible sources of error in manual counting are (a) limitations of optical resolution; and (b) the statistical error due to counting. The latter source is a measurable quantity.

In manual counting the inclusion sections were assessed using a 'Carl- Zeiss TGZ 3 Particle Size Analyzer'. The analyzer sizes the sections by equating their area to that of a circle [12].

The size distributions representative of the finest and the coarsest level are compared by manual and instrumental counting in Fig 6 and Table 5. This comparison shows that at the 95% level of confidence, the number of inclusions determined by both techniques are the same for all sizes of inclusions in the specimen of the as-cast S steel. However, for Specimen A, the distributions do not match for inclusion diameters below

TABLE 4 : INFLUENCE OF THRESHOLD SETTING, MICROSEGREGATION AND MACROSEGREGATION ON THE DETERMINATION OF INCLUSION SIZE DISTRIBUTION (NPD) - SPECIMENS ANALYZED WERE SPECIMEN B AND ITS DUPLICATE

Section group diameter limits, $\mu\text{m}$	Number of inclusions per $\text{m}^3$ , $N_{Vi} \times 10^{-9}$				
	First set of measurements (Surface 1)	After a time lapse with the threshold reset	Repolished from 240 grit emery paper		Duplicate Specimen
			Surface section 2	Surface section 3	
0.73 - 1.10	$(8.7 \pm 1.1) \times 10^5$	$(1.04 \pm 0.14) \times 10^6$	$(2.7 \pm 0.37) \times 10^6$	$(6.6 \pm 0.9) \times 10^5$	$(1.3 \pm 0.17) \times 10^6$
1.10 - 1.59	$(7.0 \pm 1.7) \times 10^5$	$(6.3 \pm 1.5) \times 10^5$	$(4.4 \pm 1.1) \times 10^5$	$(4.4 \pm 1.1) \times 10^5$	$(1.3 \pm 0.3) \times 10^6$
1.59 - 2.32	$(6.1 \pm 1.1) \times 10^5$	$(5.3 \pm 0.95) \times 10^5$	$(5.6 \pm 1.0) \times 10^5$	$(4.7 \pm 0.9) \times 10^5$	$(8.3 \pm 1.5) \times 10^5$
2.32 - 3.48	$(3.3 \pm 0.5) \times 10^5$	$(2.9 \pm 0.4) \times 10^5$	$(2.6 \pm 0.4) \times 10^5$	$(2.6 \pm 0.4) \times 10^5$	$(2.7 \pm 0.4) \times 10^5$
3.48 - 5.00	$(8.6 \pm 1.8) \times 10^4$	$(1.1 \pm 0.2) \times 10^5$	$(6.7 \pm 1.4) \times 10^4$	$(6.1 \pm 1.3) \times 10^4$	$(8.3 \pm 1.7) \times 10^4$
5.00 - 6.95	$(1.2 \pm 0.1) \times 10^4$	$(1.15 \pm 0.12) \times 10^4$	$(1.6 \pm 0.2) \times 10^4$	$(1.4 \pm 0.14) \times 10^4$	$(1.6 \pm 0.2) \times 10^4$
6.95 - 9.65	$(1.4 \pm 0.2) \times 10^3$	$(2.5 \pm 0.3) \times 10^3$	$(3.4 \pm 0.4) \times 10^3$	$(2.6 \pm 0.3) \times 10^3$	$(1.3 \pm 0.14) \times 10^3$
9.65 - 13.38	$(2.5 \pm 0.6) \times 10^2$	$(2.1 \pm 0.5) \times 10^2$	$(3.3 \pm 0.8) \times 10^2$	$(2.34 \pm 0.54) \times 10^2$	$(2.3 \pm 0.53) \times 10^1$
13.38 - 18.44	0.0	0.0	0.0	0.0	0.0
Total number of inclusions per $\text{m}^3$ , $N_V \times 10^{-15}$	$2.61 \pm 0.16$	$2.61 \pm 0.16$	$4.07 \pm 0.24$	$1.91 \pm 0.11$	$3.7 \pm 0.22$
Average diameter $\bar{D}$ , $\mu\text{m}$	$1.98 \pm 0.08$	$1.93 \pm 0.08$	$1.57 \pm 0.06$	$2.02 \pm 0.08$	$1.82 \pm 0.07$

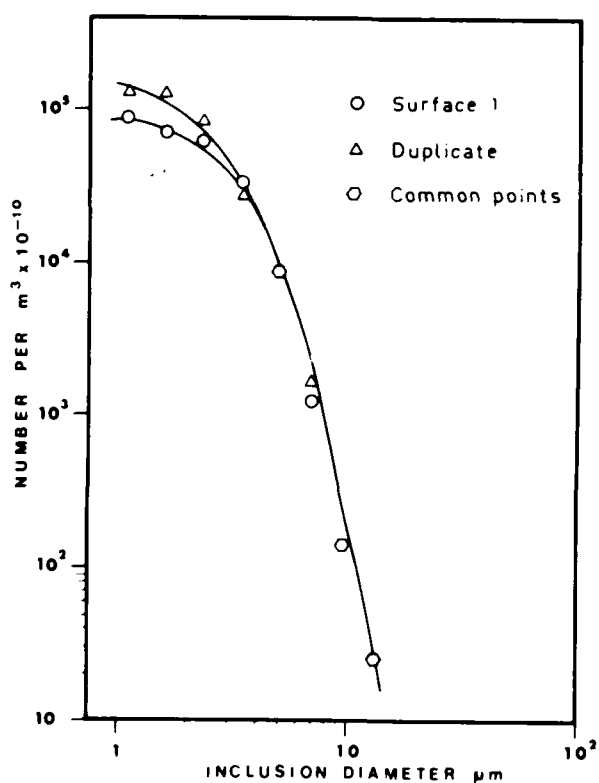


Fig. 4 - Influence of macrosegregation revealed by a comparison of the size distributions of Specimen B and its duplicate. Analysis was based on section area. The confidence limits are omitted from this figure for clarity but are given in Table 4.

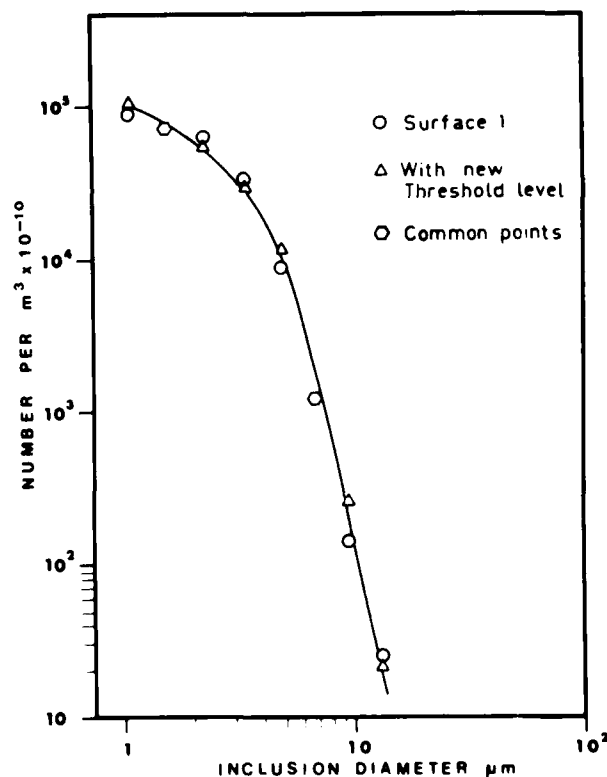


Fig. 5 - Influence of the threshold setting on the size distributions. Specimen B was analysed based on section area. The confidence limits are omitted from this figure for clarity but are given in Table 4.

TABLE 5 : COMPARISON OF THE INCLUSION SIZE DISTRIBUTIONS (NPD) DERIVED BY THE MANUAL COUNT AND THE "QUANTIMET"

As-Cast S Steel sample			Sample of Cast S Steel held at 1350 °C for 100 hours (SPECIMEN A)		
Diameter limits of section groups, $\mu\text{m}$	Number of inclusions, $N_{vi} \times 10^{-9}, \text{m}^{-3}$		Diameter limits of section groups, $\mu\text{m}$	Number of inclusions, $N_{vi} \times 10^{-9}, \text{m}^{-3}$	
	Manually Counted <sup>†</sup>	By "Quantimet" <sup>*</sup>		Manually Counted <sup>†</sup>	By "Quantimet"
0.80 - 1.18	$(1.1 \pm 0.4) \times 10^6$	$(1.5 \pm 0.2) \times 10^6$	0.73 - 1.10	$(2.1 \pm 1.2) \times 10^5$	$(5.4 \pm 0.7) \times 10^5$
1.18 - 1.76	$(1.0 \pm 0.2) \times 10^6$	$(7.4 \pm 1.8) \times 10^5$	1.10 - 1.59	$(2.1 \pm 0.53) \times 10^5$	$(2.6 \pm 0.6) \times 10^5$
1.76 - 2.33	$(3.6 \pm 0.9) \times 10^5$	$(3.0 \pm 0.5) \times 10^5$	1.59 - 2.32	$(2.8 \pm 0.5) \times 10^5$	$(2.9 \pm 0.5) \times 10^5$
2.33 - 3.47	$(1.6 \pm 0.6) \times 10^5$	$(1.1 \pm 0.2) \times 10^5$	2.32 - 3.48	$(2.2 \pm 0.34) \times 10^5$	$(2.0 \pm 0.3) \times 10^5$
3.47 - 5.00	$(2.2 \pm 1.9) \times 10^4$	$(4.6 \pm 1.0) \times 10^4$	3.48 - 5.00	$(7.5 \pm 1.0) \times 10^4$	$(9.5 \pm 2.0) \times 10^4$
5.00 - 6.95		$(6.2 \pm 0.6) \times 10^3$	5.00 - 6.95		$(2.7 \pm 0.3) \times 10^4$
6.95 - 9.73		$(1.2 \pm 0.13) \times 10^3$	6.95 - 9.65		$(6.5 \pm 0.7) \times 10^3$
9.73 - 13.38		$(1.5 \pm 0.4) \times 10^2$	9.65 - 13.38		$(7.4 \pm 1.7) \times 10^2$
13.38 - 18.44		0.0	13.38 - 18.44		0.0
Total number of inclusions $N_v \times 10^{-15}, \text{m}^{-3}$	$2.57 \pm 0.72$	$2.65 \pm 0.16$		$1.03 \pm 0.08$	$1.41 \pm 0.08$
Average diameter, $\bar{D}, \mu\text{m}$	$1.77 \pm 0.07$	$1.79 \pm 0.07$		$2.54 \pm 0.15$	$2.19 \pm 0.09$

<sup>†</sup> Because of machine limitations, the diameter limits of the section groups used for manual counting do not exactly match those used for the "Quantimet" counting. However the difference is not significant (see Fig. 6).

<sup>\*</sup> The sections were sized based on their diameter and not on their areas (see Discussion for the reasons for the choice of this method of sizing).

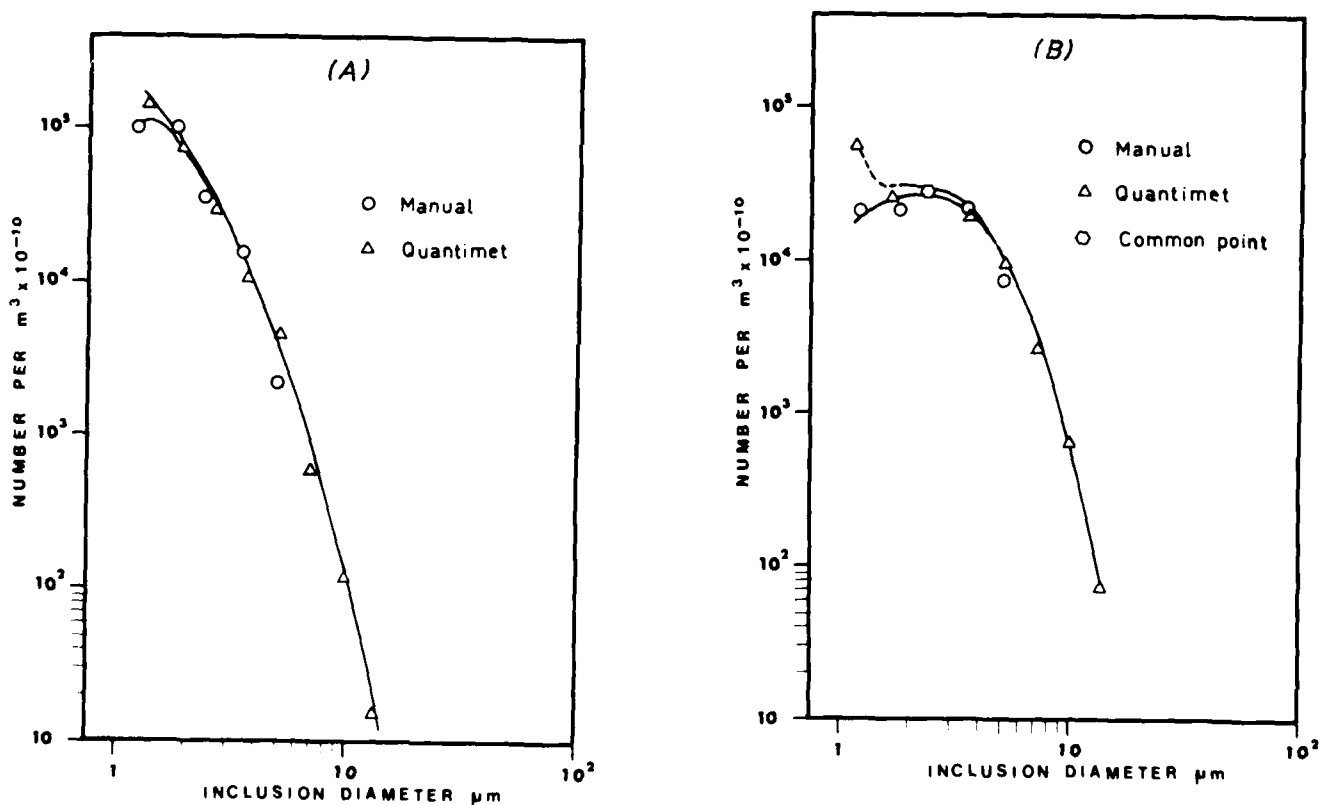


Fig. 6 - Comparison of the size distributions derived by manual and Quantimet counting for (a) as-cast S steel specimen and (b) Specimen A. The Quantimet data were collected based on section diameter for case (a) and section area for case (b). The confidence limits are omitted from this figure but are given in Table 5. (See Discussion for the significance of the broken line.)

TABLE 6: SOURCES AND MAGNITUDES OF ERRORS IN THE SIZE DISTRIBUTIONS, AND THE SIZE LEVEL AT WHICH THE INFLUENCE MAY BE NOTICED AT THE 95% LEVEL OF CONFIDENCE

Sources of error	% Error noticed in $N_{vi}$		% Difference in $N_v$	% Difference in $\bar{D}$
	Inclusion sizes influenced, $\mu m$	% magnitude		
1. Counting error	0.5 - 0.73 0.73 - 1.10 >13	98 13 >300	6	4
2. Sphericity approximation	0.73 - 1.10	45	22	8
3. Microsegregation				
(i) Surfaces 1, 2	0.73 - 1.10	52	22	12
(ii) Surfaces 1, 3	not within the examined range	-	15	1
(iii) Surfaces 2, 3	0.73 - 1.10	61	36	13
4. Macrosegregation				
(i) Specimen A	0.73 - 1.10 1.10 - 1.59	15 25	17	2
(ii) Specimen B	0.73 - 1.10 1.10 - 1.59	19 29	41	4
5. Comparison between the manual and the 'Quantimet' counting (Specimen A)	0.73 - 1.10	44	16	7.4
6. From one - factor analysis of variance total error in the system			73	17

1.10  $\mu m$ . The Quantimet has measured a larger number of inclusions than manually measured in this size range.

## DISCUSSION

The results presented so far have helped to identify the sources, which may cause variations in measured size distributions. In controlled experiments, the magnitudes of these errors were measured for each individual source. In most studies, the two parameters commonly used are the average diameter,  $\bar{D}$ , and to a lesser extent, the total number of particles per unit volume,  $N_v$ . In this section, the magnitude of the inaccuracies in these two parameters  $N_v$  and  $\bar{D}$  are estimated from a combination of all the listed sources of error. Before evaluating the total error, an attempt was made to determine which of the possible errors were contributing.

The per cent difference between the size distributions was deduced for each source of error. The comparison was made by taking into account the 95% confidence limits of the measurement of  $N_{vi}$ . The size range within which significant differences were noticed and the percentage of these differences in  $N_{vi}$ ,  $N_v$  and  $\bar{D}$  are listed in Table 6 for each source. The differences were estimated from the mean value of the two distributions used for comparison.

A comparison of the 95% confidence error range for manual and machine countings of Specimen A (Table 5) reveals the following features. The per cent errors due to counting are similar for size ranges 1.1 to 5.0  $\mu m$ , but not for the 0.73 - 1.1  $\mu m$  interval. In this one the manual counting yields an error range of 54% compared to 13% by machine counting. This comparison is valid since the magnification, and resolution in both cases were nearly equal, about 3000 x and 0.2  $\mu m$  respectively, and the area of the specimen surface examined for manual counting ( $3.58 \times 10^{-7} m^2$ ) compares well with that for the machine counting ( $3.24 \times 10^{-7} m^2$ ).

The reasons for the larger error range associated with manual counting are examined first. The British Standards [5] suggest that considerable errors can arise if the particle size is below 0.8  $\mu m$ , even though the recommended minimum measured image size of 1.5 mm in diameter is fulfilled. By using diffraction conditions, Franklin [13] deduced that for particles of diameter about five times the limit of resolution, the sizing of particles by the measurement of diameter is accurate to about 20% while the sizing based on the section area has a precision of about 40%. The resolution limits of the 125 x (N.A. = 1.3) or the 100 x (N.A. = 1.2) oil immersion objective lenses are about 0.2  $\mu m$  with a radiation of wave length 0.55  $\mu m$ . This is the smallest attainable resolution in most optical microscopes. Thus the limiting diameter for measurement is about 1.0  $\mu m$ . In actual practice the sharpness of the interface and hence the accuracy of the measured particle size is influenced by not only the diffraction condition but the optical reflectivity of the particles and the matrix and the relative flow of the materials at the interface during polishing. Under these conditions, the very large error range noticed for the interval 0.73 - 1.1  $\mu m$  during manual counting is not surprising.

In contrast the measurements by the machine displayed a narrow confidence range for this size interval. The number of particles per unit volume deduced for this size range by manual counting is much smaller than that deduced by the machine. As mentioned earlier, the manual counting does not suffer from any systematic errors arising from the machine. Hence it may be concluded that the machine over counted the sections present in the range 0.73 - 1.1  $\mu m$ . This extra count is hereafter referred to as 'noise' and is electronic in origin rather than optical. (In Figs 2 and 6 the extra count is represented by a broken line). Since the error range is drastically reduced during machine counting (cf. 13% with 54%), the noise contribution must possess a very small standard deviation, ie a near constant number of counts was added onto the actual number of sections in the range 0.73 - 1.1  $\mu m$ .

The complete size distribution derived for Specimen A on a diameter basis is not significantly different from that found by manual counting (cf. Tables 3 and 5). Similarly the as-cast S steel particle size distribution, analysed on the machine on a diameter basis, matches well with the manually counted one (Table 5 and Fig 6). From these observations the following conclusions may be drawn:



TABLE 7: ONE-FACTOR ANALYSIS OF VARIANCE APPLIED TO 19 PAIRS OF STEEL SPECIMENS ANNEALED AT 1350 °C - PARAMETERS STUDIED ARE TOTAL NUMBER OF INCLUSIONS PER UNIT VOLUME,  $N_V$ , AND AVERAGE DIAMETER OF INCLUSIONS,  $\bar{D}$

Grand mean of  $N_V = 1.56 \times 10^{15} \text{ m}^{-3}$

Grand mean of  $\bar{D} = 2.391 \text{ }\mu\text{m}$

ANALYSIS OF VARIANCE

Variation	Based on $N_V$			Based on $\bar{D}$		
	df	variance $\times 10^{-30} \text{ m}^{-6}$	F	df	variance $\mu\text{m}^2$	F
Within treatments	18	1.839		18	0.398	
Residual	19	0.672	2.74	19	0.087	4.56

df - degrees of freedom

F - variance ratio

$$\text{Standard error in } N_V = \sqrt{\frac{0.672 \times 10^{30}}{2}} = 0.58 \times 10^{15} \text{ m}^{-3}$$

% error in grand mean  $N_V$  at the 95% level of confidence = 73%

$$\text{Standard error in } \bar{D} = \sqrt{\frac{0.087}{2}} = 0.209 \text{ }\mu\text{m}$$

% error in grand mean  $\bar{D}$  at the 95% level of confidence = 17%

Interpolated value of  $F_{.05}$  for (18/19) df = 2.19

(i) The 'noise' contribution to the total count for the 0.73 - 1.1  $\mu\text{m}$  size interval occurs only for machine sizing based on section area and is nearly absent on a diameter basis.

(ii) The spherical shape approximation is valid for this system.

The results have demonstrated that machine features such as the grey level selector, optimum focus etc. do not have a significant effect on the measurements. Therefore, apart from the counting error, the other two sources are micro- and macro-segregation.

An elegant method for the estimation of the error involves the examination of the data by a one-factor analysis of variance [14,15]. The residual error [14] contains the contributions from both sources of variation, viz. the technical (ie counting error in this study) and the unknown systematic (micro- and macro-segregation variance). To apply this method, the unknown error should be completely randomised within the specimens.

Nineteen pairs of specimens were annealed at 1350 °C for different durations for the above analysis. From the specimens' size distributions,  $N_V$  and  $\bar{D}$  data were extracted and these parameters were tested for one-factor analysis of variance, Table 7. It may be

seen that the per cent errors for the system (expressed as a percentage of the grand mean value) at the 95% level of confidence are 73% and 17% for  $N_V$  and  $\bar{D}$  respectively.

An alternative basis for the representation of the size distribution is that of the volume fraction of the inclusions present in any particular size interval ( $V_{Vi}$ ). This approach results in far more emphasis being given to the larger particles and less to the large number of small particles. There are various reasons for considering that this is a valid and more reliable approach to the overall problem. The most obvious is that 90 % of the total volume of the inclusions present is contained within a few large inclusions.

The counting error in determining VFD was measured in a manner similar to that for NPD. A comparison of these results, Table 8, with those for NPD, Table 2, show that they are similar in each size interval. Therefore to determine either NPD or VFD with a given accuracy the sample area to be examined is nearly the same. In Fig 7 the measured VFD is compared with that derived from NPD by using ULI as the representative particle diameter. The two distributions match well. This suggests that NPD can be converted to VFD and vice versa without introducing errors.

The most obvious difference between the volume based and number based distributions from the same samples is the much larger mean particle diameter value of the former, Fig 8. This has two advantages viz.:

(a) the modal value falls in the range of sizes which exhibits the smallest counting errors (Tables 8 and 2).

(b) Critical parameters such as  $\bar{D}$  and the modal value are virtually unaffected by large fluctuations in the small size ranges ie below 1.6  $\mu\text{m}$ . Since it is these which are the major sources of errors in the particle size distributions based upon numbers (NPD), it follows that a VFD is inherently easier to determine with a much higher accuracy than a NPD.

A one factor analysis of variance was employed to compare the variations in  $V_V$ ,  $\bar{D}_V$ ,  $N_V$  and  $\bar{D}$  amongst duplicates of the specimens annealed at 1350 °C. At the 95% level of confidence these variations were 14%, 13%, 73% and 17% respectively. Thus determinations based on VFD exhibit the lowest scatter in the data. Therefore, much less effort is required to generate values which have an acceptably low level of error. One further modification is also worthwhile in this regard viz. the conversion of the VFD to a relative volume fraction distribution (RVFD). Previous work [9] has shown that the RVFD is independent of the choice of either ULI or IC as the representative interval diameter, if the section interval limits are based on a linear logarithmic scale. This is equivalent to stating that the RVFD gives a true characteristic of each size class. It also overcomes errors which are introduced into the VFD when there is a small drift in  $V_V$  values or considerable random fluctuation in them.

TABLE 8: THE PER CENT ERROR TO BE ANTICIPATED IN THE DETERMINATION OF THE SIZE DISTRIBUTIONS BASED ON THE VOLUME FRACTION OF INCLUSIONS WITHIN A SIZE INTERVAL - SPECIMEN: CAST 5 STEEL HELD AT 1350 °C FOR 100 HOURS (SPECIMEN A)

Diameter limits of section groups, $\mu\text{m}$	Volume fraction of inclusions ( $V_{vi}$ )	Standard deviation $s_{V_{vi}}$	% error anticipated at the 95% level of confidence with 75 fields under 125x lens and 50 fields under 32x lens
0.73 - 1.10	$3.23 \times 10^{-4}$	$5.65 \times 10^{-5}$	20
1.10 - 1.59	$5.06 \times 10^{-4}$	$1.43 \times 10^{-4}$	32
1.59 - 2.32	$1.62 \times 10^{-3}$	$2.70 \times 10^{-4}$	19
2.32 - 3.48	$4.28 \times 10^{-3}$	$1.04 \times 10^{-3}$	27
3.48 - 5.03	$4.83 \times 10^{-3}$	$1.24 \times 10^{-3}$	29
5.03 - 6.95	$2.41 \times 10^{-3}$	$1.14 \times 10^{-4}$	5
6.95 - 9.65	$1.41 \times 10^{-3}$	$1.72 \times 10^{-4}$	14
9.65 - 13.38	$3.68 \times 10^{-4}$	$1.49 \times 10^{-4}$	46
Total volume per cent of inclusions, $\sum V_{vi}$	1.58	0.189	13
Average diameter of the inclusions, $\bar{D}_v, \mu\text{m}$	5.06	0.151	3

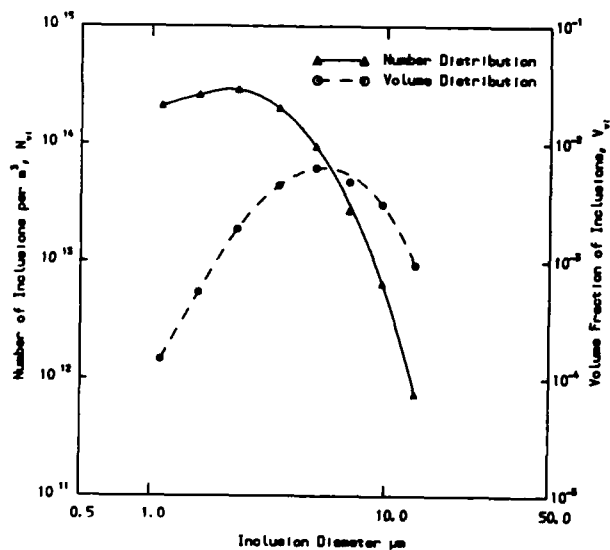


Fig. 8 - Comparison of the size distributions based on either the number of inclusions or the volume fraction of the inclusions.  $\bar{D}$  based on NPD is 2.19  $\mu\text{m}$  and  $\bar{D}_v$  based on VFD is 5.8  $\mu\text{m}$ . Specimen A was used for analysis.

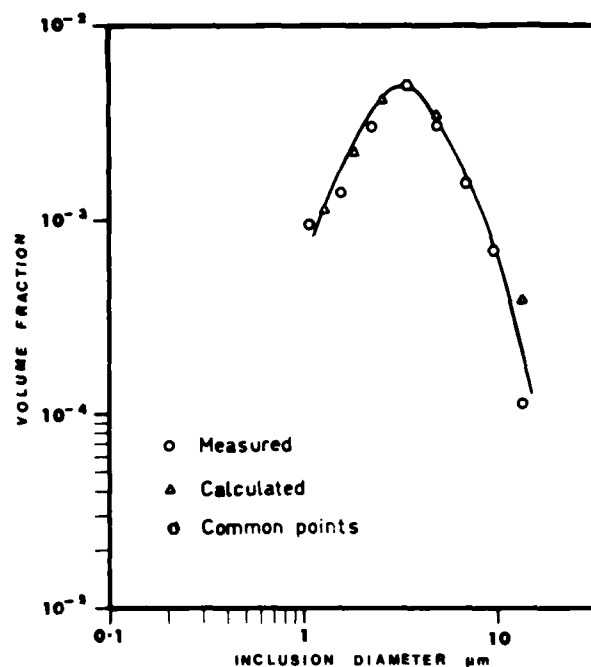


Fig. 7 - Comparison of measured and calculated volume fraction distributions (VFD) for a specimen chosen from sulphur steel ingot and annealed at 1050 °C for 50 hours. Meaningful conclusions may be drawn even without the confidence limits and therefore are omitted from the figure.

## SUMMARY

This study has identified the different sources of error in the quantitative determination of MnS type inclusion size distributions in steel. The size ranges which are influenced by these errors have also been established.

The one factor analysis of variance has been employed to determine the magnitude of the total error in the often used parameters viz. mean inclusion diameter and total number of inclusions per unit volume.

The available sectioning correction methods may be applied to this system since the spherical shape assumption for the inclusions does not introduce any significant errors.

Reasons were put forward to show that the errors which influence the size distributions based on numbers may not introduce variations in those based on volume fractions.

Although the above studies were conducted on MnS type inclusion distributions in steel the conclusions apply equally well to the quantitative optical examination of many particle systems.

## ACKNOWLEDGEMENTS

The authors are grateful to Professor E O Hall for extending to them the facilities of the department of Metallurgy at the University of Newcastle for this research. Thanks are also due to the Central Research Laboratories, Shortland of the Broken Hill Prop. Co Ltd. for the provision of the Quantimet 720 facilities and also to the Commonwealth Steel Co. Ltd for the chemical analyses of the steel samples. One of the authors (D. B. R.) is grateful to the University of Newcastle for the financial support given during the period of this research in the form of a University postgraduate Research Scholarship.

## REFERENCES

1. Bigelow L K and Flemings M C., 'Sulphide inclusions in steel', *Metall Trans B.*, 6B: 275-283 (1975).
2. Fisher C., 'New Quantimet-720', *The Microscope*, 19: 1-20 (1971).
3. Grethen E and Philippe L., 'Use of the Quantimet for the cleanness assessment of steels', *Centre Nat Rech Met.*, no 17: 53-62, (Dec 1968).
4. Brandis H., Wiebking K and Brnetzen F., 'Applicability of the quantitative television microscope (QTM) for the evaluation of cleanness of steels', *Prakt Metallogr.*, 6: 728-741 (1969).
5. British Standards, Methods for the determination of particle size of powders, BS:3406, Part 4, British Standards, London (1963).
6. Underwood E E., 'Quantitative Stereology', Addison-Wesley, Reading, Mass, Chap 5: 109-147 (1970).

7. Sims C E., 'Non-metallic constituents of steel', *Trans Met Soc., AIME*, 215: 367-393, (1959).

8. Rayaprolu D B and Jaffrey D., 'Comparison of discrete particle sectioning correction methods based on section diameter and area', *Metallography*, 15: 193-202 (1982).

9. Rayaprolu D B., 'Ostwald ripening of manganese sulphide type inclusions in steel - an analysis of techniques and errors', PhD Thesis, Department of Metallurgy, University of Newcastle, Australia (1979).

10. Hahn G J and Shapiro S S., 'Statistical models in engineering', John Wiley & Sons, New York (1967).

11. Quantimet 720, Instruction Manual, Image Analysing Computers Ltd., Cambridge.

12. Carl Ziess TGZ3, 'Particle size analyser handbook', Carl Zeiss Pty Ltd., Oberkochen.

13. Franklin A G., 'Comparison between a quantitative microscope and chemical methods for assessment of non-metallic inclusions', *J Iron Steel Inst.*, 207: 181-186 (1969).

14. Hald A., 'Statistical theory with engineering applications', John Wiley & Sons, Chap 14: 374-411, New York (1952).

15. Miller I and Freund J E., 'Probability and statistics for engineers', Prentice Hall, Engelwood Cliffs, N.J. Chap 12, (1977).

16. Cochran W G., 'Sampling techniques', 2nd ed., Chap 10: 270-291, John Wiley & Sons, New York (1963).

## APPENDIX

### GUIDELINES FOR THE DETERMINATION OF PARTICLE SIZE DISTRIBUTIONS

Principles of the recommended method are illustrated by choosing mean particle diameter as the variable of interest. However, this method holds for any other chosen parameter.

Determine the standard deviation of mean particle diameter due to the individual sources of variations viz. counting, micro- and macro- segregation. Any mean diameter measurement is a grand mean of the respective three mean diameter measurements.

$$\bar{D} = \frac{n_1 \bar{d}_1 + n_s \bar{d}_s + n_c \bar{d}_c}{n_1 + n_s + n_c}$$

where  $n_{(.)}$  refers to number of trials, and  $\bar{d}_{(.)}$  refers to the average diameter measured within those trials and

subscripts l, s and c refer to location, section and counting. From sampling theory [16] the variance of  $\bar{D}$  may be written as

$$\text{Var}(\bar{D}) = \frac{1}{n_l} s_l^2 + \frac{1}{n_s} (s_s^2 + \frac{s_c^2}{n_c})$$

where  $s_{(.)}$  refers to the standard deviation of  $\bar{d}_{(.)}$  and  $\text{Var}(\bar{D})$  is the variance of  $\bar{D}$ .

At 95% level of confidence if half the deviation is specified to be  $\epsilon$  then

$$\bar{D} \pm 1.96 \sqrt{\text{Var}(\bar{D})} = \bar{D} \pm \epsilon$$

$$\text{Var}(\bar{D}) = (\epsilon + 1.96)^2$$

Adjust  $n_l$ ,  $n_s$  and  $n_c$  such that  $\text{Var}(\bar{D})$  is of above magnitude.

# MEASUREMENT OF SPATIAL DISTRIBUTION OF INCLUSIONS

M. T. Shehata, J. D. Boyd

Metals Technology Laboratories  
CANMET - Energy, Mines & Resources Canada  
Ottawa, Ontario

## ABSTRACT

The effects of inclusions on mechanical properties of materials often depend on local values rather than mean values of quantities such as volume fraction, particle size and particle spacing. For example, a steel containing widely-spaced clusters of inclusions will have fracture properties different from one containing the same volume fraction of uniformly-spaced particles. Thus, to completely characterize inclusion distributions for correlation with mechanical properties, it is necessary to measure their spatial distribution, in addition to their size distribution and volume fraction. Modern image analysis techniques and equipment have the capability to measure and store information on the size and spatial locations of statistically-significant numbers of inclusions, and to generate the required spatial and size distributions.

This paper reviews the techniques for measuring spatial distributions, with particular reference to inclusions in steel. Three different approaches to characterizing particle spacing distributions are considered: (i) measurement of local particle density distribution; (ii) measurement of nearest-neighbour spacing distribution; and (iii) Dirichlet tessellation (based on near-neighbour spacings) and measurement of local volume fraction distribution. Measurements of inclusions in steels by all three techniques are presented, and in

each case compared with predicted values for a theoretical random distribution and a computer generated random distribution. The limitations of each technique for measuring particle-spacing distributions are discussed.

NON-METALLIC INCLUSIONS in steels have a pronounced effect on many mechanical properties such as wear (1), machinability (2), hydrogen induced cracking (3), and in particular fracture toughness (4,5). These effects depend not only on the amount, type, size and shape of the inclusions, but also on their spatial distribution (4,5). In particular, it is important whether the distribution of inclusion spacings is homogeneous or non-homogeneous. Examples of ordered, random and clustered point distributions are shown in Fig. 1. For example, it has been shown that a clustered distribution of inclusions results in lower fracture toughness than an ordered distribution (4). This may be explained in terms of the significant role of inclusions in void nucleation and/or crack initiation. It is the distribution of these voids or micro-cracks that determines the relative ease of void coalescence and accumulation of damage up to a critical local level to cause failure (4). Therefore, in order to model the mechanical behaviour of a steel containing a dispersion of inclusions (or any material containing second phase particles) it is necessary to develop techniques that quantitatively describe

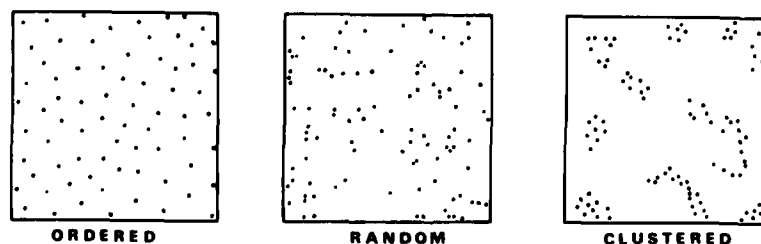


Fig. 1 - Three different point patterns showing different spatial arrangements: (a) ordered, (b) random, (c) clustered.

the characteristics of the dispersion in terms of local volume fractions and local number densities rather than overall values.

In this paper, three techniques are described to characterize the spatial distribution of inclusion dispersions in steels. For each technique, an attempt is made to quantify the degree of clustering in the distribution. The first technique is based on number density distribution measurements, sometimes referred to as sparse sampling technique or grid/quadrant counting (6). The second technique is based on nearest-neighbour spacing distribution measurements (7-9). The third technique is based on the Dirichlet tessellation (10-12) where all near-neighbours are considered rather than the nearest neighbour. The measured distributions in each case are compared with ordered, random and clustered distribution. The three techniques are evaluated and their usefulness and limitations are also discussed.

The techniques are employed in characterizing inclusion dispersions in a Ti-V microalloyed steel (13). The measurements were all made using an automatic image analysis system (Quantimet 900) with optical metallography. The measurements were made on samples obtained from the Ti-V microalloyed steel in (i) the as-cast condition, (ii) after hot rolling (80% reduction) and finish rolling temperature 700°C; longitudinal section sample, and (iii) as sample 2 but sectioned along the rolling plane section. These samples will be referred to as "as-cast", "longitudinal" and "rolling plane". An example of inclusion dispersion is shown in Fig. 2 for the inclusion population in the rolling-plane sample.

## NUMBER DENSITY DISTRIBUTION

In this method, the number of particles (inclusions) per unit area,  $N_A$ , is counted in successive locations or fields on the polished section of the steel sample. This procedure can be achieved easily by an automatic image analyzer equipped with an automated stage. A quantitative measure for the degree of inhomogeneity or clustering of the inclusion distribution in the steel sample is the standard deviation,  $\sigma$ , defined as:

$$\sigma = \sqrt{\frac{1}{n} \sum_i (N_{Ai} - \bar{N}_A)^2}$$

where  $N_{Ai}$  is the observed number of inclusions per unit area in the  $i^{\text{th}}$  location (field of view) and  $\bar{N}_A$  is the average number of inclusions per unit area in  $n$  fields viewed on the sample. Maximum homogeneity is characterized by a minimum standard deviation, and the degree of homogeneity decreases with increasing value of the standard deviation. In order to compare the relative homogeneity of inclusion dispersions in samples having different number densities the standard deviation has to be normalized by the value of the mean, i.e., the coefficient of variation,  $V$ , defined as

$$V = \frac{\sigma}{\bar{N}_A} \quad \text{should be used.}$$



Fig. 2 - Non-metallic inclusions in the rolling plane sample showing that the spatial distribution is a combination of random and clustered distributions.

The results for the number density measurements for both the as-cast and as-rolled steels are shown in Table 1.

Table 1 - Number density measurements for the as-cast steel and rolled steel.

Sample	$\bar{N}_A$	$\sigma$	$V$
As-cast	223	148	0.66
Longitudinal	337	273	0.81
Rolling plane	296	250	0.84

Note that the as-rolled steel has higher values of  $\sigma$  and  $V$  in both the longitudinal and rolling-plane sections than the as-cast steel which indicates more clustering in the as-rolled steel. Therefore, clustering of inclusions should have resulted during rolling. This may appear in contradiction with the earlier findings of Wray et al. (10) that a random array of points remains random during deformation. However, Table 1 shows that the observed clustering during rolling is accompanied by a marked increase in the number density of inclusions. The observed clustering could therefore be the result of breaking and fragmenting of large oxide or oxysulphide inclusions (or even sulphides at low rolling temperatures) into smaller inclusions. Thus, a cluster of inclusions could be the result of one large inclusion fragmented into several smaller inclusions rather than relocation of inclusions during rolling.

It should be noted that the number density technique has an important limitation in quantifying the inhomogeneity of inclusion dispersions. The measured variation may depend on the area of the measuring field relative to the area or the size of the clusters. For example, if the field area is so large that it contains a number of clusters, one may anticipate that the standard deviation will be very small. In fact, such a large field size does not sense the variation in the number density from the clustered region to the nonclustered region since both regions are contained in the measured field.

Table 2 - Coefficient of variation of number density measurements  
as a function of the area of the measuring field

Sample	Field area			
	0.96 mm <sup>2</sup>	0.24 mm <sup>2</sup>	0.06 mm <sup>2</sup>	0.015 mm <sup>2</sup>
As-cast	0.23	0.34	0.51	0.66
Longitudinal	0.23	0.38	0.62	0.81
Rolling Plane	0.31	0.49	0.69	0.84

In other words, a large measuring field implies a quasi-homogeneous distribution. The effect of field size is shown in Table 2. Note that the coefficient of variation increases for all samples as the area of the measuring field decreases. It is therefore suggested that the field area should be as small as the area of a typical cluster in order for the number density variation technique to be able to sense clusters. For example, the field area that should be used for the inclusion dispersion shown in Fig. 2 should not be larger than the size of the typical cluster of  $\sim 150 \times 100 \mu\text{m}$ .

#### NEAREST NEIGHBOUR SPACING DISTRIBUTION

First, all x and y co-ordinates of all particle centroids in the dispersion are obtained, and the distances between all pairs of particles are calculated. In a dispersion of N particles, the total number of paired spacings is  $N(N-1)/2$ . However, only one spacing for each particle is the smallest spacing corresponding to its nearest neighbour. Therefore, there are N nearest-neighbour spacings in a dispersion of N particles. These nearest-neighbour spacings can be measured easily by automatic image analysis, and a frequency distribution can be determined readily. An example is shown in Fig. 3. To describe the distribution as being ordered, random or clustered, comparisons should be

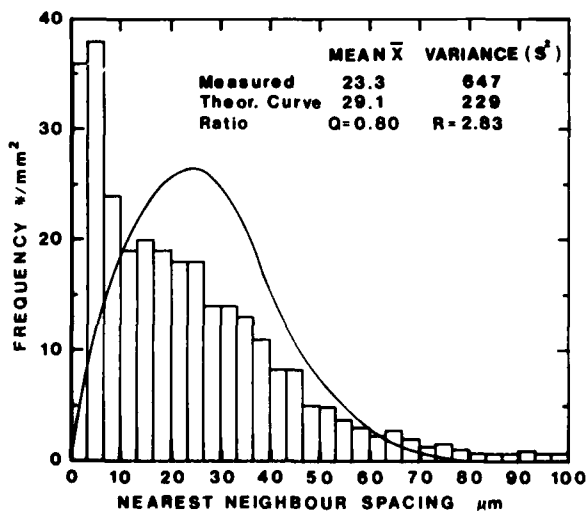


Fig. 3 - Measured nearest-neighbour spacing distribution for inclusions in the rolling plane sample compared to a Poisson's distribution.

made between the mean nearest neighbour spacing and its variance with the expected values obtained for ordered, random and clustered dispersions of points. For an ordered distribution, a hexagonal arrangement of points can be assumed (8). The expected mean nearest neighbour spacing for this ordered distribution is given by:

$$E(\chi) = \frac{1}{\sqrt{N_A}}$$

where  $N_A$  is the average number of points per unit area. The expected variance  $E(s^2) = 0$ . For a random dispersion of points, a Poisson's distribution can be assumed (9). The probability distribution function of nearest-neighbour spacing  $\chi$  is given by:

$$F(\chi) = 2\pi N_A \chi \exp(-\pi N_A \chi^2)$$

The expected mean for nearest neighbour spacing is:

$$E(\chi) = \frac{1}{2\sqrt{N_A}}$$

and expected variance

$$E(s^2) = \frac{4 - \pi}{4\pi} \cdot \frac{1}{N_A}$$

For a dispersion consisting only of clusters, the expected mean for nearest neighbour spacing

$$E(\chi) < \frac{1}{2\sqrt{N_A}}$$

and the expected variance

$$E(s^2) < \frac{4 - \pi}{4\pi} \cdot \frac{1}{N_A}$$

Therefore, it is possible to characterize the dispersion by comparison of the mean nearest neighbour spacings and its variance with the expected values obtained for a random distribution. Based on the ratio Q of the observed to the expected (for random) mean nearest neighbour spacing and the ratio R of the observed to the expected variance of

Table 3 - Measured mean nearest-neighbour spacings ( $\bar{x}$ ) and variances ( $s^2$ ) compared with expected values for a Poisson's distribution

Sample	$\bar{x}$ , $\mu\text{m}$	$S^2$	$E(\bar{x})$	$E(s^2)$	Q	R
As-cast	31.9	588	33.6	305	0.95	1.93
Longitudinal	24.8	582	27.2	201	0.91	2.91
Rolling plane	23.3	647	29.1	229	0.80	2.83

the nearest neighbour spacing the comparisons can be made as follows:

For: random dispersion  $Q \approx 1$ ,  $R \approx 1$   
ordered dispersion  $2 > Q > 1$ ,  $0 < R < 1$   
clustered dispersion  $0 < Q < 1$ ,  $0 < R < 1$

Note that for a dispersion containing sets of clusters superimposed on a background of random points (see for example Fig. 3),

$$Q < 1, \quad R > 1$$

The observed and expected mean nearest-neighbour spacing and its variance for the inclusion dispersion in the rolled steel is shown in Fig. 3, and for all samples the results are reported in Table 3. All Q values are less than one, and all R values are greater than one, which indicates that the inclusions exist in clustered sets superimposed on a background of randomly distributed inclusions for both the as-cast as well as the rolled steel. However, the deviation from randomness is much greater in the as-rolled steel than the as-cast steel as reflected by the lower values for Q and higher values for R.

The nearest-neighbour spacing technique can be very useful in describing the observed inclusion distribution as being ordered, random, clustered or composed of clusters superimposed on random inclusion distribution. It is the last distribution that is observed most frequently. In this case, the nearest-neighbour spacing technique can give some indication of the extent of clustering, but it is not a very sensitive technique since it is based on the nearest-neighbour only (7). In addition, the technique does not provide any description for clusters as to their size and spacing. To obtain this information, a complete mapping of the inclusion distribution is required. Such mapping can be provided, for example, by the Dirichlet tessellation technique which is based on all near neighbours, and can yield additional information on the surroundings of each point in the distribution. The Dirichlet tessellation technique is described in the following section.

#### DIRICHLET TESSELATION

The Dirichlet tessellation is a geometrical construction of a network of polygons around the points in a point distribution. The result of the tessellation process is the

division of the plane into convex polygons each surrounding a single point. Each polygon is uniquely defined by the positions of all near neighbours around the point. The polygons are constructed by the normal bisectors of all the lines joining the particular point to all neighbouring points as shown in Fig. 4. Note that each polygon (called a Dirichlet cell) encloses a region from the matrix for each point which is closer to that point than any other point in the point distribution. The cells are used to obtain information about the surroundings of each point in the distribution since all near neighbours are associated with the construction of the boundaries of a given cell. Near-neighbour distances, the number of near-neighbours about each point, and the area and the shape of the cells can be used to characterize the dispersion. In addition, comparisons can be made with a Dirichlet network constructed for a random dispersion of points.

To construct the Dirichlet network for an inclusion dispersion, the coordinates of the centroids of inclusions and the area of each inclusion are recorded using an automatic image analysis system. A computer program developed at MTL (formerly PMRL) is then used to construct normal bisectors and assign a unique area (Dirichlet cell) to each inclusion in the dispersion. The computer program takes care of edge effects where cells around inclusions at the

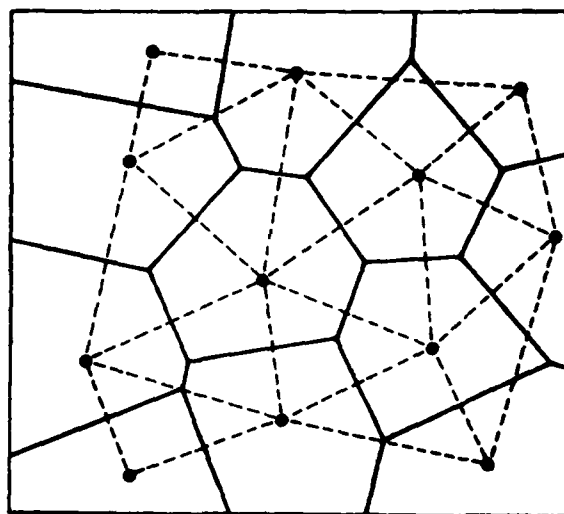


Fig. 4 - Geometrical construction of Dirichlet cells for a point array (6).



edge of one field are constructed by considering inclusions in the field as well as inclusions in the neighbouring field. Figure 5 shows the Dirichlet network for the inclusion dispersion in the as-cast steel. For the rolled steel, the Dirichlet network for the inclusion dispersion in the longitudinal plane is shown in Fig. 6 and in Fig. 7 for the rolling plane. For comparison, a Dirichlet network was constructed for a random dispersion of points where the x and y coordinates of the dispersion were obtained by a random generator. The Dirichlet network for the random dispersion which has the same number per unit area as the longitudinal plane is shown in Fig. 8 as an example. The area distributions for the Dirichlet cells constructed for the steel samples as well as the random dispersions are shown in Fig. 9, 10 and 11, and the results are reported in Table 4. Note here that the results of the area

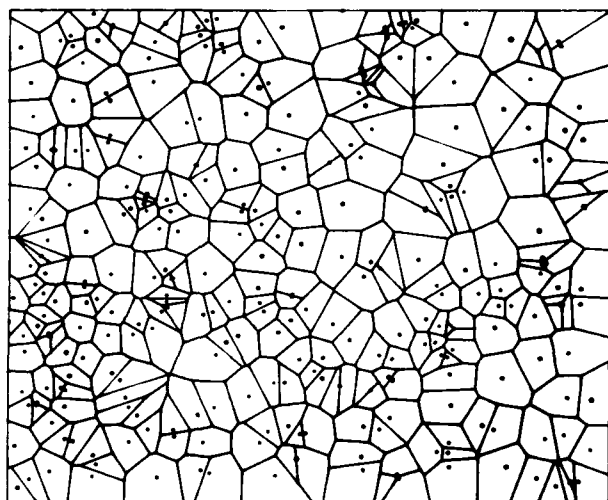


Fig. 5 - Dirichlet network for the inclusion distribution in the as-cast sample.

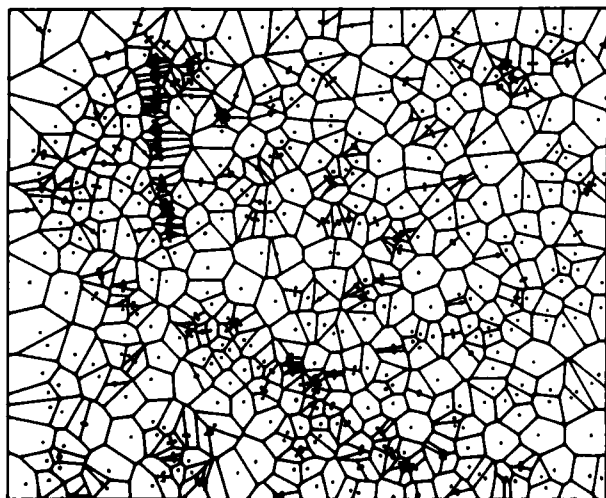


Fig. 6 - Dirichlet network for the inclusion distribution in the longitudinal sample.

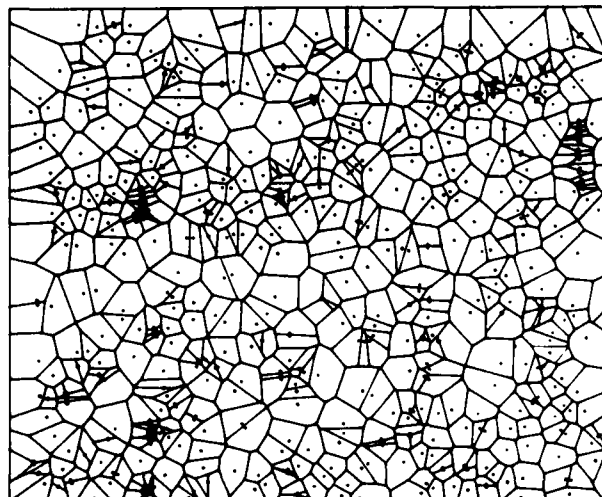


Fig. 7 - Dirichlet network for the inclusion distribution in the rolling plane sample.

distribution of the cells constructed for the randomly generated point dispersion shown in Fig. 9, 10 and 11 follow a Poisson's distribution. This is also reflected by the value of the standard deviation,  $\sigma$ , and coefficient of variation,  $V$ , which is very close to that of a Poisson's distribution:

$$\sqrt{\frac{4 - \pi}{4\pi}} = 0.52$$

In addition, comparison of values of  $\sigma$  and  $V$  shown in Table 4 indicate that the inclusion dispersion in the as-cast steel ( $V = 0.64$ ) is not random but closer to random than the as-rolled steel in the longitudinal plane ( $V = 0.79$ ) and in the rolling plane ( $V = 0.76$ ).

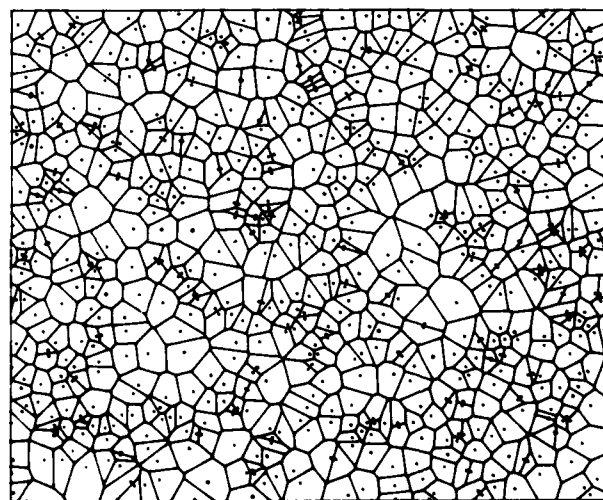


Fig. 8 - Dirichlet network for the computer-generated random distribution corresponding to the longitudinal sample.

Table 4 - Measured Dirichlet area distributions for inclusion dispersion in the steel samples compared with values obtained for computer-generated random distributions.

Sample	Average area, $\bar{A}$ $\mu\text{m}$	Standard deviation, $\sigma$	Coefficient of variation, $V$
As-cast sample	3173	2037	0.64
As-cast random	3173	1696	0.53
Longitudinal sample	1404	1107	0.79
Longitudinal random	1406	749	0.53
Rolling plane sample	1532	1166	0.76
Rolling plane random	1528	835	0.55

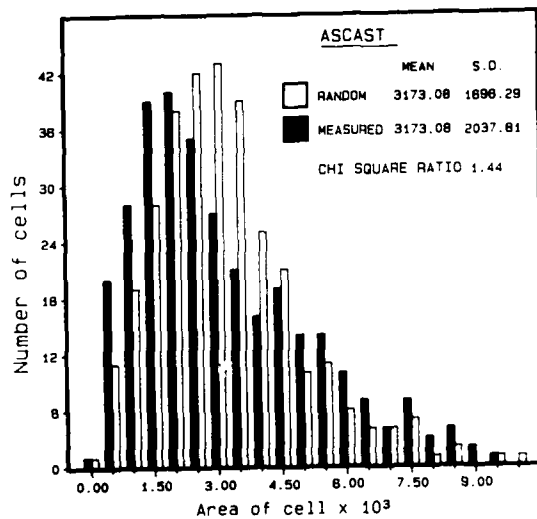


Fig. 9 - Area distributions for the Dirichlet networks for the as-cast sample and the corresponding random dispersion.

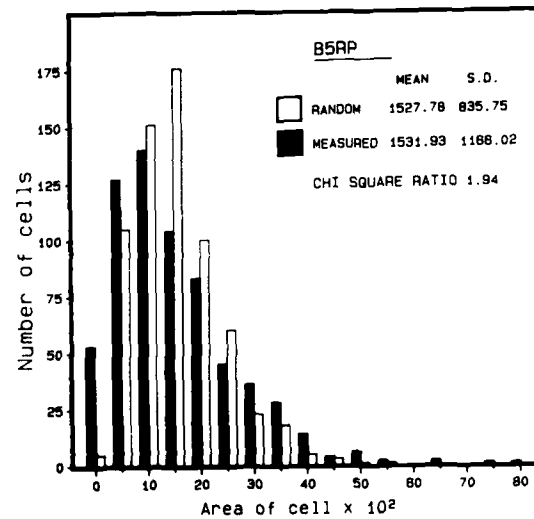


Fig. 11 - Area distributions for the Dirichlet networks for the rolling plane sample and the corresponding random dispersion.

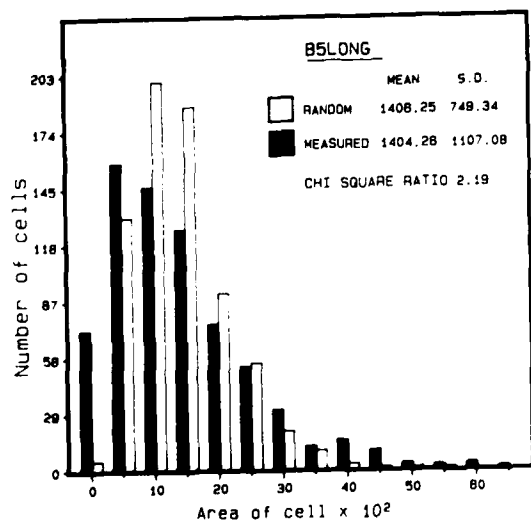


Fig. 10 - Area distributions for the Dirichlet networks for the longitudinal sample and the corresponding random dispersion.

An important advantage to the Dirichlet tessellation method is that it can be used to yield parameters which relate more directly to fracture properties, namely the local volume fraction of inclusions which is equivalent to the local area fraction. This local area fraction takes into account two important parameters that relate directly to the fracture process. The size of inclusions which relate to crack initiation and the size of the Dirichlet cell giving an indication of near-neighbour distances which relate to crack propagation. It is possible to calculate the area fraction for each inclusion as the ratio of the area of the inclusion to the area of the cell around it. For this reason, the areas of the inclusions were recorded together with the coordinates of the centroids and the computer program was expanded to obtain the local area fraction for the inclusion dispersion. In addition, random dispersions of local area fractions were also generated by dispersing inclusions of various sizes at random into Dirichlet cells constructed for a random dispersion as explained above. In this case, the random size distribution of inclusions was made to follow a log normal distribution which is found

Table 5 - Measured local area fraction distributions compared with values obtained for computer generated random distribution.

	Average local area fraction ( $\times 10^2$ )	Standard deviation, $\sigma$ ( $\times 10^2$ )	Coefficient of variation, V
As-cast sample	0.147	0.237	1.61
As-cast random	0.128	0.174	1.36
Longitudinal sample	0.605	1.83	3.02
Longitudinal random	0.283	0.347	1.23
Rolling plane sample	0.745	3.68	4.94
Rolling plane random	0.284	0.391	1.38

to be a very good approximation for the inclusion size distributions observed for many steels. The randomly generated log-normal distribution was also made to have the same mean and standard deviation as that observed for the measured sample. The results for the local area fraction distribution together with comparisons of the corresponding random dispersion for all steel samples are shown in Fig. 12-14, and are also given in Table 5. Note that the standard deviation and the coefficient of variation (represented by the slope in the logarithmic probability plots in Fig. 12-14) are higher for all steel samples than the random cases, and it is significantly higher for the as-rolled steel both in the longitudinal and rolling plane samples.

Another advantage of the Dirichlet tessellation method is that one can identify clustered regions and the degree of clustering from local area fraction values of the Dirichlet region for the whole inclusion dispersion. An example for this is shown in Fig. 15, where the clustered regions are identified by comparing the local area fraction for each Dirichlet region with the average local area fraction.

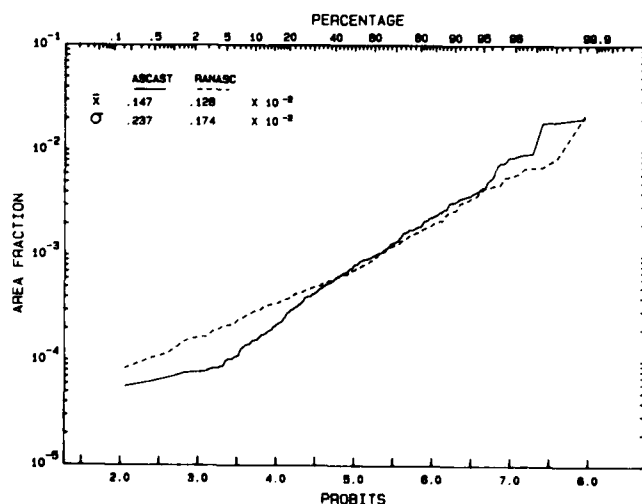


Fig. 12 - Local area fraction distributions for the as-cast sample and the corresponding random dispersion.

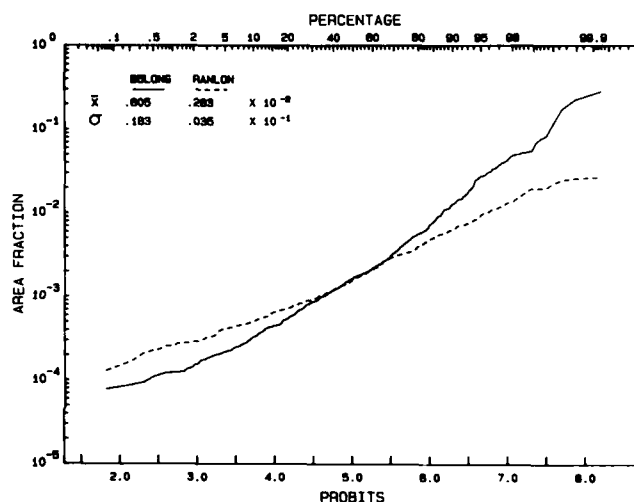


Fig. 13 - Local area fraction distributions for the longitudinal sample and the corresponding random dispersion.

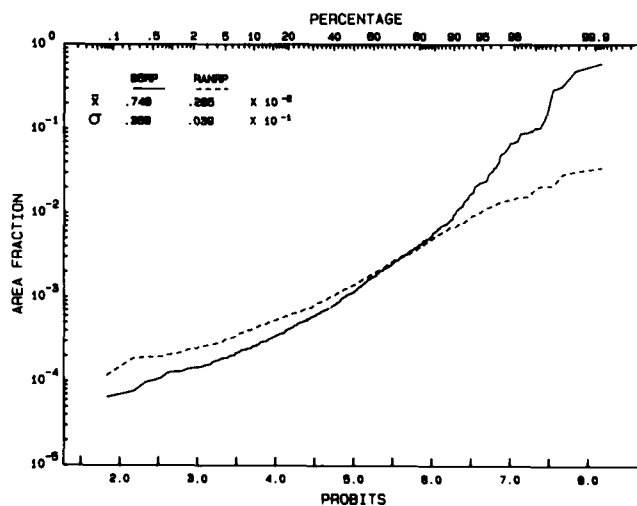


Fig. 14 - Local area fraction distributions for the rolling plane sample and the corresponding random dispersion.

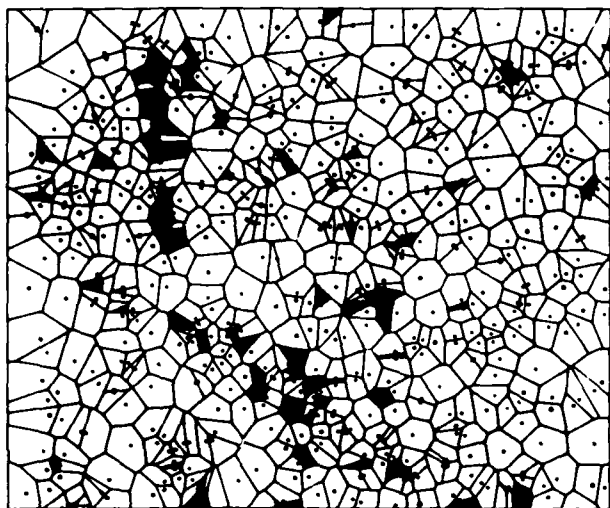


Fig. 15 - Dirichlet network for the inclusion distribution in the longitudinal sample as in Fig. 6, but the clustered regions having local area fraction higher than the average local area fraction are identified.

### SUMMARY AND CONCLUSIONS

1. This paper describes three techniques to characterize the spatial distribution of inclusions in steels using an image analysis system. The techniques are evaluated and their usefulness and limitations are also discussed.
2. The technique that is based on the number density variation is shown to be dependent on field size. It is necessary that the field area should be as small as the area of a cluster in order for the technique to sense clusters. A large measuring field would imply a quasi-homogeneous distribution.
3. The nearest-neighbour spacing distribution technique can be used to describe an inclusion distribution as ordered, random, clustered or composed of clusters superimposed on random distribution. The last case occurs frequently, and this technique can be used to give some indications to the extent of clustering. However, the technique is not very sensitive to clustering since it is based on the nearest-neighbour only.
4. The Dirichlet tessellation technique is based on all near neighbours, and can be used to yield parameters which relate more directly to fracture properties, namely the local volume fraction which could be used to identify clustered regions, and the degree of clustering in these regions.
5. The above techniques were employed in characterizing inclusion dispersions in a Ti-V microalloyed steel, in the as-cast and as-rolled conditions. The measurements

showed that the as-rolled steel contains more clusters of inclusions and a larger number density than the as-cast steel. This is explained by the breaking and fragmentation of large oxide or oxysulphide inclusions into clusters of smaller inclusions during rolling.

### ACKNOWLEDGEMENTS

The authors would like to thank B.R. Casault for his technical assistance, G. Lambert for his contribution with the Dirichlet tessellation program and J.D. Embury for useful discussions and for reviewing the manuscript.

### REFERENCES

1. D.M. Fegredo, J. Kalousek, M.T. Shehata and A. Palmer "The effect of sulphide and oxide inclusions on the wear rates of a standard C-Mn and a Cr-Mo alloy rail steel"; *Journal of Wear*, in press.
2. M.T. Shehata, V. Moore, D.E. Parsons and J.D. Boyd "Characterizations of non-metallic inclusions in steels"; *Microstructural Science, ASM/IMS*, vol. 12, 329-344; 1984.
3. M.T. Shehata, G.J. Bieffer and J.D. Boyd "Effect of non-metallic inclusions on stepwise cracking behaviour of linepipe steel"; *Microstructural Science, ASM/IMS*, vol. 13, 263-277; 1985.
4. J.D. Embury and G. Burger "The influence of microstructure on toughness"; *Proceedings of the 7th International Conference on the Strength of Metals and Alloys*, Pergamon Press, vol. 2, 1893-1915; 1985.
5. W.A. Spitzig, J.F. Kelly and O. Richmond "Quantitative characterization of second-phase populations"; *Metallography* 18; 235; 1985.
6. P.J. Diggle "Statistical analysis of spatial point patterns"; Academic Press, Chapters 4 and 5; 1983.
7. H. Schwartz and H.E. Exner "The characterization of the arrangement of feature centroids in planes and volumes"; *J. Microscopy*, 129, 155; 1983.
8. S. DeVos "The use of nearest neighbour methods"; *Tijdschrift voor Econ. en Soc. Geografie*, 64, 307; 1973.
9. E.E. Underwood; *Quantitative Stereology*; Addison-Wesley, Reading, MA; Chapter 4; 1970.
10. P.J. Wray, O. Richmond and H.L. Morrison "Use of Dirichlet tessellation for characterizing and modelling nonregular dispersions of second-phase particles"; *Metallography* 16, 39; 1983.

11. B.N. Boots "The arrangement of cells in random networks"; Metallography 15, 53; 1982.
12. I.K. Crain "The Monte-Carlo generation of random polygons"; Computers and Geosciences 4, 131; 1978.
13. B. Dogan, L.E. Collins and J.D. Boyd "Effect of thermomechanical processing on the microstructure and mechanical properties of a Ti-V-N steel"; Metallurgical Transactions; in press.

# EFFECT OF INCLUSION DISTRIBUTION ON THE INITIATION OF DEFECTS

**Paul S. Steif**

Mechanical Engineering Dept.  
Carnegie-Mellon University  
Pittsburgh, Pennsylvania 15213 USA

**Satish Iyengar**

Statistics Department  
University of Pittsburgh  
Pittsburgh, Pennsylvania 15261 USA

## ABSTRACT

Clustering of inclusions, as it affects the initiation of crack-like defects, is studied theoretically. This is done by combining a stress analysis which includes interactions between inclusions with assumed statistical distributions of inclusion spacings. It is found that reduced clustering can result in lower tendencies to initiate defects.

## INTRODUCTION

The initiation of transverse defects in rail steels under service conditions often occurs near inclusions. Producing cleaner steels, that is, steels with lower inclusion content and smaller inclusions, can to some extent ameliorate this problem. It is also possible, however, that the tendency for defects to initiate can be lessened by insuring that inclusions are well distributed and do not cluster together. To examine this possibility theoretically, we study the dependence of defect initiation on the spatial distribution of inclusions. Finally, some conclusions are drawn regarding the efficacy of manipulating the inclusion distribution to reduce the frequency of defects.

## PROBLEM STATEMENT AND ANALYSIS

The inclusions we choose to focus on are those taking the form of stringers, that is, inclusions which are long in a single dimension. We idealize these inclusions to be infinitely long cylinders. The configuration we study, therefore, is a distribution of parallel cylindrical inclusions, located in the steel matrix material (Figure 1). To simulate the shearing deformation associated with a wheel contacting the rail head, we imagine this body is subjected to a longitudinal shearing,  $\tau_0$ , as shown. The goal is to calculate the fraction of inclusions at which defects will initiate given some information about the distribution of inclusion sizes and the distribution of inclusion locations.

Following Marich and Maass[1], we adopt the following fracture-mechanics type initiation criterion:

$$\tau_{\text{local}} \sqrt{D} \geq K_0 \quad (1)$$

where  $\tau_{\text{local}}$  is the locally prevailing shear stress,  $D$  is the inclusion diameter and  $K_0$  is a toughness-like parameter which characterizes the resistance of the steel to the initiation of a defect at an inclusion.  $K_0$  depends on both the properties of the steel and the inclusion in a manner which generally is of primary significance, but is not of concern here. If a single inclusion were isolated in a large body of material, then  $\tau_{\text{local}}$  would be the remotely applied shear stress  $\tau_0$ .  $K_0$ , therefore, incorporates the effect of the stress concentration associated with a single inclusion. The means by which  $\tau_{\text{local}}$  differs from  $\tau_0$  is by having nearby inclusions interacting with the inclusion under consideration.

Let there be some given distribution of inclusion diameters. Then, *assuming the inclusions are isolated* (that is, neglecting inclusion interactions), one can calculate the number of inclusions that would initiate defects. This number would correspond to the number of inclusions that have diameters satisfying

$$D \geq \left( \frac{K_0}{\tau_0} \right)^2 \quad (2)$$

Since the effect of nearby inclusions will likely be to increase  $\tau_{\text{local}}$  above  $\tau_0$ , we consider equation (2) to represent a lower bound on the number of defects initiated.

Consider now real (non-isolated) distributions of inclusions. We break this calculation into two parts: (i) the probabilistic calculation of inclusion locations and diameters, and (ii) the calculation of the locally prevailing stress, given the relative locations of inclusions. We first turn to the stress analysis.

The problem of calculating the stress field in a body with a general distribution of inclusions is intractable. We, therefore, employ an approximate approach which we suggest is useful for the present problem in which the overall density of inclusions is low. This approach views the locally enhanced stress as due to the *pairwise interaction* of inclusions. We make use of the solution to the problem depicted in Figure 2. The part of the solution which we can extract is the average shear stress  $T$  along the line joining the inclusions; i.e.,

$$T = \frac{1}{2s} \int_{-s}^s \tau_{yz} dx \quad (3)$$

We now make the further assumption that the inclusions are not well-bonded to the steel. Since any friction stress is likely to be very low, the inclusions act as if they were holes - or inclusions with vanishingly small moduli. For the particular case of two nearby holes, an analysis similar to that given by Budiansky and Carrier[2], yields the following result for the average stress  $T$ :

$$T = \tau_o \sqrt{\frac{2D+s}{s}} \quad (4)$$

This stress enhancement associated with interacting inclusions will be used below; that is,  $T$  will replace  $\tau_{local}$  in equation (1). It is reasonable to use that average stress  $T$  to replace  $\tau_{local}$ , and not actual stress right at the inclusion, because the toughness parameter  $K_o$  (as defined above) already incorporates the stress concentration associated with a single inclusion.

The procedure for calculating the number of inclusions which initiate defects is as follows. Consider an inclusion with diameter  $D_n$ . Find its nearest neighbor, and, based on their separation, find the enhanced average stress  $T$ . Then, use the defect initiation criterion (1), with the local stress  $\tau_{local}$  set equal to  $T$ , to determine if this inclusion will initiate a defect. For simplicity, we continue to use the stress enhancement formula (4), with  $D$  representing the average of the diameters of the inclusion in question and its nearest neighbor. Now the initiation criterion reduces to

$$D \geq \omega \left[ \frac{L-D}{L+D} \right] \quad (5)$$

where,  $L = s+D$  is the separation of inclusion centers, and  $\omega = (K_o/\tau_o)^2$  depends on the toughness and the applied stress. Thus, the applied stress enters into the calculation via the parameter  $\omega$ ; the results given below are for a single value  $\omega = 90 \mu m$ . A physical interpretation of  $\omega$  is given below.

Consider now the second aspect of the calculation: the distributions of the inclusion diameters and the inter-inclusion distances. A crucial assumption we make is that the distribution of inclusion diameters is statistically independent of the distribution of inter-inclusion distances. Following Marich and Maass[1], we assume the probability density for the inclusion diameters is of the form

$$p_D(D) = aD^b \quad (6)$$

That is, the fracture of inclusions having diameters between  $D$  and  $D + dD$  is  $p_D(D)$ .

We now turn to the key variable of interest in this paper: the distribution of inter-inclusion distances. In essence, this distribution quantifies the degree of inclusion clustering. We intend to choose distributions which simulate a wide range of possible clustering. The distributions to be considered are:

- (1) No clustering
- (2) Minimal clustering
- (3) Random distribution of inclusions
- (4) Greater degrees of clustering

The case of no clustering has been mentioned earlier. It assumes all inclusions are effectively isolated from one another. This means that  $L \rightarrow \infty$ , and, hence, the initiation criterion is

$$D \geq \omega \quad (7)$$

This case, which corresponds to an infinite nearest neighbor distance, is only appropriate for vanishingly small volume fractions of inclusions. For any finite volume fraction, the inclusions will have a finite nearest neighbor distance. Note that equation (7) provides a physical interpretation of  $\omega = (K_o/\tau_o)^2$ : inclusions (of toughness  $K_o$ ) which have a diameter greater than  $\omega$  will be initiated under the stress  $\tau_o$ .

This suggests what probably is the lowest amount of clustering that is theoretically possible for a material with a finite volume fraction of inclusions: inclusion centers that are equally spaced, arranged, for example, as a square array (see Figure 3). Such a "distribution" is not achievable, but it provides a baseline for comparing subsequent results where inclusion interactions are accounted for.

Let the neighboring centers in the array be a distance  $L$  apart; then,  $L$  can be related to the areal density of inclusion,  $\rho$ , by

$$\rho = \frac{\pi}{4} \frac{E(D^2)}{L^2} \quad (8)$$

where  $E(D^2)$  is the expected value of  $D^2$ . For a given

density,  $\rho$ , and a given distribution of diameters, the inter-inclusion spacing can be determined, and, from (5), the number of defects.

Next, we consider the inclusion centers to be randomly distributed in the plane according to a Poisson process. This process is characterized by a single variable  $\lambda$ , which has the following interpretation: the expected value for the number of inclusions in an area  $A$  is equal to  $\lambda A$ . Thus,  $\lambda$  is related to the *number* density of inclusions. In this area  $A$ , the expected inclusion area is

$$\lambda A \frac{\pi}{4} E(D^2) \quad (9)$$

from which one finds that  $\lambda$  is related to the inclusion density by

$$\lambda = \frac{4}{\pi} \frac{\rho}{E(D^2)} \quad (10)$$

The fraction of inclusions that initiate defects given this distribution (or any distribution based on a random process) is likely to correspond to the minimum defect initiation rate that could *practically* be achieved by realistic techniques which disperse inclusions.

Finally, we introduce a family of inclusion-center distributions which feature degrees of clustering which are greater than that realized in the case of a random distribution. There are, of course, many ways of simulating clustering. The distributions that we chose are generated as follows (see Figures 4). First, we cast down points according to the Poisson process mentioned above. (These points are referred to as parents.) Then, around each such parent, we place  $K$  additional inclusions (called children) randomly on a circle of radius  $R$  centered at the parent. Finally, we erase the parents and take each child to constitute an inclusion center. There are now three parameters which describe the inclusion-center distribution:  $\lambda$  (describing the distribution of parents),  $K$  and  $R$ . If  $K$  were equal to 1, then the final distribution would be essentially equivalent to the random distribution. Once  $K$  is greater than 1, clustering will increase as  $R$  decreases; this occurs more rapidly if  $K$  is larger.

Note that the parameters  $K$  and  $R$  are simply a means of inducing clustering. To limit the degree of artificiality in the procedure adopted, we introduce a more intuitive measure of clustering. We define a clustering index,  $\gamma$ , to be the mean nearest neighbor distance between inclusion centers divided by the mean nearest neighbor distance between inclusion centers in the case of a random distribution. Thus, the smaller is  $\gamma$ , the greater is the departure from randomness and the greater is the degree of clustering. Below, we show that the increase in the probability of defect initiation associated

with clustering depends primarily on  $\gamma$  and not on  $K$  and  $R$  individually.

## RESULTS

Results are presented in Figure 5 for the three inclusion distributions. The upper curve (horizontal) represents the initiation probability (or fraction of inclusions which initiate defects) assuming isolated inclusions; the intermediate curve assumes a square array; and the lower curve represents a random distribution. Clearly, spacing inclusions apart from one another lowers the likelihood of defects initiating. To obtain these results, we have taken  $b = 3$ ,  $\omega = 90 \mu\text{m}$ , and the inclusion diameters to range from  $2 \mu\text{m}$  to  $150 \mu\text{m}$ .

We now turn to the results for greater degrees of clustering. On the vertical axis of the graph in Figure 6, we have plotted the probability of defect initiation ( $P_{cl}$ ) relative to the probability of defect initiation assuming random distribution of inclusion centers ( $P_{ran}$ ). This is shown as a function of the clustering index  $\gamma$ , for different values of  $K$ . The overall inclusion density has been fixed at 0.01%. As must be the case, the probabilities are equal when  $\gamma \rightarrow 1$ . Of principal interest is that the probability of defect initiation decreases by one or more orders of magnitude as the degree of clustering is moved to that associated with a random distribution. Also, note that the dependence on  $K$  is relatively slight. This shows that the results depend primarily on  $\gamma$ , and only very weakly on the precise combination of  $K$  and  $R$  which was used to achieve that degree of clustering.

To gain some sense of the relative improvements brought about by changing the clustering and changing the overall inclusion density, consider Table 1. Successive columns (left to right) correspond to decreasing degrees of clustering, as measured by  $\gamma$ . Successive rows (top to bottom) correspond to decreasing inclusion densities, as measured by  $-\log \rho$ . Using the present analysis to find the optimum approach to decreasing the likelihood of defects clearly requires a greater understanding of the difficulty and cost of achieving diminished clustering.

## SUMMARY

A means of estimating the effect of inclusion clustering on defect initiation at inclusions has been developed. Clustering has been incorporated into our calculation of defect initiation by including the stress enhancement associated with the presence of the inclusion's nearest neighbor. The dependence of defect initiation on this stress enhancement has been studied for various spatial distributions of inclusions. We found that greater improvements in the defect initiation tendency can sometimes be achieved by reducing the clustering, rather than by lowering the overall inclusion volume fraction.



## REFERENCES

1. Marich, S. and Maass, U., 1986, "Higher axle loads are feasible - economics and technology agree," Third International Heavy Haul Railway Conference, Vancouver, British Columbia, Association of American Railroads, Chicago, IL, p. IA-1-1.
2. Budiansky, B. and Carrier, G.F., 1984, "High shear stress in stiff fiber composites," *J. Appl. Mech.*, **51**, p. 733.

## ACKNOWLEDGEMENTS

The authors wish to thank Dr. Roger Steele of the Association of American Railroads for stimulating discussions on the subject of failure in rail steels. Support by the Association of American Railroads and the Department of Mechanical Engineering, Carnegie-Mellon University is gratefully acknowledged.

TABLE 1. Defect initiation probabilities

	$\gamma$	0.050	0.125	0.250	0.375	0.500	0.625	0.750	0.875	0.950	1.000
-log p											
1		0.000	0.005	0.085	0.203	0.291	0.366	0.440	0.533	0.624	0.707
2		0.002	0.269	0.450	0.619	0.738	0.842	0.952	1.104	1.280	1.481
3		0.249	0.694	0.903	1.092	1.226	1.346	1.475	1.664	1.910	2.266
4		0.669	1.161	1.380	1.577	1.716	1.841	1.976	2.179	2.454	2.906
5		1.133	1.640	1.860	2.057	2.194	2.316	2.448	2.542	2.896	3.274

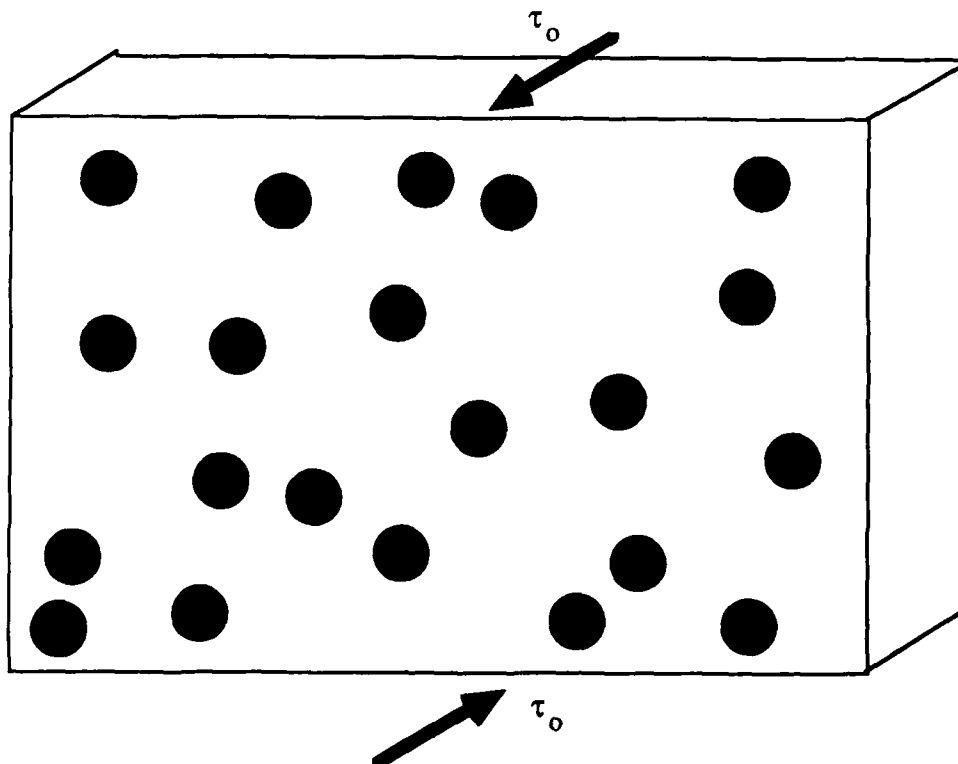


Figure 1. Schematic of loaded solid containing inclusions.

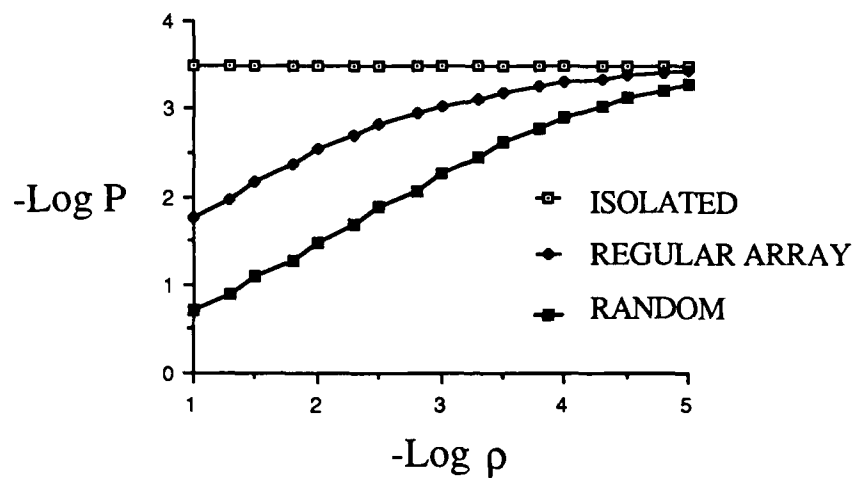


Figure 5. Comparison of defect initiation for regular array and random distributions.

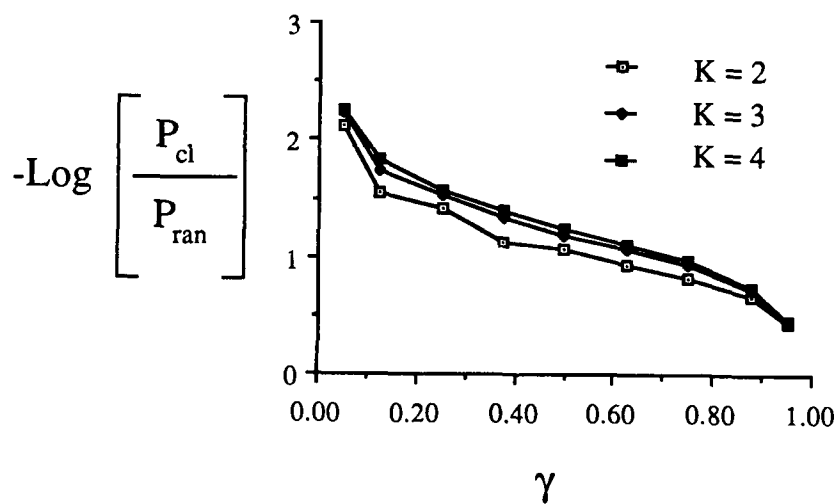


Figure 6. Defect initiation for varying degrees of inclusion clustering.

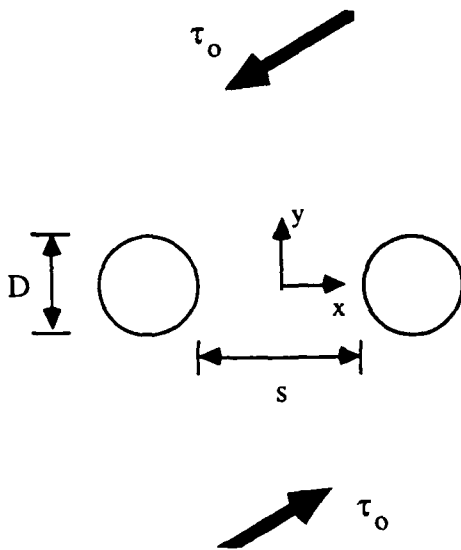


Figure 2. Schematic of interaction of two inclusions.

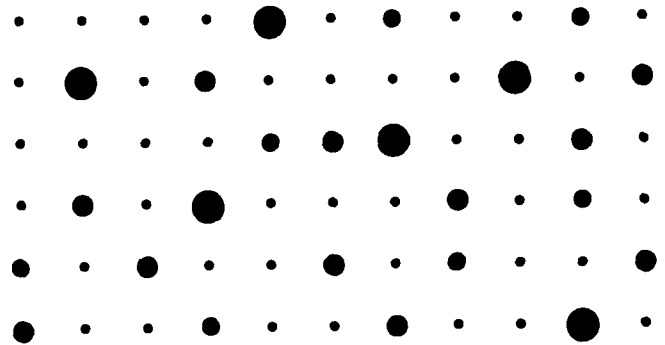


Figure 3. Schematic of regular array of inclusions.

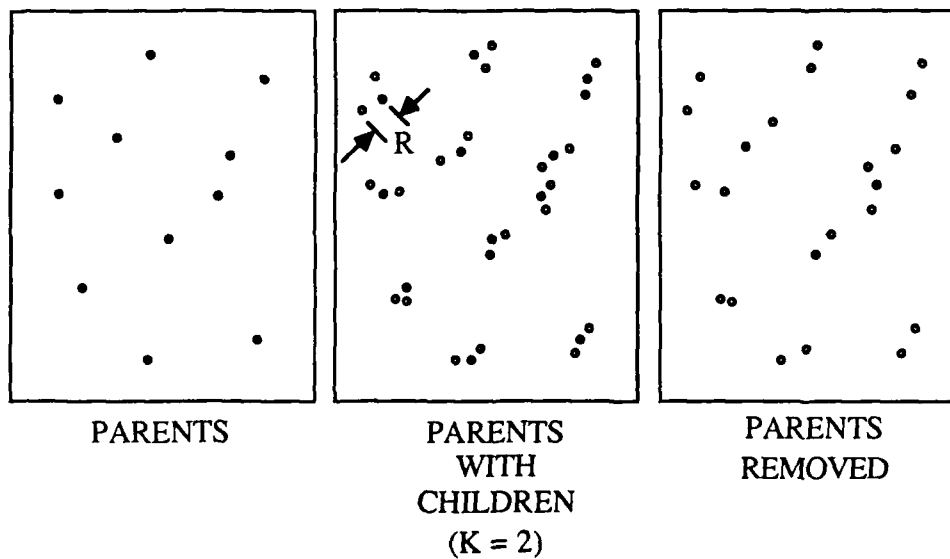


Figure 4. Schematic of process for introducing clustering.

# RARE EARTH INCLUSIONS AND CRACKING IN ERW PIPE

L. R. Cornwell, W. L. Bradley

Texas A&M University  
College Station, Texas, USA

## ABSTRACT

Analysis of cracks near the welds in electrical resistance welded (ERW) pipe showed that for all the pipes examined, rare-earth sulphides containing cerium and lanthanum were always associated with the cracks. These sulphide inclusions appear to form in layers parallel to the rolling direction and very close to the edge of the sheet. The layers are a result of segregation in the ingot during solidification. Cracks detected by ultrasonic inspection are cause for rejection of pipe and can result in lower yields. Suggestions are made for avoiding the segregation of these rare-earth sulphides.

IT IS WELL KNOWN that sulphide shape control in hot rolled steel plate improves the through thickness ductility. This improvement is important in the prevention of lamellar tearing during welding and in preventing cracking during bending operations. Steel treated in this way is often used for ERW pipe but it has been found that a crack often occurs close to the weld. This crack because of its shape is usually called a hook crack and is detected during ultrasonic non-destructive examination (NDE). If these cracks exceed 12.5% of the wall thickness then the pipe must be rejected according to American Petroleum Institute (API) standards. Much of the ERW pipe produced is used by the oil industry but as far as the authors are aware no failures have been traced to these cracks. Nevertheless since these cracks often exceed the defect size allowed by API a significant percentage of ERW pipe may be rejected.

Attempts to eliminate hook cracks have been made by reducing the sulphur content which in turn reduces the sulphide inclusion count. Griffing and Meinzen<sup>1</sup> claim that a magnesium desulphurization treatment prevented the

formation of cracks during subsequent ERW fabrication. Similarly Shinozaki et al<sup>2</sup> found that hook cracking was suppressed in flash-butt welded joints in steel wheel rim manufactured by using a steel with a low sulphur content.

These results obviously suggest a relationship between the presence of sulphides and the occurrence of hook cracks in ERW pipe. The objective of the work described here was to determine how the presence of sulphide inclusions resulted in hook cracks. The study was limited to steels which had been treated with rare earth metals to achieve shape control of the sulphides and were cast into ingots.

## EXPERIMENTAL

Samples were chosen from ERW pipe in which cracks had been detected by ultrasonic inspection. These samples were taken from the defective pipes in two ways. Sections, typically one to two feet long, were cut from the pipe in the region of the defect. In some cases the pipe was crushed by a hydraulic press to cause a longitudinal fracture through the wall thickness which usually exposed the crack surface. These samples containing both a crack surface and a fracture surface were examined in the SEM. Some of these samples were also sectioned normal to the fracture plane and prepared for examination of the microstructure by optical microscopy.

Other samples were obtained by cutting sections through the wall thickness and normal to the axis of the pipe but in the vicinity of a crack. Longitudinal samples were also taken from the pipe to examine the microstructure in the rolling direction. In both cases the samples were prepared for metallographic examination by optical and SEM/EDS microscopy.

The chemistry of the steels examined is given in Table 1 along with the wall thickness. The sulphur contents were around 0.02%. The steels had been treated in the ladle with Mischmetal but no analysis was made for the

residual rare earth metals.

## RESULTS AND DISCUSSION

The appearance of the crack surface along with the induced fracture surface is shown in Fig. 1. In some cases the crack surface was black indicating oxidation because the crack penetrated the surface. In other cases the crack surface was clean. The cracks could be as much as 20% of the wall thickness and several feet in length. An optical micrograph shown in Fig. 2 illustrates the unusual shape of the crack which gives rise to the name hook crack. Observation of the relationship between the crack shape and microstructure clearly shows that the crack follows the deformation pattern induced by the upset during electrical resistance welding.



Crack Surface

Fig. 1 - Photograph of crack and broken surface. 7.5X

The photomicrograph in Fig. 2 shows the position of the weld line with respect to the hook crack and appears to indicate no direct connection between them. The crack intersects the surface at the weld line but this is probably a coincidence. The opposite end of the crack turns roughly 90° and becomes a circumferential crack. In some cases this circumferential crack can extend for up to 5 mm. Such a crack is shown in Fig. 3 in which a line of inclusions is also obvious extending from the end of the crack.

Weld Interface

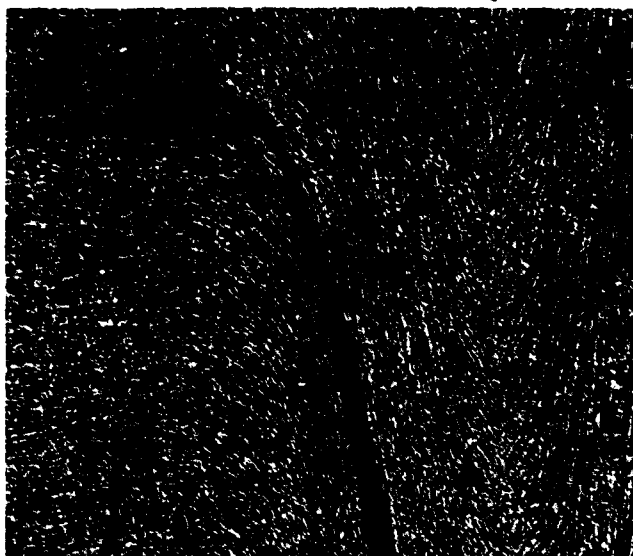


Fig. 2 - Optical photomicrograph of cross-section through pipe wall at weld hook crack. 50X



Fig. 3 - SEM of end of a hook crack and associated inclusions.

Examination of crack surfaces in the SEM confirmed the presence of large numbers of inclusions as shown by Fig. 4. A through wall thickness metallographic specimen in the longitudinal direction near the crack in Fig. 3 shows a line of inclusions which is visible to the naked eye. The position of this line coincides with the end of the crack shown in Fig. 3. Chemical analysis of these inclusions by EDS showed them to be rare earth sulphides of cerium and to a lesser extent of lanthanum (Fig. 5).

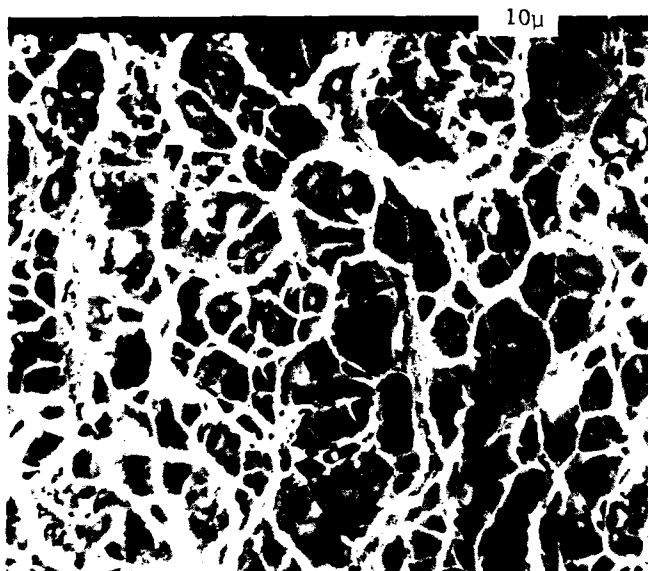


Fig. 4 - SEM of crack surface showing sulphide inclusions.

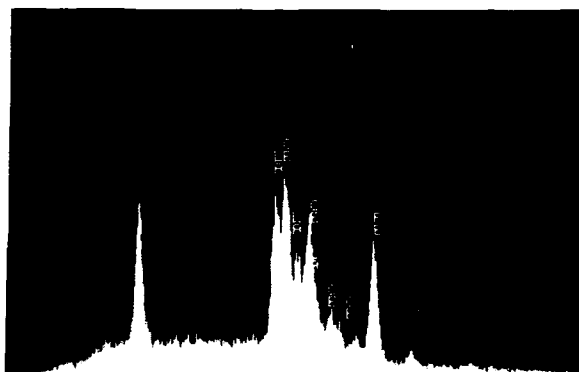


Fig. 5 - EDS of particles showing presence of cerium, lanthanum and sulphur.

In order to determine if these inclusions were oxysulphides, Auger Electron Spectroscopy was used to test for the presence of oxygen in the particles. In the two specimens examined no significant amounts of oxygen were detected hence oxysulphides are discounted.

All the hook cracks examined in this study were associated with rare-earth sulphides which have a planar distribution close to the edge of the skelp. Indeed one approach to preventing hook cracks was by trimming more from the edge of the skelp but without significant success. During welding when the edges are upset the hook cracks always follow the flow of metal and in particular in the locations where excessive sulphide inclusions occur. These observations and those of Emi et al.<sup>3</sup> point to segregation of rare-earth sulphides during solidification in the ingot. This segregation seems particularly excessive towards the bottom of the ingot.

Emi et al.<sup>3</sup> have developed a model to explain this segregation. They suggest that

as dendrites grow inwards from the mold wall rare earths and sulphur are enriched in the vicinity of the solidifying front owing to the partition of the solutes. When the solubility product reaches a critical value precipitation occurs followed by a further period of enrichment and subsequent precipitation. Some precipitates are transported by convective flow of the melt to the bottom of the ingot. This model predicts layers of rare-earth sulphides parallel to the mold walls and ultimately to the surface of rolled strip. The results of this investigation seem to support this model. These authors also suggest that keeping the atomic concentration ratio (ACR) below 1.8 where

$$ACR = \frac{1}{4.37} \frac{[\%RE_{eff}]}{[\%S]}$$

will eliminate segregation. For ERW pipe the sulphur content should be kept below 0.003% although this is to prevent hydrogen cracking and not hook cracks.

Some approaches to the prevention of hook cracks are as follows. A logical step would seem to be to reduce the number of inclusions by reducing the sulphur content. In a case previously cited<sup>1</sup>, hook cracking in ERW pipe made from strand cast steel was eliminated by magnesium injection in the ladle to reduce the sulphur content below 0.01%. In the other study<sup>2</sup> previously mentioned, hook cracks were suppressed by keeping the sulphur content below 0.005%. In the first case calcium was also used for sulphide shape control but not in the second case.

In addition to the above approach we suggest two others for consideration. Since oxysulphides were not found in the steel it is possible they are light enough to float to the top of the ingot. If this is the case then sulphides might be removed by converting them to oxysulphides by control of ladle chemistry. Another approach would be to minimize sulphide segregation. Evidence was found during this investigation that the use of fluted molds tends to promote sulphide segregation. Hence for the problem of hook cracks encountered here an obvious strategy is used for straight walled molds. So far it has not been possible to test either of these suggestions.

#### SUMMARY

Hook cracks close to the weld line in ERW pipe are associated with segregation of rare-earth sulphides. The rare-earths are cerium and lanthanum which are added to the steel for sulphide shape control. Prevention of these cracks can be achieved by removing the inclusions by reducing the sulphur level to prevent their formation or by ensuring they float to the top of the ingot. A second approach is to eliminate the segregation by control of the solidification process.

# REFERENCES

1. N.R. Griffing and D.E. Meinzen, "Mg Injection for Steel Ladle Desulphurization of Al-Killed Grades," 66th Steel Making Conference, Atlanta, pp. 351-355, AIME, 1983.
2. M. Shinozaki, M. Hashimoto, T. Kato and T. Irie, "Development of Hot-Rolled High-Strength Steel Sheets for Wheel Rim Use," Kawasaki Steel Technical Report, No. 6, pp. 21-31, Sept. 1982.
3. T. Emi, O. Haida, T. Skuraya and K. Sanbongi, Steelmaking Proceedings, Vol. 61, Chicago, AIME, April 1978.

Table 1 - Sections of Pipe With Hook Cracks

<u>Heat Number</u>	<u>Ladle Chemistry wt%</u>					<u>Crushed or Uncrushed</u>	<u>Color</u>	<u>Gauge mm(in.)</u>
	C	Mn	S	P	Si			
17258	.26	1.25	.016	.011	.13	U		7.7(.304)
57340	.29	1.39	.017	.01	.14	U		13.8(.545)
57370	.28	1.38	.02	.007	.12	C/U	Black	13.8(.545)
17128	.15	.70	.012	.011	.05	U		14.8(.582)
26489	.27	1.34	.014	.009	.13	U		14.8(.582)
26461	.25	1.12	.018	.01	.13	C	Black	13(.514)
16886	.27	1.33	.022	.011	.16	C	Black	8.9(.350)
57364	.34	1.35	.012	.01	.19	C	Clean	13.8(.545)
26605	.25	1.17	.022	.013	.12	C/U	Clean	11.3(.445)
26619	.18	1.16	.015	.006	.20	U		12.3(.485)
26513	.25	1.17	.019	.01	.12	C	Black	8(.315)
17392	.16	1.19	.015	.007	.20	C	Clean	12.4(.490)

# THE ROLE OF INCLUSIONS ON DEFORMATION AND FRACTURE UNDER TENSILE STRESS IN STEEL

A. R. He (He Zerong), L. Zheng

Dept. of Mech. Eng., Fuzhou University  
Fuzhou, Fujian, China

## ABSTRACT

By using SEM and the technique of replicas observed in situ, the mechanical behaviours of inclusions under tensile stress and the role of inclusions on the deformation and fracture of matrix in steel have been studied. Coarse, especially coarse rod-shaped inclusions are cracked first and probably at a stage as early as an elastic one, and then followed by fine inclusions. The rod-shaped inclusions undergo multiple internal fracture, while the spherical ones nucleate cracks by interfacial separation. The matrix around the inclusions is always slipped after rather than before the cracking of coarse inclusions. When the stress increases, the slips would further be developed, densified and concentrated at the local micro-region near the cracked inclusions, or at grain boundaries, or in some grains with favourable orientation. Meanwhile, the slipped regions tend to join together. Eventually, final fracture occurs and the main crack propagates close to, but not at, the heavily slipped regions containing the coarse cracked inclusions. The above-mentioned results are interpreted in terms of the theory of the elastic incompatible deformation between the inclusions and matrix, and the effect of notch ahead of crack.

The inclusions in steel, like micro-notches or blocks to pile up dislocations depending on their strength, always play an important role on stress concentration. Therefore, the deformation and fracture processes under loading would first take place at inclusions or around them. However as to the processes, particularly the details of the inclusions themselves and their adjacent matrix in steel there are not yet enough direct experimental evidences, so the mechanism of the effect of inclusions on deformation and fracture are not very clear.

Although the dynamic observation in situ of the specimen under stress directly in SEM by using a tensile holder or in TEM by using a specimen elongating holder has been made recently, it is still difficult to predict in which micro-region would the fracture occur, as the fracture always takes place at the end of deformation. In other words, it is difficult to carry out the dynamic observation previously to aim precisely at the inclusions which play an important role in final fracture. In this investigation a standard plate tensile specimen with a single edge notch is used. It is electro-polished and chemically etched and then pulled intermittently with the same loading increment. A series of corresponding plastic replicas are taken from the surface of the specimens. The replicas are observed along a route traced from a loaded specimen with an obvious crack back to that with a very small, even no strain. Thus, the morphology change of inclusions near the main crack and their adjacent matrix under loading has been surveyed, and the whole processes from deformation to fracture of inclusion and steel clarified. On this basis we are able to propose the mechanism of the effect of inclusions on deformation and fracture in steel.

## EXPERIMENTAL PROCEDURES

The material used is a mild steel sheet with the following compositions (wt%): C 0.06; Si 0.33; Mn 0.43; S 0.045; P 0.032; Fe rem. The steel sheet is cut  $\rightarrow$  930°C normalized  $\rightarrow$  machined to form a standard plate tensile specimen with single edge notch, as shown in Fig. 1. The specimens are electro-polished and chemically etched by using 10% perchloric acid and 90% glacial acetic acid and by etching in 4% nital respectively to reveal microstructure. On the surface of the specimen ahead of notch, two rows of micro-indentations marks are pressed by micro-indenter. The spacing between the indentation is 3 mm, and a replica is ob-



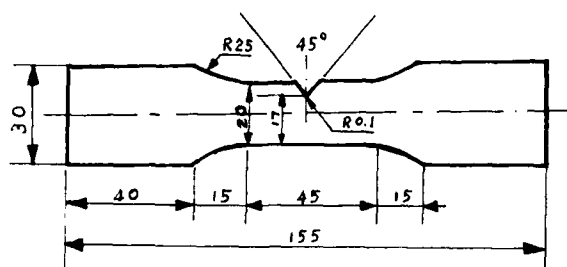


Fig. 1 Tensile specimen drawing, all dimensions in mm

tained on the specimen surface to serve as a reference. The specimen is then pulled to various intermittent points (I.P.): 0, 1, ... 7, 8 (fracture point) by the same loading increment as shown in Fig. 2 by a universal test machine WE-60 with a loading velocity of 4 mm.min<sup>-1</sup>. A series of corresponding plastic replicas are taken from the surfaces of specimen at every interruption until just before the final fracture. The load and elongation corresponding to each interrupted point are recorded directly by the test machine. Their plastic elongation ahead of notch in an intermittent interval can be measured by the corresponding difference of the spacing between the two rows of micro-indentation on the replicas, and thus the true stress and strain can be calculated.

Following the work of Brown and Smith<sup>[1]</sup>, a piece of Bioten plastic film is softened by immersion in acetone and applied to the strained specimen surface for about 3-5 mins. The replica is then carefully peeled off the surface and placed on a specimen stage made of

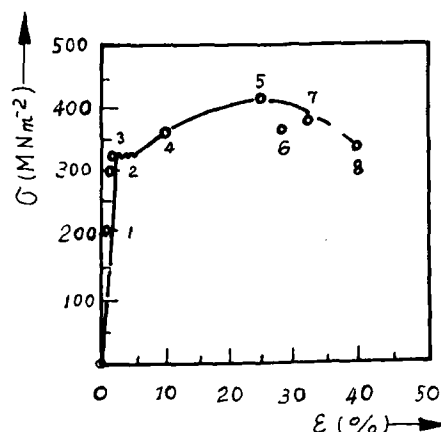
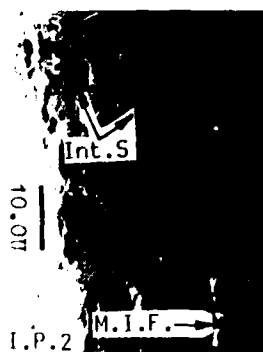


Fig. 2 - curve of serial intermittent tensile, I.P.:0,1,...7,8 (fracture point)

aluminium with the replicated portion facing upward, and coated for 5-10 seconds with platinum in an Eilo-1B5 coating unit. The coated replicas are observed and photographed by in situ technique in SEM JSM-35CF with a low accelerating voltage (10KV). The replicas were examined sequentially from a loaded specimen (where a crack is obvious) to a almost unloaded specimen, so that the morphology change of the inclusions could be examined. For comparison, some surface morphologies of specimen (Fig. 3.a; Fig. 6.b) has also been photographed directly. Here attention should be paid to the difference between the morphology of replica and that of specimen surface. The concave and convex contrast on the replica and specimen photographs are opposite. That means the concave region such as the grain boundaries, cracks and slip steps on the specimen surface are convex one on the replicas. They appeared as white regions on the replica photographs of SEM rather than black one as observed on the routine metallographic photographs. On the contrary, the convex one such as



(a)



(b)



(c)



(d)

Fig. 3 Inclusion cracking (a) interfacial separation(Int.S) and multiple internal fracture(M.I.F). (b) coarse rod-shaped inclusion (I<sub>1</sub>) multiple fraction, (c,d) fine inclusions (I<sub>2</sub>,I<sub>3</sub>) cracking

matrix grain appeared as black region on the replica photographs.

## RESULTS AND DISCUSSIONS

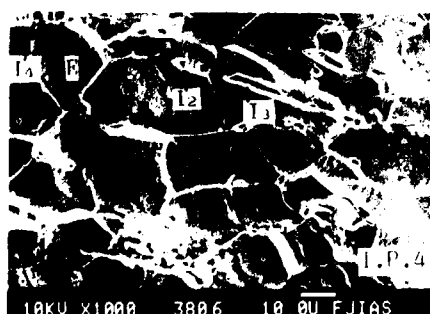
**THE MECHANICAL BEHAVIOURS OF INCLUSION IN STEEL UNDER STRESS** The inclusion morphology change corresponding to some main interrupted points is shown in Fig. 3. It can be seen that before the tensile test there is already a crack in the coarse rod-shaped inclusion  $I_1$ . The crack may have formed in the previous hot working process. With the progress of elongating process of specimen, even at a stage as early as elastic, with no slip line, i.e., no micro-plastic deformation in evidence on the specimen surface, the coarse inclusions have already been cracked. The spherical ones always appeared as the separation of interface between the inclusion and matrix (Fig. 3.a. Int.S), while the rod-shaped ones as the multiple internal fracture along the direction vertical to the tensile direction (Fig. 3.a. M.I.F.; b.  $I_1$ ). The fine inclusions such as  $I_2$ ,  $I_3$ , however, are not fractured yet. With the advance of tensile, especially as it passes over the yield point, the cracks within inclusion  $I_1$  increase (Fig. 3.b. I.P.2,3), and on the other hand the above-mentioned processes also occur in fine inclusions such as  $I_2$  (Fig. 3.d). Although the multiple internal fracture of rod-shaped inclusion has already been discovered by Broek<sup>[2]</sup> in the aluminum alloy, the critical strain  $\epsilon_{if}$  for the emerging of multiple internal fracture has not yet been found. It is shown from Fig. 3 that the multiple internal fracture in the coarse rod-shaped inclusions may occur at a stage as early as elastic, even at a micro-elastic stage. This is obviously due to the difference between the elastic modulus of inclusion  $E_i$  and that of matrix  $E_m$ , leading to two different elastic strains  $\epsilon_i$  and  $\epsilon_m$  under the same tensile stress. Moreover, this is also due to the fact that the plastic deformation in both inclusions and matrix does not start yet, and therefore there are no slips to eliminate the above-mentioned difference in the elastic strains. Thus we can see that the only way to make  $\epsilon_i$  and  $\epsilon_m$

compatible is that the weak and brittle inclusions should be fractured first. In light of the energy equilibrium principle, the authors<sup>[3]</sup> have deduced an Eq. relating  $\epsilon_{if}$  to the geometric parameters of inclusion shape as

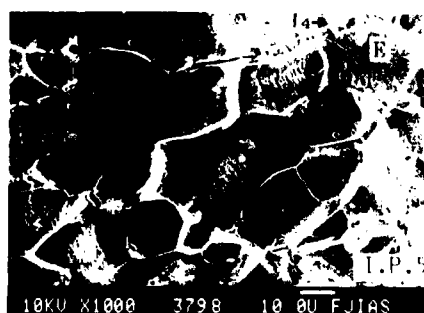
$$\epsilon_{if} = \left( \frac{4\gamma_f}{E_i L} + \frac{4l\gamma_i}{E_i L T_i} \right)^{1/2} \quad (1)$$

where  $\gamma_f$  is the surface energy of inclusion,  $L$  the length,  $l$  the internal fracture width and  $\gamma_i$ , the radius of inclusion, from Eq.(1) it can be seen that the larger, especially the longer the inclusion, the easier will the multiple internal fracture be. Thus the coarse rod-shaped inclusions should usually fracture first before its adjacent matrix deforms plastically. Then, with the increase in the stress as well as strain, the fine and short ones will also fracture.

**THE EFFECT OF INCLUSION ON THE PLASTIC DEFORMATION OF MATRIX** Fig. 4 is a micrograph showing the relation between the inclusion fracture and the plastic deformation of matrix. It is found from Fig. 4.a that although inclusion  $I_4$  itself has already been fractured, there is still no slip band, i.e., micro plastic deformation observed in evidence within the matrix around  $I_4$ . However, it can be seen from Fig. 4.b that there are a lot of slip bands in the matrix (E) around the multiple internal fractured inclusion ( $I_4$ ). Although the phenomenon of slip bands appearing on the matrix around the multiple internal fracture inclusion or carbides has been discovered<sup>[2,4]</sup>, there are still no direct experimental evidence to confirm whether the matrix slip or inclusion multiple internal fracture appears first? Barnby<sup>[5]</sup> has observed many slip bands in matrix around the multiple internal fractured coarse carbide in stainless steel, which led to the conclusion that the fracture is caused by the concentrated local stress resulting from the matrix slip bands. This is in agreement with Smith theory<sup>[6]</sup>. Can the same reason be used to explain the multiple internal fracture of inclusions? However, there is no doubt from Fig. 4.a and b that the rod-shaped inclusion fractures first, and the ma-



(a)



(b)

Fig. 4 Inclusion cracking relates to matrix slip (a) inclusion ( $I_2, I_4$ ) cracking before matrix slip, (b) matrix (E) slipping around inclusion ( $I_4$ ) multiple fracture

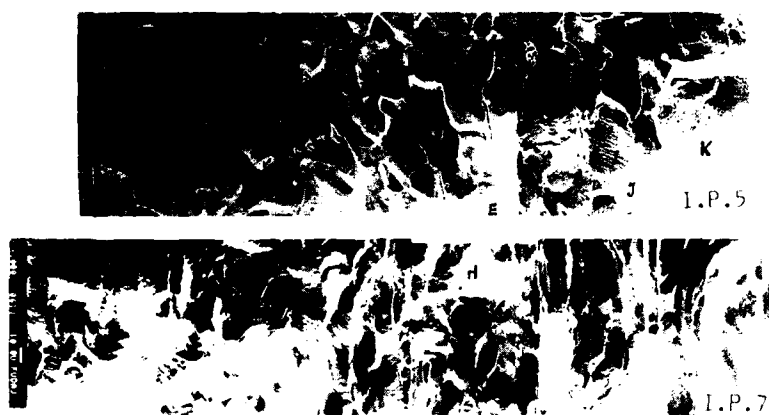


Fig. 5 Inclusion and matrix slip under tensile stress  
A, B, ... the marking of some key grains

trix slips plastically next. Obviously, this is due to the fact that the internal fracture of inclusion produces micro-notches, which leads to the stress concentration, and the stress induces slips in the region around notches. Certainly it is not due to the dislocation pile-up at inclusion resulting from the matrix slip that leads to the stress concentration and makes inclusion fracture. Therefore, the same reason can not be used to explain the multiple internal fracture for carbides and inclusions, at least, for the weak and brittle inclusions.

With further increase in stress and strain during the tensile test, fine inclusions would be able to crack and the matrix around them to deform plastically or the other local micro-regions in matrix to slip. As a result, the slipped regions joined together gradually as shown in Fig. 5.

**INCLUSION RELATES TO FRACTURE** Although the plastic deformation usually takes place

and advances in the matrix around coarse multiple internal fractured inclusions as in the case mentioned above, the final fracture appeared not just at, but close to, the fractured inclusions or their adjacent matrix with heavy plastic deformation, as shown in Fig. 6. This is interpreted by means of the notch effect of multiple internal fracture in inclusions. The matrix around the fractured inclusions slips on account of the stress concentration first. Then, on the one hand the matrix is work hardened, and on the other hand the stress is released, redistributed and its maximum  $\sigma_{max}$  moves toward the interface between the region plastically deformed and that elastically deformed ahead of plastic deformed region. As the above-mentioned process is carried out continuously, the  $\sigma_{max}$  leaves apart from the inclusions and increases gradually, as shown in Fig. 7. If the  $\sigma_{max} > \sigma_f$ , such as at A, B, a crack will initiate over there. This is in agreement with experimental results,

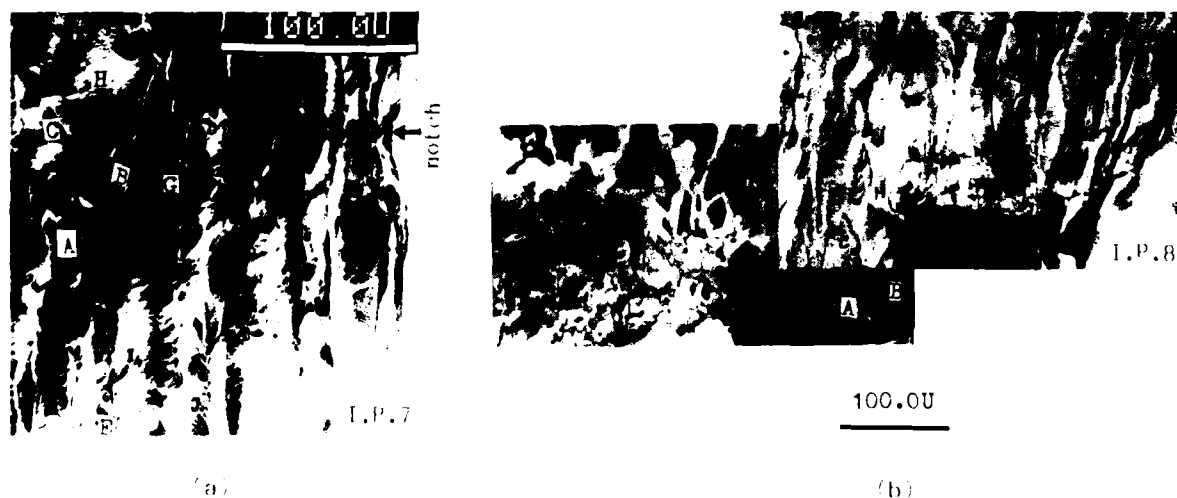


Fig. 6 Inclusion relates to fracture

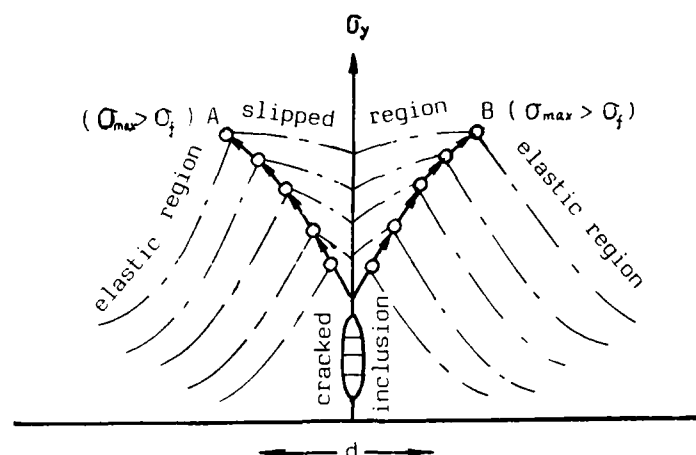


Fig. 7 Schematic drawing of plastic deformation and stress distribution around cracked inclusion

as shown in Fig. 6.

### CONCLUSIONS

By using SEM and the technique of replica, the dynamic processes of deformation and fracture of inclusion and its adjacent matrix during the tensile process in steel may be observed in situ on a series of replicas.

Coarse rod-shaped brittle inclusions are fractured multiply at a stage probably as early as an elastic one. This is due to the difference between the elastic modulus of inclusion and that of matrix, leading to the different elastic strains. As a result, the weak and brittle inclusions are fractured first.

Multiple internal fracture produces many micro-notches, which cause the stress concentration in micro-region and lead to the slip predominant over there rather than the slip which causes the inclusion multiple fracture.

Final fracture appears not in the regions of multiple fractured inclusion and the matrix around them with heavy plastic deformation,

but close to the regions and at the interfaces between the region of elastic deformation and that of plastic deformation. This is due to the fact that the micro-notches effect causes stress and strain concentration and redistribution ahead of the multiple fracture of inclusion. The final fracture takes place, therefore, at the interface between the elastic region and plastic one with maximum stress  $\sigma_{max} > \text{material fracture strength } \sigma_f$ .

### REFERENCES

- [1] Brown, R. and G.C. Smith, *Metallograpgy*, 15, 269 (1982)
- [2] Broek, D., *Engng. Fract. Mech.*, 5, 55(1973)
- [3] He, Z.R., *Proceedings of ICM-5 (Beijing)*, 1, 349 (1987)
- [4] Broek, D., *Inter. Met. Rev.*, 19, 135 (1974)
- [5] Barnby, J.T., *Acta Met.*, 15, 903 (1976)
- [6] Smith, E., *Proceedings of the Conference on "The Physical Basis of Yield and Fracture"* (Oxford), *Inst. of Physics and Phys. Soc.*, 36 (1966)

# ROLES OF INCLUSIONS IN STEEL FOR THE FATIGUE PROPERTIES AND MACHINABILITY PROBLEMS

**Toru Araki**

Kobe Steel, Ltd.  
Marunouchi, Tokyo-100 Japan

## ABSTRACT

Experimental results of the author's series of studies on the inclusions in steel are summarized in connection with some new experimental knowledge on the fatigue properties and the machinability of steels. The roles of the inclusion in the plastic behaviors of steel matrix in a weak strain range of fatigue phenomena versus a very high strain range of machining processes are compared and discussed in relation with the influences of the inclusions to the incubation and initiation of fatigue crack and to the shear stress in the primary and secondary shear flow zone of the cutting process. In the case of the soft ferritic phase, the inclusions have no substantial influence, however at higher strength level the fatigue damage by repeated stress in the microstructure is strongly influenced by the stress raising effect of inclusion depending on its shape, size, physical and mechanical properties. After nucleation of microcrack, the interface strength between inclusion/matrix plays a role. In the case of machining process the formation behaviors of chip are influenced by the built-up edge at lower cutting speed and by the heavily flowed layer at higher cutting speed, both of which are significantly affected by the extremely elongated non-metallic inclusions.

THE MECHANICAL PROPERTIES of steel are significantly dependent on the included foreign phases with a size order of more than micrometers, in particular the fracture related properties such as fatigue properties and workability (1,2). The roles of nonmetallic and metallic inclusions in steel with respect to these mechanical behaviors are closely related to the microstructural metallurgical factors as well as the mechanical ones.

Therefore, in order to well understand the influence of the inclusions to the material behavior of practical steel and to know the principles underlying the interactions between them, it must be necessary to consider the whole phenomena from a microstructural standpoint as well as the mechanical, elastic and plastic concept.

In this review paper, the main interest will be focussed on the fatigue properties and the machinability problems, and some knowledge on the role of inclusions and concepts to interpret the phenomena are demonstrated and discussed.

## INFLUENCE OF INCLUSIONS IN STEEL

### 1 GENERAL VIEW OF INCLUSION VS FATIGUE--

The influence of inclusions in steel depends on the size, shape and qualities of the respective inclusion in a specified dispersion mode as well as the mechanical properties of the steel matrix;

Table 1 Classification of inclusions with respect to characteristics

symbol	typical substances	characteristics
(N1)	MnS sulfides tellurides etc	<u>soft</u> in elasticity, <u>low</u> yield shear <u>strong</u> interface with steel.
(N2)	Mn·SiO <sub>3</sub> basic silicates Ca·Al·SiO <sub>x</sub> basic aluminates Mn·Ti·Ox	<u>medium</u> in elasticity and <u>brittle</u> at room temperature. <u>soft</u> in plasticity at elevated temperatures.
(N3)	SiO <sub>2</sub> (hard silicates)	<u>hard</u> in elasticity and <u>brittle</u>
(N4)	Al <sub>2</sub> O <sub>3</sub> hard aluminate $\alpha$ -alumina titan-nitrides	<u>very hard</u> in elasticity, <u>high</u> yield stress, <u>not enough</u> strong interface with steel matrix. <u>rigid</u> at elevated temperature.
(M1)	Pb, Bi, (metals insoluble in steel matrix)	<u>very soft</u> and liquescent at an elevated temperature.
(M2)	Ag (metals insoluble in steel)	<u>soft</u> , liquescent at higher temperature

the elasto plastic behaviors of the both phases have close and complicated interaction to each other [3].

A primary way of classification of such inclusions in steel in relation with the referred mechanical properties will be useful for understanding the above subjects. The inclusions can be classified as the following Table 1 by a typical way with their representative characteristics:

As a first approximation in the case of low stress high cycle fatigue, the mechanical factors of the above inclusion can be estimated with a elastic stress concentration caused by the difference of elasticity between the inclusion and the steel matrix.

An ellipsoidal inclusion, after Edwards' calculation [4], causes a stress concentration as a function of elasticity ratio  $E'/E$ . For example in the case of MnS, (N1), the ratio of elastic moduli of inclusion/matrix is around 2/3, where by the applied stress in matrix at the end interface of the inclusion will be raised by a factor of 1.4.

In the case of a pore in the matrix, i.e.  $E'/E \rightarrow 0$ , the concentration factor will go up to 2.1 ~3.0 depending on the shape of the ellipsoid, whereas the rigid and hard inclusion such as  $\alpha$  alumina, (N4), will bring a concentration factor

less than unity, that means the applied stress will be locally lightened.

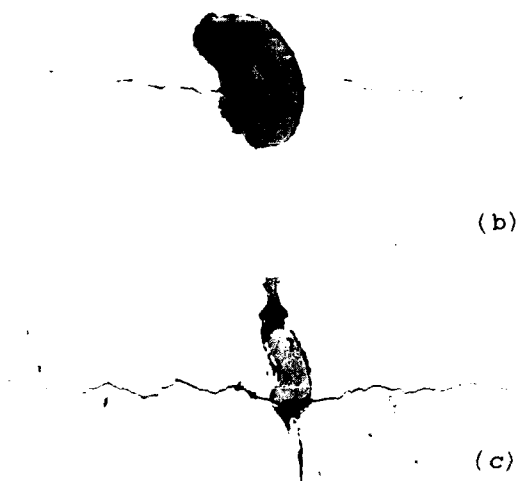
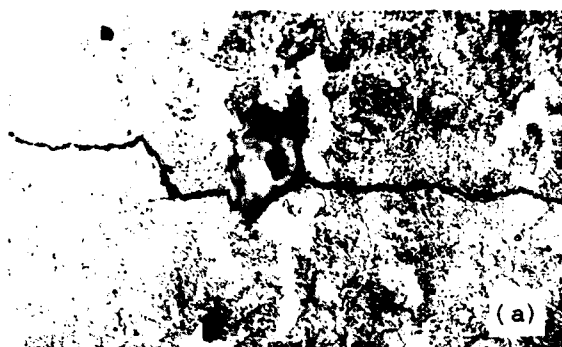
If this concept is ideally valid for the dispersed inclusions and the steel matrix behaves nearly elastic, the intensity of fatigue damage caused by cyclic stressing must be simply dependent on the elasticity ratio and the shape factor of the inclusion.

However, actually observed fatigue damage is much dependent on the size factor as well as the shape, because of the microplastic flow behavior around the inclusion [5]. Besides, there might be an additional factor of residual stress due to the different thermal expansion coefficients, and also of an evolved gap by decohesion of the inclusion/matrix interface or fracturing in the inclusion [6,7]. The generated gap will act as a high stress raiser because of its  $E'/E = 0$ .

Some examples of the nucleation of fatigue crack from inclusions are shown in Fig. 1. It is clearly visible that microcracks are generated and grown from:

- interface of an inclusion/matrix by separation,
- heterogeneity or defect inside an inclusion by fracture/cracking.
- interface of two coexisting phases in an inclusion by separation/cracking.

The stress/strain concentrating effect of an inclusion will be macroscopically intensified by



(b)

(c)

Fig. 1 Photographs of initiation of fatigue cracks at inclusions

clustering or chain-like arrangement of plural number of inclusions with various sizes. In most observed cases a large inclusion with notch-like interface become preferably a nucleus of the fatigue crack, but high density of dispersed inclusions acts as promoting the crack propagation  $\langle 5 \rangle$ .

On the other side, influence of the plastic behavior of steel matrix is important in connection with the above said effects of inclusion. For instance in the case of very soft ferritic matrix of a mild steel, dispersed hard inclusion (alumina) acts as a strengthening factor in fatigue durability more than the strengthening in

yield stress  $\langle 5 \rangle$ . Strengthening by such particle dispersion is increased with decreasing the size and spacing of the particle  $\langle 5 \rangle$ . In this case the ferritic phase has an enough cyclic ductility resulting in a long lasting cyclic hardening behavior at higher stressing.

In the case of much higher strength level of so-called high strength steels, influence of the inclusions on fatigue becomes dramatically different, and even hard and rigid (N4) inclusions are usually detrimental for the fatigue durability measured by endurance limit, it is as discussed above with the stress concentration factor of generated gap or void associated with strain localization or decohesion of interface as well as internal cracking of inclusion  $\langle 6,7 \rangle$ .

Fatigue behaviors of steel matrix strengthened by various microstructural mechanism were reviewed elsewhere  $\langle 1,2 \rangle$  in respect with the fatigue crack propagation rate together with ductility and toughness of the materials.

The strengthened matrix has a trend of cyclic softening behavior; i.e., microscopically, early degradation at strain concentrated region, and macroscopically, gradual increase of plastic strain which will result in a nucleation of growable fatigue crack  $\langle 2 \rangle$ . The propagation rate of fatigue crack is generally assisted by higher density of dispersed inclusions, in particular, the size and the more angular shape seem to promote the propagation of crack from the early stage.

Effective critical size of inclusion to substantially deteriorate the fatigue durability has been discussed in many reports, although the analyzed values of size were widely scattered because of the variety of strengthened microstructures of the steel matrix and species of inclusions.

In a case of Japanese standard machine-structural steels with tempered martensite in tensile strength range of 700–1300 Pa, it is statistically analyzed that the critical size of inclusion is  $\sim 45$  micrometers  $\langle 8 \rangle$ , having a correlated threshold strength or hardness derived from many observed data of endurance limit by rotating bending test.

There are some trial of describing the fatigue limit with the applying stress ratio  $R = -1$  in a relationship with the threshold stress intensity factor range,  $\Delta K_{th}$ , of the propagation of the initial microcrack with a size of  $a$ . With a zero order approximation, the fatigue limit will be expressed as the following form of equation:

$$\sigma_w = A a^x \quad (1)$$

where  $A$  is a constant dependent on the strength of steel, and  $x$  is an exponent near  $1/6$  (by Y. Murakami et al. (1987))

In actual cases, the microstructural factor of the steel matrix is known as sensitive to the fracture toughness and fatigue degradation nature other than its hardness or strength value  $\langle 1,2 \rangle$ . The said  $\Delta K_{th}$  value is also not in a simple parallel relationship with  $\sigma_w$ .  $\Delta K_{th}$  is rather inversely correlated with  $\sigma_w$  in the cases of dual phase (ferritic-martensitic) steels as well as the highly thermo-mechanically controlled-rolled steels ( R. O. Ritchie (1987), M. Schaper et al. (1985)) .

These typical examples seem to mutually have strong microstructural factors in affecting initiation and propagation of the nucleated fatigue cracks through, e. g., the crack closure phenomena of the evolved crack and meandering /deflection behavior of the propagating crack.

There were also a simple approach to the effects of nature of the steel matrix on the fatigue endurance limit in connection with the shape factor of inclusion. Fig. 2 illustrates a trial of quantitative expression of the influence of the work hardening coefficient  $n$  of the steel matrix on the endurance limit  $\sigma_w \langle 3,5 \rangle$  as a function of shape factor  $k$  of the inclusion with a specified critical size.

It would be concluded that the initiation of growable fatigue crack is much influenced by

- (a) the damaging of matrix concerning cyclic softening characterized by the operating strengthening mechanisms in the microstructure of matrix  $\langle 1,2 \rangle$ ,

- (b) large size and angular shape of inclusion  $\langle 5 \rangle$ ,

- (c) fracture strength of the inclusion or interface with the matrix  $\langle 6,7 \rangle$ .

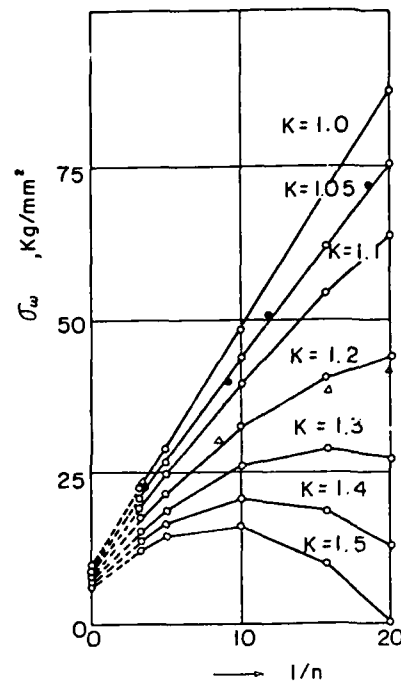


Fig. 2 Fatigue endurance limit vs inverse work-hardening coefficient  $n^{-1}$  of matrix as a function of shape factor  $k$  of inclusion

For the propagation in relatively low cycle high stress fatigue, the growth rate of fatigue crack is further more influenced by the total amount of inclusions above a subcritical size, e.g. over 10 micrometers  $\langle 5 \rangle$ , at high strength levels of steels.

## 2. IMPROVEMENT OF MACHINABILITY BY INCLUSION --

As one of the workability of steel materials the machinability has been and still now holds very significant meaning in the productivity problems in industry. Machinability is used to be differently evaluated by various methods, e.g. lathe turning, drilling, milling and broaching etc., and the criteria for evaluation are usually divided into four groups according to the purpose: tool life, cutting resistance, surface finish and chip disposability.

Effects of inclusions in steel can be analyzed by the classification (N) and (M) shown in table 1 in the preceding page.

Soft, plastic inclusions such as (N1)-MnS, MnTe and (M)-Pb, Bi, Ag are in most cases favorable



for machinability as known well as the free-machining additives. Soft submicron oxides dispersed in ferritic matrix seem also favorable <12>, however the principal effects of sulfide type inclusion in free cutting steels are concerned with size of micrometer order. Improvement of machinability by (N1) type inclusion is, in general, exhibited in the following way:

(a.) Strong influence on the formation of BUE (built up edge) <13> toward small and more stable BUE at higher cutting speed; improving tool life and lessening cutting resistance, better finish at lower cutting speed but slightly worse at higher cutting speed because of the trend of still remaining BUE <9,14>.

(b.) Assisting micro- and macro-shear rupture in the chip formation at the primary shear zone; lessening cutting resistance and better chip breakability (disposability) <9,15>.

(c.) Extremely elongated at the secondary shear region and also extruded as film-wise at and near the interface between workpiece and tool rake; resulting in effective lessening of the apparent frictional stress and increase of the chip shear angle linked with low cutting resistance <14,5,9>.

Improvement by (M)-type metallic inclusions is expected also in a similar mechanism, but these inclusions are generally very finely dispersed, so that it is different in the following particular points:

(a) Promotion of shear rupture through microcrack assisted by liquidation of metallic inclusion at  $250\sim 300^{\circ}\text{C}$ . <9>

(b) Efficient improvement (by Pb, Bi) of the chip-disposability by the said liquid embrittlement, as well as the cutting resistance at low cutting speed. <9>

(c) Decrease of cutting resistance despite lower temperature at cutting regions, especially at heavily flowed layer at the secondary shear region <16>, as referred to Fig. 3.

Basic silicate inclusions, (N2) group, play an important role in improvement of tool life at higher cutting speed with the carbide tools containing  $\text{TiC}$ . Mechanisms underlying this improvement are concerned with the hot plasticity

and wetting (adhering) property of such silicate at the chip/tool interface <9>. Hot-plastic (N2)-silicate inclusions (or aluminate, titanate) <17,16,19,9> can form a film layer on the tool surface building-up by sticking, which act as a diffusion barrier <17> between work piece and tool material, and prevent the deterioration and attrition of the tool. In this mechanism the optimum temperature of softening and sticking of the inclusion corresponds to the temperature of the cutting tool surface <20,9>.

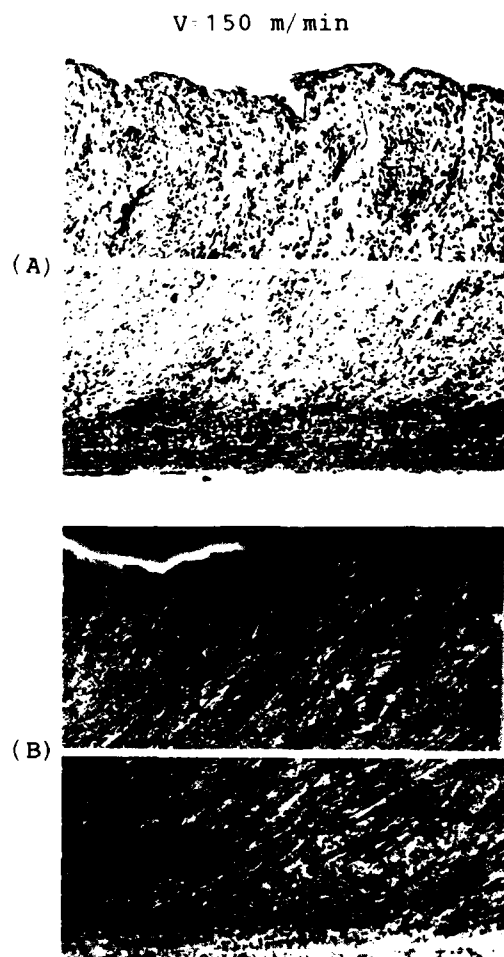


Fig.3 Microphotographs of machined chips, showing separately upper surface and back-face. Workpiece material: Cr-Mo 4135 steel with (A) Spheroidized (HV=150),  $\mu=18\mu\text{m}$  (B) Quench-tempered (HV=290),  $\mu=9\mu\text{m}$ , where:  $\mu$  means thickness of heavily flowed layer at the secondary shear region of chip backface.

## COMPATIBLE INFLUENCES ON FATIGUE AND MACHINABILITY

In the practical structural steels, the overall influences of various inclusions should be considered on the required mechanical properties. Effects of the above discussed respective inclusion on both fatigue property and machinability are widely different to each other in mechanism, so that it is needed to know the functions of the individual group of inclusions to both of the properties in actual steel design.

Among the preceding six inclusion groups (N4) too much hard inclusion is mostly detrimental for fatigue durability of strengthened steels because of its no adaptability for micro-plastic behavior of the steel matrix, and also detrimental for machinability because of its abrasive nature to the tool wear.

In order to avoid such negative influence, the usual aluminum deoxidation process of steel is often modified by other process: e.g. vacuum degassing to oxygen amount less than 8 ppm, calcium deoxidation, sulfur addition etc.

In the case of a prior need in improving machinability, appropriate amount of (N2)-calcium aluminate and (N1)-sulfide will contribute to better machinability in terms of tool life with less sacrifice in fatigue property <22>. The size and shape of these inclusions have significant meaning for influencing fatigue crack behaviors just as already discussed.

When (M1)-lead addition is applied for free machinability, the fatigue properties are virtually not affected at the room temperature in the high strength steels up to 1200 MPa, provided the dispersion of lead particles is fine ( $\leq 4$  micrometers) and uniform, and no other detrimental inclusions are associated.

There seems to be a discrepancy that existence of inclusions (foreign phases) in steel is likely to promote the micro-cracking at a strained site of matrix, which fact is favorable for machinability but generally harmful for the fatigue durability of the steel material. However, in

comparing the fatigue property of minute cyclic straining with the machining process by extremely high strain of shear flowing, there is a fundamental difference in the strain range and the functioning temperature at the subjected site of the steel material <16,19>.

Accordingly the function of inclusions in influencing both the fatigue properties and the machinability must be considered on a separate basis to each other:

- a) At the stage of fatigue crack initiation in a strengthened steel, existing inclusions will play a role as a stress raiser, resultantly causing strain concentration, sometime resulting in void or gap, and promote the damaging of the steel matrix <1,2,23> by cyclic straining; the largest size, shape and nature of the inclusions will become the dominant factors.
- b) At the stage of fatigue crack propagation, the primary factor will be the dispersed inclusions which act as crack promoter by joining one to another, and the secondary the function of accelerating damaging in the heavily cyclic-strained zone at the propagating crack tip <9>. A tiny particles, e.g. less than 5 micrometers, will have no meanings at a usual high strength level for fatigue <9>.
- c) In the case of machining at a lower cutting speed, the function of inclusions on decisively modifying the formation of built-up edge, e.g. by MnTe, Pb, MnS, is important for free machinability; the size, shape, and the amount of the free machining inclusions are the major factors.  
The amount and size of detrimental (very hard) inclusions such as  $\alpha$ -alumina and high silico-aluminate give negative factor but it can be modified by altering its melting and softening temperature and coexistence with sulfide inclusions.
- d) In the high cutting speed range, the behavior of the steel matrix at the heavily flowed layer in the secondary shear region <16,9> has an

important meaning together with the building up of thin film layer of inclusion-originated material at the interface or on the surface of the cutting tool <17,18,21,22,23,,9> .

Thus we could find a possibility of compatible influence of the both competing properties, fatigue durability and machinability of steel, by controlling the quality and quantity of appropriate sort of inclusions.

#### REFERENCES

- 1 T.Araki; Tetsu to Hagane (Journ. Iron Steel Inst.Jpn.), 69(1983) p.1372
- 2 T.Araki; HSLA'85, Beijing, CSM-ASM (1986) p.256 in English
- 3 M.Sumita, I.Uchiyama, T.Araki; Trans.Ir.St Inst.Jpn, 14(1974)p.275
- 4 R.Edwards; J.Appl.Mech. 18(1951)p.19
- 5 M.Sumita, I.Uchiyama, T.Araki; Tetsu to Hagane, 57(1971)p.335, p.298
- 6 T.Araki, T.Shih, R.Sagawa; ditto , 57(1971)p.2042, 56(1970)p.1737
- 7 T.Shih, T.Araki, R.Sagawa; Trans.Inst.Jpn, 13(1937)p.11
- 8 S.Nishijima, K.Tanaka, H.Sumiyoshi; Adv.Fracture Res., '84, New Delih (1984)3.p.1719
- 9 T.Araki; Nishiyama Memorial Tech.Semin., Ir.St.Inst.Jpn, 96(1984)p.1
- 10 T.Araki; R and D, Kobe Steel Tech.Rep.36(1986)p.7
- 11 T.Araki, S.Yamamoto; Proc.Jpn-Ussr Jointsymp.Phys.Metallu.(1975)p.36
- 12 L.M.Riekels; Machinability Engg.Materials, '82, Rosemont, ASM(1983), P.42-64
- 13 H.Yaguchi; Mater.Sci.Engg., 80(1986)2, p.L27-30
- 14 S.Ramalingam, J.D.Watson; Mecha.Working Steel Processing XVIII, '80, TORONTO, Ir.Steel Soc.AIME(1981), p.94
- 15 R.Milovic, J.Wallbank; Machin Engg.Materi.Int.Conf.Chicago, ASM.(1987)p.23
- 16 T.Araki, S.Yamamoto, H.Nakajima; Strategy Automation Machin.I.C. Orlando, ASM Int.(1987)p.73
- 17 T.Araki, S.Yamamoto, M.Kanao; Proc.Int.Conf.Prod.Engg.Tokyo (1974)p.550
- 18 T.Araki, S.Yamamoto, M.Kanao; Proc.Forum Infuluence Metallu.Machinability, ASM, Chicago(1975)p.1
- 19 T.Araki, S.Yamamoto, M.Osawa; Machinability Engg.Materials, Proc.Int.Conf. Rosemond ASM (1983) p.3
- 20 T.Ito; Mech.Working.Steel Process. XIII, Pittsburgh, (1975)ISS/AIME, p.213
- 21 S.Katayama, N.Onodera, T.Imai, N.Suzuki et al; Seitetsu Kenkyu (326) (1987) p.62
- 22 D.J.Naylor, M.L.Pickett; Eur.Rep.Comm.(1983) EUR-8626, p.179
- 23 S.Horib, R.Sagawa, T.Fujita, T.Araki; Tetsu to Hagane, 64(1978) p.268, 65(1979) p.80
- 24 M.Nakamura, H.Takeshita, T.Sasaki, T.Kooka; Tetsu to Hagane, 72(1986) s.648

# THE ROLE OF INCLUSIONS IN CORROSION FATIGUE CRACK GROWTH OF PRESSURE VESSEL STEELS IN HIGH TEMPERATURE REACTOR WATER

Hannu Hänninen, Markku Kempainen, and Kari Törönn

Technical Research Centre of Finland  
Metals Laboratory  
Kemistintie 3  
SF-02150 ESPOO, Finland

## Abstract

The influence of nonmetallic inclusions on the corrosion fatigue crack propagation properties of reactor pressure vessel steels in high temperature, high pressure reactor water environments has been examined. After corrosion fatigue testing, the test specimens have been analysed fractographically and metallographically by studying the cross-sections of the specimens. In addition, the nonmetallic inclusion distributions have been analysed by sulfur printing and with an image analyzer system in conjunction with SEM. Inside the corrosion fatigue crack the dissolving MnS inclusions control the local chemistry, which has been examined by using artificial crevices and through Auger and X-ray photoelectron spectroscopy of the corrosion products at the crack tip. It is proposed that the local sulfur-rich chemistry inside the crack is controlling the amount of brittle crack growth in corrosion fatigue. The correlation between the relative amount of brittle crack growth and the environmental crack growth rate enhancement factor has been also calculated. Finally, the corrosion fatigue crack growth mechanisms are discussed based on the role of nonmetallic inclusions producing microcracking ahead of the main crack tip inside the plastic zone and on their effects on changing crack tip chemistry more aggressive and conducive to hydrogen absorption at the crack tip region.

SULFUR CONTENT OF THE PRESSURE VESSEL STEELS has been established to be one of the major variables in determining the corrosion fatigue crack growth in LWR environments (1 - 5). The chemistry and electrochemistry inside the crack is affected by the dissolution of the MnS inclusions of the steel. Exposure of the MnS inclusions at the crack tip is affected by many additional parameters like the form, size, and amount of MnS inclusions on the crack path. The

MnS inclusions dissolve in LWR water (6 and 7) and form sulfur ions inside the crack. A schematic picture of the anticipated reactions is presented in Fig. 1, which predicts that in addition to  $\text{Fe}_3\text{O}_4$  (magnetite),  $\text{FeS}$  and  $\text{FeS}_2$  (iron sulfides) could also be stable phases inside the cracks. Moreover, the impurities from bulk water can migrate into the crack, affect the crack-tip chemistry, and form stable corrosion products.

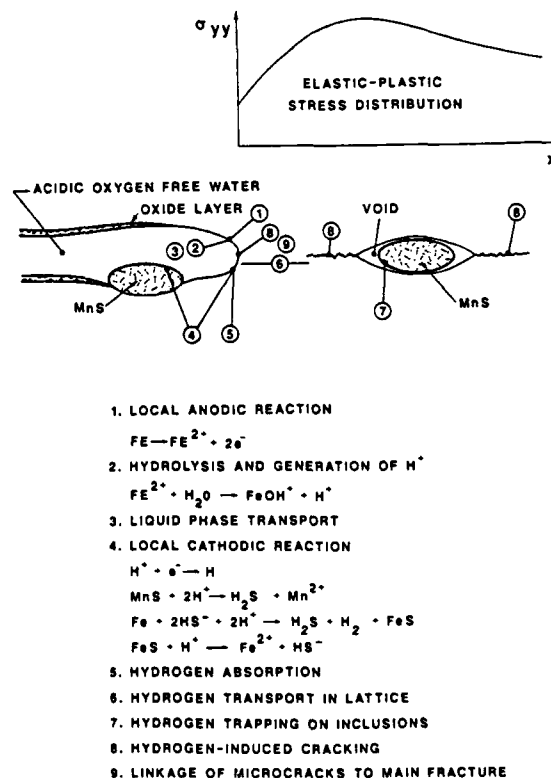


Fig. 1 - Schematic of the corrosion reactions and hydrogen-induced crack growth model proposed for corrosion fatigue crack growth of reactor pressure vessel steel in LWR water (8).

Reactor pressure vessel steels are known to crack in oxygenated high temperature pure water (BWR conditions) by a stress corrosion cracking (SCC) mechanism both in static tests (9) and in dynamic SSRT tests (10 - 19). Reactor pressure vessel steels have exhibited susceptibility to SCC in high temperature PWR primary side water as well, if the corrosion potential is raised above  $\sim -200$  mV(SHE) by external potential control (11, 20, 21 and 22). Thus, there seems to be both in BWR and PWR conditions a critical potential for corrosion crack initiation at about  $-200$  mV(SHE). However, there are indications in SSRT tests that, e.g., the MnS inclusions in the SSRT specimen surface debond from the matrix and form crevices inside which an aggressive environment is generated by dissolution of MnS and the minimum cracking potential can be lowered (for A 508 steel) to about  $-400$  mV(SHE) (10). Similarly Klemetti and Hänninen (19) observed SCC in an ICCGR round robin test in which the corrosion potential was decreased from the susceptible SCC potential region into the anticipated safe region. Sulfate addition to high temperature water has exhibited also a marked decrease in the critical potential for SCC of pressure vessel steels (23).

Phenomenologically, environment-sensitive cracking occurs in SSRT testing of reactor pressure vessel steels in high temperature water with effects similar to the case of corrosion fatigue. Marked environmental enhancement can, however, occur in corrosion fatigue of pressure vessel steels in PWR primary water conditions where the corrosion potential is about  $-700$  mV(SHE), which is much lower than the minimum stress corrosion cracking potential obtained in SSRT tests, about  $-200$  mV(SHE).

Speidel and Magdowski (9) after summarizing the environment-sensitive crack growth data of pressure vessel steels in high temperature water were able to conclude that sulfur content of the steel has no measurable effect on the stress corrosion crack growth rate and that there is no measurable indication of the effect of oxygen content or corrosion potential on growth rates of stress corrosion cracks. Only a small percentage of their fracture mechanics specimens indicated crack growth, suggesting it was important that the crack tip was initially located in a metallurgically inhomogeneous region. If so, it would be probable that this region was able to change the crack-tip conditions with respect to the bulk water, e.g. through dissolution of MnS particles as proposed by Hänninen et al. (4) and Klemetti et al. (6). Effects of dissolution of MnS particles on crevice chemistry have been shown experimentally by using artificial crevices by Ford et al. (24) and Illi et al. (25): when the amount of aggressive species increases, pH reduces, and conductivity increases. It has also been shown (19, 26) that really in anticipated local crack-tip conditions, saturated MnS solution, pressure vessel steels are susceptible to SCC even at very low

corrosion potentials at  $80^{\circ}\text{C}$ , and more recently similar results have been obtained at reactor operating temperature  $288^{\circ}\text{C}$  for MnS-saturated PWR-water (57).

#### EFFECT OF SULFUR ON CYCLIC CRACK GROWTH RATE

The ASME Section XI curves for CF crack growth have been recognized to be conservative for some RPV steels, and it has been found that the level of sulfur in the steel has an important effect. High levels of sulfur in pressure vessel steels have resulted in crack growth rates predicted by the Code curves, but lower levels of sulfur ( $< 0.010$  wt.%) have produced significantly less enhancement. It was first thought that a quantitative measure might be readily available from the material chemistry, but further studies have shown that the sulfur effect is much more complex, being related to the size, form and distribution on the MnS inclusions. Plate materials contain a wide range of sizes and forms of MnS inclusions, while they are generally much smaller and more spherical in forgings, and even smaller in welds. Therefore the threshold sulfur for significant environmental enhancement appears to vary according to the product form. For plates, as shown in Fig. 2, even a low sulfur content can result in enhanced crack growth. On the other hand, Fig. 3 shows that forgings with low bulk sulfur contents can

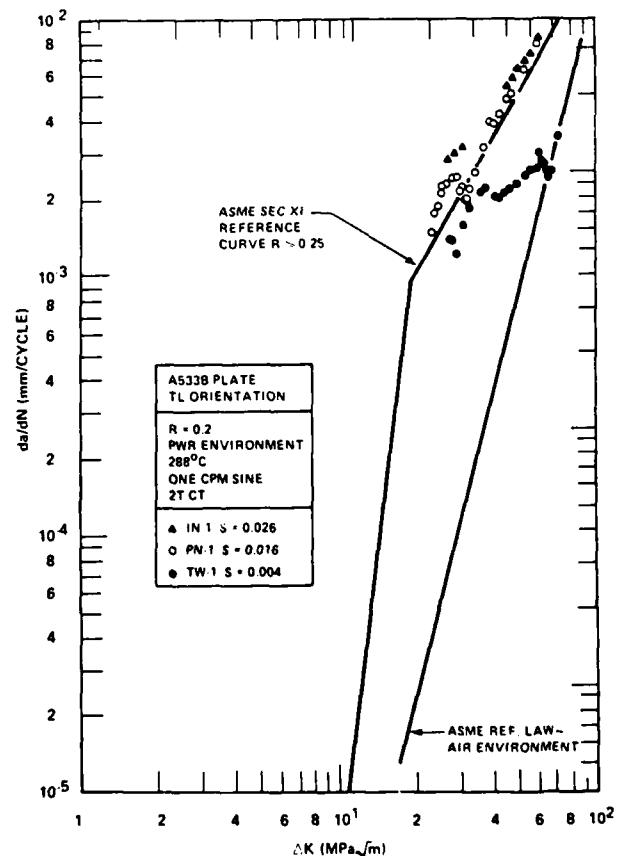


Fig. 2 - Effect of sulfur content on fatigue crack growth of A533B plates in PWR environment at  $R = 0.2$  (46).

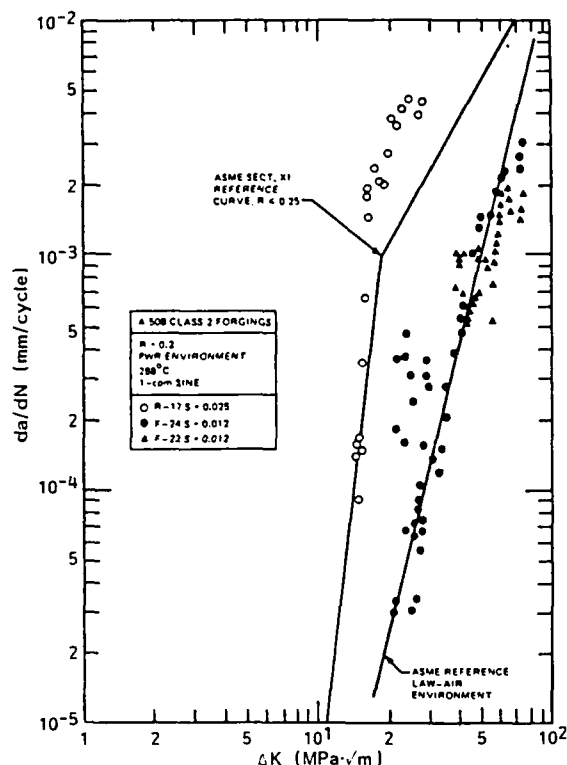


Fig. 3 - Effect of sulfur content on fatigue crack growth of A508-2 forgings in PWR environment at  $R = 0.2$  (46).

show very little enhancement, and similar results have been found for welds (46).

Bamford et al. (2) have studied in addition to sulfur contents and product forms of A533-B steels also the effects of a crack plane and propagation orientation with respect to the rolling direction of the plate on crack growth rate. Some of these results are shown in Fig. 4; some other results are shown in Figs. 5a and 5b. In summary, steels of low sulfur content generally exhibit only a slight increase in crack growth rates compared with those in air, but this may be due as much to the fact that the MnS inclusions in these steels are more spherical, rather than elongated or plate-like. Equally important is the orientation of the crack plane with respect to the inclusion axes. When the crack plane contains the long axis of the inclusions, the degree of environmental assistance is increased, often dramatically. The L-S orientation (sulfide stringers oriented perpendicular to the cracking plane) induces lower growth rates than either the T-L or L-T orientations, which are similar. Since the L-S orientation represents the largest volume of contiguous MnS intersected by the crack (volume ratio) but the smallest area of MnS (area ratio), it is reasonable to assume that incomplete dissolution of contiguous MnS occurs and therefore that the area ratio intersected by the crack is the dominant factor. There is also some evidence that steels of low sulfur content can produce high crack growth rates (2), and conversely, that

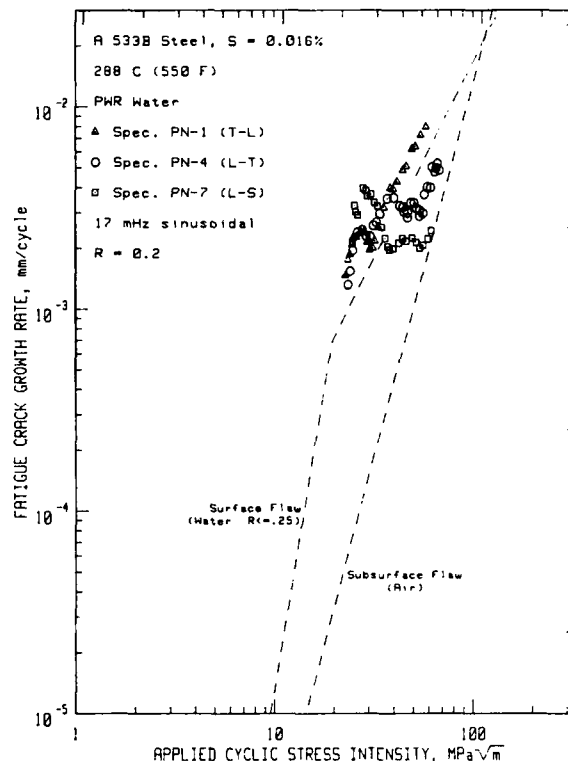


Fig. 4 - Fatigue crack growth rate vs. applied  $\Delta K$  for an A533-B steel of medium sulfur content tested at  $R = 0.2$ . These results show a high degree of environmental assistance, and a strong orientation effect (2).

steels of medium sulfur content exhibit little environmental effect (4).

Parallel results have been obtained by Slama et al. (1, 47). Fig. 6 shows results for steels of two sulfur levels, tested under PWR conditions at  $R = 0.2$  and a 17-mHz triangular waveform. These results show that increasing the sulfur content to 0.018 % results in crack growth rates which reside well outside the ASME reference line for  $R \leq 0.25$ , in spite of the triangular waveform, which has yielded consistently lower growth rates than sinusoidal waveforms.

Research at the UKAEA-Harwell laboratory has produced consistently lower crack growth rate results than results at other laboratories. A two-laboratory intercomparison study (48) was undertaken to try to sort out the reason for the discrepancy. Results of nominally identical tests of low (0.006 % S) and medium (0.012 % S) sulfur steels at both laboratories yielded the results shown in Fig. 7, with the UKAEA results (shaded symbols) a factor of ten or more lower than the Westinghouse results. Additional tests at Harwell, on steels of even higher sulfur contents, consistently yielded results well below the ASME reference lines for the appropriate load ratio (49). Harwell test rig is a high flow rate rig and Westinghouse autoclaves are stagnant or low flow rate autoclaves. Thus, the

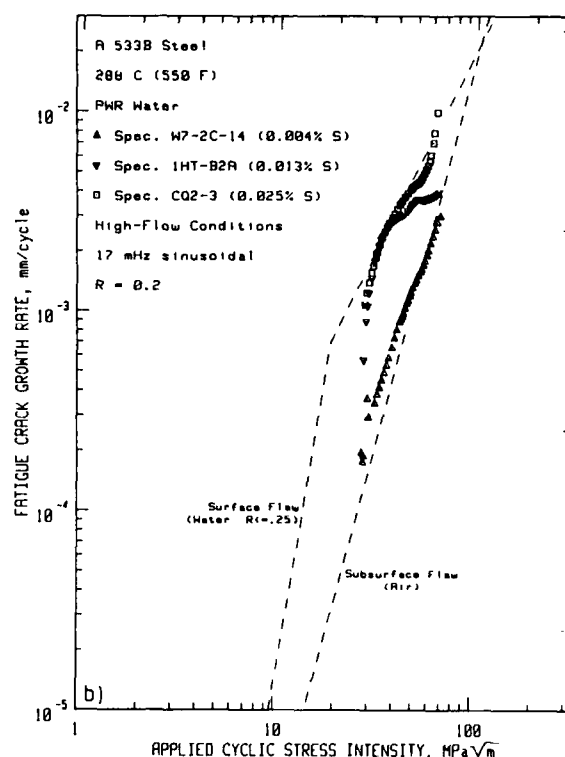
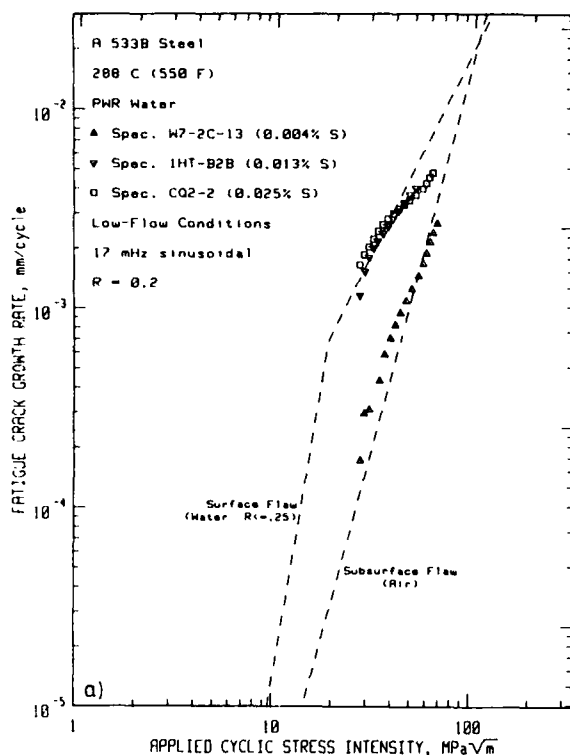


Fig. 5 - Fatigue crack growth rates vs. applied  $\Delta K$  for multispecimen tests of steels of three sulfur levels but identical crack plane orientation at two environmental flow rates: (a) 50 l/h and (b) 3000 l/h. Note that flow rate appears to have no effects in this case, but growth rates are strongly dependent on sulfur content of steels (5).

effect of solution flow rate on the crack growth rate for a medium sulfur, low-alloy steel tested in deaerated, 288 °C water can be also seen in Fig. 7. High flow rate is interpreted as flushing out the crack tip sulfur content resulting from dissolution of MnS in the crack. Similar data are observed for low vs. high sulfur steels tested at low flow rates as mentioned above; below 0.01 % S the data fall near the lower curve. However, this difference in high and low flow rates does not always exist as can be seen in case of results in Fig. 5.

Van Der Sluys (3) has made a unique test of a composite specimen, composed of sections of steel of different sulfur contents, electron beam welded together and formed into a specimen such that the crack proceeded through the various sections. The results of constant  $\Delta K$  tests of this specimen are shown in Fig. 8. These results show clearly the influence of the sulfur content on crack growth rates, and the dependence on the test frequency. For the higher sulfur content section increasing growth rates with decreasing test frequency, i.e. time-dependent crack growth, is typical.

The comparison of the cyclic crack growth rate properties of A533B, A508-2 and CrMoV reactor pressure vessel steels in simulated PWR conditions has revealed considerable differences (27, 50). A rather pronounced environmental

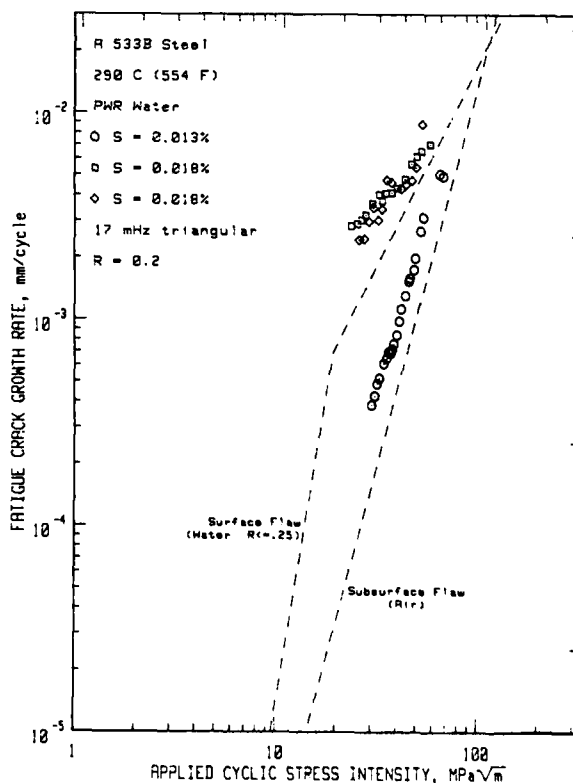


Fig. 6 - Fatigue crack growth rates vs. applied  $\Delta K$  for steels of two different sulfur contents, tested at  $R = 0.2$  and a 17-mHz triangular waveform (1).

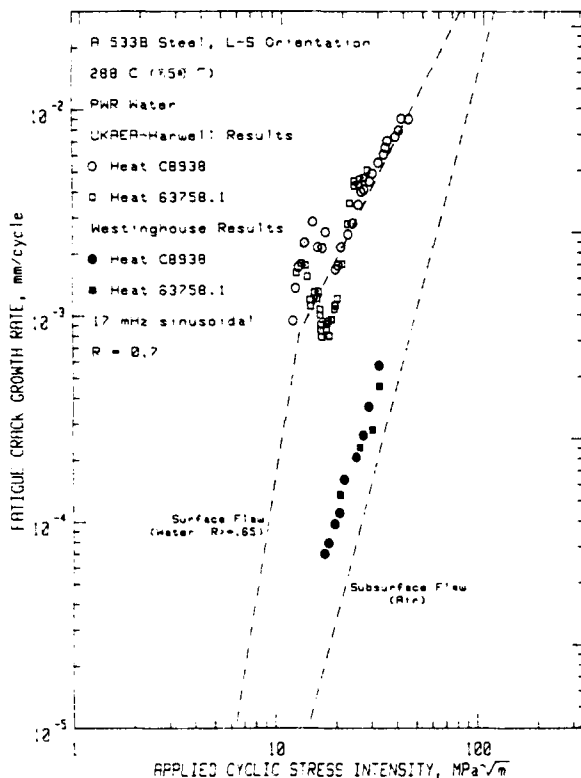


Fig. 7 - Fatigue crack growth rates vs. applied  $\Delta K$  for steels of low sulfur contents, tested under similar conditions at two different laboratories (48).

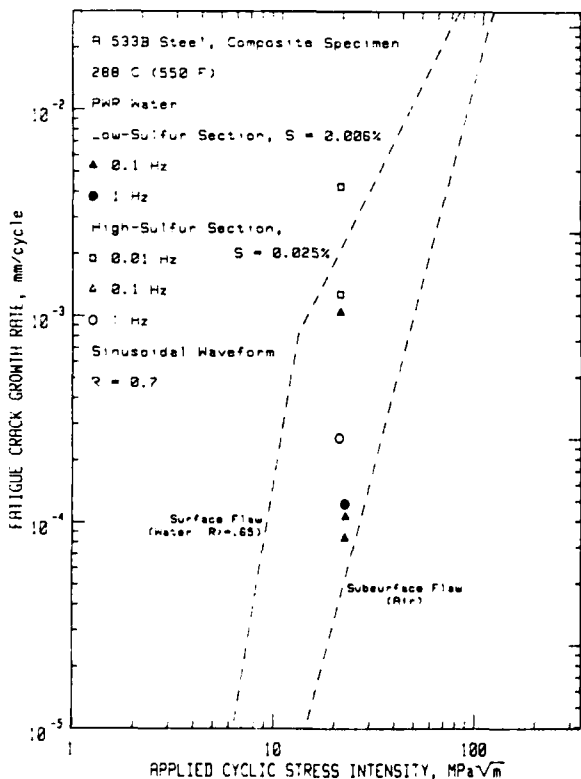


Fig. 8 - Fatigue crack growth rates vs. applied  $\Delta K$  for a composite specimen tested in constant  $\Delta K$  mode. Low sulfur section results are shaded (3).

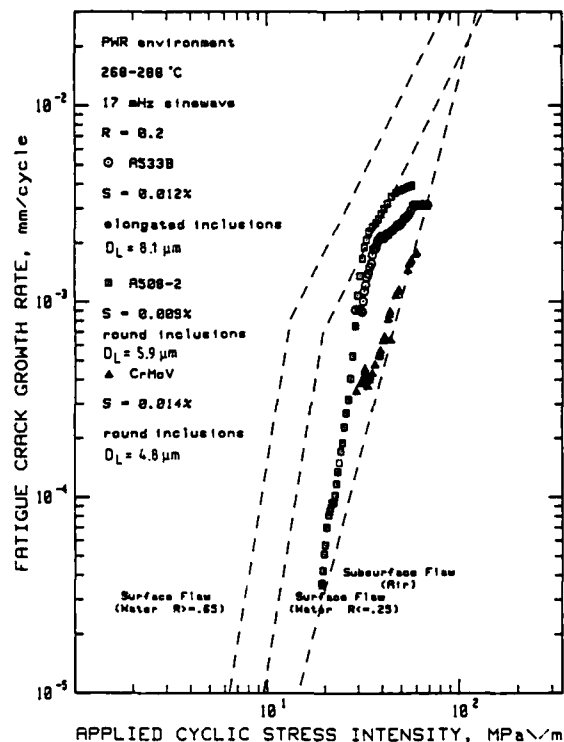


Fig. 9 - Influence of MnS inclusion morphology and distribution on cyclic crack propagation rates at 288°C in A533B, A508-2, and CrMoV steels having about the same sulfur level (50).

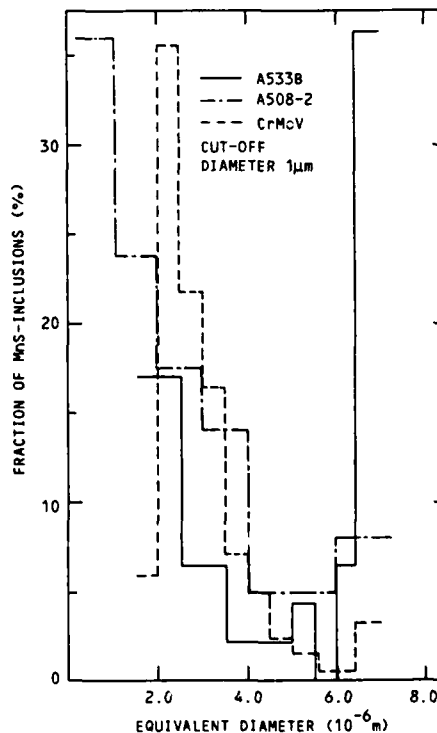


Fig. 10 - Inclusion size distributions on the crack planes in A533B, A508-2 and CrMoV steels (27, 50).



influence was found in A533B, whereas only a minor effect was seen in CrMoV steel (Fig. 9). The cyclic crack growth rates were connected to the sulfur contents of the test materials, and therefore sulfur prints and MnS-inclusion analyses were performed on the test materials. The studied heats contained 0.09 - 0.014 % of sulfur, but a marked difference in the inclusion distribution was found (Fig. 10). The fraction of large (larger than 5  $\mu$ m) inclusions is noticeably greatest in the A533B steel. It was also found that mainly the large inclusions were highly elongated, and that in the CrMoV steel these MnS-inclusions were almost non-existent. The MnS-inclusions in the CrMoV-steel were also analyzed to be mixed with oxides. This difference in inclusion type, morphology and distribution is thought to cause the different behaviour of these steels (4, 27, 50).

Although it is evident that sulfur has an important role in environment-sensitive crack growth, Figs. 11a and b show an extensive scatter when data is compared from many laboratories (47, 51). This scatter in test results is clearly connected to S-content, product form and test procedures in different laboratories. However, much more work is needed for better understanding the differences in crack growth behaviour between different material heats.

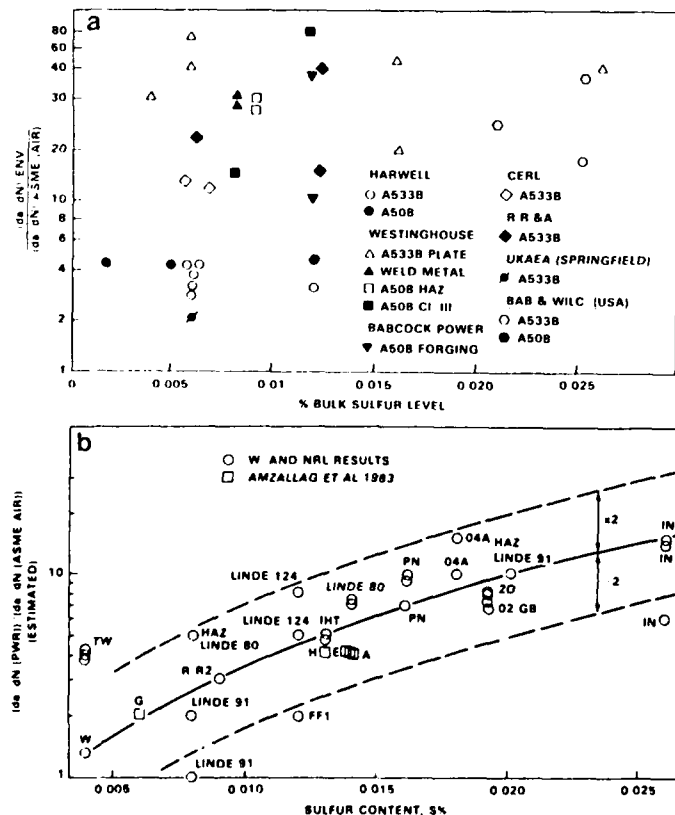


Fig. 11 - (a) Effect of bulk sulfur level on the cyclic crack growth in RPV materials in PWR water environment ( $R = 0.7 - 0.85$ ; 1 cpm sine waveform) (51). (b) Effect of sulfur on cyclic crack growth (47).

The possibility of anionic impurities in the autoclave water contributing to inter-laboratory variability has been investigated, concentrating on sulfur-containing species since these may also be present in the crack enclave due to dissolution of sulfur in the steel (52). The influence of water purity can be shown on the EAC susceptibility, Fig. 12, as moving the EAC boundary towards higher flow rates and lower sulfur steels. The boundary is moved still further with oxygen present in addition to sulfate. The possible presence of sulfur-containing, or other impurity species may explain some of the inter-laboratory variability in crack growth data which has been reported.

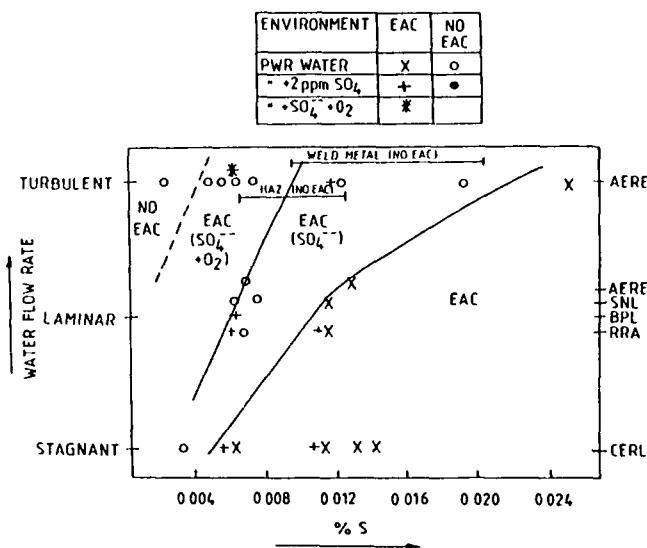


Fig. 12 - EAC susceptibility of RPV steels in PWR water, with and without sulfate contamination (based on corrosion fatigue data at 0.0167 Hz,  $R = 0.7$ ) (52).

Further studies have been concentrated on the fractographic features of the corrosion fatigue fracture surfaces (4, 28, 53 - 56). In an extensive study carried out with the International Cyclic Crack Growth Rate Group (ICGR) round robin specimens (28), it was concluded that whenever environmental enhancement in the cyclic crack growth rate was observed, the fracture morphology changed from typical ductile striations into more planar, fan-shaped surfaces, the fans often starting from inclusions (Fig. 13). These two basic fracture morphologies co-existed, however, but the relative amount of planar, fan-shaped areas increased with increasing environmental enhancement, Fig. 14.

The MnS-inclusions have an important role in the crevice chemistry: in neutral or slightly acid conditions prevailing inside the crack due to the hydrolysis of anodically dissolved metal ions, the MnS inclusions act as local cathodes and dissolve forming H<sub>2</sub>S. The dissolution behaviour of MnS inclusions of A533B pressure vessel

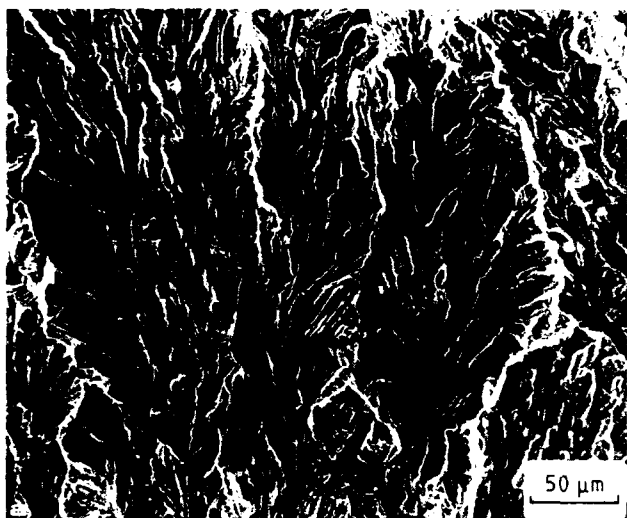


Fig. 13 - Examples of typical fan-shaped brittle striated fracture areas in A533B steel specimen 1HT49 (a) and 1HT19 (b). Note the spreading of the fan from inclusions in (b) (28).

steel in light water reactor environments and in sulphuric acid solutions has been studied, and the polarization curves of the steel and synthetic MnS were measured (6). The formation of  $H_2S$  leads to increased hydrogen absorption and the absorbed hydrogen is diffusing along the stress gradient ahead of the crack tip. The MnS inclusions have also another role in the environment sensitive cracking; namely they act as preferential trapping sites for hydrogen. The trapped hydrogen can cause brittle-like hydrogen-induced fracture nucleation at inclusions ahead of the main crack tip inside the plastic zone (4).

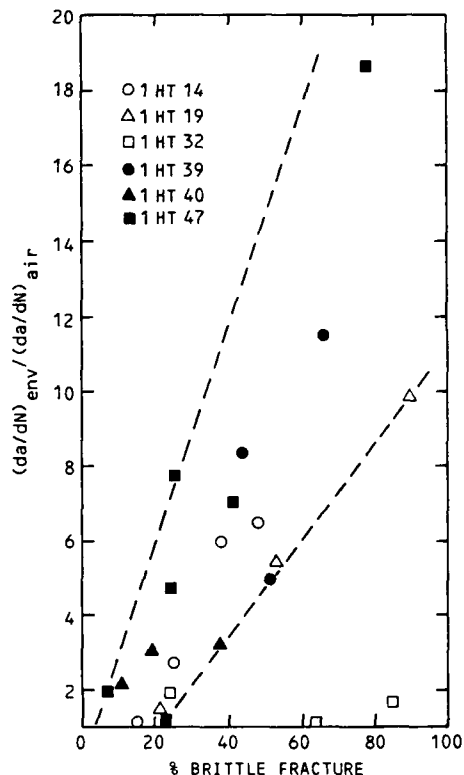


Fig. 14 - The correlation between the relative amount of brittle-like fracture and the environmental crack growth rate enhancement factor (28).

#### FRACTOGRAPHY

The fractographic examination has revealed three different fracture morphologies:

- transgranular, ductile striated fracture
- transgranular, brittle striated fracture and
- striationless, cleavage-like fracture.

Typical examples of the three morphologies are shown in Fig. 15. The cleavage-like fracture morphology in Fig. 15 exhibits tunnel-like features. A comparison between brittle striated corrosion fatigue fracture and true quasi-cleavage fracture (obtained by fracturing at liquid nitrogen temperature) is also shown in Fig. 15. Similar overall features are evident: the brittle striations seem to be superposed on cleavage planes. It is also evident that the fan-shaped patterns seen on brittle striated corrosion fatigue fracture surfaces are at least partly connected to the microstructure of the steel, as fan-shaped features are observed also on the true quasi-cleavage fracture surface.

The brittle fracture mode usually does not cover the whole fracture surface at a particular

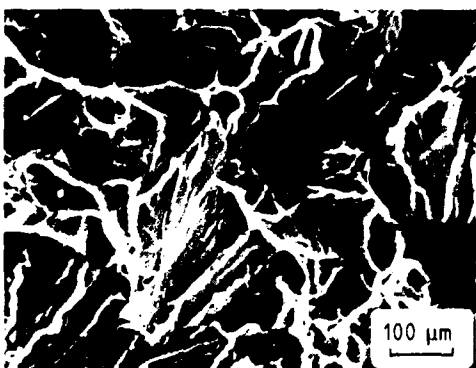
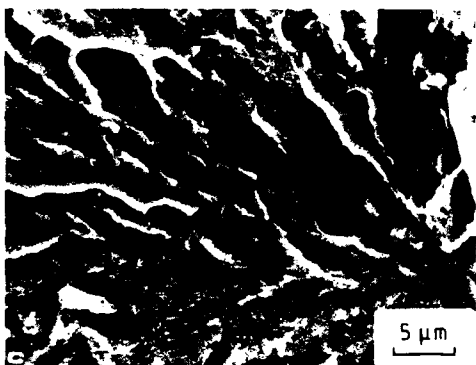
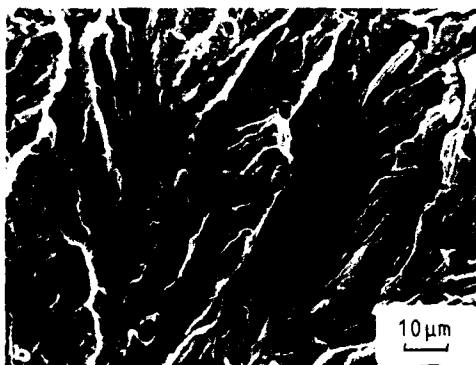
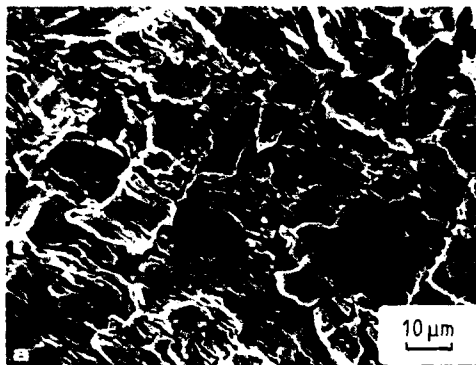


Fig. 15 - Typical examples of (a) ductile striations, (b) brittle striations, (c) striationless cleavage-like fracture in corrosion fatigue and (d) obtained after test termination at liquid nitrogen temperature (28).

$\Delta K$ -level, but rather is seen to coexist with ductile striated areas. The relative amounts of these two fracture modes depend on the extent of environmental enhancement. When the environmental enhancement in the crack growth rate increases, the striations become brittle. The striationless brittle fracture mode is sometimes, but not always, observed when the environmental enhancement factor approaches its maximum value. In the last part of a typical corrosion fatigue test, when the bend-over towards the air line occurs, coarser brittle striations appear and the amount of ductile striated area also increases (Fig. 16).

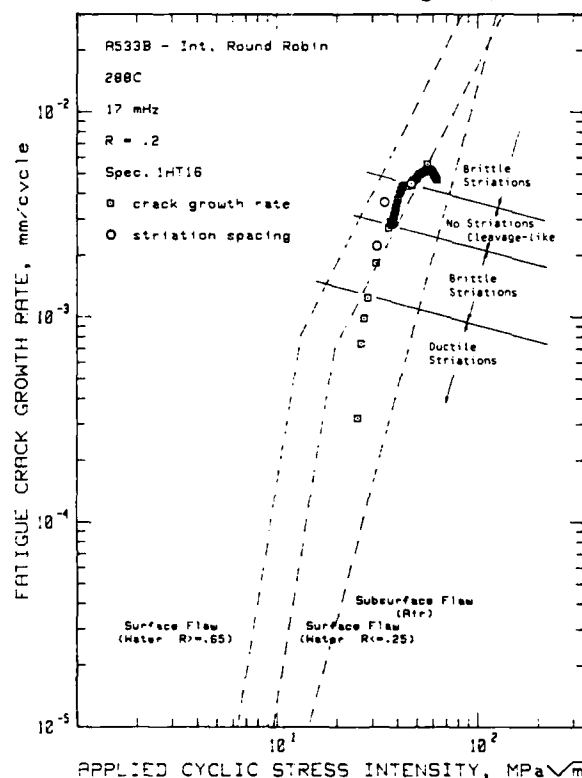


Fig. 16 - Location of the four fractographically different crack growth areas as compared to the  $da/dN$ - $\Delta K$  results and the comparison between striation spacings and observed crack growth rates in A533B specimen 1HT16 (28). The striation spacing corresponds well with the observed crack growth rates.

The fan-shaped brittle striated fracture surface features often spread from the MnS-inclusion colonies. Another feature typically associated with environmentally enhanced crack growth is the terraced appearance caused by elongated MnS-inclusions located away from the main crack path, Fig. 17. The depth of the terraces was less than 40  $\mu m$  as measured of cross-sections. These terraces are joined to the main fracture surface by ductile tearing. In fatigue tests in air, the inclusion clusters produce similar terraces in smaller numbers, but in this case no brittle areas are observed around the inclusions. Figure 17 shows a terrace next to the precrack tip. The terraces were,

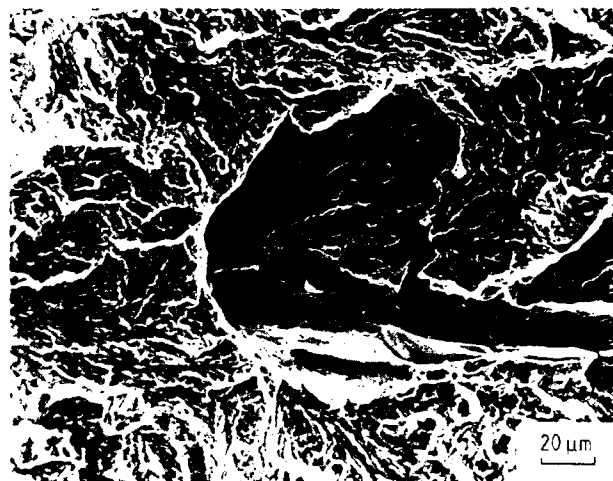
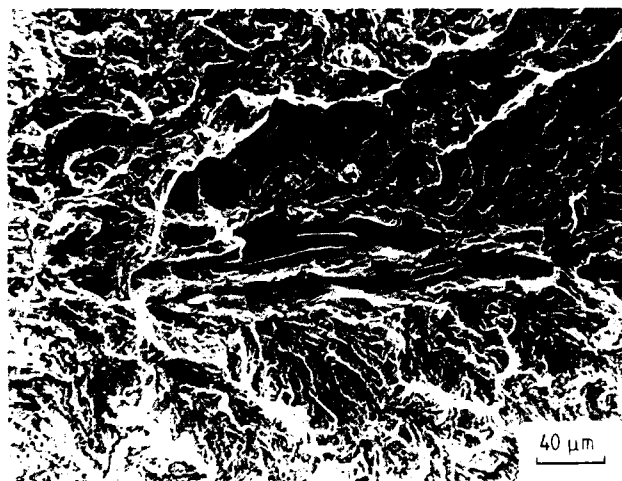
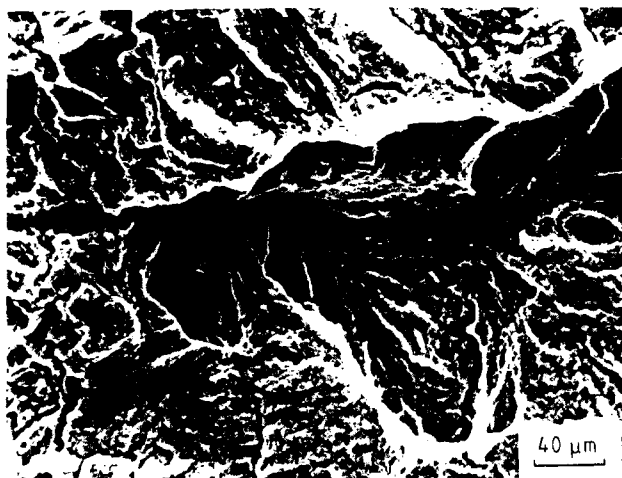


Fig. 17 - Terraced corrosion fatigue fracture surface morphology in A533B steel specimen LHT14 produced by MnS-inclusions at different levels from the main crack path. The corresponding  $\Delta K$  values are (a) 29 MPa/m, (b) 49 MPa/m, (c) 64 MPa/m, and (d) 69 MPa/m. Note that the inclusions are not fully dissolved close to the crack tip (4).

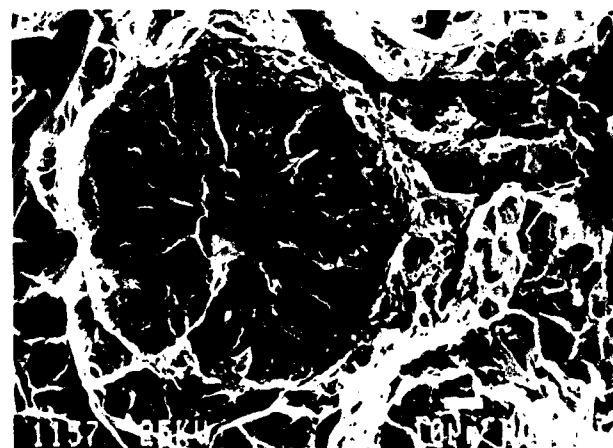
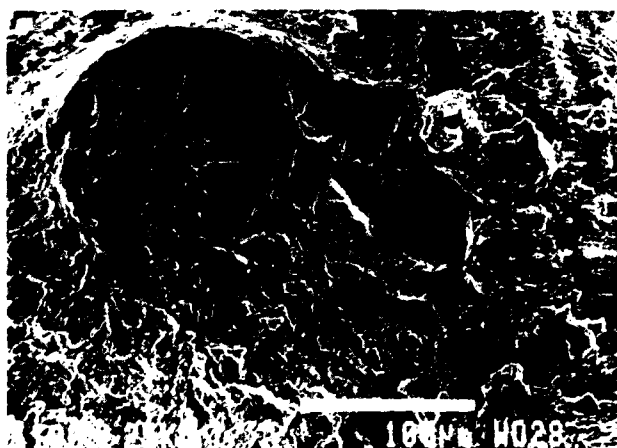


Fig. 18 - (a) Fractograph of a nearly circular area of brittle-like appearance and no evidence of striations; this region, found on the low sulfur A533-B steel (W7-2C-14, 0.004 % S) (see Fig. 5b), is presumed to have formed by hydrogen cracking (5). (b) Hydrogen cracking located in the uncracked region of the same specimen ahead of the fatigue crack tip; this region was opened up during the post-test fracture.

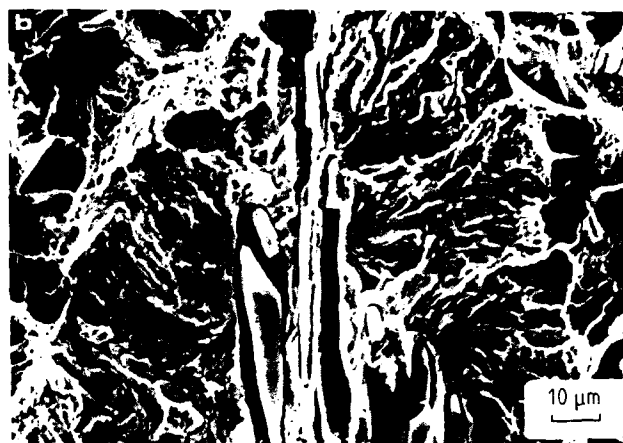
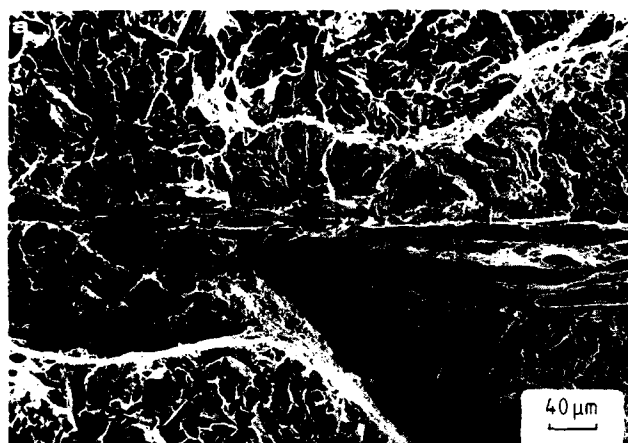


Fig. 19 - (a) An example of the effect of dense inclusion stringers on the crack tip morphology in A533B steel specimen 1HT14. (b) Detail of the crack tip. Note the local crack growth direction parallel to the main crack front adjacent to the inclusions (4).

however, mainly observed at high  $\Delta K$ -levels near the final corrosion fatigue crack tip, Fig. 17b to d. The morphology of these terraces indicated that inclusions in the crack tip stress field can initiate cracking ahead of the main crack front. Thus, inclusions away from the main crack path can also be associated with the crack. This increases the number of MnS-inclusions exposed on the fracture surface. The exposed MnS-inclusions are dissolved during the corrosion fatigue test leaving empty sites. However, closer to the crack tip partly dissolved MnS-inclusions are observed, and immediately adjacent to the crack tip, undissolved inclusions are present. Thus, the dissolution of the MnS-inclusions requires a significant period of exposure to the high-temperature water environment.

A connection between the local density of MnS-inclusions and the brittle type of fracture surface is apparent, and considerably fewer inclusions have been seen on the ductile striated fracture surface. In the ductile fracture surface, small brittle regions are sometimes associated with the inclusions, Fig. 18. In areas containing a dense distribution of elongated MnS-inclusions, the crack tip can propagate much faster than in the surrounding areas. Figure 19a shows an example of a crack tip bulge along elongated MnS-inclusion stringers, having a typical brittle mode of propagation. The crack tip is surrounded by mechanical cleavage cracking produced at liquid nitrogen temperature subsequent to the test. Fig. 19b shows a detail of the crack tip and reveals brittle striations. The inclusions are not dissolved: they have broken along matrix/inclusion phase boundaries and contain some cracks.

In some cases inclusions seem to be capable of producing brittle cracking around them ahead

of the crack tip. Fig. 20 shows an example of brittle cracking (which differs from mechanical cleavage fracture) around an inclusion ahead of the final crack tip. When a microcrack advances from the inclusion ahead of the crack tip, the fracture surface can be striationless as shown in Fig. 20 or brittle striated (Fig. 21), suggesting that the microcracks can propagate also intermittently ahead of the crack tip. The crack growth from the inclusion in Fig. 21 has taken place near the location of maximum stress ahead of the corrosion fatigue crack tip parallel to the crack front. In this direction the microcrack stays in the area of maximum stress. This kind of local crack growth is typically observed in brittle areas around inclusions in terraces. This supports the idea that the terraces are formed ahead of the main crack tip and then linked to the main crack front by ductile tearing.

In summary, the microscopic features of the fracture surfaces of A533B steel CF specimens have been studied indicating that the brittle mode of fracture seems to originate mainly from inclusion clusters. Ductile striated areas can be observed between brittle areas. The brittle mode of fracture seems to be generally more pronounced in the middle of the specimens where the crevice chemistry conditions are established.

#### SLOW STRAIN RATE TESTS

Slow strain rate tests in pure high temperature water initiate SCC above about  $-200 \text{ mV}_{\text{SHE}}$ . Crack initiation is taking place generally at corrosion pits which form on sites of surface MnS inclusions, Fig. 22a. Then the initiated cracks spread like fans from the initiation sites. This is similar what happens



Fig. 29 - (a) and (b) Brittle cracking around a MnS-inclusion ahead of the crack tip in A533B steel specimen 1HT14. The CF crack tip is on the lower part. (c) Detail of the brittle cracking morphology next to the inclusion (4).

inside the CF cracks, Fig. 13b. Local chemical and electrochemical conditions leading to this kind of cracking have been simulated by performing the SSRT-tests in MnS-saturated pure water at 30 °C (26) and in MnS-saturated PWR-water at 288 °C (57), Figs 22b and c. In MnS-saturated conditions SSRT-tests with notched specimens are able to produce similar environment-sensitive cracking than inside CF cracks. The potential dependence of this cracking seems to be in accordance with hydrogen absorption kinetics from  $H_2S$  containing environments (26). At reactor temperature the crack growth rate in these SSRT-tests is about  $2 \times 10^{-5}$  m/s (57) which is comparable with the maximum values obtained with different fracture mechanics specimens both in cyclic and static tests. The corrosion potential in PWR-water varies from  $-700 \dots -800$  mV<sub>SHE</sub> to  $-500 \dots -600$  mV<sub>SHE</sub> due to MnS (57), i.e. into the stability area of  $Fe_3O_4$  and  $H_2S$  in Pourbaix-diagram of Fe, and S, respectively, Fig. 23.

#### SURFACE SPECTROSCOPY

Information on the role of sulfur in corrosion fatigue crack growth of pressure vessel steels has been obtained by using recently available spectroscopic ESCA and Auger techniques to reveal the amount of sulfur and other impurities in the crack-tip oxide layer as well as their chemical state, i.e., the valence state (29, 30). Specimens were selected representing both the high and low crack growth rates of the similar pressure vessel steels. Fracture surfaces of low sulfur and medium sulfur steels, as well as steels with different MnS particle sizes and distribution were compared. Also artificial crack-tip simulating specimens were studied.

The oxide on the corrosion fatigue fracture surfaces formed in PWR-water conditions was found to be  $Fe_3O_4$  (magnetite) as is expected on the basis of the electrochemical data. Sulfur was observed on the top of the oxide surface mainly as a sulfate which probably was an arti-

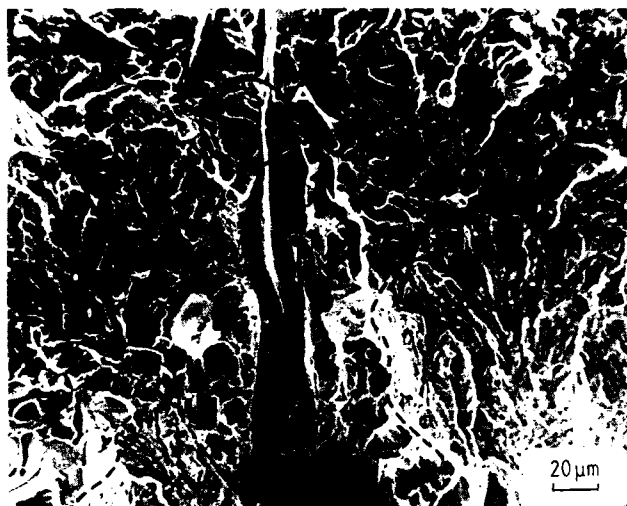


Fig. 21 - (a) Cracking starting from a MnS-inclusion ahead of the main crack tip (A) in A533B steel specimen 1HT39. (b) A detail of A. Note that the fracture surface of the microcrack is striated (28).

fact due to oxidation during the exposure to the aerated conditions. Analysis of the Fe  $2p_{3/2}$  line showed that the major sulfur species was  $FeS_2$ . Also  $FeS$  was observed after sputtering, but because its line is very near the line of  $FeO$  (which is known to result from the sputtering of  $Fe_3O_4$ ), it was not certain from which phase the information came. This finding confirms MnS-rich crack tip chemistry and the earlier electrochemical findings (31 - 33) that the electrochemical conditions inside the crack are in the area of Fe-S- $H_2O$  Pourbaix diagram where both  $Fe_3O_4$  and  $FeS_2$  are stable phases (Fig. 23) (34). Also the corrosion potentials (-550...-600 mV<sub>SHE</sub>) in MnS-saturated PWR-water experiments are based on the fact that  $FeS_2$  is a stable phase (57). In addition, in these conditions Mn is soluble, as can be seen from

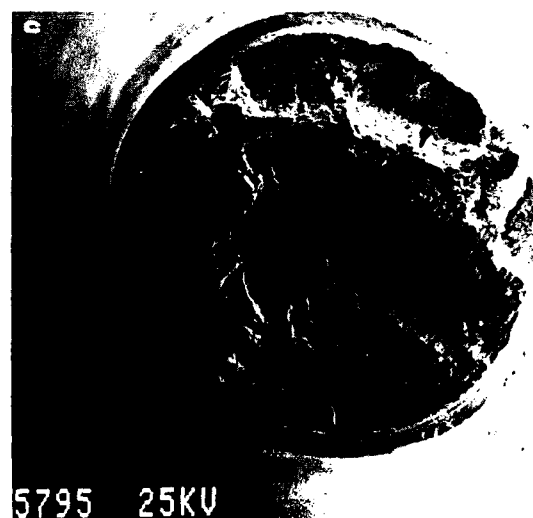
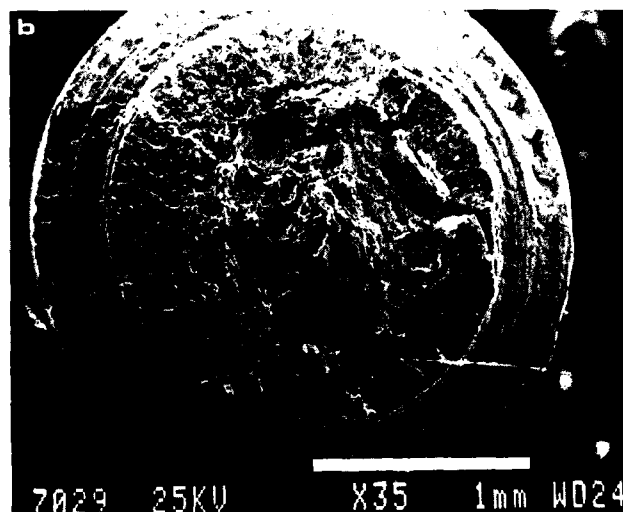
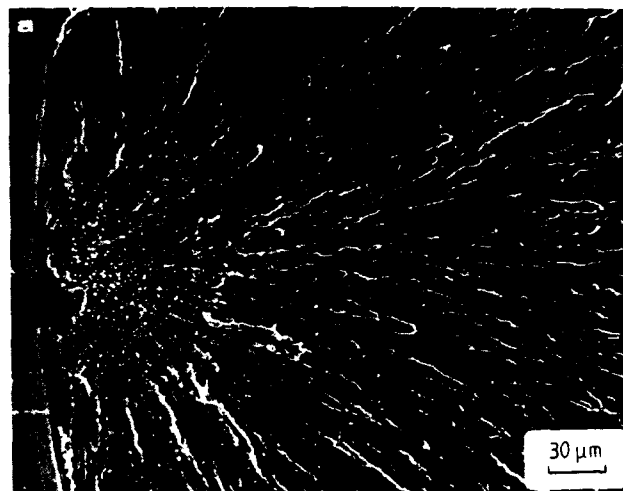


Fig. 22 - (a) Fractograph of SSRT-specimen of A508 steel tested in pure water containing 400 ppb  $O_2$  (ECP: +80...+100 mV<sub>SHE</sub>) (19). (b) Typical fracture surface of a A508 steel SSRT-specimen (tested at -360 mV<sub>SHE</sub> in MnS-saturated pure water at 80 °C) showing the notch, brittle transgranular SCC area and ductile final fracture (26). (c) Fracture surface of prefatigued A533-B steel formed in MnS-saturated PWR-water at 288 °C (E = -590 mV<sub>SHE</sub>) (57).

the Mn-S-H<sub>2</sub>O Pourbaix diagram (Fig. 24). Therefore, Mn was not generally observed to be present in the oxide phase of the corrosion fatigue fracture surfaces.

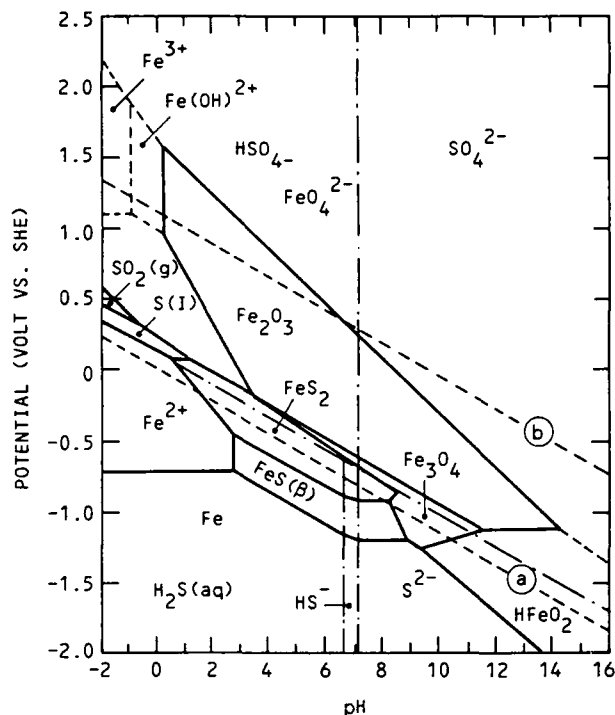


Fig. 23 - Potential-pH diagram for Fe-S-H<sub>2</sub>O at 300 °C:  $a(\text{ion}) = 10^6$ ,  $a(\text{dissolved sulfide}) = 10^{-1}$ ,  $a(\text{gas}) = 1$ , and  $a(\text{solid}) = 1$  (34).

Generally, the amount of sulfur in the oxide layer was about 3 at. %, and sulfur seemed to be present deep in the oxide phase. In specimens where a high crack growth rate was observed, the amount of sulfur generally at the crack tip was double (6 at. %) to that in the middle of the fracture surface behind the crack tip. The fracture surface oxide of the low sulfur steel contained 1 to 4 at. % S without showing any marked enhancement in the crack growth rate. Therefore, it cannot be concluded, based on these results, if there are any critical amounts of sulfur in the oxide phase which is needed for enhancing the corrosion fatigue crack growth rate.

#### DISCUSSION

Recently, it has been thought generally that the environmental enhancement of corrosion fatigue crack growth of pressure vessel steels in LWR conditions is related to the sulfur content of the steels. Therefore, many national programs have been initiated to study the effects of sulfur content of the pressure vessel steel on corrosion fatigue crack growth: in UK

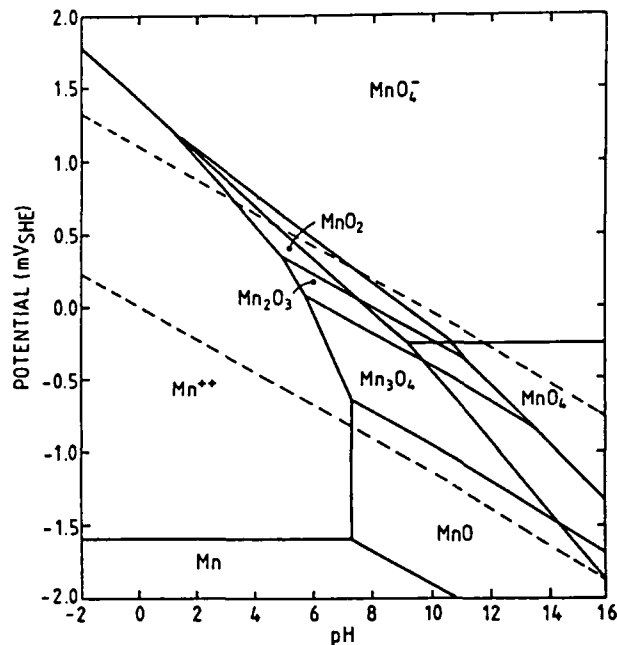


Fig. 24 - Potential-pH diagram for Mn-S-H<sub>2</sub>O at 300 °C. (P. Scott, Communication at ICCGR Meeting, Warrington, UK, May 1984).

(35), France (36), Japan (37), and in the USA (5, 38 - 40). The effects of size and distribution of MnS inclusions on corrosion fatigue crack growth have been studied especially in Finland (4, 27, 28). In order to understand the results obtained, mechanistic interpretations for the role of sulfur in the corrosion fatigue crack growth have to be found. Some supporting research has already been completed; the role of sulfur in anodic dissolution and hydrogen uptake has been discussed (7 and 41 - 46). The problem is complex because the chemistry and electrochemistry inside the crack seem to favour both reactions (8, 25 and 31 - 33).

In corrosion fatigue crack growth, hydrogen sulfide has been recently proven to be the principal species responsible for observed enhancement of the fatigue crack growth rates in light water reactor conditions (45) by injecting ppm levels of hydrogen sulfide into the corrosion fatigue crack tip of a low sulfur steel. In addition to MnS iron sulfide is also soluble in the crack-tip environment and can supply hydrogen sulfide in the crack-tip environment to sustain enhanced crack growth, as happened in the case of Van Der Sluys and Emanuelson's experiment (45), where high crack growth rate continued after injection of hydrogen sulfide into the crack tip of low sulfur pressure vessel steel was stopped. In order to understand mechanistically the role of sulfur in the corrosion fatigue crack growth, the effects of sulfur in anodic dissolution and in hydrogen uptake have to be studied in much more detail.



## CONCLUSIONS

The following main conclusions can be drawn based on the role of MnS inclusions in corrosion fatigue crack growth in reactor pressure vessel steels in simulated reactor water:

- Whenever environmental enhancement of the cyclic crack growth rate is observed, brittle features in fracture morphology (brittle striations or striationless cleavage-like fracture) are seen, although not throughout the entire fracture surface. In the absence of environmental enhancement, the fracture surfaces generally show ductile striations.
- Brittle features are usually associated with the manganese sulfide inclusions; brittle crack growth often spreads like a fan from an inclusion cluster. Considerably fewer inclusions are seen on ductile striated fracture surfaces than on brittle striated fracture surfaces.
- Inclusions can generate localized micro-cracking in front of the main crack tip, seen as terraces on the fracture surface and in metallographic sections.
- The oxide of the corrosion fatigue fracture surface (PWR-conditions) is in the form of magnetite ( $\text{Fe}_3\text{O}_4$ ). Sulfur was found to be basically in the form of  $\text{FeS}_2$ , but existence of  $\text{FeS}$  could not be excluded.
- Based on the presence of magnetite and  $\text{FeS}_2$ , the crack-tip conditions can be located in the potential-pH diagram indicating neutral or slightly acid conditions where the corrosion potential is around -500 mV(SHE) or less.
- The critical amount of sulfur in the oxide phase required to produce the high corrosion fatigue crack growth rates has not yet been revealed.
- The observed fractographic and metallographic features are consistent with hydrogen induced cracking as the main mechanism of environmentally enhanced cyclic crack growth.

## ACKNOWLEDGEMENT

This paper is a part of the Structural Materials in Nuclear Power Plants Programme funded by the Ministry of Trade and Industry in Finland and the Technical Research Centre of Finland.

## REFERENCES

1. Slama, G. and Rabbe, P., Proceedings of the 5th SMIRT Post-conference seminar, Paris, France, 1981, pp. 311-325.

2. Bamford, W. H., Geschini, L.J. and Jacko, R.J., Heavy Section Steel Technology Report for July-September 1983, USNRC Report NUREG/CR-3334, Vol. 3, March 1984, pp. 97-114.
3. Van der Sluys, A., Progress Report, October 1, 1982 to April 30, 1983. Project 1325-1. Electric Power Research Institute, Palo Alto, CA, July 1983.
4. Hänninen, H., Törrönen, K., Kemppainen, K. and Salonen, S., Corrosion Science, Vol. 23(6), 1983, p. 663-679.
5. Cullen, W.H., Kemppainen, M., Hänninen, H. and Törrönen, K., USNRC Report NUREG/CR-4121, Feb. 1985.
6. Klemetti, K., Hänninen, H., Törrönen, K., Kemppainen, M. and Pessa, M., Proc. of the Intern. Symp. on Environmental Degradation of Materials in Nuclear Power Systems - Water Reactors, Myrtle Beach, SC, Aug. 22-25, 1983, pp. 368-383.
7. Ford, F.P., Performance and Evaluation of Light Water Reactor Pressure Vessels, R. Rungta, J.D. Gilman and W.H. Bamford (Eds.), PVP-119, American Society of Mechanical Engineering, New York, 1987, pp. 43-62.
8. Hänninen, H., Illi, H., Törrönen, K. and Vulli, M., Proc. of the 2nd Intern. Atomic Energy Agency Specialists' Meeting on Subcritical Crack Growth, Japan, May 15-17, 1985, W.H. Cullen, Ed. USNRC Conf. Proc. NUREG/CP-0067, Vol. 2., Apr. 1986, pp. 179-200.
9. Speidel, M.O. and Magdowski, R.M., SMIRT Post Conf. Seminar No. 2, Session II, Davos, Switzerland, Aug. 24-25, 1987.
10. Hurst, P., Appleton, D.A., Banks, P. and Raffel, A.S., Corrosion Science, Vol. 25, 1985, pp. 651-671.
11. Congleton, J. and Hurst, P., Proc. of the 2nd Intern. Atomic Energy Agency Specialists' Meeting on Subcritical Crack Growth, W.H. Cullen, Ed., USNRC Conf. Proc. NUREG/CP-0067, Vol. 1, 1986, pp. 181-197.
12. Cowen, H.C., Hurst, P. and Lloyd, G.J., *ibid*, pp. 439-463.
13. Hurst, P., Banks, P., Pemberton, G. and Raffel, A. S., Proc. of the 2nd Intern. Symp. on Environmental Degradation of Materials in Nuclear Power Systems - Water Reactors, ANS, 1986, pp. 645-655.

14. Indig, M.E., Weber, J.E. and Weinstein, D., Review in Coatings and Corrosion, Vol. 5(1-4), 1982, pp. 173-225.
15. Pednekar, S., Mizuno, T., Szklarska-Smialowska, Z. and MacDonald, D.D., Corrosion/82, Houston, TX, Paper No. 244, 1982.
16. Choi, H., Beck, F.H., Szklarska-Smialowska, Z. and MacDonald, D.D., Corrosion, Vol. 38, 1982, pp. 136-144.
17. Lenz, E., Wieling, N., Neubrech, G., Proc. of the 2nd Intern. Atomic Energy Agency Specialists' Meeting on Subcritical Crack Growth, W.H. Cullen, Ed. USNRC Conf. Proc. NUREG/CP-0067, Vol. 2, 1986, pp. 455-473.
18. Kuniya, J., Masaoka, I., Sasaki, R., Itoh, H. and Okazaki, T., Trans. ASME Journal of Pressure Vessel Technology, Vol. 107, 1985, pp. 431-435.
19. Klemetti, K. and Hänninen, H., Proc. of the 2nd International Symp. on Environmental Degradation of Materials in Nuclear Power Systems - Water Reactors, ANS, 1986, pp. 70-76.
20. Congleton, J., Shoji, T. and Parkins, R.N., Corrosion Science, Vol. 25, 1985, pp. 633-650.
21. Congleton, J. and Parkins, R.N., Corrosion 87, NACE, Houston, TX, Paper No. 105, 1987.
22. Congleton, J. and Shoji, T., Structural Mechanics in Reactor Technology, Vol. F: LWR Pressure Components, Wittmann, F.H., Ed., A.A. Balkema, Boston, MA, 1987, pp. 265-270.
23. Shoji, T. and Takahashi, H., Intern. Cyclic Crack Growth Rate Meeting, Aug. 11-14, 1987, Erlangen/Stuttgart, FRG.
24. Ford, F.P., Taylor, D.F., Andresen, P.L. and Ballinger, R.G., Final Report, NP-5064M, Electric Power Research Institute, Palo Alto, CA, Feb. 1987.
25. Illi, H., Chanfreau, E. and Hänninen, H., Corrosion chemistry within pits, crevices and cracks. A. Turnbull, Ed., National Physical Laboratory, 1987, pp. 271-286.
26. Hänninen, H., Illi, H. and Kemppainen, M., Proceedings NATO Advanced Research Workshop Chemistry and Physics of Fracture. R.M. Latanision, Ed., Martinus Nijhoff Publishers BV, Dordrecht, The Netherlands, 1987, pp. 246-651.
27. Törrönen, K., Saario, T., Hänninen, H., Kemppainen, M. and Salonen, S., Fracture and the role of microstructure, Vol. II, Fatigue. Maurer, K.L. and Matzer, F.E., Eds., EGF, U.K., 1982, pp. 539-544.
28. Törrönen, K., Kemppainen, M. and Hänninen, H., Final Report, EPRI NP-3483, Electric Power Research Institute, Palo Alto, CA, May 1984.
29. Hänninen, H., Vulli, M. and Cullen, W.H., Third Intern. Symp. on Degradation of Materials in Nuclear Power Systems - Water Reactors. Michigan, USA, 1987. 10 p.
30. Hänninen, H.E., Vulli, M. and Cullen, W.H., U.S. Nuclear Regulatory Commission, Washington, DC, NUREG/CR-4863 MEA-2194, 1987.
31. Gabetta, G. and Buzzanca, G., Proc. of the 2nd Intern. Atomic Energy Agency Specialists' Meeting on Subcritical Crack Growth, W.H. Cullen, Ed. USNRC Conf. Proc. NUREG/CP-0067, Vol. 2, Apr. 1986, pp. 153-178.
32. Combrade, P., Foucault, M. and Slama, G., *ibid*, pp. 201-218.
33. Ford, F.P. and Combrade, P., *ibid*, pp. 231-268.
34. Chen, C.H., Aral, I. and Theus, G., EPRI NP-3137, Palo Alto, CA, June 1983.
35. Tice, D.R., Atkinson, J.D. and Scott, P.M., Proc. of the 2nd Intern. Atomic Energy Agency Specialists' Meeting on Subcritical Crack Growth, W.H. Cullen, Ed. USNRC Conf. Proc. NUREG/CP-0067, Vol. 1, Apr. 1986, pp. 251-282.
36. Amzallag, C., Bernard, J.L. and Slama, G., *ibid*, pp. 283-308.
37. Kitagawa, H., Nakajima, H., Nagata, N., Sakaguichi, Y. and Iwadate, T., *ibid*, pp. 135-164.
38. Cullen, W.H., *ibid*, pp. 339-356.
39. Bamford, W.H. and Wilson, I.L.W., *ibid*, pp. 317-338.
40. Van Der Sluys, W.A. and Emanuelson, R.H., *ibid*, pp. 199-218.
41. Ford, F.P., *ibid*, pp. 3-72.
42. Cullen, W., Gabetta, G. and Hänninen, H., USNRC Report NUREG/CR-4422, Dec. 1985.
43. Hänninen, H., Törrönen, K., and Cullen, W.H., Proc. of the 2nd Intern. Atomic Energy Agency Specialists' Meeting on Sub-

- critical Crack Growth, W.H. Cullen, Ed. USNRC Conf. Proc. NUREG/CP-0067, Vol. 1, Apr. 1986, Pp. 73-98.
44. Atkinson, J.D. and Forrest, J.E., *ibid*, pp. 153-178.
  45. Van Der Sluys, W.A. and Emanuelson, R.H., Third Intern. Symp. on Environmental Degradation of Materials in Nuclear Power System - Water Reactors, Aug. 30 - Sept. 3, 1987, Traverse City, MI, 1987.
  46. Bamford, W.H. and Wilson, I.L., Structural Mechanics in Reactor Technology. Vol. F., F.H. Wittman, Ed., A.A. Balkema, Boston, MA, 1987, pp. 137-141.
  47. Amzallag, C., Bernard, J.L. and Slama, G., Int. Symp. in Environmental Degradation of Materials in Nuclear Power System - Water Reactors, Myrtle Beach, South Carolina, August 22-25, 1983, pp. 15-17.
  48. Scott, P.M., Truswell, A.E. and Druce, S.G. Corrosion, Vol. 40(7), 350-357 (1984).
  49. Scott, P.M. and Truswell, A.E., Journal of Pressure Vessel Technology, Vol. 105, 1983, pp. 245-254.
  50. Törrönen, K., Saario, T., Hänninen, H. and Kemppainen, M., IAEA Specialists' Meeting "Corrosion and Stress Corrosion of Steel Pressure Boundary Components and Steam Turbines", Espoo, Finland, Nov. 22-25, pp. 127-146.
  51. Van Der Slyus, W.A. and Emanuelson, R.H., Proc. of the 2nd Intern. Atomic Energy Agency Specialists' Meeting on Subcritical Crack Growth, W.H. Cullen, Ed., USNRC, Conf. Proc. NUREG/CP-0067 MEA-2090, Vol. 1, Apr. 1986, pp. 199-218.
  52. Tice, D.R., Atkinson, J.D. and Scott, P.M., *ibid*, pp. 251-281.
  53. Bulloch, J.H. and Buchanan, L.W., Corrosion Science, Vol. 24(8), 1984, pp. 661-674.
  54. Atkinson, J.D., Bulloch, J.H. and Forrest, J.E., Proc. of the 2nd Intern. Atomic Energy Agency Specialists' Meeting on Subcritical Crack Growth. W.H. Cullen, Ed., USNRC, Conf. Proc. NUREG/CP-0067 MEA-2090, Vol. 2, Apr. 1986, pp. 263-291.
  55. Bulloch, J.H., Theoretical and Applied Fracture Mechanics, Vol. 7, 1987, pp. 7-18.
  56. Swan, D.I. and Chapman, O.J.V., Environmentally Assisted Cracking: Science and Engineering, ASTM STP. To be published.
  57. Hänninen, H. and Cullen, W., Int. Conf. on Environment-Assisted Fatigue, Sheffield University, UK, 12-14 April, 1988. To be published.

# PLATE-LIKE RIGID INCLUSIONS AND DUCTILE-BRITTLE TRANSITION

Ing-Hour Lin

Fracture and Deformation Division  
Institute for Materials Science and Engineering  
National Bureau of Standards  
Boulder, Colorado 80303 USA

## ABSTRACT

A simple dislocation-crack-inclusion model is proposed to study inclusion embrittlement. Before, we derived the elastic interaction among screw dislocations, a plate-like rigid inclusion, and a crack under antiplane shear strain. Here, we apply these results to dislocation emission and crack-tip breakaway. When an inclusion is very close to the crack tip, the total image force on a dislocation is enlarged and a ductile-to-brittle crossover of the intrinsic character of cracks may be induced. The breakaway of a shielded crack, triggered by void nucleation at the inclusion, is discussed.

IN THIS PAPER WE propose a simple dislocation-crack-inclusion model with which we can study the mechanical roles of a plate-like rigid inclusion on fracture embrittlement. We work in mode III because simple analysis results can be derived. These illustrate the physical situation. We leave the more realistic but mathematically complex mode I case to another study.

In the model we consider the elastic interaction among screw dislocations, a plate-like rigid inclusion, and a crack under applied anti-plane shear strain. The boundary conditions on the surfaces of the elastic defects are, respectively, zero traction on the crack and zero displacement on the

inclusion. These boundary conditions induce image forces on dislocations and local stress concentrations on the crack and the inclusion. Dislocation-crack interactions and their important role in fracture problems are well documented. The current state of the subject is described in [1-10]. Likewise, dislocation-inclusion interactions and their role in both void nucleation at inclusions and second-phase particle cracking are also well developed [11-13]. Perhaps the best known example is the application of carbide cracking at grain boundaries in developing a cleavage fracture model to predict the fracture toughness increase in mild steels with increasing temperature [14]. However, so far the dislocation-crack interaction under the influence of an inclusion has not been fully analyzed because the mixed boundary conditions at the surfaces of cracks and inclusions lead to difficult analysis in the presence of a dislocation. Also, since a plate-like rigid inclusion lying on the cleavage plane has no interaction with a crack under antiplane shear strain, the analysis is further simplified considerably and will make mathematical analysis tractable when screw dislocations are present. The physical origin of this zero interaction force is explained in the next section. The purpose of this paper is to use results of our recent work on dislocation-inclusion interactions [15] in the well-known dislocation-crack interaction to construct a dislocation-crack-inclusion model to study two fundamental fracture problems related to inclusions: dislocation emission at crack tips under the influence of inclusion; and void nucleation and propagation at inclusions under the influence of cracks and dislocations.

\* Contribution of the National Bureau of Standards, not subject to copyright.

In the next section the dislocation-crack-inclusion model is presented, and then the results are applied to study effects of inclusion on dislocation emission in Section 3 and inclusion-induced cleavage fracture in Section 4. Finally, we present our conclusions in Section 5.

#### DISLOCATION-CRACK-INCLUSION MODEL

Consider the elastic interaction among a set of screw dislocations, a plate-like rigid inclusion and a crack under antiplane shear strain, which is characterized by the applied stress intensity factor  $K$  for the crack. (In our model the applied shear stress is  $\sigma_{32}$ ; so there is no applied  $K$ -field for the inclusion). Let the crack and the inclusion, respectively, occupy the  $-x_1$  half and  $+x_1$  half of the  $x_1x_3$  plane, with the crack tip at the origin and the inclusion tip at  $x_1 = w$  (Fig. 1).

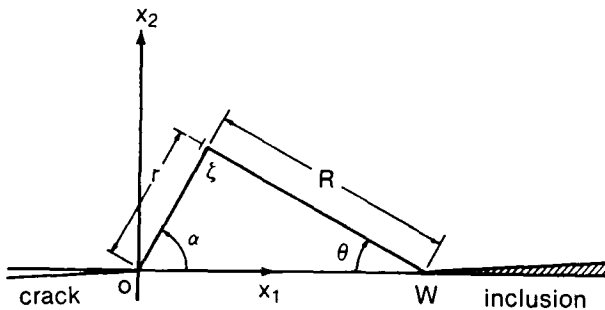


FIGURE 1. - Coordinate system for dislocation-crack-inclusion interaction. The crack tip is at the origin with cleavage plane along the negative  $x_1$  axis. The inclusion is along the positive  $x_1$  axis and with its tip at  $x_1 = w$ . The dislocation is at  $\xi$  measured from the crack tip.

In the absence of the inclusion the stress potential caused by the crack and dislocations is known [10]. The stress potential caused by dislocation-inclusion interaction is derived and will be published elsewhere [15]. Because there is no crack-inclusion interaction under this loading condition, the dislocation-crack-inclusion interaction can be constructed by the superposition of the dislocation-crack and dislocation-inclusion interactions. This zero interaction force stems from the fact that the stress component  $\sigma_{13}$ , generated by the crack, is zero on the inclusion surfaces. So the equivalent zero displacement boundary condition is automatically satisfied. Without showing the detailed calculation, the forces on the crack and the inclusion and each of the dislocations can be expressed, respectively,

$$\bar{f}_c = -\frac{k^2}{2\mu}$$

$$k = K - \sum_j \frac{\mu b_j}{2\sqrt{2\pi}} \left( \frac{1}{\sqrt{\xi_j}} + \frac{1}{\sqrt{\xi_j}} \right) \quad (1)$$

$$\bar{f}_R = -\frac{k_R^2}{2\mu}$$

$$k_R = \sum_j \frac{i\mu b_j}{2\sqrt{2\pi}} \left( \frac{1}{\sqrt{\xi_j}} - \frac{1}{\sqrt{\xi_j}} \right) \quad (2)$$

$$\begin{aligned} \bar{f}_d = & \frac{Kb}{\sqrt{2\pi\xi}} - \frac{\mu b^2}{4\pi} \left( \frac{1}{2\xi} + \frac{1}{\sqrt{\xi}(\sqrt{\xi} + \sqrt{\xi})} + \right. \\ & \left. + \frac{1}{2\xi} - \frac{1}{\sqrt{\xi}(\sqrt{\xi} + \sqrt{\xi})} \right) \\ & + \sum_j' \frac{\mu b b_j}{4\pi} \left( \frac{1}{\xi - \xi_j} - \frac{1}{\xi - \xi_j} + \right. \\ & \left. + \sqrt{\frac{\xi_j}{\xi}} \frac{1}{\xi - \xi_j} + \sqrt{\frac{\xi_j}{\xi}} \frac{1}{\xi - \xi_j} - \right. \\ & \left. - \frac{1}{\sqrt{\xi}} \left[ \frac{1}{\sqrt{\xi} + \sqrt{\xi_j}} - \frac{1}{\sqrt{\xi} + \sqrt{\xi_j}} \right] \right) \quad (3) \end{aligned}$$

The force is given as a vector  $f$  in the complex plane on the crack, inclusion and dislocation, respectively,  $\mu$  is the shear modulus,  $b$  is the Burgers vector of a reference dislocation, and  $b_j$  is the Burgers vector of all other dislocations. Note that  $b$  has a sign and may be plus or minus for the screw dislocations, which are at position  $\xi$  in the complex plane with the crack tip at the origin. The variable  $\xi_j$  is related to  $\xi_j$  by  $\xi_j = \xi_j - w = R_j e^{i\theta_j}$  measured from the inclusion tip. The sum over  $j$  is a sum over the dislocation distribution.  $\Sigma'$  denotes a sum over all dislocations except that for which the force is being calculated.  $k$  and  $k_R$  are respectively the local stress intensity factors for the crack and the inclusion. If the Burgers vector has a positive sign, then the crack tip becomes shielded but the inclusion tip is antishielded.

In equilibrium, the elastic forces in Eq. (1), Eq. (2), and Eq. (3) will be balanced by other lattice force, such as surface tension effects at the crack tip and inclusion tip or Peierls forces, etc. at the dislocations.

Thus

$$f_c = 2\gamma \quad (4)$$

$$f_R = 2\gamma_R \quad (5)$$

$$\bar{f}_d = \sigma_f b \quad (6)$$

$\gamma$  is the intrinsic surface energy,  $\gamma_R$  is the surface tension at the inclusion/matrix interface, while  $\sigma_f$  is an assumed friction stress acting on a dislocation.

#### DUCTILE/BRITTLE TRANSITION

A crack that can spontaneously emit dislocations will lead to a ductile fracture, while a crack stable against such emission will lead to brittle fracture. In this section the effect of an inclusion on dislocation emission at crack tips will be analyzed. The critical  $k$  for emission,  $k_e$ , is obtained by calculating the force on an emerging dislocation as a function of its distance from the crack tip, and as a function of  $k$ . Let  $\alpha$  be the rotation angle between the original  $x_1$  direction and the slip plane. Then for any complex vector,  $A$ , its value in the slip plane coordinates (Fig. 2), is

$$(A)_{\text{slip}} = A e^{-i\alpha} \quad (7)$$

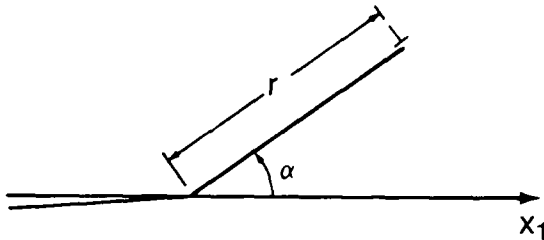


FIGURE 2. - Slip-plane coordinates. In slip-plane coordinates, the new coordinates are related so the new  $x_1$  direction lies along  $r$  and  $\alpha$  is the angle of rotation between the original and the new  $x_1$  axis lying on the cleavage plane.

In the slip plane coordinates, the force on a dislocation in the slip direction is calculated from the first two terms shown in equation (3),

$$\text{Re} \left[ \bar{f}_d \right]_{\text{slip}} = \frac{bk \cos(\alpha/2)}{\sqrt{2\pi r}} - \frac{\mu b^2}{4\pi r} \left[ 1 + \frac{\sin(\alpha + \theta)}{\sin \alpha} \sin^2 \frac{\theta}{2} \right] \quad (8)$$

In this calculation, Eq. (3) is used with  $K$  set equal to  $k$ , and without counting the interactions with other dislocations, under the assumption that they are far from the crack. The force on the dislocation caused by

the crack is positive or negative, depending on the sign of the Burgers vector. The image force on the slip plane is always attractive.

The function on the right in equation (8) is zero at a critical value of  $r$ . For smaller  $r$ , the dislocation is attracted to the crack tip, and for larger  $r$ , the dislocation is repelled. Equation (8) is based on line singularity cracks and dislocations. Both cracks and dislocations, however, possess nonlinear regions at their centers within which elastic arguments do not apply. If this joint core size for the crack plus emerging dislocation exceeds the point of zero of force in Eq. (8), then the attractive region will not be sensed, and the dislocation will be spontaneously emitted. Putting  $r$  equal to the core size,  $r_0$ , just described and writing the condition for the zero force, we then have a value of  $k$  that describes the onset of dislocation emission.

$$k_e = \frac{\mu b}{2\sqrt{\pi r_0} \cos(\alpha/2)} \left[ 1 + \frac{\sin(\alpha + \theta)}{\sin \alpha} \sin^2 \frac{\theta}{2} \right] \quad (9)$$

Since the extra term in the bracket is positive, equation (9) shows that the intrinsic character of the core crack crosses over from ductile to brittle if the plate-like rigid inclusion is very close to the crack tip and if the dislocation is not emitted on the cleavage plane.

#### INCLUSION INDUCED CLEAVAGE FRACTURE

Generally, external sources of dislocations emit as many positive as negative Burgers vectors (conservation of total Burgers vector). The antishielding dislocations are in general attracted and disappear at the crack surfaces and one would expect dislocation clouds associated with the crack tip to have excess shielding dislocations. These shielding dislocations shield the crack tip from the applied stress intensity factor but increase the stress concentration at the inclusion tip when the shielding clouds are enlarged as the applied load is increased. If the crack tip is well shielded, then the shielded crack tip can break away when voids are generated because the antishielding caused by voids can enhance the driving force at the crack tip. In this section, the fracture

toughness of inclusion-induced cleavage fracture will be estimated. In terms of a super-dislocation representation, let the shielding cloud be represented by a super-Burgers vector  $B$ , located at  $(r, \alpha)$ , measured from the crack tip. From Eq. (1) and Eq. (2), the local- $k$  can be written

$$k_c = K - \frac{\mu B \cos(\alpha/2)}{\sqrt{2\pi r}} \quad (10)$$

$$k_R = \frac{\mu B}{\sqrt{2\pi r}} \sin \frac{\theta}{2} \sqrt{\frac{\sin \theta}{\sin \alpha}} \quad (11)$$

Voids are generated at the inclusion tip when  $k_R$  reaches a critical value characterized by

$$k_R = \sqrt{4\mu\gamma_f} \quad (12)$$

$$\gamma_f = \gamma_m + \gamma_I - \gamma_R$$

Here  $\gamma_m$ ,  $\gamma_I$ , and  $\gamma_R$  are respectively the intrinsic surface energy of the matrix, the inclusion, and the interface between the inclusion and the matrix. Crack breaks away when the  $k_c$  in Eq. (10) is larger than the local equilibrium conditions shown in Eq. (4). However, Eq. (4) still applies for estimating the lower bound of fracture toughness. Combining Eq. (10) and Eq. (11) and using Eq. (4) and Eq. (12), then the critical  $K$  for inclusion induced cleavage fracture can be expressed by

$$K = K_c = 2\sqrt{\mu\gamma_c} \left[ 1 + \frac{\cos \frac{\alpha}{2}}{\sin \frac{\theta}{2}} \sqrt{\frac{\gamma_f \sin \alpha}{\gamma_c \sin \theta}} \right] \quad (13)$$

In terms of  $J_c = K_c^2/2\mu$ , the value of  $J_c$  can be calculated as a function of angles  $\alpha$  and  $\theta$ . The result shown in Table 1 shows that  $J_c$  increases with the decrease of  $\theta$  when the slip angle  $\alpha$  is chosen as a constant 45 degrees.  $J_c/2\gamma_c$  varies from 1.93 to 259 as  $\theta$  angle varies from 90 to 5 degrees. These results are consistent with the slip induced cleavage fracture model developed by Ritchie, Knott, and Rice [14], in which the fracture toughness increases with the characteristic distance where the microcracking occurs.

Table 1

The variation of  $J_c$  with the critical angle  $\theta$  when a void is generated at the inclusion.

$\theta$	$J_c/2\gamma_c$
5	259
10	40.6
30	4.40
45	2.73
60	2.20
75	2.00
90	1.93

We note that  $k_R$  in Eq. (11) is an odd function and goes to zero if the shielding cloud is symmetrically distributed, but  $k_c$  in Eq. (10) is an even function so both the symmetrical and antisymmetrical dislocation distribution would contribute to the fracture toughness. When this property is taken into the modeling, the predicted toughness would be much higher than that shown in Eq. (13).

#### CONCLUSIONS

From this study, there emerge three conclusions:

1. The total image force for a dislocation near a crack tip is enhanced when a plate-like rigid inclusion is on the cleavage plane.
2. Because of the image force enhancement, the intrinsic character of cracks crosses over from ductile to brittle if a plate-like rigid inclusion is very close to the crack tip.
3. Inclusion-induced cleavage fracture triggered by void nucleation at the inclusion is analyzed qualitatively. The fracture toughness will depend on the details of the shielding dislocation configuration.

#### ACKNOWLEDGEMENTS

It is a pleasure to acknowledge the role R. Thomson played in this study. The author has benefited from frequent discussions of shielded cracks in steady state motion and the general physics of the crack breakaway from the dislocation screen.

# REFERENCES

1. Ohr, S.M. Scripta Metall. 20, 1465 (1986).
2. Anderson, P.M. and Rice, J.R., Scripta Metall. 20, 1467 (1986).
3. Thomson, R., Scripta Metall. 20, 1473 (1986).
4. Li, J.C.M., Scripta Metall. 20, 1477 (1986).
5. Weertman, J., Scripta Metall. 20, 1483 (1986).
6. Burns, S.J., Scripta Metall. 20, 1489 (1986).
7. Michot, G. and George, A., Scripta Metall. 20, 1495 (1986).
8. Ohr, S.M., Scripta Metall. 20, 1501 (1986).
9. Thomson, R., Solid State Physics, eds. Ehrenreich, H. and Turnbull, D., Academic Press, New York) 1986, Vol. 39, p. 1.
10. Lin, I.-H. and Thomson, R., Acta Met. 34, 187 (1986).
11. Stroh, A.N., Proc. Roy. Soc. London A223, 548 (1955).
12. Stroh, A.N., Adv. Phys. 6, 418 (1957).
13. Smith, E., Proc. Conf. Phys. Basis of Yield and Fracture, Inst. Phys. and Phys. Soc. (London), Oxford, 36 (1966).
14. Ritchie, R.O., Knott, J.F., and Rice, J.R., J. Mech. Phys. Solids 21, 395 (1973).
15. Lin, I.-H., to be published.



# INCLUSIONS AND THEIR INFLUENCE ON CORROSION AND CORROSION-ASSISTED FRACTURE

**William E. White**

Ryerson Polytechnical Institute  
Toronto, Ontario, Canada

## ABSTRACT

Localized corrosion in steels is an insidious process. The mechanisms can be complex and are often not well-understood. Inclusions in the steel often aggravate further the processes of corrosion and corrosion-assisted fracture. The roles played by inclusions in the nucleation of pitting corrosion and in corrosion-assisted crack initiation and growth are explored.

It is shown that specific operative damage mechanisms, whether by corrosion or corrosion-induced fracture, depend on a number of inter-related factors, including the physical, physical-chemical, and electrochemical nature of the inclusions; the characteristics of the metal matrices; the chemical, electrochemical, and physical-chemical properties of the corrosive environments; temperature, pressure, velocity, and pH. Finally, it is shown that 'in situ' environmental changes, often arising as a consequence of the chemical and/or electrochemical reactions taking place, increase further the complexities involved in understanding the fundamental mechanisms related to damage initiation and accumulation.

THE STRUCTURAL DEPENDENCE OF MATERIALS' properties has been well-documented. Properties and materials performance may depend on atomic structure, microstructure and/or macrostructure. Although structure-property relationships are important, the behavior of materials is also strongly influenced by environmental interactions.

Inclusions normally comprise a part of the microstructures of materials. Inclusions may be an integral part of materials design; introduced specifically to enhance strength [1-3], fatigue resistance [4-6], or other desirable properties; or inclusions may be consequential to particular methods of

materials manufacture [7-9]. Whatever are their origins, inclusions will influence, to some degree, materials behaviour, including susceptibilities to corrosion and corrosion-assisted fracture [10-20].

In this paper, the roles of inclusions on susceptibilities to localized corrosion and fracture are examined, and various damage mechanisms are discussed as they are influenced by the character and morphologies of the inclusions, the characteristics of the surrounding metal matrices, and the chemistries of the corrosive environments.

## INCLUSIONS

The types, sizes, morphology, and compositions of inclusions in steels will depend on the steel type and manufacturing practise [7-9]. Several principal types of sulfide inclusions have been described in the literature [7,8]. Globular, randomly-dispersed, sulphide inclusions are common to steels with high oxygen contents, the inclusions precipitating initially as liquid droplets in the solidifying steel [8], (Figure 1). These sulphides, (type I), often have multiplex structures, and may contain silicates and/or oxides.

Type II inclusions form in deoxidized steels (silicon, or aluminum killed), and precipitate interdendritically late in the solidification process [8]. The morphology in the cast steels can best be described as thin, chain-like, and often with a fan-like structure, (Figure 2), although many are rod-shaped or oval. Alumina and silicates may also be associated with sulphides, depending on the de-oxidation practise.

Type III sulphides are usually angular, equiaxed, and dispersed randomly, (Figure 3). They are monophase, not associated with oxides or silicates, nor is there elemental substitution for the manganese [8].

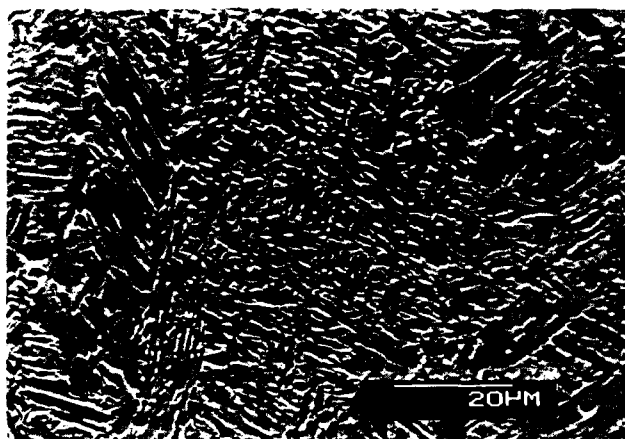


Fig. 1 -- Scanning Electron Micrograph Showing Randomly Dispersed Globular (Type I) Inclusions in a 'Cast' Steel: 2 percent nital etch



Fig. 2 -- Oval, Rod-Shaped, Fan-Like Interdendritic Inclusions in a 'Cast' Steel. Optical Micrograph, 2 percent nital etch

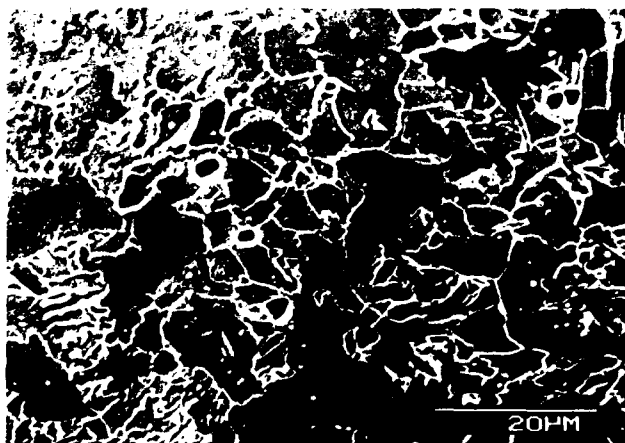


Fig. 3 -- Scanning Electron Micrograph Showing Type III Sulphide Inclusions in a 'Cast' Steel: 2 percent nital etch.

The compositions of inclusions may vary widely, and, for example, manganese sulphide can accommodate considerable amounts of other transition elements to form (Mn,Me)S-type sulphides [8]. Often, the composition will influence inclusion hardness, and this will influence the shape in rolled products. Inclusions may be elongated (Figure 4), or fragmented (Figure 5).

Rare-earth metals, along with zirconium, and calcium can be used to reduce or eliminate manganese sulphide because their sulphide-forming tendencies are considerably greater than that of manganese. Consequently, CaS, ZrS, and rare-earth (RE) sulphides, (RE)S, (RE)<sub>x</sub>S<sub>y</sub>, and oxysulphides, (RE)<sub>2</sub>O<sub>2</sub>S, may be found in steels [9].

In addition to sulphides, a wide variety of oxides may be present in the steels, including FeO, MnO, (Fe,Mn)O, FeAl<sub>2</sub>O<sub>4</sub> (hercynite), Al<sub>2</sub>O<sub>3</sub>, Cr<sub>2</sub>O<sub>3</sub>, SiO<sub>2</sub> (silicates) and spinels, such as Ni<sub>x</sub>Fe<sub>1-x</sub>O<sub>4</sub>. An excellent review on oxides in steels has been written by Philbrook et al [21].

In summary, it is important to understand that inclusions in steels may vary widely in type, chemical composition, morphology, and complexity; these variables, in turn, influencing the corrosion and fracture resistances of the steels. The major classes of inclusions are listed in Table I.

#### INCLUSIONS AND CORROSION

Inclusions in steels usually will promote localized corrosive attack, facilitating the development of corrosion pits. The pitting corrosion mechanisms will depend on many factors indigenous to the inclusion, the metal matrix, and the corrosive environment acting singly, or conjointly. Pitting may be initiated by dissolution of the inclusion (by chemical or electrochemical means), (Figure 6); by preferential interfacial corrosion of the surrounding metal matrix (Figure 7); by preferential attack of a portion only of multiphase inclusions (Figure 8), or from disbondment along the interface between the inclusion and the metal matrix leading to crevice-type corrosion [22].

Preferential dissolution of inclusions may occur by chemical or electrochemical means, depending on the chemical, physical chemical, and/or electrochemical properties of the inclusion, and the nature of the particular corrosive media in contact with it. The electrochemical nature of the surrounding metal matrix will also influence the mechanism of attack of the inclusion.

Sulfide dissolution kinetics may be the controlling factor in the pit initiation process. In these cases, the kinetics are influenced by the morphology of the inclusions

TABLE I.  
INCLUSIONS IN STEEL

Malleable Inclusions	Slightly Malleable Inclusions	Hard Nonmalleable Inclusions
1. Sulfides** [MnS, FeS, (MnFe)S, (FeCrMn)S]	1. Silica-rich Glasses* [(Fe, Mn)O.XSiO <sub>2</sub> ]	1. Silica [SiO <sub>2</sub> ]*
2. Basic Silicate Glasses* [2FeO.SiO <sub>2</sub> ; 2MnO. SiO <sub>2</sub> ; 2(FeMn)O. SiO <sub>2</sub> ...]	2. Sulfides of Ti and Zr** [TiS, ZrS ....]	2. Hercynite [FeAl <sub>2</sub> O <sub>4</sub> ]**
	3. Siliceous Chromites [(Fe, Mn)O.Cr <sub>2</sub> O <sub>3</sub> + SiO <sub>2</sub> ]**	3. Alumina [Al <sub>2</sub> O <sub>3</sub> ]**
	4. Zircon [ZrO <sub>2</sub> .SiO <sub>2</sub> ]*	4. Chromite [Fe, MnO.Cr <sub>2</sub> O <sub>3</sub> ]
	5. MnO <sub>2</sub> ** [FeO.TiO <sub>2</sub> ]*	5. Ilmenite
	6. FeO*, MnO*	6. Vanadium Spinel [FeO.V <sub>2</sub> O <sub>3</sub> .2SiO <sub>2</sub> ]*
		7. Mullite (3Al <sub>2</sub> O <sub>3</sub> .2SiO <sub>2</sub> )*
		8. Spinel [MgFe <sub>2</sub> O <sub>4</sub> ]** [MnFe <sub>2</sub> O <sub>4</sub> ]**

\*\*\* Type 'A' Inclusions: Good Electron Conductors

\*\* Type 'B' Inclusions: Limited Ability to Conduct Electrons

\* Type 'C' Inclusions: Non-Conductors

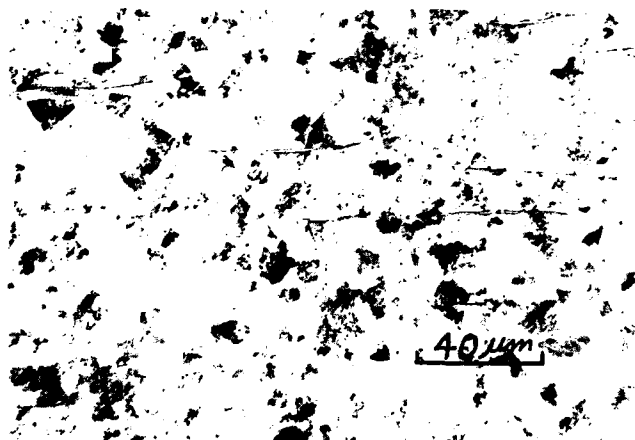


Fig. 4 -- Optical Micrograph Showing Elongated Sulphide Inclusions in Rolled Steel: 2 percent nital etch



Fig. 5 -- Fragmented, Hard, Inclusion Stringers, in a Rolled Steel: Optical Micrograph; 2 percent nital etch

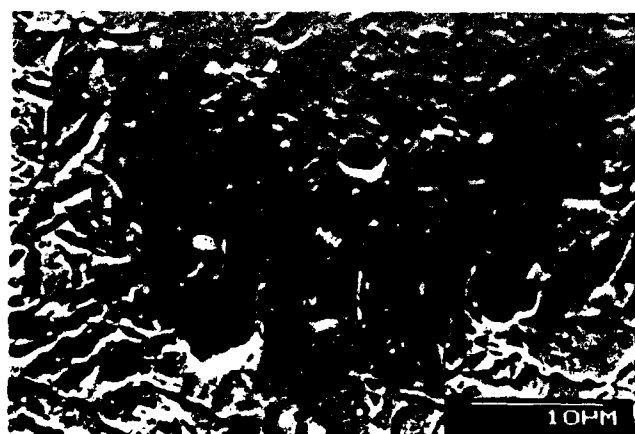


Fig. 6 -- Scanning Electron Micrograph Showing the Development of Corrosion Pits by Preferential Chemical Dissolution of Non-Metallic Inclusions

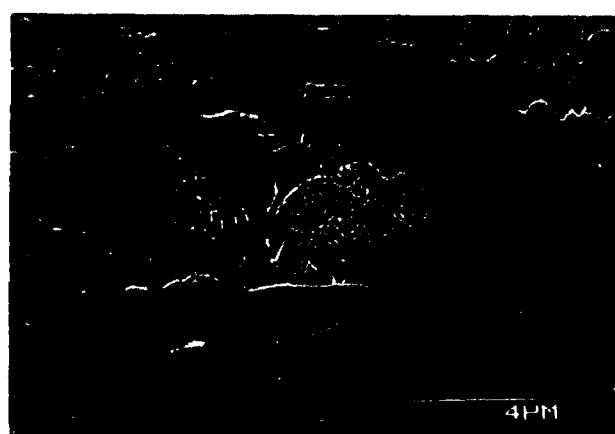


Fig. 7 -- Scanning Electron Micrograph Showing Corrosion Pits by Preferential corrosion of metal matrix surrounding inclusions.

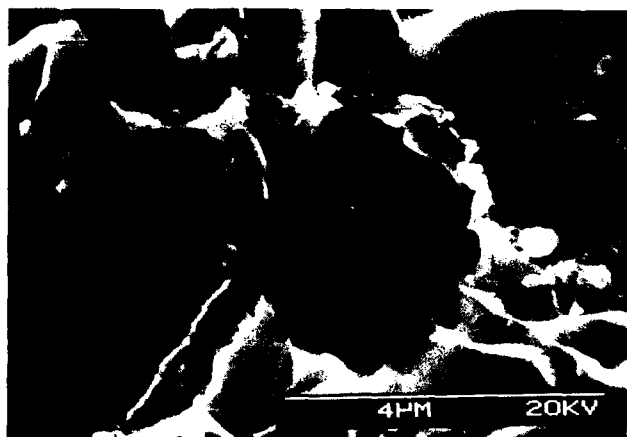


Fig. 8 -- Scanning Electron Micrograph Showing Selective Dissolution of a Multiphase Inclusion in Steel

exposed to the electrolyte, temperature, electrolyte composition, and the spectrum of sulphide inclusion compositions present in the alloy [23]. Sulphide inclusions to a small extent are electron conductors and can be polarized to approach the potentials of the surrounding steel matrices [24].

The mechanisms of dissolution will depend on both the degree that the inclusions are electron conductors, and on the solubility of the inclusions in the electrolyte. The inclusions in Table I have been categorized according to the relative abilities to conduct electrons. Type 'A' inclusions, which are reasonably good electron conductors may dissolve by electrochemical mechanisms, depending on the electrochemical characteristics of the surrounding metal matrices. The type 'B' inclusions, which are partial or poor conductors, may dissolve by chemical or electrochemical means; whereas, inclusions that are non-conductors (Type C) will dissolve usually by chemical means.

Accelerated electrochemical tests have been developed to study pitting phenomena in steels [25,26]. In conventional steels, it is often the case that the potentials of the inclusions are more noble than those of the surrounding steel matrix. In these cases, polarization of the steel will cause it to corrode preferentially, the inclusion being protected by the surrounding steel acting as a sacrificial anode. For example, during corrosion studies of steel in permafrost [25,26], corrosion pits were observed to be initiated by preferential corrosion of the surrounding metal matrix and analyses showed that the reversible electrode potentials for electrochemical corrosion of the inclusions were more noble than that for the corrosion of iron to the soluble cation state. Two examples follow:

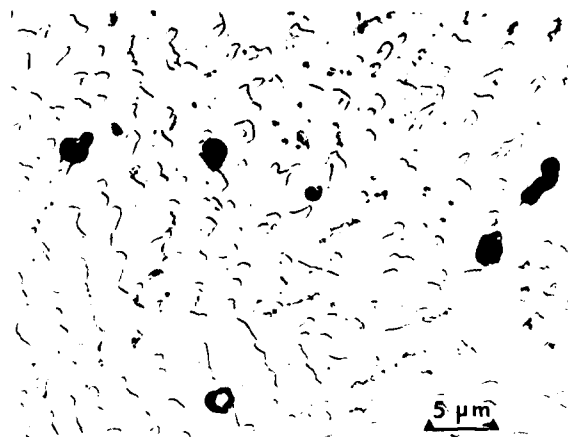
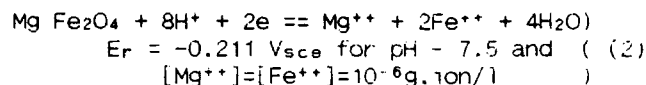
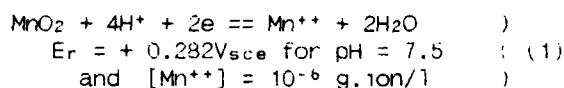
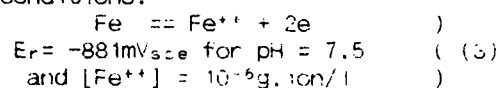


Fig. 9 -- Preferential Electrochemical Dissolution of Delta Ferrite, Second Phase Particles in AISI Type 316L Stainless Steel Weld Metal



In both of the above examples, the equilibrium potentials ( $E_r$ ) for electrochemical dissolution of the oxide ( $\text{MnO}_2$ ), and the spinel ( $\text{MgFe}_2\text{O}_4$ ),  $+282\text{mV}_{\text{sce}}$  and  $-211\text{mV}_{\text{sce}}$  respectively were determined to be more noble than the equilibrium potential of  $-881\text{mV}_{\text{sce}}$  for corrosion of steel by equation (3) under the same test conditions.

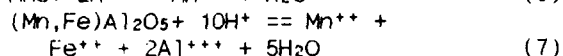
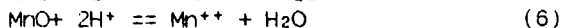
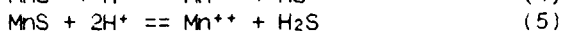


Inclusions in stainless steels, however, may dissolve by electrochemical means because the surrounding passive steel matrix will be at a potential more noble than that of the inclusions [23,24].

It has also been observed and is well-established that freely conducting second phase particles in austenitic steels in appropriate electrolytes will dissolve preferentially by electrochemical (bi-metal) corrosion mechanisms (Figure 9).

Dissolution by chemical mechanisms (Figure 6) will depend on the solubility index of the inclusions, which will be influenced by such factors as temperature, pressure, velocity, pH, and electrolyte composition, among other factors [22,23,28]. The rate of corrosion pit formation will depend on a number of factors in a complex fashion. For example, chemical dissolution of inclusions may change the

corrosivity of the electrolyte locally, thereby accelerating corrosion of the surrounding metal matrix [22,26].



The rate of dissolution of the inclusions in (4) to (7) above will depend on pH and other factors; but clearly, even slow rates of dissolution will alter the chemistry of the aqueous environment. The stability of the aqueous  $\text{H}_2\text{S}$ , the hydrosulphide ion,  $\text{HS}^-$ , and even dissociation to produce the bisulphide ion,  $\text{S}^{2-}$  will depend on pH. In these instances, corrosion of the steel will be accelerated. The production of  $\text{HS}^-$  from reaction (4), has been shown to accelerate the corrosion of steel (reaction(3)), to form iron sulphide,  $\text{FeS}$  [25].

Crevice corrosion has also been observed at inclusion/matrix interfaces [22], as may be seen in Figure 10. Often the fundamental mechanism will be differential concentration cell corrosion.

Pitting corrosion may also be initiated by selective leaching of individual phases of multi-phase inclusions as shown in Figure 8 [22,25,26]. Selective dissolution may be a consequence of chemical or electrochemical corrosion depending on the characteristics of the component phases.

Finally, not all inclusions are attacked even though conditions may appear similar. In Figure 11, the angular inclusion (top of Figure) has been attacked, but the elongated multiphase inclusion has not been attacked.

#### INCLUSIONS AND FRACTURE

Environmentally-assisted fracture of metal components involves the conjoint action of corrosive media and stress (residual and/or applied) to promote failure by fracture in a shorter time than would the separate and isolated effects of either the stress or the environment. It is not intended to differentiate between the (often) subtle differences between stress-corrosion cracking (SCC), sulphide stress cracking (SSC), chloride stress cracking (CSC), hydrogen-assisted cracking (HAC), and other forms of stress and corrosion-related fracture mechanisms. Rather, it is intended only to present some examples of the potential role(s) played by inclusions in the fracture processes.

Inclusions often are preferred sites for the initiation of corrosion pits as has been shown in the foregoing text. The corrosion pits, once they are well-developed will act as sites where stress is concentrated, from which cracks will initiate and grow, as may be seen

in Figure 12. Anodic stress corrosion cracking was observed in studies of metallic orthopaedic implant failures [33], and not only were inclusions active sites for pit initiation by electrochemical mechanisms, but inclusions assisted crack growth as propagation from inclusion to inclusion was observed metallographically as the cracks progressed (Figure 12).

The degree of corrosion pit development, as well as crack initiation and growth, often will depend on a number of inter-related and complex factors. Not all corrosion pits will initiate cracks. Corrosion pits may not develop extensively due to spontaneous repassivation [23]; the development of deep penetrating pits depending often on the competing processes of passivation and passivation breakdown. The chloride ion has been shown to be especially damaging, not only adsorbing to metal surfaces [34,35], but the adsorption of  $\text{Cl}^-$  is often non-uniform, especially when the metal is stressed. The  $\text{Cl}^-$  ion apparently will migrate up the stress field, collecting at localized points of highest stress [35].

Passivation breakdown can occur chemically in the presence of  $\text{Cl}^-$  and other harmful anions; or mechanically by stress-rupture of passivating films [36]. During pitting attack, the metal undergoes corrosion and hydrolyses with a decrease in pH [37], (increase in acidity). In fact, 'in situ' localized chemical compositional changes have been shown to take place as corrosion proceeds. No matter what is the pH of the bulk solution, it has been shown experimentally, that the pH in the root of a corrosion pit will always be acidic [38,39]. Studies have also confirmed acid conditions in crevices, and within stress-corrosion cracks [36,40].

Acidification and changes in chloride concentrations generate severe and hostile environments that often promote cracking. Additionally, electrochemical potential modifications as a consequence of the chemical changes and the stress fields (in stressed components) facilitate crack initiation and growth in metal components.

It has been well-documented that inclusions act as sites from which hydrogen-induced-cracking and blister cracks are initiated [29-32]. Inclusions act as sinks for the collection of hydrogen generated from corrosion reactions. As monatomic hydrogen ingresses into the metal lattice and collects at inclusions, the nascent hydrogen combines to form diatomic hydrogen with a consequent pressure build-up. Once the pressure reaches a critical value, cracking results. As pressure builds up in inclusions near the surface, blister cracks may form (Figure 13). Otherwise linear cracking, or step-wise cracking (Figure 14) may be observed.

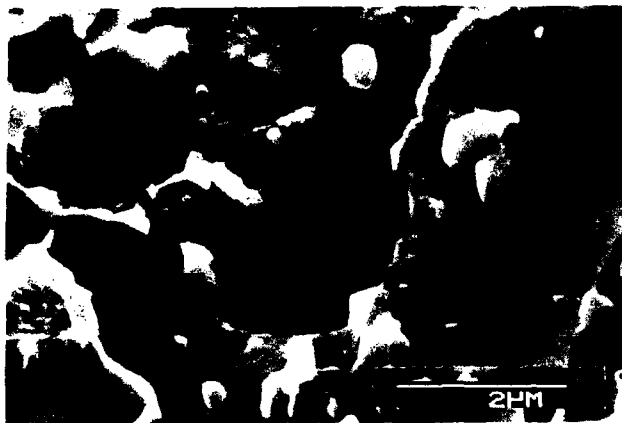


Fig. 10. -- Scanning Electron Micrograph Showing Crevice Corrosion at Inclusion-Steel Interface

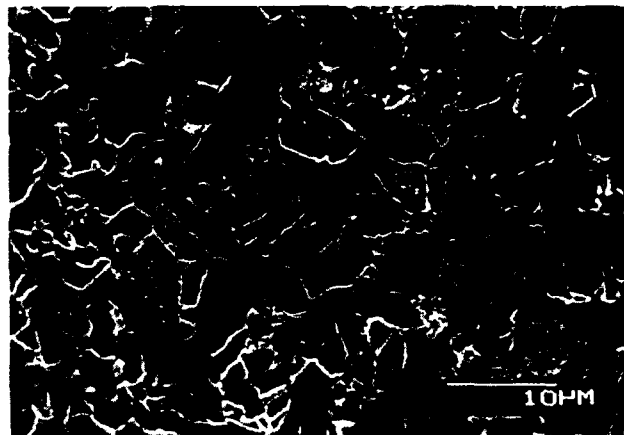


Fig. 11 -- Scanning Electron Micrograph Showing Selective Corrosion of Angular Inclusion 'A', (top), but No Corrosion of Multiphase Inclusion 'B' (bottom)



Fig. 12 -- Optical Micrograph Showing Anodic Stress-Corrosion Cracks Initiating from Corrosion-Pits. Note Also Crack Propagation Being Assisted by the Inclusions: Diluted Aqua Regia Etch [33]



Fig. 14 -- Hydrogen Induced Step-Wise Cracking in Rolled, Low-Alloy Steel: 2 percent nital etch [32]

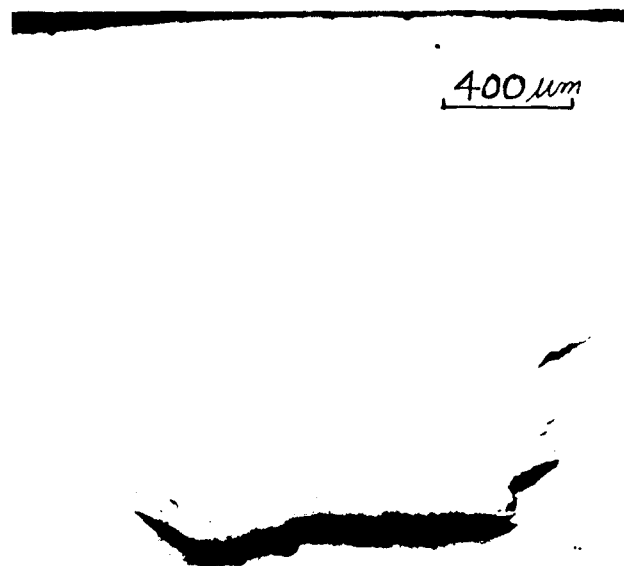


Fig. 13 -- Hydrogen-Induced Cracking Adjacent to Surface of Steel Causing the Formation of Blisters: The Common Term is Blister Cracking: 2 percent nital etch [32]

## SUMMARY AND CONCLUSIONS

The mechanisms of corrosion pit nucleation and growth are not fully understood. The interplay between many factors can influence strongly both pit initiation, and the kinetics of pit growth. Often 'in situ' environmental changes increase the complexity even further. In this paper, it has been shown that the role of inclusions in corrosion pit development and the mechanisms of pitting damage will depend on the morphology of the inclusions exposed to the electrolyte, temperature, electrolyte composition, pressure, velocity, the spectrum of inclusion compositions, and the nature of the metal matrices surrounding the inclusions.

Inclusions might facilitate localized corrosion in one or more of the following ways:

- (1) chemical dissolution of the inclusion;
- (2) electro-chemical dissolution of the inclusion;
- (3) electrochemical corrosion of the surrounding metal matrix;
- (4) selective dissolution of certain phases in multi-phase inclusions by chemical or electrochemical means;
- (5) crevice corrosion at disbonded inclusions; and
- (6) combinations of the above due to 'in situ' environmental changes as damage progresses.

Finally, it was also shown that inclusions can adversely influence environmentally-induced fracture processes by acting as sites of stress concentration concomitant with the development of corrosion pits, and by acting as sites for the collection of diatomic hydrogen, the pressure increases ultimately leading to crack initiation and growth.

## REFERENCES

1. Felback, D.K. "Introduction to Strengthening Mechanisms", Prentice-Hall Inc., N.J. (1968)
2. Dieter, G.E. "Mechanical Metallurgy", McGraw-Hill Book Co., N.Y., p. 190 (1977)
3. LeMay, I., "Principles of Mechanical Metallurgy", Elsevier, N.Y., p. 155 (1981)
4. Borik, F., Justusson, W.M., and V.F. Zackay, Trans ASM, 56, 327-333 (1948)
5. Orowan, E., "Symposium on Internal Stress in Metals", Inst. of Metals, London, p. 451 (1948)
6. LeMay, I., "Principles of Mechanical Metallurgy", Elsevier, N.Y., p. 304 (1981)
7. Pehike, R.D., and T. Fuwa, Int. Met. Rev., 30, 125 (1985)
8. Hale, G.E. and J. Nutting, Int. Met. Rev., 29, 273-298 (1984)
9. Waudby, P.E., Int. Met. Rev., 23, 74-98 (1978)
10. Frankel, G.S. et al, Corrosion, 43, 429-436 (1987)
11. Wranglen, G. "Localized Corrosion", NACE-3, p. 462, (1974)
12. Beifer, G.J., Materials Performance, 21, 19-25, (1982)
13. Venkatasubramanian, T.V., and T.J. Baker, Metal Science, 18, 241-250 (1984)
14. Iino, M., Met. Trans. 9A, 1581-1588 (1978)
15. Lea, C., Corrosion, 40, 337-345 (1984)
16. Agarwala, V.S. and N. D. Greene, Metallography, 20, 277-285 (1987)
17. Wranglen, G., Corrosion Science, 14, 331-342 (1974)
18. Pumphrey, P.H., Corrosion, 36, 537-543 (1980)
19. Taira, T., et al, Corrosion, 40, 478-486 (1984)
20. Shel, S.A. and C. D. Kim, Corrosion, 41, 12-18 (1985)
21. Philbrook, W.O., et al, Int. Met. Rev., 22, 187-221 (1977)
22. Srivastava, S.C., and M.B. Ives, Corrosion 43, 687-692 (1987)
23. Manning, P.E., Duquette, D.J., and W. F. Savage, Corrosion, 36, 313-319 (1980)
24. Eklund, G., J. Electrochem. Soc., 123, 170-174 (1976)
25. White, W.E. and R. J. King, Microstructural Science, 11, 436-455 (1983)
26. King, R.J., "Corrosion of Steel Weldments in Permafrost", PhD Thesis, The University of Calgary, Calgary, Canada, (1983)
27. Eklund, G., Scand. J. Metall., 1, 331-338 (1972)
28. Manning, P.E., Duquette, D.J., and W.F. Savage, Corrosion, 35, 151-150 (1979)
29. Moore, E.M., and J. J. Warga, Materials Performance, 15, 17-24 (1976)
30. Wilde, B.E., et al, Corrosion, 36, 625-632 (1980)
31. Yoshino, Y., Corrosion, 39, 435-443 (1983)
32. Flanders, N., Tennant, R., and W. E. White, Microstructural Science, 15, 227-239 (1987)
33. White, W.E., and I. LeMay, Microstructural Science, 3B, 911-925 (1975)
34. Nielsen, N.A. Corrosion, 20, 104t-109t (1964)
35. Bergen, C.R., Corrosion, 20, 269t-274t (1964)
36. White, W.E., Postlethwaite, J., and I. LeMay, Microstructural, 145-157 (1976)
37. Hoar, T.P., "NACE-3, Localized Corrosion" 112-115 (1974)
38. Pickering, H.W. and R.P. Frankenthal, J. Electrochem, 1297-1304 (1972)oc.,
39. Pourbaix, M., "NACE-3, Localized Corrosion", 12-32 (1974)
40. Marek, M., and R.F. Hochman, Corrosion, 26, 5-6 (1970)

# INCIDENCE OF ALUMINUM INCLUSIONS ON THE OCCURRENCE OF SEAMS IN HOT AND COLD ROLLED STRIP

Rafael Colás, Eduardo Lee, Jesús Valdés, Antonio Valdés,  
Hector Montemayor, Augusto M. Estrada, Jorge G. Arias

Hylsa, S.A. de C.V.  
División Aceros Planos  
A.P. 996  
64000 Monterrey, N.L., México

Miguel A. Cisneros

Centro de Graduación e Investigación  
Instituto Tecnológico de Saltillo  
Apdo. Postal 84-C  
Saltillo, Coah. México

## ABSTRACT

A high incidence of the defect known as seam was found in hot and cold rolled strip of low carbon steel. Those seams were due to mechanical (scratches during rolling) or metallurgical (blowholes or inclusions) features. It was deduced that the most important parameter, related to inclusion content, was the amount of aluminum added in the ingot mould, that will affect their quantity and distribution. It was concluded that non-deformable inclusions (like  $\text{MnO} \cdot \text{Al}_2\text{O}_3$  and  $\text{Al}_2\text{O}_3$ ) close to the ingot surface were responsible for the occurrence of the defect. A mechanism responsible for the origin of the defect is proposed.

INCLUSIONS IN METALS have a negative influence on almost all mechanical properties [1-3]. During straining, the inclusions may or may not deform plastically depending on their chemical composition and the working temperature. The most critical case is that of non-spherical, undeformable particles that will break during deformation [2,3]. In this case, the metal matrix has to deform around the inclusion, creating cavities or causing deformation damage which act as nucleation sites for fatigue cracks or as zones of internal weakness during further processing [2-5]. There is a general agreement about the amount, size and distribution levels of inclusions in metals that are processed under highly tensile conditions [2,5-8].

One evidence of inclusions in hot or cold rolled strip is the occurrence

of the so called seams defects, characterized by long lines along the rolling direction [9,10]. Those defects are sometimes confounded with surface scratches produced during rolling, and those from exposed blowholes [11,12].

The aim of this work is to correlate the incidence of seams with the amount of aluminum added in the ingot mould during teeming of a low carbon rimming steel.

## EXPERIMENTAL PROCEDURE

A 100 metric tons heat of rimming steel was prepared in an electric furnace. The chemical composition, after additions in ladle, is given in Table 1.

Table 1. Chemical composition of the steel (wt. %).

C	Mn	P	S	Cu	Ni	O
0.07	0.30	0.010	0.012	0.02	0.03	0.0318

The steel was teemed into 5,000 kg ingots. The teeming was started at 1576°C. The rimming action was controlled with granulated aluminum added to the bottom third of the ingot. Seven ingots in which the amount of Al ranged between 300 and 4,500 g were used in the test. The resulting free oxygen in the ingot, and the rimming action level are shown in Table 2. The oxygen was calculated after assuming a 50% recovery of Al.

The ingots were hot rolled to 2.16 mm (0.085") thick coil, pickled in sulphuric acid, cold rolled to 0.46 mm (0.018"), batch annealed, temper rolled and sectioned in sheets 2.29 m (90") long. The surface quality was assessed from sheets taken along the coil. An ar-



bitrary visual qualification from 0 (worst) to 10 (best) was given to both surfaces of the selected sheets.

Table 2. Results of addition of Al.

Aluminum [g]	Free oxygen [ppm]	Rimming action
300	291	vigorous
800	247	vigorous/moderate
1,400	194	slow
4,500	—	non existent

The mechanisms by which the inclusions convert into seams was studied by means of scanning electron microscopy of samples taken from ingots and along the rolling process. In this last case, it was necessary to identify the plane and direction of rolling, Fig. 1. This figure will be used later when referring to those planes and directions.

## RESULTS AND DISCUSSION

The qualification of the coils as a function of the addition of aluminum is shown in Fig. 2. It can be seen that the surface quality deteriorates as the Al is increased. This behaviour is not only due to the amount of alumina in the steel, but also due to the reduction of oxygen available for the rimming action [1,3,13-17]. As the rimming action decreases, the blowholes are trapped closer to the surface, and, if oxidized during soaking, they can produce seams [18-20]. Also, if the rimming action is poor, the inclusions will not be able to float, and will be trapped by the solidification front [14,21].

It was found that the incidence of seams was not constant along the length of the coil in steels that had 300 and 800 g of aluminum, Fig. 3. The bottom of the ingot, where the blowholes are closer to the surface [16-19], had the lowest qualifications. The steel with 4,500 g of Al, Fig. 4, did not show any significant difference along the coil. This might well be due to the fact that the Al is added at the bottom third of the ingot, and, in the case of the addition of 800 g, the rimming action will be increasing as liquid iron keeps pouring. There will be no difference in killed ingots (4,500 g of Al) because there will always be an excess of aluminum to react with the oxygen of the steel.

When observing the corner samples of the ingots by SEM, it was found that the inclusions were formed by alumina, Figs. 5 and 6, or by the spinel  $\text{Al}_2\text{O}_3\text{-MnO}$ , Fig. 7. It was observed a tendency

for the occurrence of the former type of inclusions as the aluminum added to the ingot was increased.

In general, it is considered that the alumina inclusions have spherical or elliptic forms, clustering around certain regions, Fig. 5, but, as can be seen from Fig. 6, the clusters are the intersection of the polishing plane with dendritic inclusions [3,22]. Those inclusions do not deform during either hot or cold rolling, but break [1-3,23].

When observing the rolling plane (RP) of a 25.4 mm (1") thick plate, that had an addition of 4,500 g of Al a series of small cavities or holes were found along the rolling direction, Fig. 8, left by alumina inclusions, Fig. 9. The longitudinal plane (LP) of the same plate show a series of cracks along the rolling direction (RD), Fig. 10. X-ray maps show that the Al was localized in certain places along the cracks, Fig. 11. Higher magnification of the area of Fig. 10 show that the cracks were interconnecting small alumina inclusions, Fig. 12, explaining the Al distribution of Fig. 11.

Comparing the size of the alumina inclusions in the ingot that had an addition of 4,500 g of Al, Figs. 5 and 6, with that of the plate, Fig. 9, it can be easily deduced that the original dendrites broke down. The way in which the new inclusions are connected by cracks is shown in the diagram of Fig. 13. Here, we consider that the dendrite will break after the steel matrix has reached certain strain level. As the rolling proceeds, the steel keeps deforming as the temperature decreases, decreasing at the same time the ductility of the steel. Under this conditions, it would be possible to find certain places in which the steel has developed the tendency for strain localization [24], that will generate the cracks shown in Fig. 10.

The difference in color between the seams and the steel [9, 10], might well be due to the changes in the surface roughness, produced by the stress field around the particles, of the coil. Some of the seams peel-off leaving dull sites [20] as result of the cracks interconnecting small inclusions.

## CONCLUSIONS

From the experimental heat it was concluded that the incidence of seams increases as the amount of Al added to control the rimming action increases. The incidence of seams in steels with small amounts of Al was higher in the sheets coming out from the bottom of the

ingot. There was not appreciable difference in the incidence of seams in the coil that had 4.5 kg of Al. This might well be due to the excess of aluminum to react with the oxygen dissolved in the steel poured into the ingot.

It was found a tendency for the occurrence of  $Al_2O_3$  over  $Al_2O_3$ -MnO inclusions as the aluminum added to the ingot was increased.

The mechanism responsible for the formation of seams is the breakage of dendritic indeformable inclusions. This breakage generates strong stress fields around the particles.

#### REFERENCES

1. R. Kiesling: Non-Metallic Inclusions in Steel, The Metals Soc., 1978.
2. W.C. Leslie: ISS Trans, 2, 1 (1983).
3. D.C. Hilty and D.A.R. McKay: Electric Furnace Steelmaking, C.R. Taylor and C.C. Custer, eds., ISS-AIME, 1985, 237.
4. F. Moussy and C. Quennavat: Effects and Control of Inclusions and Residuals in Steels, The Metallurgical Soc. of CIM, 1985, IV-1.
5. D.J. Harris and T.C. Waram: *ibid*, IV-27.
6. H.-J. Fleischer, E. Schulz and K. Bohnke: Clean Steel, The Metals Soc., 1983, 10.
7. F. Komai and K. Miyamura: *ibid*, 373.
8. N.H.H. Beyer, P. Biesboer, A. van der Heiden, P.J. Kreijger, J. Schade van Westrum and A.P. Welboren: *ibid*, 406.
9. Verein Deutscher Eisenhüttenleute: Surface Defects on Cold Rolled Strip and Sheet, 1967; Surface Defects in Hot Rolled Flat Products, 1978, Düsseldorf.

10. Unión de Empresas Siderurgicas: Album de defectos de productos siderúrgicos. Parte IV: Bandas laminadas en caliente, bandas laminadas en frío, 1983.
11. R.S. Patil, G.W. Henger and R.J. Glatthorn: Mechanical Working and Steel Processing XXI, ISS-AIME, 1984, 99.
12. R.M. Hudson: Mechanical Working and Steel Processing XXIV, ISS-AIME, 1987, 173; Iron Steelmaker, 14 (1), 30 (1987).
13. G.R. St. Pierre and C.W. Weidner: Proc. ICSTIS, Suppl. Trans. ISIJ, 11, 555 (1971).
14. J.M. Svoboda: Gases in Cast Metals, Cast Metals Inst., 1976, 1.
15. G.R. Fitterer: Electric Furnace Proceedings, Vol. 35, ISS-AIME, 1977, 302.
16. V. Parma and A. Hutla: Hutnicke Listy, 25, 241 (1979).
17. E.T. Turkdogan: 5<sup>th</sup> Int. Iron Steel Congr. Process Techn. Proc., Vol. 6, ISS-AIME, 1986, 767.
18. T. Araki, M. Hashio and Y. Kitagawa: Sum. Met., 17, 339 (1965); BISI trans. 5447.
19. V. Parma: Hutnicke Listy, 22, 826 (1967).
20. L. Mihok, A. Holly, O. Kozar and S. Simonak: Hutnicke Listy, 30, 695 (1985); BISI trans. 25526.
21. E.T. Turkdogan: Chemical Metallurgy of Iron and Steel, Iron Steel Inst., 1973, 153.
22. R.A. Rege, E.S. Szekeres and W.D. Forgeng: Metall. Trans., 1, 2652 (1970).
23. E.T. Turkdogan: *ibid* Ref. 6, 75.
24. J.A. Schey: J. Appl. Metalwork., 1, 48 (1980).

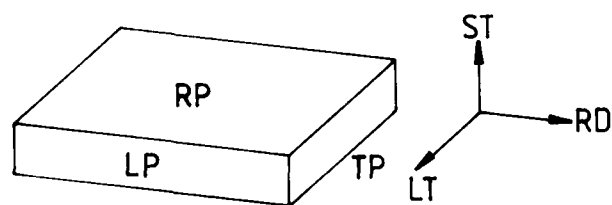


Fig. 1. Diagram used to identify metallographic specimens taken along the rolling process. Planes: RP - rolling, LP - longitudinal, TP - transversal. Directions: RD - rolling, LT - long transversal, ST - short transversal.

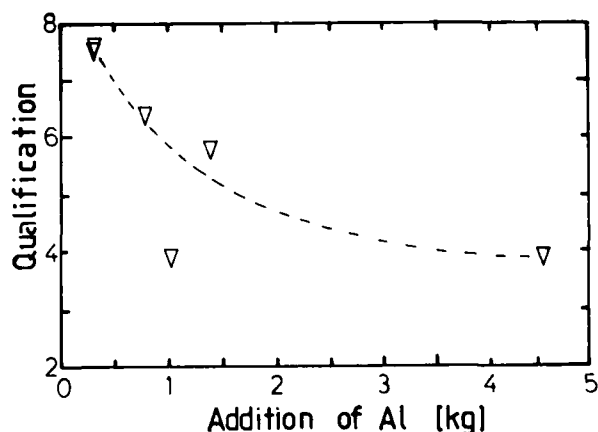


Fig. 2. Qualification of the coils as a function of the addition of Al.

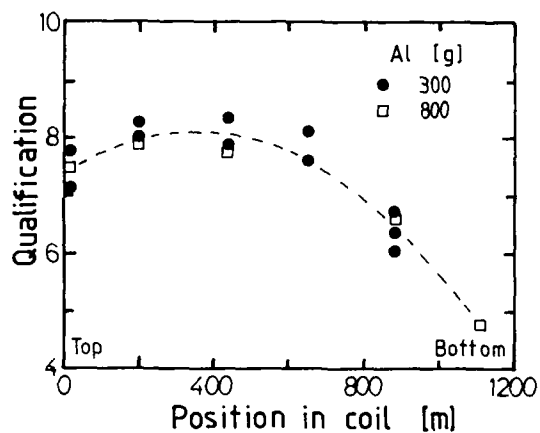


Fig. 3. Qualification along the length of the coils in steels that had an addition of 300 and 800 g of Al.

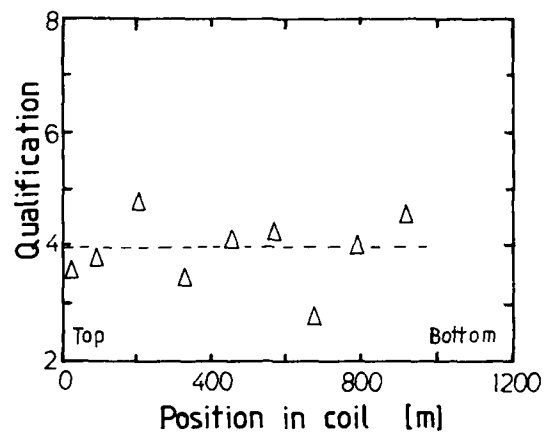


Fig. 4. Qualification along the length of the coils in steels that had an addition of 4500 g of Al.

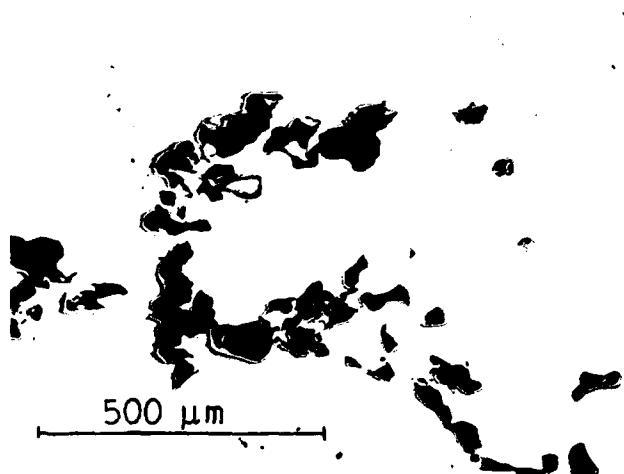
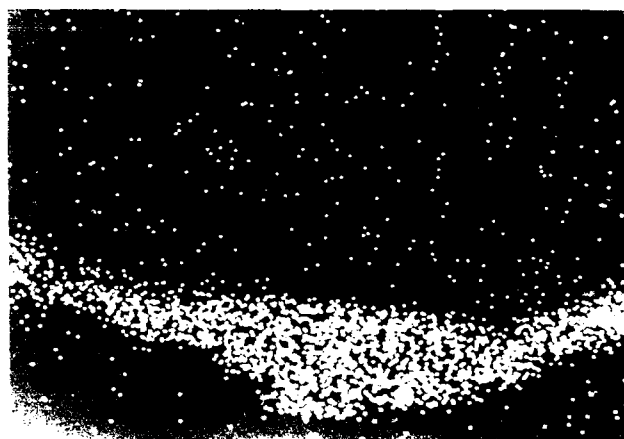


Fig. 5. Optical micrograph of a cluster of alumina inclusions.



Fig. 6. SEM micrograph of the cluster of inclusions.

(b)



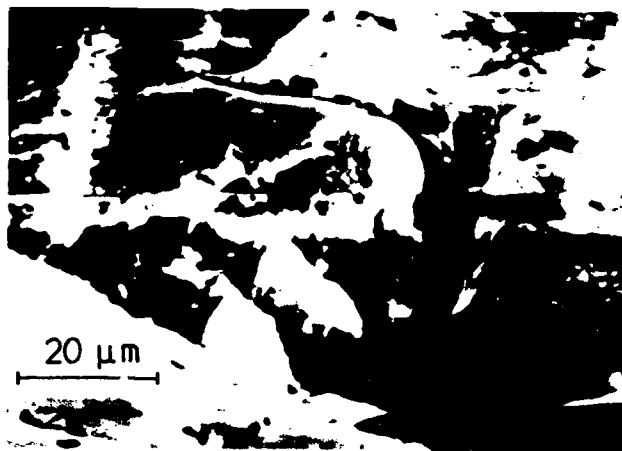


Fig. 10. SEM of the longitudinal plane (LP) of the plate of Figs. 8 and 9 showing cracks along the RD.

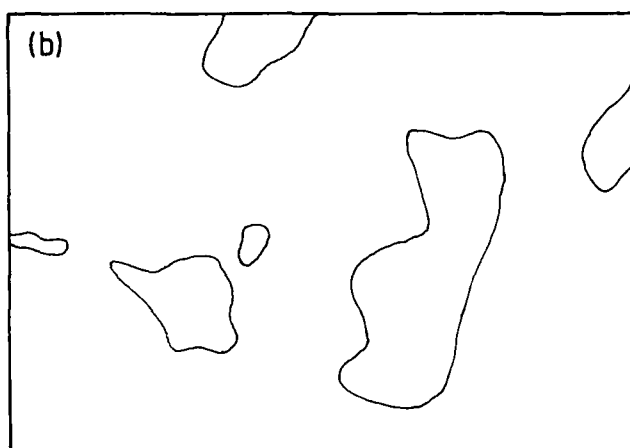
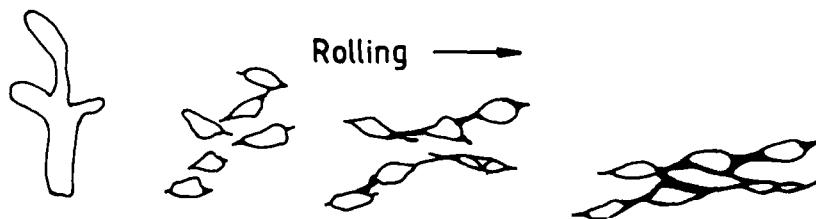


Fig. 11. X-ray map of Al over the region of Fig. 10 (a). Regions in which the Al is concentrated to a higher degree (b).



Fig. 12. Lower magnification of the region shown in Fig. 10. The place in which the cracks interconnect small inclusions is marked by an ellipse.

Fig. 13. Diagram showing the way in which the inclusions of Fig. 12 are formed.



# NUCLEATION OF ACICULAR FERRITE ON OXYGEN-RICH INCLUSIONS

Maurizio Ferrante, Kazuyuki Akune

Universidade Federal de São Carlos  
13.560 - São Carlos - Brazil

## ABSTRACT

This work describes an investigation performed with the objective of testing the hypothesis that differential contraction stress between oxygen-rich inclusion and austenitic matrix plays an important role in the formation of acicular ferrite in weld metal. The study was conducted on welds having a "duplex" austenitic-ferritic microstructure; transmission electron microscopy was employed in order to check for dislocations surrounding the inclusion whose composition was determined by electron-probe microanalysis. Using the relevant physical constants for the matrix and inclusion, numerical values for the thermal contraction stresses and size of the elasto-plastic zone were determined. TEM observation showed that deoxidation products were almost invariably surrounded by dislocations and calculation confirmed that the thermal contraction stresses reached values well above the matrix yield limit. The concept of intragranular nucleation of ferrite on these dislocations was then extended to a series of ten welds obtained under such conditions as to exhibit a range of oxygen levels and a variety of deoxidation products. The results of this analysis confirmed the validity of the thermal contraction stress model, thus emphasizing the significance of parameters such as elastic modulus and thermal expansion coefficient of the deoxidation products.

IN RECENT YEARS a number of studies underlined the importance of oxygen in the formation of weld metal microstructure. Thus it has been recognized that together with Mn, Si and microalloying elements, oxygen-rich inclusions have a profound effect on hardenability whose correct level produces acicular ferrite-rich microstructures. It is clear from the literature, e.g., the extensive work of Garland & Kirkwood that a high proportion of that microstructural feature is always associated with high toughness (1,2).

Early studies concentrated on the importance of parameters such as volume fraction and size

distribution of the deoxidation products. Accordingly, Cochrane & Kirkwood proposed a mechanism in which inclusions would control the austenitic grain size via the restriction of grain boundary mobility (3). As a consequence, hardenability was bound to change, thus determining the final microstructure. The above authors mentioned the range 300 - 400 ppm as the oxygen level which would optimize the weld metal hardenability and produce high proportions of acicular ferrite. Another approach was followed by Abson, Dolby & Hart; it relies upon the fact that acicular ferrite nucleates intragranularly and concludes that transformation is enhanced by the oxides acting as substrates (4). It is apparent that the model emphasizes the importance of the interface inclusion/matrix, in other words, composition and degree of crystallinity of the former are as important as the spatial parameters since they determine its efficiency as substrate. This recognition gave origin to a number of studies aiming to elucidate the nature of the inclusions and its relationship with the type of flux employed in the welding process. For instance, Pargeter produced a full description of the oxides composition of 22 different welds (5). One of the important conclusions of his work concerns the association between aluminium-bearing inclusions and high levels of acicular ferrite. On the other hand, oxides containing manganese and silicon were found in weld metal whose microstructure exhibited coarse grain boundary ferrite and ferrite with aligned martensite, austenite and carbide (MAC).

The importance of taking into account the nature of the deoxidation products has been underlined by a number of examples showing lack of correlation between microstructure and oxygen level. Regarding the austenite grain boundary pinning effect, some investigators reported a constant grain size giving different microstructures (6,7). Additionally, in the context of the direct nucleation model, Pargeter (5), and also Mills, Thewlis & Whiteman (8) observed little change of size distribution and inter-inclusion

spacing with oxygen level.

The present work was undertaken in order to examine a third mechanism which can be considered as a variant of the direct nucleation model. It is based on the fact that weld metal deoxidation products are characterized by thermal expansion coefficients which are much smaller than the matrix. As a consequence, contraction stresses will arise and, if the matrix yield stress is exceeded, dislocations will be formed providing nucleation sites for ferrite. Therefore, transformation will take place in a "volume" rather than on a surface, meaning that a higher number of sites is activated. In the following, an experiment designed to test the thermal contraction model will be presented; some of this work has already been presented in a more extended form (9). Moreover, data from actual welds performed on API 5L X65 linepipe steel will be discussed within the framework of the model.

#### EXPERIMENTAL

Using a consumable wire of nominal composition 24 Cr 5 Ni (wt%), weld beads were obtained by submerged arc under a heat input of 2.8 KJ/mm on a AISI 304 steel plate. Deposition of four passes ensured that no dilution effects would alter the composition from that of an austenitic-ferritic duplex steel. A suitable heat treatment was performed in order to firstly dissolve all the carbides and austenite and, subsequently, cause the precipitation of austenite from the ferritic matrix. Materials and methods were chosen in order to produce a system which allows visualization of the nucleation events and eventual dislocation networks formed around the deoxidation products.

Five different submerged-arc welds were obtained on API 5L X65 linepipe steel, using a variety of consumable combinations and a heat input of 4.4 KJ/mm. The microstructure was characterized by point counting in terms of acicular ferrite volume fraction.

#### RESULTS AND DISCUSSION

The average chemical composition of the inclusions observed in the 25 Cr 5 Ni weld metal is shown in Table I. Also included are the relevant physical constants which will be used in the calculation of the thermal stresses. It can be seen that the oxides are basically  $Al_2O_3$ ,  $MnO$   $SiO_2$ . Figure 1 is a typical microstructure of the weld metal after solubilization at 1300°C and isothermal heat treatment at 800°C, 5 min. The micrograph shows austenite precipitated in a ferritic matrix; a correlation between oxide inclusion and the austenite is clearly seen. The TEM micrographs of Figure 2 reveals some examples of plastically deformed regions surrounding the inclusions. The precipitation observed in Figure 2-b was caused by a short 500°C anneal introduced in order to ensure that dislocations were true features instead of arti-

facts associated to stress relaxation during foil preparation. A number of observations confirmed that a large proportion of inclusions were surrounded by dislocations. Finally, two nucleation events are illustrated by Figure 2-c.

The chemical composition of the welds obtained on the API 5L X65 steel is shown in Table II, which includes some welds studied by Pargeter(5). It can be seen that within each group (1 to 5 and 6 to 10), the elements which most influence hardenability, C Mn and Mo, do not show great variation, while a range of oxygen is present. The same Table also contains the proportion of acicular ferrite and the composition of the dominant type of inclusion, obtained either by microanalysis (Pargeter) or by analogy between the welding fluxes employed in the present work with the ones used by the above author. The correlation between the nature of the deoxidation products and the proportion of acicular ferrite of the welds can be seen in Figure 3 where numbers in brackets indicate the oxygen content. The meaning of  $R/R_1$  will be discussed more extensively but it can be anticipated that this parameter is a quantitative measure of the extension of the plastic zone which surrounds the oxides.

From Figure 3 it is apparent that the proportion of acicular ferrite bears no relationship with the weld metal oxygen content. Thus, it is not possible to simply reduce the direct nucleation model to a one-to-one correlation between inclusion and intragranularly nucleated ferrite grains but it is necessary to take into account the nature of the deoxidation products. In this respect a number of authors have underlined the importance of the degree of lattice misfit between inclusion and matrix. This has recently been demonstrated by Mills, Thewlis and Whiteman (8), who tabulated the misfit values between ferrite and a number of different substrates. They concluded that  $TiO/TiN$  and galaxite ( $Al_2O_3$ ), exhibit very low misfit values with ferrite and therefore can be seen as effective nucleation substrates. However, in the above context galaxite is the most favourable phase, so it is not very clear why the highest proportion of acicular ferrite was detected in welds characterized by high titanium content.

The authors also claim that since  $TiO/TiN$  are formed as discrete particles on the inclusion surface they can act as multiple substrates thus increasing the number of nucleation events associated to a single inclusion, independently of its bulk composition. This interpretation is not supported by the data presented by Saggese et al (10), who examined a series of welds with similar Ti content and proportions of acicular ferrite ranging from 17 to 85%. In fact, the above authors concluded that the formation of that microstructural constituent was favoured by Al-rich rather than Mn-rich inclusions, Ti having been detected in both types of oxides.

Referring to Figure 3 it can be seen that the three types of deoxidation products are ordered in terms of  $R'/R_1$ . This parameter was obtained making use of expressions developed by Brooksbank

& Andrews (11). Details of these calculations have already been reported (9) and results are summarized in Figure 4 in terms of reduced shear stress as a function of distance from the inclusion centre. Therefore  $R'/R_1$  is understood as the ratio of the outer radius of the elasto-plastic zone of the matrix and the radius of the inclusion. In other words, it is a measure of the effect of the contraction stresses. Data for  $Al_2O_3MnO SiO_2$  in a ferritic matrix can be used to compare the calculated with the observed  $R'/R_1$ . Figure 2-a,b confirms that both values are of the same order, giving to the validity of the above calculations. Finally, a more complete test of the present model can be made referring to Figure 3 in which the proportion of acicular ferrite of the API 5L X65 welds and some of Pargeter samples (5) are plotted against  $R'/R_1$  in an austenitic matrix. It has already been mentioned that these data show no correlation between microstructure and oxygen content. However, it is apparent that the percentage of acicular ferrite increases with  $R'/R_1$  that is to say, with the extension of the plastically deformed zone. This trend is very clear if one compares weld metal in which  $MnO SiO_2$  predominates, with the other two series of welds but not when galaxite and  $Al_2O_3 MnO SiO_2$  are analyzed; the expected superiority of welds containing the latter type of inclusion over the ones richer in  $Al_2O_3$  is not totally confirmed by the data. In principle this can be ascribed to small differences in chemical composition of the different samples, and the presence of Nb in welds 1 to 5, only. Thus the behaviour of samples 4 and 5 can be explained by taking into account the effect of Nb on weld metal microstructures, namely a decrease in the proportion of acicular ferrite (12). Another possibility is that since galaxite and  $Al_2O_3SiO_2MnO$  are very close in terms of  $R'/R_1$ , the thermal contraction effect is swamped by small differences of chemical composition.

#### CONCLUSIONS

1. There are evidences that thermal contraction stresses originate dislocations which surround oxide inclusions. These defects can enhance intragranular nucleation of acicular ferrite in weld metals.
2. Calculation shows that plastic zone around the oxides extends to distances comparable to their radius. These distances are related to the thermal expansion coefficients of the matrix and the inclusions and increase with their numerical difference. In the particular case of  $Al_2O_3SiO_2 MnO$  in a ferritic matrix, there is a satisfactory agreement between microstructural observations and theoretical calculation.
3. Examination of 10 weld metal samples shows a positive correlation between the proportion of acicular ferrite and size of the plastic zone.

#### REFERENCES

- (1) Garland, J.C. & Kirkwood, P.R., BSC Report PROD/499/I/74/C.
- (2) Ibidem, BSC Report PROD/MISC/91/74/C.
- (3) Cochrane, R.C. & Kirkwood, P.R., International Conference on "Trends in Steels and Consumables for Welding", pag. 103, The Welding Institute, London (1978).
- (4) Abson, D.J., Dolby, R.E. & Hart, P.H., *idid* pag. 75.
- (5) Pargeter, R.J., The Welding Institute Research Report n° 151/1981.
- (6) Terashima, H. & Tsuboi, J., *Met. Constr.* 14, 472 (1982).
- (7) Ito, Y., Nakanishi, M. & Komizo, Y., *Met. Constr.* 14, 648 (1982).
- (8) Mills, A.R., Thewlis, G. & Whiteman, J., *Mat. Sci. and Technol.* 3, 1051 (1987).
- (9) Ferrante, M., Akune, K. & Odainai, M., *J. Mat. Sci.*, 22, 351 (1987).
- (10) Bhatti, A.R., Saggase, M.E., Hawkins, D.E., Whiteman, J.A. & Golding, M.S., *Weld. J.*, 63, 224-s (1984).
- (11) Brooksbank, D. & Andrews, K.W., *J.I.S.I.*; 210, 246 (1972).
- (12) Watson, M.N., Harrison, P.L. & Farrar, R.A., *Weld and Met. Fabr.*, 49, 101 (1981).



Table I - Mean inclusion composition (%) and physical constants. 25 Cr 5 Ni weld metal.

Al	Si	Cr	Mn	Fe	O (balance)
7.7	24.8	3.1	21.0	1.5	41.9
	<u>Inclusion</u>		<u>Ferritic Matrix</u>		<u>Austenitic Matrix</u>
$\nu$	1/3		1/3		1/3
E	$2 \times 10^{11}$		$7 \times 10^{10}$		$5 \times 10^{10}$
$\alpha$	$2 \times 10^{-6}$		$18 \times 10^{-6}$		$22 \times 10^{-6}$
R <sub>1</sub>	$5 \times 10^{-7}$		$1.3 \times 10^{-5}$		$1.3 \times 10^{-5}$
Y	-		$1 \times 10^8$ (at 800°C)		$1 \times 10^8$ (at 500°C)

$\nu$  = Poisson Ratio

E = Elastic Modulus

$\alpha$  = Mean linear coefficient of thermal expansion

R = Radius of inclusion

Y = Yield stress of the matrix

Table II - Chemical Composition of welds and inclusions; percentage of acicular ferrite

Weld	C	Mn	P	S	Mo	Nb	Si	O	Inclusion	% A.F.
1	0.09	1.46	0.016	0.006	0.19	0.08	0.45	546	MnO SiO <sub>2</sub>	57
2	0.08	1.89	0.019	0.005	0.25	0.06	0.32	357	Al <sub>2</sub> O <sub>3</sub> MnO	70
3	0.07	1.52	0.018	0.004	0.20	0.06	0.36	507	Al <sub>2</sub> O <sub>3</sub> MnO	71
4	0.06	1.66	0.017	0.005	0.19	0.07	0.21	178	Al <sub>2</sub> O <sub>3</sub> MnOSiO <sub>2</sub>	65
5	0.07	1.37	0.019	0.004	0.20	0.07	0.28	363	Al <sub>2</sub> O <sub>3</sub> MnOSiO <sub>2</sub>	62
6	0.09	0.82	0.016	0.009	0.01	-	0.32	220	MnO SiO <sub>2</sub>	41
7	0.09	1.17	0.018	0.021	<0.01	-	0.47	610	MnO SiO <sub>2</sub>	27
8	0.10	1.30	0.020	0.005	0.02	-	0.17	250	Al <sub>2</sub> O <sub>3</sub> MnO	74
9	0.07	1.80	0.031	0.013	<0.01	-	0.39	440	Al <sub>2</sub> O <sub>3</sub> MnOSiO <sub>2</sub>	82
10	0.09	1.27	0.011	0.005	<0.01	-	0.10	190	Al <sub>2</sub> O <sub>3</sub> MnOSiO <sub>2</sub>	70

1 to 5: this work

6 to 10: Pargeter data (5)

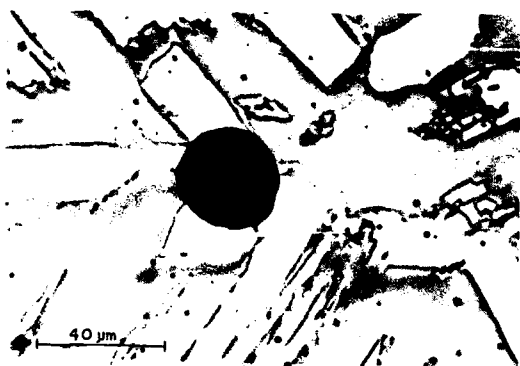
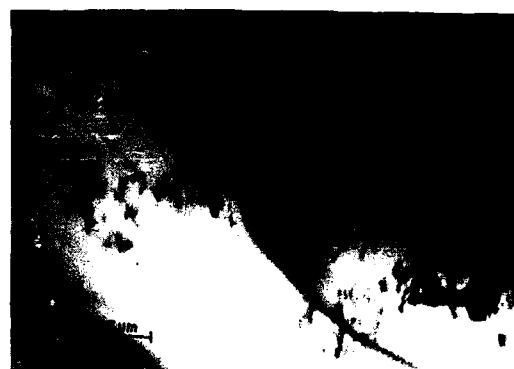


Figure 1: Typical microstructural features observed in the 25 Cr 5 Ni weld metal. Light phase is austenite precipitated on a ferritic matrix.



a



b



c

Figure 2: Transmission electron micrographs of 25 Cr 5 Ni weld metal. Dislocations associated to inclusions can be seen in a and b. An example of nucleation of austenite at an oxygen-rich inclusion is shown in c.

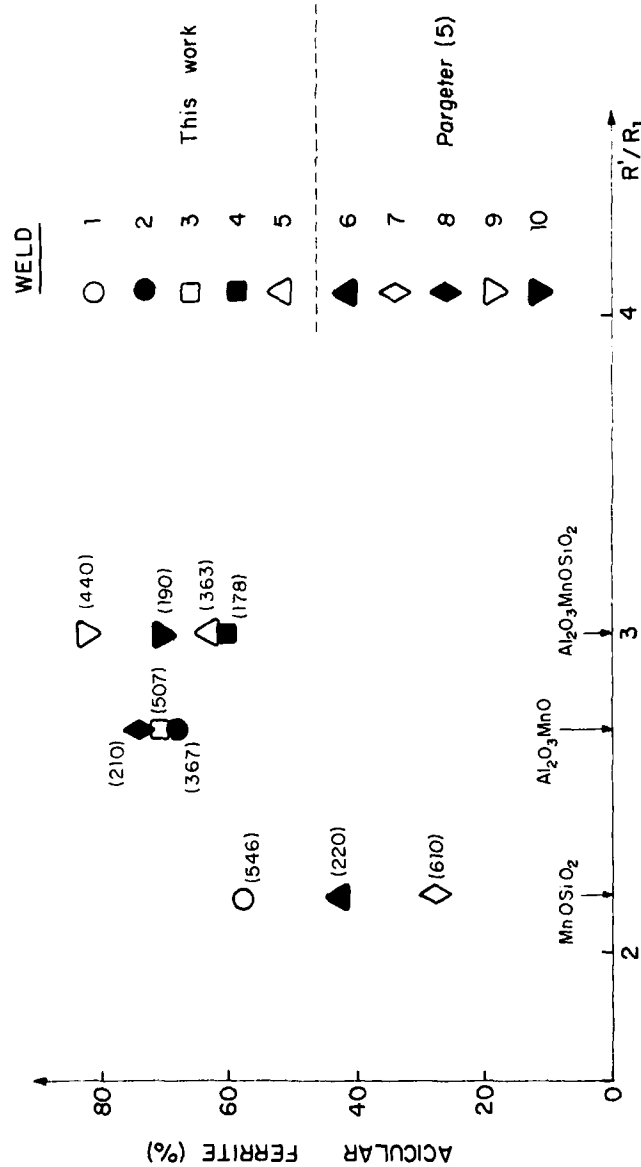


FIG. 3 — Acicular Ferrite Content of a series of API 5LX65 welds, as a function of the nature of the deoxidation products.

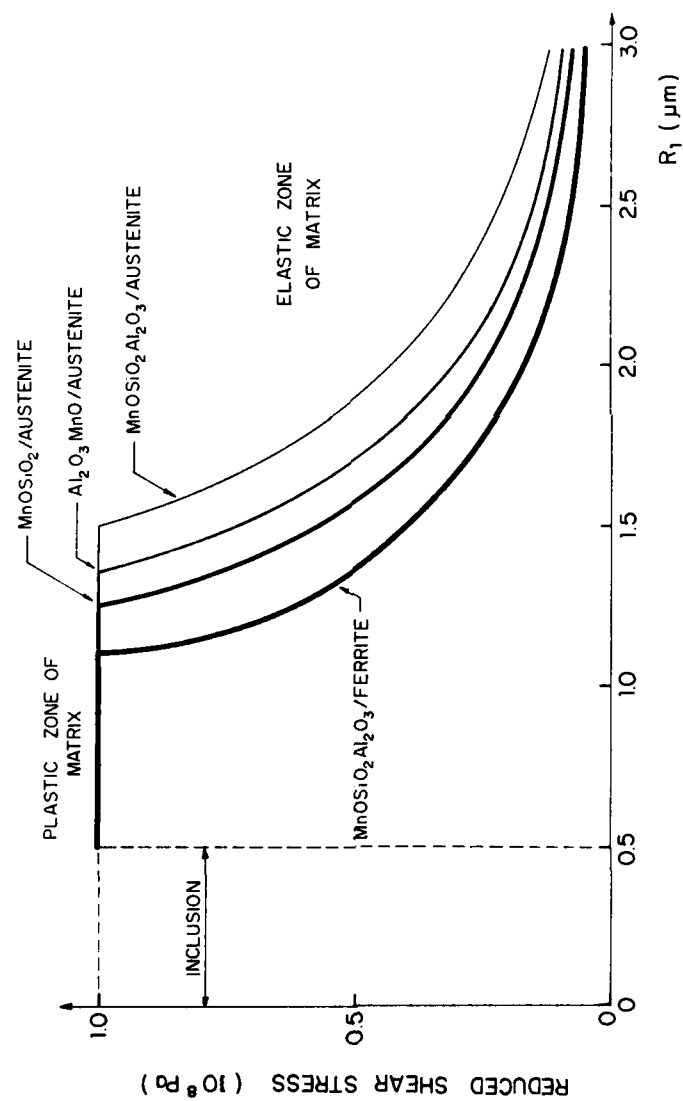


FIG. 4 — Stress distribution around spherical inclusions.